

Dipl.-Phys. Hauke Gravenkamp

**Numerical methods for the simulation
of ultrasonic guided waves**

Die vorliegende Arbeit entstand an der BAM Bundesanstalt für Materialforschung und -prüfung. Von der Fakultät Architektur, Bauingenieurwesen und Umweltwissenschaften der Technischen Universität Carolo-Wilhelmina zu Braunschweig zur Erlangung des Grades eines Doktors der Naturwissenschaften (Dr. rer. nat.) genehmigte Dissertation.

Eingereicht am: 06. Januar 2014

Disputation am: 14. April 2014

Berichterstatter/in: Prof. Dr.-Ing. Sabine Langer, TU Braunschweig
Prof. Dr. rer. nat. Marc Kreuzbruck, BAM Berlin
Prof. Dr. Chongmin Song, UNSW Sydney

Impressum

**Numerical methods for the simulation
of ultrasonic guided waves**

2014

Herausgeber:

BAM Bundesanstalt für Materialforschung und -prüfung

Unter den Eichen 87

12205 Berlin

Telefon: +49 30 8104-0

Telefax: +49 30 8112029

E-Mail: info@bam.de

Internet: www.bam.de

Copyright © 2014 by

BAM Bundesanstalt für Materialforschung und -prüfung

Layout: BAM-Referat Z.8

ISSN 1613-4249

ISBN 978-3-9816380-4-2

Numerical methods for the simulation of ultrasonic guided waves

Dissertation

von

Dipl.-Phys. Hauke Gravenkamp

geboren am 13.06.1983

aus Hamburg

2014

Abstract

Ultrasonic guided waves offer a wide range of applications in fields such as non-destructive testing, structural health monitoring or material characterization. They can be excited in thin-walled structures and propagate over comparably long distances. Due to their complex and dispersive propagation behavior, numerical methods are often required in order to analyze the guided wave modes that can be excited in a given structure and to simulate their interaction with defects.

In the work presented in this thesis, highly efficient numerical methods have been developed that are specifically optimized for guided wave problems. The formulation is based on the Scaled Boundary Finite Element Method (SBFEM). The SBFEM is a semi-analytical method which evolved from the concept of Finite Elements but requires the discretization of the boundary of the computational domain only. To compute dispersion curves and mode shapes of guided waves, only the cross-section of the waveguide is discretized in the Finite Element sense, while the direction of propagation is described analytically. The wavenumbers of guided wave modes and the corresponding mode shapes are obtained as the eigenvalues and eigenvectors of a frequency-dependent Hamiltonian matrix. For the discretization, higher-order spectral elements are employed, leading to very low computational costs compared to traditional Finite Elements. Particular formulations are presented for plate structures as well as axisymmetric waveguides, where only the through-thickness direction has to be discretized. For the cases where the waveguide is embedded in or coupled to a quasi-infinite medium, a dashpot boundary condition is proposed in order to account for the effect of waves being transmitted into the surrounding medium. Though this approach is not exact, it leads to sufficiently accurate results for practical applications, while the computational costs are typically reduced by several orders of magnitude compared to other Finite Element based approaches.

As a particular application, an experimental set-up for material characterization is discussed, where the elastic constants of the waveguide's material are obtained from the analysis of waves propagating through the waveguide. A novel solution procedure is proposed in this work, where each mode of interest is traced over the required frequency range. The solutions are obtained by means of inverse iteration.

To demonstrate the potential of the SBFEM for non-destructive testing applications, the interaction of guided wave modes with cracks in plates is simulated in the time domain for several examples. Particularly for the modeling of cracked structures, the SBFEM is very well suited, since the side-faces of the crack do not require discretization and the stress-singularity at the crack tip does not introduce additional difficulties. Hence, the computational costs can be reduced by typically a factor 100 compared to traditional Finite Elements and the meshing is straightforward.

Contents

Nomenclature	xi
1 Introduction	1
2 Fundamentals	11
2.1 Linear elastodynamics	11
2.1.1 Governing equations	11
2.1.2 Plane strain and plane stress	14
2.2 The Finite Element Method	15
2.3 The Scaled Boundary Finite Element Method	20
3 Derivation for plate structures	25
3.1 SBFEM formulation for guided waves in plates	27
3.2 Discretization using high-order spectral elements	34
3.2.1 Shape functions	35
3.2.2 Numerical integration	36
3.2.3 Element order	37
3.2.4 Plates with varying material parameters	38
3.3 Properties of the eigenvalue problem	39
3.3.1 Properties of the coefficient matrices	39
3.3.2 Hamiltonian structure	39
3.3.3 Algorithms	40
3.4 Group velocity	41
3.5 Shear-horizontal modes	43
3.6 Anisotropy	45
3.7 Details on the implementation	46
3.7.1 Non-dimensionalization	46
3.7.2 Parallelization	46
3.8 Numerical examples	47
3.8.1 Homogeneous plate	47
3.8.2 Layered composite	51
3.8.3 Functionally graded material	53

4	Extension to arbitrary cross-sections	57
4.1	Three-dimensional waveguides	58
4.2	Discretization of three-dimensional waveguides	61
4.2.1	Two-dimensional higher-order elements	61
4.2.2	Symmetry	62
4.3	Mode-tracing	64
4.4	Numerical examples	68
4.4.1	Isotropic circular rod	68
4.4.2	Square pipe	71
5	Axisymmetric waveguides	75
5.1	Axisymmetric formulation of the SBFEM	77
5.2	Real coefficient matrices	81
5.3	Longitudinal and torsional modes	84
5.3.1	Longitudinal modes	84
5.3.2	Torsional modes	85
5.4	Solid cylinders	86
5.5	Numerical examples	87
5.5.1	Isotropic homogeneous pipe	88
5.5.2	Layered rod	90
5.5.3	Anisotropic pipes	92
5.6	Convergence and adaptive meshing	94
6	Embedded waveguides	99
6.1	SBFEM formulation for embedded waveguides	101
6.1.1	One-dimensional dashpot boundary condition	101
6.1.2	Application to plate structures	103
6.1.3	Application to axisymmetric waveguides	106
6.1.4	Absorbing region	107
6.2	Numerical examples	109
6.2.1	Plate attached to infinite medium	109
6.2.2	Varying acoustic impedances	111
6.2.3	Timber pole embedded in soil	115
7	Novel solution procedure	117
7.1	Background	117
7.1.1	Motivation	117
7.1.2	Fundamental equations	119
7.2	Solution procedure	121
7.2.1	Linear approximation	121
7.2.2	Initial values	122
7.2.3	Mode-tracing	126
7.2.4	Inverse iteration	126

7.3	Details of the implementation	128
7.3.1	Dimensionless parameters	128
7.3.2	Adaptive meshing	129
7.3.3	Parallelization	129
7.3.4	The L(0,0) mode	129
7.4	Numerical examples	130
7.4.1	Natural polypropylene (PPN)	130
7.4.2	Polyphenylene oxide (PPO-GF30)	135
8	Simulations in the time domain	137
8.1	SBFEM formulation in the time domain	138
8.2	Problem definition	141
8.3	Discretization	143
8.4	Results	143
8.4.1	Comparison with Finite Element Analysis	143
8.4.2	Reflection of the fundamental Lamb wave modes from a crack	148
9	Concluding remarks	155
	Appendix A	157
A.1	Parameters used for the simulation in Section 1	157
A.2	Equations related to Section 2.3	158
A.3	Equations related to Section 5.2	159
A.4	Inverse iteration for a generalized eigenvalue problem	162
	Bibliography	163
	List of Figures	187
	List of Tables	191
	Acknowledgements	193

Nomenclature

Roman letters

a	Dimensionless frequency
A_i	Amplitude of incident mode
A, B	Amplitudes of waves in one-dimensional approximation
$\mathbf{A}_1, \mathbf{A}_2$	Coefficient matrices of a generalized eigenvalue problem (Section 7.2.1)
$\mathbf{A}, \mathbf{B}, \mathbf{C}$	Coefficient matrices of a quadratic eigenvalue problem (Section 7.2.2)
$\mathbf{b}_1, \mathbf{b}_2, \mathbf{b}_3, \mathbf{b}_4$	Component matrices
$\mathbf{B}_1, \mathbf{B}_2$	Components of shape functions and their derivatives
\mathbf{B}	Strain-displacement transformation matrix
\tilde{c}	Wave velocity in surrounding medium
c_g	Group velocity
c_{gP}	Group velocity approximated by Padé expansion
c_{gT}	Group velocity approximated by Taylor expansion
c_l	Longitudinal wave velocity
c_p	Phase velocity
c_s	Shear wave velocity
$\underline{\underline{\mathbf{C}}}$	Stiffness tensor
\mathbf{C}_0	Damping matrix
d_a	Thickness of absorbing region

D	Elasticity matrix
\tilde{E}	Elastic modulus of surrounding medium
E₀, E₁, E₂	SBFEM coefficient matrices
f	Frequency
f_1, f_2	Volume fractions of a functionally graded material
$\hat{\mathbf{f}}$	External forces
\mathbf{f}_n	External nodal forces
g	Number of degrees of freedom
G	Shear modulus
G_r, G_i	Real and imaginary part of a complex shear modulus
G_a	Shear modulus of absorbing region
h	Thickness of a plate or pipe
i	Imaginary unit
I_n	$n \times n$ identity matrix
$ \mathbf{J} $	Jacobian determinant
J	Jacobian matrix
J_{2g}	Hamiltonian symmetry operator
k	Wavenumber
\tilde{k}	Wavenumber of propagating mode
k_P	Wavenumber approximated by Padé expansion
k_T	Wavenumber approximated by Taylor expansion
k_r, k_i	Real and imaginary part of a complex wavenumber
K	Kinetic energy
K_h	Continued fraction expansion of the stiffness matrix
K	Stiffness matrix
l	Element length

L	Symmetry axis
\mathbf{L}	Differential operator
m	Circumferential order of a mode
M_{cf}	Order of continued fraction
\mathbf{M}_0	Mass matrix
\mathbf{M}	Arbitrary matrix (Chapter 7); Low-order mass matrix (Chapter 8)
\mathbf{M}_h	Continued fraction expansion of the mass matrix
n	Number of nodes
n_λ	Number of wavelenghts in through-thickness direction
N_i	Shape function corresponding to node i in local coordinates
\hat{N}_i	Shape function corresponding to node i in global coordinates
\mathbf{N}	Matrix of shape functions
\mathbf{v}	Continued fraction expansion of displacements
p	Element order
p_z	z component of Poynting vector
P_z	Integrated power flow
P	Pressure distribution
P_p	Legendre polynomial of order p
q	Damping coefficient
\mathbf{q}_n	Internal nodal forces
$\hat{\mathbf{q}}_n$	Internal nodal forces of mode with negative eigenvalue
\mathbf{Q}	Three-dimensional damping coefficient
r_i	Inner radius of a hollow cylinder
r_a	Position within absorbing region
R_c	Ratio of acoustic impedances
R_p	Relative power flow through waveguide

R_{S_0}, R_{A_0}	Reflection parameters
\mathbf{r}	External forces continued fraction expansion
\mathbf{R}	Rotation matrix
S	Strain energy density
\mathbf{S}	Dynamic stiffness matrix
t	Time
u_{ij}	Displacement of node j in i -direction
\tilde{u}	Displacement in surrounding medium
U	Strain energy
\mathbf{u}	Displacement vector
\mathbf{u}_n	Nodal displacements
$\hat{\mathbf{u}}_n$	Nodal displacement amplitudes
$\hat{\mathbf{u}}_n^-$	Displacements of mode with negative eigenvalue
$\hat{\mathbf{u}}_r$	Displacements in rotated coordinate system
$\tilde{\mathbf{u}}_m$	Fourier component of the displacements
w_i	Quadrature weights
W	External work
x, y, z	Cartesian coordinates
$\mathbf{y}_n, \mathbf{z}_n$	Vectors of nodal coordinates
z, θ, r	Cylindrical coordinates
\mathbf{Z}	Z-matrix
\mathbf{Z}_e	Z-matrix of an embedded waveguide

Greek letters

$\alpha_0, \alpha_1, \beta_1, \beta_2$	Padé coefficients
β	Minimum angle of waves being radiated into the surrounding medium

γ_{ij}	Shear strain components
$\gamma_0, \gamma_1, \gamma_2, \gamma_3$	Taylor coefficients
Γ	Boundary of a computational domain
δ_{ij}	Kronecker delta
∂_x	Partial derivative with respect to x
Δ_k	Relative deviation of wavenumbers
Δ_{c_g}	Relative deviation of group velocities
Δ_c	Relative deviation of phase velocities
Δ_a	Relative deviation of attenuations
Δ	Total deviation
ε_{ij}	Strain components
ε_i	Normal strains
$\tilde{\varepsilon}$	Strains in surrounding medium
$\boldsymbol{\varepsilon}$	Strain vector
$\delta\boldsymbol{\varepsilon}$	Virtual strains
$\underline{\boldsymbol{\varepsilon}}$	Infinitesimal strain tensor
ζ	Local coordinate
η	Local coordinate
κ	A small real value
λ	Eigenvalue; Lamé parameter (Section 3.8.3)
$\tilde{\lambda}$	Eigenvalue of propagating mode
ν	Poisson's ratio
ξ	Scaling direction
ω	Angular frequency
Ω	Computational domain

Ω_e	Domain of one element
ρ	Mass density
$\tilde{\rho}$	Mass density of surrounding medium
σ_i	Normal stress components
$\tilde{\sigma}$	Stresses in surrounding medium
σ	Stress vector
$\underline{\underline{\sigma}}$	Stress tensor
τ	Shift applied to eigenvalues
τ_{ij}	Shear stress components
τ	Surface tractions
$\delta\mathbf{u}$	Virtual displacements
φ_{ij}	Angle between two eigenvectors
ϕ	Vector of nodal displacements and forces
Φ	Eigenvector corresponding to negative eigenvalue
ψ	Amplitudes of nodal displacements and forces

Other symbols

∇	Nabla operator
----------	----------------

Abbreviations

ARPACK	Arnoldi Package
b.c.	Boundary condition
BEM	Boundary Element Method
DOF	Degrees of freedom
EFIT	Elastodynamic Finite Integration Technique
FEA	Finite Element Analysis

FEM	Finite Element Method
LAPACK	Linear Algebra Package
MAC	Modal assurance criterion
NDT	Non-destructive testing
SAFE	Semi-Analytical Finite Element Method
SBFEM	Scaled Boundary Finite Element Method
SHM	Structural health monitoring
WFE	Waveguide Finite Element (Method)

Chapter 1

Introduction

Background The work presented in this thesis is motivated in the context of non-destructive testing (NDT) and structural health monitoring (SHM). Numerous techniques have already been developed to assess the integrity of structures in engineering applications [1]. The most common approaches utilize, for instance, ultrasonic waves [2], radiography [3], eddy current [4], magnetic fields [5] or infrared thermography [6]. Each of the methods reveals particular advantages and drawbacks and can only be applied effectively to a limited class of structures and defects. While some techniques are optimized for a time-saving evaluation of large structures [7, 8], others can be employed to find near-surface micro-cracks in small specimen [9, 10]. In many cases, highly problem-dependent requirements, such as limited accessibility, complex geometries, inhomogeneities or strong anisotropy effects have to be considered. Consequently, the development and improvement of non-destructive testing techniques is still a relevant and rapidly evolving research field.

One of the oldest and most-widely used classes of NDT methods utilizes ultrasonic waves to detect defects in a structure or to assess its geometry or material properties [11, 12]. In traditional ultrasonic testing, typically a short pulse is induced in the specimen, using an ultrasonic transducer (Figure 1.1) [2]. A significant amount of wave energy is reflected from cracks, flaws or abrupt changes in material properties (generally speaking, from changes in the acoustic impedance). Provided that the wave velocity in the material under consideration is given, the reflector's position can be estimated from the time of flight of the reflected signal. If the wave velocity is a priori unknown, it can often be deduced from a reflection off the back wall of the specimen.

Obviously, even for the simplest structures, the actual wave propagation is more complicated than indicated in Figure 1.1 [13, 14]. Results of a two-dimensional Finite Element Analysis are presented in Figure 1.2 to visualize wave propagation in a quasi-infinite solid. A pulse containing few cycles is applied normal to a small area on the boundary of a solid domain (Figure 1.2a). The size of the domain is large compared to the wavelength of sound waves that are excited at the chosen frequency.¹ Figure 1.2b shows a snapshot of the waves propagating through the solid. The pulse is separated into several components, traveling at different velocity. The

¹The geometry and material parameters used for the simulation are presented in Appendix A.1.

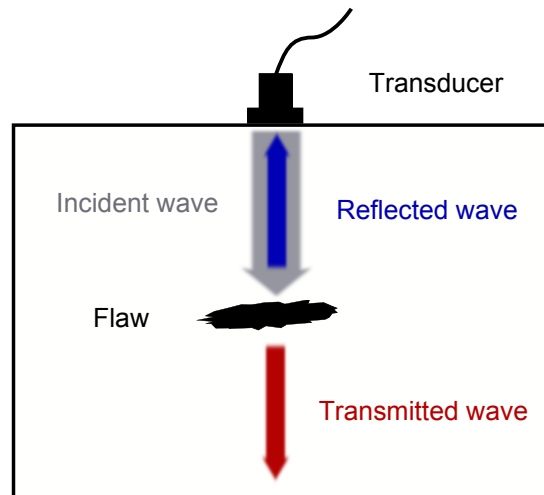


Figure 1.1: Detection of a defect by means of traditional ultrasonic material testing.

majority of ultrasonic testing techniques rely on longitudinal waves, since they have the highest wave velocity and can generally be excited with high amplitude. Then again, certain applications exist that utilize the propagation behavior of shear waves, e. g. for the non-destructive evaluation of welds. The velocity of shear waves is roughly two times smaller for many solids. In case of normal excitation as in the given example, shear waves are divided into two wave packages. These wave packages penetrate the solid under an angle that depends on the material's elastic parameters. In addition to longitudinal and shear waves, surface or interface waves (in the present example Rayleigh waves [15–17]) can be excited, which propagate with a velocity slightly lower than the shear wave velocity.

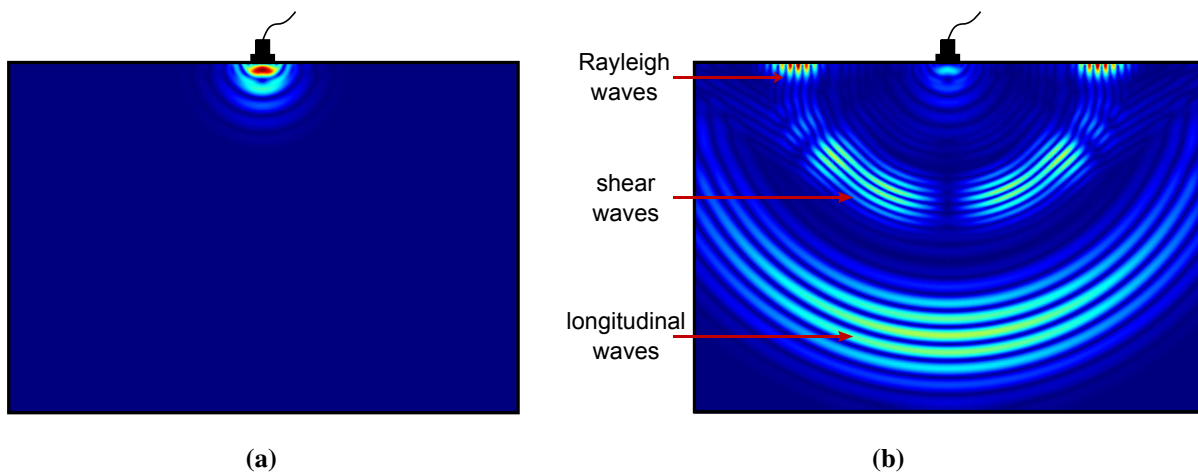


Figure 1.2: (a) Excitation of waves in a large homogeneous solid. (b) Propagation of longitudinal, shear and Rayleigh waves.

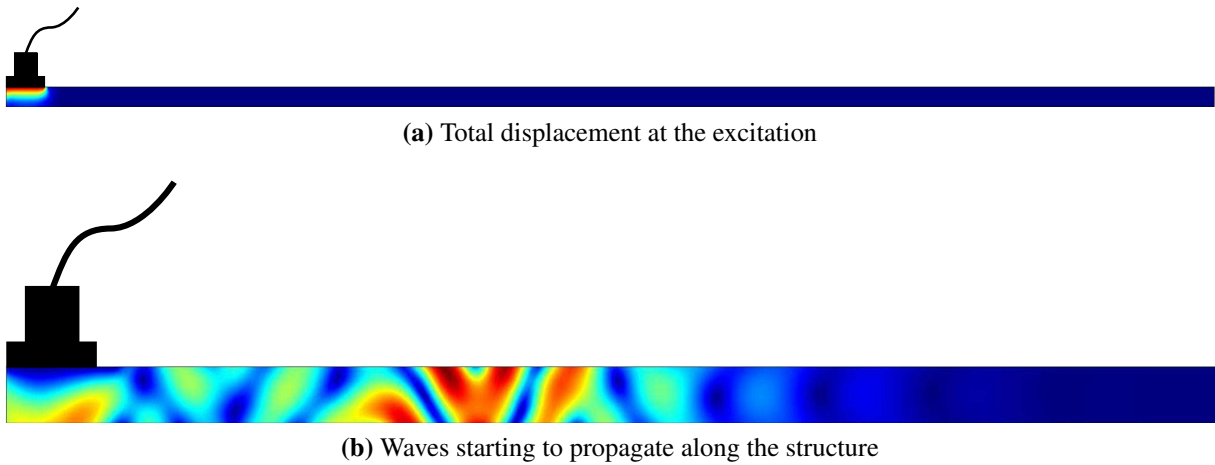


Figure 1.3: Cross-sectional view of a homogeneous plate with an ultrasonic transducer coupled to the upper surface. When exciting an ultrasonic pulse (a) a complex displacement field is induced in the vicinity of the excitation (b).

Let us now assume that instead of a quasi-infinite media, the same ultrasonic transducer is placed on the surface of a thin plate (i. e. the thickness is comparable to the ultrasonic wavelengths of longitudinal and shear waves at the given frequency), as shown in Figure 1.3a. Obviously, we cannot expect longitudinal and shear waves to propagate independently through the media. Quite the contrary, the whole thickness of the plate close to the transducer position is subjected to stresses almost instantaneously. The superposition of vertical and horizontal movements results in a complex displacement field depending on frequency, thickness, material parameters and boundary conditions. As a consequence, a rather complicated and rapidly evolving disturbance starts propagating along the thin structure (Figure 1.3b). This phenomenon is referred to as *guided waves* [18], due to the geometrical restrictions imposed on the wave propagation. Even though the current work addresses elastic guided waves in solids, very similar considerations can be applied to acoustic or electromagnetic waves [19]. A principal characteristic of guided waves is their tendency to form certain propagating modes that can travel along the structure. This effect can be observed in the presented simulation at some distance from the point of excitation (Figure 1.4) and is best visible when plotting the horizontal and vertical displacement amplitudes separately. In the given example, two propagating modes with very different wavelengths and velocities are excited, so that after a relatively short time two well-separated wave packages can be observed. The faster mode shows mainly horizontal displacements (Figure 1.4a) while in the slower mode vertical displacements are dominant (Figure 1.4b).

In the through-thickness direction, each mode creates a characteristic field distribution (mode shape), somewhat similar to standing waves in any other confined geometry. Along the structure this displacement field propagates as a harmonic wave with a characteristic wavenumber. The modes are generally strongly dispersive, i. e. the mode shapes and wavenumbers (and hence the phase and group velocities) depend on frequency. This is due to the fact that, for varying

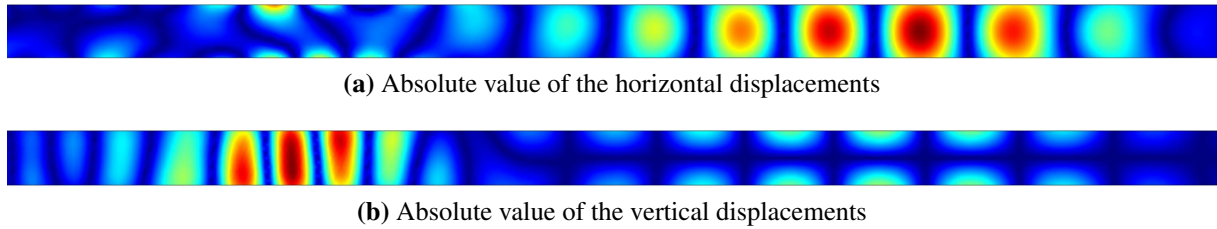


Figure 1.4: (a) Horizontal and (b) vertical displacements of the fundamental guided wave modes.

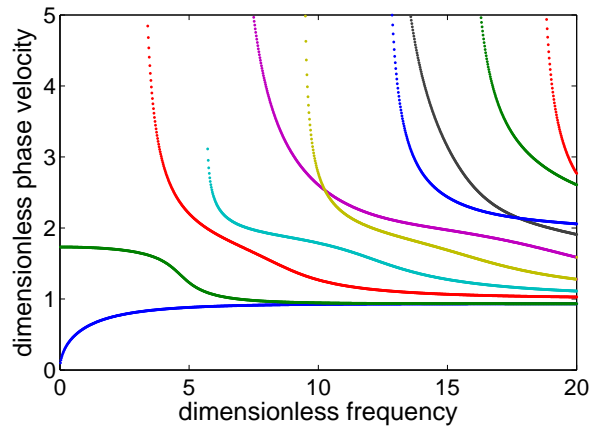


Figure 1.5: Phase velocities of propagating modes in a homogeneous isotropic plate.

frequency, the ratio of wavelength to thickness of the structure changes (for both longitudinal and shear waves). The number of propagating modes that can be excited in the structure, increases with frequency, tending towards infinity. Figure 1.5 shows a typical dispersion diagram for a simple plate, where the phase velocities are plotted as a function of (dimensionless²) frequency. The computation of these dispersion properties and the corresponding mode shapes plays a predominant role in this thesis.

Guided waves in homogeneous isotropic plates were described analytically back in 1917 by Horace Lamb [20] and are nowadays commonly referred to as *Lamb waves*. Later elastic guided waves in different structures, such as cylinders [21], pipes or rails [22] were analyzed theoretically and experimentally. It was noticed long ago that ultrasonic guided waves can be used in non-destructive testing [23–29] and structural health monitoring [30–32] of thin structures. As they propagate along the structure, they can be reflected by defects in the material similarly to traditional ultrasonic testing. The advantage of utilizing guided waves resides in the fact that

²Dimensionless parameters are defined in Section 3.7.1.

they can propagate over comparably long distances³, while inducing stresses throughout the whole thickness. Hence, they can be used to test a large part of the structure with a single excitation, rather than scanning the complete surface with an ultrasonic transducer. Even though the sensitivity is typically low compared to conventional ultrasonic testing, guided waves can be an adequate tool for time efficient testing of e. g. large plate structures or pipelines.

More recently, it has been suggested to employ guided waves in material characterization applications [33–36]. For instance, the elastic constants of a cylinder can be deduced by analyzing guided wave propagation through the material. In a different approach, the density of a fluid is determined by analyzing its effect on the wave propagation in an immersed waveguide [37–39].

Dispersion relations An obvious problem arising in most applications of guided waves lies in the fact that typically complex signals have to be evaluated. Depending on frequency, a high number of modes can be excited in a waveguide, each of them having its own characteristic phase and group velocity. Moreover, the excitability of the modes as well as their sensitivity to different types of defects differs greatly in a given set-up. For this reason, sophisticated analytical and/or numerical calculations are involved to plan and conduct experiments. Additionally, advanced signal processing has to be applied in order to analyze the results. The first crucial step is usually to obtain the dispersion curves and mode shapes of propagating modes that can be excited within the frequency range of interest. In order to do that, wave propagation is typically modeled in an infinite waveguide with the given cross-section. This can be a difficult and computationally expensive task, depending on geometry and material properties. For the simplest case of Lamb waves in homogeneous isotropic plates, the wave propagation can be described analytically by imposing adequate boundary conditions to the elastodynamic wave equation [15]. As a result, equations for the wavenumbers of Lamb waves that can propagate in the plate are obtained. However, to solve for the wavenumbers, sophisticated root-finding algorithms have to be employed. The main difficulty lies in the fact that an a priori unknown number of solutions have to be found, while standard root-finding algorithms converge to one solution only. Similar problems occur when describing wave propagation in homogeneous axisymmetric structures [40].⁴ Many attempts have been made to model more complex structures analytically, but the scope is fairly limited [41, 42].

A well-known approach that can be utilized to compute dispersion curves for layered plates and axisymmetric structures is the *Transfer Matrix Method* [43, 44]. Later, the *Global Matrix Method* [45–47] was introduced as an extension, mainly to avoid numerical problems at high frequencies. The basic idea of these matrix methods is to describe the reflection and transmission at each interface between two layers (or a layer and a surrounding medium or vacuum). A matrix that relates the displacement field at these interfaces is assembled. Non-trivial so-

³Since guided waves propagate within a confined space rather than being dissipated into a large volume, their attenuation is small compared to ultrasonic waves in a quasi-infinite media.

⁴In this introduction, a very brief overview of the different classes of approaches is given. More detailed discussions of the techniques available for different geometries are presented at the beginning of the corresponding chapters.

lutions are found by setting the determinant of this matrix to zero, which again leads to a root-finding problem for the wavenumbers. Matrix methods have been employed for various different problems [48, 49]. The commercial software *disperse* [50, 51], used for calculating dispersion relations for plates and cylinders, as well as the free *Matlab* code *PCDisp* [52, 53], used for cylindrical waveguides, make use of these matrix methods. However, the solution can be very cumbersome for complex structures, for instance if many layers, anisotropy or material damping have to be considered.

From today's point of view, an obvious idea to model waveguides of complex geometry is to employ the Finite Element Method (FEM). Early attempts to deal with this class of problems were presented by Gladwell and Tahbaldar [54]. As the Finite Element Method has been further developed and become more popular, it has been utilized by numerous authors for the simulation of guided waves (see e. g. [55–57]). Recently, it has been demonstrated how modern commercial Finite Element software can be employed to obtain dispersion relations by discretizing a representative part of the structure [58]. In contrast to that, rather specialized Finite Element based techniques have been developed for guided wave modeling. In one approach a unit length section of a three-dimensional waveguide is assessed [59]. This idea is often referred to as Waveguide Finite Element (WFE) method. Somewhat similarly, models have been presented that involve a Finite Element discretization of the waveguide's cross-section only [60–63]. This approach, nowadays mostly known as Semi-Analytical Finite Element (SAFE) Method has been applied to composite plates [64, 65], anisotropic composite cylinders [66, 67], axisymmetric damped waveguides [68], as well as rods and rails [22]. The software *GUIGUW* [69], which uses a SAFE formulation is under development and free demo versions are already available. The major drawback of these Finite Element based approaches is that they generally lead to high computational costs, particularly for high frequencies. The computational times required by these approaches are not acceptable in many applications, for instance when the dispersion relations have to be computed many times in the frame of an inverse analysis. A different problem (that will be focused on in detail in Chapter 6) lies in the fact that it is very cumbersome to model the interaction of guided waves with a surrounding media using Finite Elements. This drawback becomes crucial in many engineering applications, for instance when modeling buried pipes, poles embedded in soil or plates immersed in a fluid.

Time domain analysis The computation of dispersion relations and mode shapes is an essential task in most applications of guided waves and the first crucial step in order to analyze the wave propagation in the waveguide of interest. However, it often does not suffice to predict the propagation in a realistic structure. For instance, in non-destructive testing applications we are interested in modeling the interaction of an ultrasonic pulse with different types of defects in the material. Furthermore, a realistic waveguide can reveal changes in geometry or material properties along the propagation direction or it may be subjected to complex boundary conditions. In order to conduct a simulation of the entire set-up, a fully numerical modeling is required. Again, the most common approach is the Finite Element Method, as it is a very general and flexible tool, where arbitrary geometries or materials and numerous different boundary conditions can be described. Unfortunately, the simulation of guided waves is computationally

extremely expensive due to the typically large dimensions of the structures, high frequencies (leading to small time steps in the simulation) and correspondingly small wavelengths (requiring very fine spatial discretization) [70]. Additionally, when modeling cracked structures, an extremely fine discretization is needed due to the stress singularity at the crack tip. Several alternative methods have been applied to the simulation of guided waves, leading to comparable computational costs. For instance, the well-known Boundary Element Method (BEM) can be employed [71–73]. Using this method, only the boundary of the computational domain is discretized, which reduces the dimension of the resulting matrix equations but imposes restrictions on the properties of the domain. For instance, this method is not well-suited if the distribution of material parameters is complex or if small cracks are introduced in the structure. Furthermore, the modeling of anisotropic materials is not trivial. Other numerical methods that can be found in the literature include traditional Finite Differences (FD) [74] or the Elastodynamic Finite Integration Technique (EFIT) [75, 76].

The Scaled Boundary Finite Element Method As an alternative to the previously mentioned numerical approaches, the Scaled Boundary Finite Element Method (SBFEM) has been proposed by Wolf and Song in the 1990s [77–79] and evolved rapidly over the last years. This method originated from concepts to model unbounded domains using Finite Element techniques [80]. Its basic idea is to only discretize the boundary of a computational domain and translate the resulting mesh along a *scaling direction* in order to describe the complete geometry. This generally leads to semi-analytical equations for the physical variables (details will be presented in Chapter 2.3). This concept has been extended to describe bounded domains by scaling the discretization of the boundary with respect to a *scaling center*, which is positioned somewhere in the interior of the domain. Both formulations for bounded and unbounded domains have been applied successfully to many problems in elastostatics [81, 82] and elastodynamics [83–85] as well as diffusion [86]. In many applications it drastically reduces computational costs compared with the traditional Finite Element Method. Particularly, this method is advantageous when modeling cracked structures. As has been demonstrated in numerous applications [87–89], the side-faces of a simple crack do not require discretization and the stress-singularity can be treated in an elegant way. Recently, sophisticated solution procedures have been developed that are suited to employ the SBFEM for elastodynamic problems at high frequency⁵ [90]. However, the current work is, to the author’s knowledge, the first attempt to apply this method to the modeling of ultrasonic wave propagation.

The SBFEM is a promising tool for the analysis of guided waves for several reasons. First, we are typically addressing large but highly regular structures. These geometries can be described effectively by discretizing the boundary only. Second, in NDT and SHM applications the interaction of ultrasonic waves with cracks is of interest. The efficient discretization of cracks is one of the major advantages of this method. Third, in these applications, simulations typically have to be performed many times with slightly varying geometry or material parame-

⁵From the perspective of numerical analysis, high frequency means that the smallest relevant wavelength is significantly smaller than the dimension of the structure. Hence, the frequency range has to be discussed in conjunction with the material parameters and the typical size of the structure, see Section 3.7.1.

ters. This is done either for numerical studies to analyze the interaction of wave modes with different defects, or to solve an inverse problem. The simple discretization of the geometry and particularly a crack allows for a highly efficient re-meshing in the SBFEM, compared to standard FEM approaches.

Outline In the following chapter, some basic concepts are presented that will be referred to throughout the thesis. The required governing equations of elastodynamics are briefly summarized in the first section. After that, some very basic Finite Element techniques are described as far as they are essential to understand the derivation of the Scaled Boundary Finite Element Method. A short introduction to the SBFEM is given to explain the underlying concept and highlight the differences and commonalities with traditional Finite Elements.

Chapter 3 addresses guided waves in plate structures. An approach is developed to compute dispersion relations and mode shapes. For additional information, the reader is also referred to the corresponding publications [91–93]. It is based on the SBFEM but is highly specialized for the application of guided waves and hence is derived in much detail. Only the through-thickness direction of a plate structure has to be discretized in the Finite Element sense, while the direction of propagation is described analytically. For the discretization, a recently developed class of higher-order spectral elements is employed that drastically increases computational efficiency. Additionally, a new approach to compute the group velocities of propagating modes is derived in this work.

In Chapters 4 and 5 the computation of dispersion relations is extended to include general three-dimensional waveguides of arbitrary cross-section (see also [94, 95]) and axisymmetric waveguides [96–98], respectively. The extension to the three-dimensional case is generally straightforward but involves a discretization with two-dimensional elements. This can be cumbersome and computationally much more expensive than in the case of plate structures. It is discussed how two-dimensional higher-order elements can be applied effectively and how symmetry axes can be utilized to reduce computational costs. In addition, a novel mode-tracing algorithm is developed in order to determine which solutions in the dispersion curves represent the same modes. For the modeling of axisymmetric waveguides, the governing equations are formulated in a cylindrical coordinate system. The displacement field in the circumferential direction is decomposed by means of a Fourier series. As a result, only the through-thickness direction of the waveguide has to be discretized, similarly to the case of plate structures.

In Chapter 6, embedded waveguides are discussed [99]. This topic is of high relevance in many practical applications, but the modeling of embedded waveguides is extremely cumbersome and computationally expensive in other approaches. In this work, the effect of the surrounding medium is approximated by a simple dashpot boundary condition that can easily be implemented and does not require any additional degrees of freedom compared to a free waveguide.

A novel solution procedure for particular applications is presented in Chapter 7 (see [100]). It is based on the SBFEM formulation but uses a different technique to solve for the wavenumbers and mode shapes of propagating modes. In contrast to the general formulation, it is possible to selectively trace the modes that can be excited in a given set-up. This procedure can be highly

advantageous in terms of computational efficiency.

Chapter 8 applies the general transient elastodynamic formulation of the SBFEM to the simulation of guided waves in plates [101–104]. In particular, the presented work focuses on the interaction of the fundamental Lamb wave modes with cracks of different depth and opening angle. The efficiency of the SBFEM is highlighted by comparing the results with standard Finite Element Analysis.

Chapter 9 gives a short conclusion of the presented work and discusses possible further developments and additional applications.

Chapter 2

Fundamentals

2.1 Linear elastodynamics

2.1.1 Governing equations

This work focuses on wave propagation in solid media. Since the amplitudes of ultrasonic waves that are excited in non-destructive testing applications are generally very small, we can assume linear material behavior. For linear elastic media, the governing equation relating stresses and strains at any point of the domain under consideration, is the generalized Hooke's law [105]

$$\underline{\underline{\boldsymbol{\sigma}}} = \underline{\underline{\mathbf{C}}} : \underline{\underline{\boldsymbol{\varepsilon}}} \quad (2.1)$$

where $\underline{\underline{\boldsymbol{\sigma}}}$ and $\underline{\underline{\boldsymbol{\varepsilon}}}$ denote the Cauchy stress tensor and the infinitesimal strain tensor, respectively, and $\underline{\underline{\mathbf{C}}}$ is the fourth-order stiffness tensor. For instance, in a three-dimensional Cartesian coordinate system the stress and strain tensors read

$$\underline{\underline{\boldsymbol{\sigma}}} = \begin{bmatrix} \sigma_{xx} & \sigma_{xy} & \sigma_{xz} \\ \sigma_{yx} & \sigma_{yy} & \sigma_{yz} \\ \sigma_{zx} & \sigma_{zy} & \sigma_{zz} \end{bmatrix}, \quad \underline{\underline{\boldsymbol{\varepsilon}}} = \begin{bmatrix} \varepsilon_{xx} & \varepsilon_{xy} & \varepsilon_{xz} \\ \varepsilon_{yx} & \varepsilon_{yy} & \varepsilon_{yz} \\ \varepsilon_{zx} & \varepsilon_{zy} & \varepsilon_{zz} \end{bmatrix} \quad (2.2)$$

When modeling ultrasonic wave propagation, we are mainly interested in the resulting displacement field. Denoting the three-dimensional displacement vector at a given position by $\mathbf{u} = [u_x \ u_y \ u_z]^T$, the strain-displacement relationship is given by

$$\underline{\underline{\boldsymbol{\varepsilon}}} = \frac{1}{2}(\nabla \mathbf{u} + (\nabla \mathbf{u})^T) \quad (2.3)$$

with the Nabla operator ∇ . Note that $\nabla \mathbf{u}$ denotes a dyadic product, hence the components of the strain tensor are explicitly given by

$$\underline{\underline{\boldsymbol{\varepsilon}}} = \begin{bmatrix} \partial_x u_x & \frac{1}{2}(\partial_y u_x + \partial_x u_y) & \frac{1}{2}(\partial_z u_x + \partial_x u_z) \\ \frac{1}{2}(\partial_x u_y + \partial_y u_x) & \partial_y u_y & \frac{1}{2}(\partial_z u_y + \partial_y u_z) \\ \frac{1}{2}(\partial_x u_z + \partial_z u_x) & \frac{1}{2}(\partial_y u_z + \partial_z u_y) & \partial_z u_z \end{bmatrix} \quad (2.4)$$

where ∂_i denotes the partial derivative with respect to i . It follows immediately from Equation (2.4) that the strain tensor is always symmetric, hence it consists of six independent components. Using index notation, these components can be written as

$$\varepsilon_{ij} = \frac{1}{2}(\partial_i u_j + \partial_j u_i) \quad (2.5)$$

with $\varepsilon_{ij} = \varepsilon_{ji}$. Using Voigt notation for symmetric tensors [106], we can collect the six independent components in one strain vector, rather than dealing with a second-order tensor. This notation is generally favorable when applying numerical methods in order to avoid the use of redundant components and higher-order tensors. We define the strain vector as

$$\boldsymbol{\varepsilon} = [\varepsilon_x \ \varepsilon_y \ \varepsilon_z \ \gamma_{yz} \ \gamma_{xz} \ \gamma_{xy}]^T \quad (2.6)$$

with

$$\varepsilon_i \equiv \varepsilon_{ii} \quad (2.7a)$$

$$\gamma_{ij} \equiv 2\varepsilon_{ij} = \partial_i u_j + \partial_j u_i \quad (2.7b)$$

The components γ_{ij} are commonly referred to as engineering shear strains. With these definitions, the strain-displacement relationship can compactly be written as

$$\boldsymbol{\varepsilon} = \mathbf{L} \mathbf{u} \quad (2.8)$$

Here \mathbf{L} denotes the three-dimensional differential operator

$$\mathbf{L} = \begin{bmatrix} \partial_x & 0 & 0 & \partial_y & \partial_z & 0 \\ 0 & \partial_y & 0 & \partial_x & 0 & \partial_z \\ 0 & 0 & \partial_z & 0 & \partial_x & \partial_y \end{bmatrix}^T \quad (2.9)$$

Analogously to Equation (2.6) we define the stress vector as

$$\boldsymbol{\sigma} = [\sigma_x \ \sigma_y \ \sigma_z \ \tau_{yz} \ \tau_{xz} \ \tau_{xy}]^T \quad (2.10)$$

Here we simply define⁶

$$\sigma_i \equiv \sigma_{ii} \quad (2.11a)$$

$$\tau_{ij} \equiv \sigma_{ij} \quad (2.11b)$$

Hook's law in vector notation reads

$$\boldsymbol{\sigma} = \mathbf{D}\boldsymbol{\varepsilon} \quad (2.12)$$

where \mathbf{D} is the 6×6 elasticity matrix. For instance, in case of an isotropic material the elasticity matrix is given by

$$\mathbf{D} = \frac{2G}{(1-2\nu)} \begin{bmatrix} 1-\nu & \nu & \nu & & & \\ \nu & 1-\nu & \nu & & & \\ \nu & \nu & 1-\nu & & & \\ & & & \frac{1-2\nu}{2} & & \\ & & & & \frac{1-2\nu}{2} & \\ & & & & & \frac{1-2\nu}{2} \end{bmatrix} \quad (2.13)$$

with the shear modulus G and Poisson's ratio ν . If the stresses are given, the strains can be obtained after inversion of the elasticity matrix (which is always non-singular and symmetric):

$$\mathbf{D}^{-1}\boldsymbol{\sigma} = \boldsymbol{\varepsilon} \quad (2.14)$$

Denoting by $\hat{\mathbf{f}} = [\hat{f}_x \hat{f}_y \hat{f}_z]^T$ any loads acting on the solid, the equilibrium equations of elastostatics are given by

$$\sigma_{ji,j} + \hat{f}_i = 0 \quad (2.15)$$

or

$$\mathbf{L}^T \boldsymbol{\sigma} + \hat{\mathbf{f}} = 0 \quad (2.16)$$

Adding an inertial term leads to the equation of motion [105]

$$\mathbf{L}^T \boldsymbol{\sigma} - \rho \ddot{\mathbf{u}} + \hat{\mathbf{f}} = 0 \quad (2.17)$$

where \mathbf{u} is the displacement vector, $(\ddot{\cdot})$ denotes the second derivative with respect to time and ρ is the mass density. Equation (2.17) is also known as the elastodynamic wave equation. It can be transferred into frequency domain to read

$$\mathbf{L}^T \boldsymbol{\sigma} + \omega^2 \rho \mathbf{u} + \hat{\mathbf{f}} = 0 \quad (2.18)$$

with ω being the angular frequency.

⁶The variables τ_{ij} are only introduced to distinguish between normal and shear stresses according to common practice.

2.1.2 Plane strain and plane stress

It is often desirable to simplify the modeling of a physical process by replacing the domain of interest by an adequate two-dimensional geometry. However, in general elastodynamics there is no unique two-dimensional representation of the governing equations. Instead one usually chooses between two approximations, namely the *plane strain* and *plane stress* assumption, respectively. Assume for instance the displacement field is independent of one coordinate, say x . This approximation is often valid if the domain of interest is of quasi-infinite dimension in this direction. If this is the case, the strains are restricted to the yz -plane, hence the plane strain assumption is valid. The strains are then written as⁷

$$\boldsymbol{\varepsilon} = [\varepsilon_y \ \varepsilon_z \ \gamma_{yz}]^T \quad (2.19)$$

and the elasticity matrix in case of isotropic material behavior⁸ follows from Equation (2.13) by eliminating the rows and columns corresponding to the unused degrees of freedom:

$$\mathbf{D}_{\text{pl.strain}} = \frac{2G}{(1-2\nu)} \begin{bmatrix} 1-\nu & \nu & & \\ \nu & 1-\nu & & \\ & & & \frac{1-2\nu}{2} \end{bmatrix} \quad (2.20)$$

The plane stress approximation on the other hand is applied when the stresses can be assumed to have non-zero values only within a plane, e. g.

$$\boldsymbol{\sigma} = [\sigma_y \ \sigma_z \ \tau_{yz}]^T \quad (2.21)$$

The strains are obtained by eliminating the unused degrees of freedom from the inverse of the elasticity matrix \mathbf{D}^{-1} (cf. Equation (2.14)). Inverting the resulting matrix again yields the elasticity matrix in the plane stress approximation:

$$\mathbf{D}_{\text{pl.stress}} = \frac{2G}{1-\nu} \begin{bmatrix} 1 & \nu & & \\ \nu & 1 & & \\ & & & \frac{1-\nu}{2} \end{bmatrix} = \begin{bmatrix} \frac{E}{1-\nu^2} & \frac{E\nu}{1-\nu^2} & & \\ \frac{E\nu}{1-\nu^2} & \frac{E}{1-\nu^2} & & \\ & & & G \end{bmatrix} \quad (2.22)$$

with the Young's modulus $E = 2G(1 + \nu)$. Note that in terms of implementation both approximations differ only by the definition of the elasticity matrix. In both cases the strains, stresses and displacements are restricted to one plane. The difference is that when using the plane strain/stress assumption the unused strain/stress components are neglected initially and the resulting stresses/strains are obtained based on this simplification.

⁷For the sake of conciseness, the same symbols are used irrespective of the coordinate system, when the meaning is obvious from the context.

⁸If general anisotropy has to be considered, all strain components can be coupled. In this case the plane strain assumption often does not yield a satisfactory approximation (see Section 3.6).

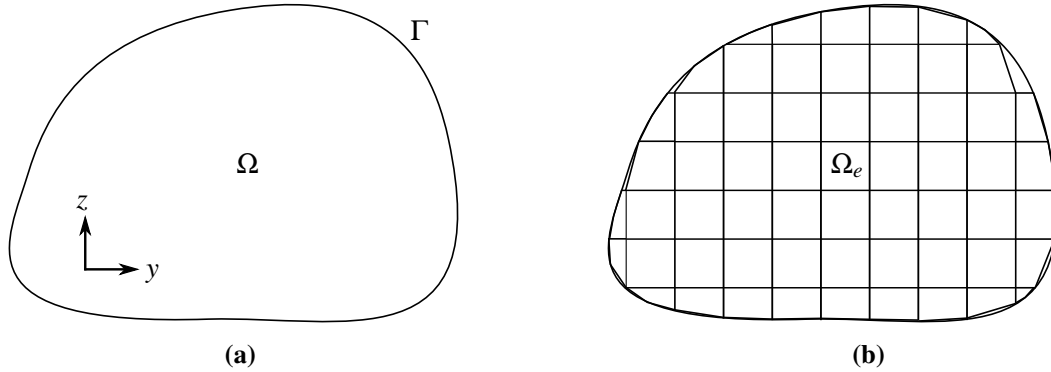


Figure 2.1: (a) Computational domain Ω with boundary Γ ; (b) schematic discretization using four-sided elements.

2.2 The Finite Element Method

The purpose of this and the following section is to briefly introduce the concept of the Scaled Boundary Finite Element Method in comparison with the traditional Finite Element Method. For conciseness, the formulation will be restricted to the simple case of two-dimensional elastostatics. Only the most essential equations that are required to clarify the underlying concepts will be presented in this chapter. For a more detailed description of the existing formulations, the reader is referred to well-known textbooks on the FEM [107–109] as well as key publications on the SBFEM [77, 78, 90, 110] and the only textbook on this method published so far [79]. For the particular case of ultrasonic waves in elastic waveguides, special formulations of the SBFEM will be derived in detail in the following chapters.

Consider a two-dimensional arbitrarily shaped (but finite) domain, denoted by Ω as indicated in Figure 2.1a. For now, it is assumed to consist of a homogeneous solid medium, hence the governing equations formulated in the previous section can be applied. The idea of the traditional FEM is to divide the computational domain Ω into a finite number of subdomains (elements) Ω_e , such that (Figure 2.1b)

$$\Omega \approx \sum_e \Omega_e \quad (2.23)$$

Within each element, it is assumed that the (unknown) displacement field can be approximated using simple polynomial functions of given order, the so-called shape functions. In our two-dimensional example, these polynomials are functions of both y and z and they are used to approximate both components of the displacement vector separately. For instance, consider a rectangular element, on which we choose to approximate the displacement field by second-order (*quadratic*) polynomials in each direction.⁹ Generally the approximation is unique, if the displacements are known at a sufficient number of points, depending on the order of the poly-

⁹This type of element is very common in traditional Finite Element analysis. However, there are numerous other possibilities that will not be discussed here. In the SBFEM we choose four-sided (if not one-dimensional) isoparametric higher-order spectral elements that will be introduced in the following chapters.

nomials. Consequently it suffices to compute the solution at a given number of discrete points rather than trying to solve for the continuous displacement field. The discrete points are referred to as nodes.

More precisely, one shape function $\hat{N}_i(y, z)$ is assigned to each node within an element. The shape function corresponding to node i is defined to equal one at this node and zero at all other nodes. Examples are presented in Figures 2.2a and 2.2b. The analytical functions for this type of two-dimensional element are given in Table 2.1.

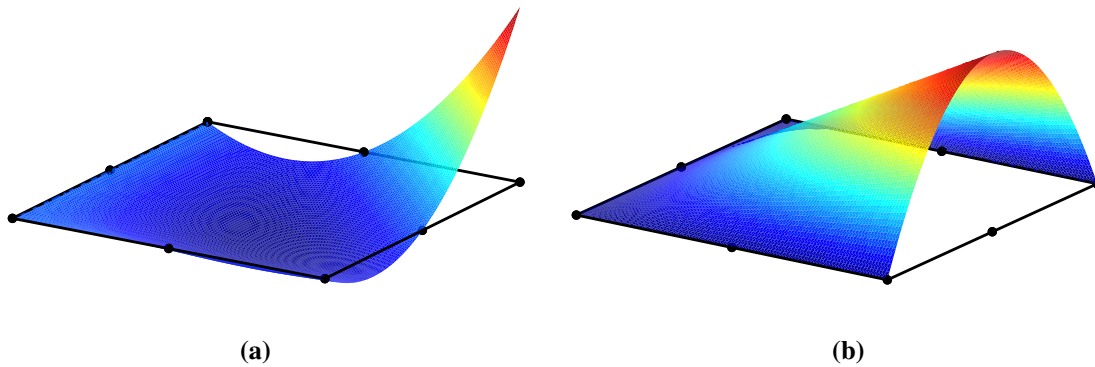


Figure 2.2: Rectangular element and examples for quadratic shape functions corresponding to (a) a corner node and (b) a node on the edge.

Table 2.1: Nodal coordinates η_i , ξ_i and corresponding shape functions for a quadratic element in one and two dimensions [111].

i	2D		1D	
	(η_i, ξ_i)	$N_i(\eta, \xi)$	η_i	$N_i(\eta)$
1	(1, 1)	$\frac{1}{4}(1 + \eta)(1 + \xi) - \frac{1}{2}N_5 - \frac{1}{2}N_8$	-1	$\frac{1}{2}(1 - \eta) - \frac{1}{2}(1 - \eta^2)$
2	(-1, 1)	$\frac{1}{4}(1 - \eta)(1 + \xi) - \frac{1}{2}N_5 - \frac{1}{2}N_6$	0	$(1 - \eta^2)$
3	(-1, -1)	$\frac{1}{4}(1 - \eta)(1 - \xi) - \frac{1}{2}N_6 - \frac{1}{2}N_7$	1	$\frac{1}{2}(1 + \eta) - \frac{1}{2}(1 - \eta^2)$
4	(1, -1)	$\frac{1}{4}(1 + \eta)(1 - \xi) - \frac{1}{2}N_7 - \frac{1}{2}N_8$		
5	(0, 1)	$\frac{1}{2}(1 - \eta^2)(1 + \xi)$		
6	(-1, 0)	$\frac{1}{2}(1 - \eta)(1 - \xi^2)$		
7	(0, -1)	$\frac{1}{2}(1 - \eta^2)(1 - \xi)$		
8	(1, 0)	$\frac{1}{2}(1 + \eta)(1 - \xi^2)$		

We define the vector of nodal displacements \mathbf{u}_n , which consists of all displacement components at all nodes

$$\mathbf{u}_n = [u_{y1} \ u_{z1} \ u_{y2} \ u_{z2} \ \dots \ u_{yn} \ u_{zn}]^T \quad (2.24)$$

with n being the number of nodes. The displacement vector at any point inside the element is obtained as

$$\mathbf{u}(y, z) = \hat{\mathbf{N}}(y, z) \mathbf{u}_n \quad (2.25)$$

with

$$\hat{\mathbf{N}}(y, z) = \begin{bmatrix} \hat{N}_1(y, z) & 0 & \hat{N}_2(y, z) & 0 & \dots & \hat{N}_n(y, z) & 0 \\ 0 & \hat{N}_1(y, z) & 0 & \hat{N}_2(y, z) & \dots & 0 & \hat{N}_n(y, z) \end{bmatrix} \quad (2.26)$$

Hence, the displacement at a given point is approximated as the sum over all shape functions, each one weighted with the displacement at the corresponding node, for instance

$$u_y(y, z) = \sum_{i=1}^n \hat{N}_i(y, z) u_{yi} \quad (2.27)$$

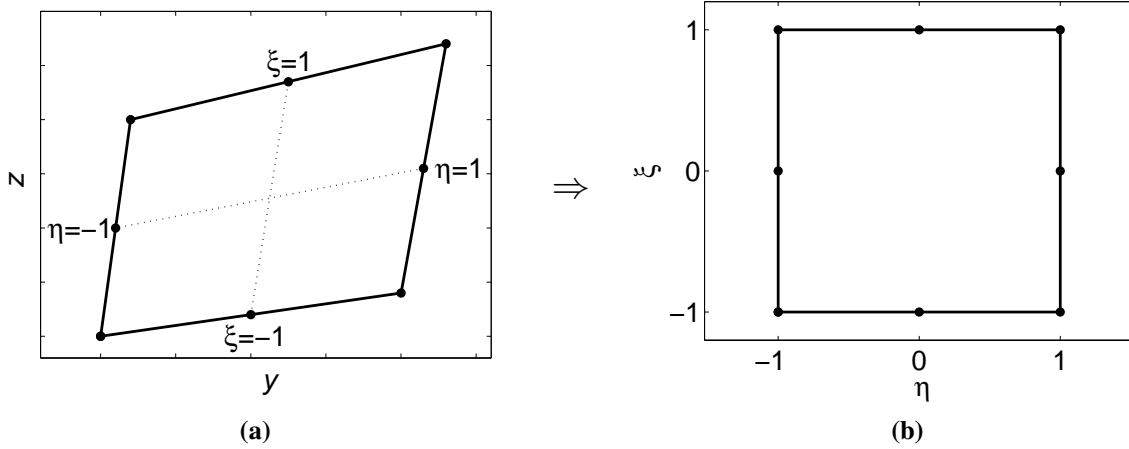


Figure 2.3: (a) Distorted four-sided element and (b) mapped element in local coordinate system.

In practice, the elements of a given discretization will differ in shape in order to best approximate the domain of interest. To simplify the implementation, each element is transformed into a local coordinate system (η, ξ) . The local coordinates are defined to equal 1 and -1 at the element edges (Figure 2.3a). This coordinate transformation can be interpreted as mapping the arbitrary four-sided element on a standard square element (Figure 2.3b). Formally, the coordinate transformation is defined by the Jacobian matrix

$$\mathbf{J} = \begin{bmatrix} \partial_{\eta} y & \partial_{\eta} z \\ \partial_{\xi} y & \partial_{\xi} z \end{bmatrix} \quad (2.28)$$

The shape functions can be defined in the local coordinate system (denoted by $N_i(\eta, \xi)$ and $\mathbf{N}(\eta, \xi)$, respectively), hence they are identical for all elements. The derivatives of the shape functions with respect to the Cartesian coordinates are obtained as

$$\begin{Bmatrix} \partial_y N_i(\eta, \xi) \\ \partial_z N_i(\eta, \xi) \end{Bmatrix} = \mathbf{J}^{-1} \begin{Bmatrix} \partial_\eta N_i(\eta, \xi) \\ \partial_\xi N_i(\eta, \xi) \end{Bmatrix} \quad (2.29)$$

In order to obtain a solution for the displacement field, a weak form of the governing equations is usually derived by applying either the method of weighted residuals or the potential energy principle. While both approaches lead to mathematically equivalent formulations, the potential energy principle is preferred in this work since it seems more intuitive from the viewpoint of physics. The total potential energy of the domain Ω in absence of body loads¹⁰ reads [112]

$$\Pi = \int_{\Omega} S(\boldsymbol{\epsilon}) \, d\Omega - \int_{\Gamma} \mathbf{u}^T \hat{\mathbf{f}} \, d\Gamma \quad (2.30)$$

where $S(\boldsymbol{\epsilon})$ denotes the strain-energy density, which can be defined by

$$\boldsymbol{\sigma} = \frac{\partial S(\boldsymbol{\epsilon})}{\partial \boldsymbol{\epsilon}} \quad (2.31)$$

The second term in Equation (2.30) describes the work associated with external forces acting on the boundary Γ .

The first variation of Equation (2.30) is given by

$$\delta \Pi = \int_{\Omega} \delta \boldsymbol{\epsilon}^T \frac{\partial S(\boldsymbol{\epsilon})}{\partial \boldsymbol{\epsilon}} \, d\Omega - \int_{\Gamma} \delta \mathbf{u}^T \hat{\mathbf{f}} \, d\Gamma = 0 \quad (2.32)$$

Using Equations (2.31) and (2.8) yields

$$\int_{\Omega} \delta(\mathbf{L}\mathbf{u})^T \boldsymbol{\sigma} \, d\Omega - \int_{\Gamma} \delta \mathbf{u}^T \hat{\mathbf{f}} \, d\Gamma = 0 \quad (2.33)$$

We can now substitute the nodal displacements to obtain

$$\int_{\Omega} \delta(\mathbf{L}\mathbf{N}\mathbf{u}_n)^T \boldsymbol{\sigma} \, d\Omega - \int_{\Gamma} \delta(\mathbf{N}\mathbf{u}_n)^T \hat{\mathbf{f}} \, d\Gamma = 0 \quad (2.34)$$

Note that each entry of \mathbf{u}_n describes a displacement component at one node, which is independent of the coordinates. Hence we can write

$$\delta \mathbf{u}_n^T \left(\int_{\Omega} (\mathbf{L}\mathbf{N})^T \boldsymbol{\sigma} \, d\Omega - \mathbf{f}_n \right) = 0 \quad (2.35)$$

¹⁰Body loads are caused by forces that act on the computational domain (in contrast to surface tractions that are applied on the boundary). Typical examples in elastodynamics are gravity or centrifugal forces. These effects will always be neglected in this work.

where \mathbf{f}_n are the external nodal forces. We define the strain-displacement transformation matrix

$$\mathbf{B} = \mathbf{L}\mathbf{N} \quad (2.36)$$

which contains the spatial derivatives of the shape functions:

$$\mathbf{B} = \begin{bmatrix} \partial_y N_1 & 0 & \dots & \partial_y N_n & 0 \\ 0 & \partial_z N_1 & \dots & 0 & \partial_z N_n \\ \partial_z N_1 & \partial_y N_1 & \dots & \partial_z N_n & \partial_y N_n \end{bmatrix} \quad (2.37)$$

Note that, since the shape functions are known polynomials, their derivatives can be calculated explicitly. Substituting Equations (2.8) and (2.12) for the strains and stresses into (2.35) and using Equation (2.36) yields

$$\delta \mathbf{u}_n^T \left(\int_{\Omega} \mathbf{B}^T \mathbf{D} \mathbf{B} \mathbf{u}_n \, d\Omega - \mathbf{f}_n \right) = 0 \quad (2.38)$$

Since the virtual displacements $\delta \mathbf{u}_n$ are arbitrary, we obtain

$$\left(\int_{\Omega} \mathbf{B}^T \mathbf{D} \mathbf{B} \, d\Omega \right) \mathbf{u}_n - \mathbf{f}_n = 0 \quad (2.39)$$

The integral only contains known functions. We define the stiffness matrix

$$\mathbf{K} = \int_{\Omega} \mathbf{B}^T \mathbf{D} \mathbf{B} \, d\Omega \quad (2.40)$$

so that

$$\mathbf{K} \mathbf{u}_n - \mathbf{f}_n = 0 \quad (2.41)$$

In the implementation, the integration in Equation (2.40) is generally performed numerically, using e. g. Gauss quadrature. Equation (2.41) is a linear system of equations. In order to create a well-defined physical problem, we have to impose adequate boundary conditions, i. e. everywhere on the boundary either the displacements (*Dirichlet boundary condition*) or forces (*Neumann boundary condition*) will be given.¹¹ After the boundary conditions have been enforced by substituting the corresponding values in the vectors \mathbf{u}_n and \mathbf{f}_n , Equation (2.41) can be solved using standard algorithms.

¹¹*Robin boundary conditions*, which state a relationship between the approximated function and its normal derivative are common in other applications of the FEM but will not be discussed here.

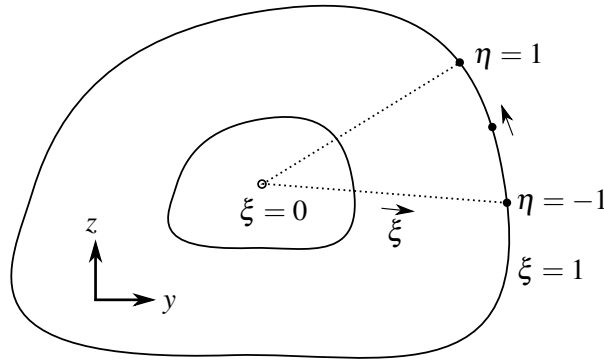


Figure 2.4: Discretization using the Scaled Boundary Finite Element Method.

2.3 The Scaled Boundary Finite Element Method

When applying the concept of the Scaled Boundary Finite Element Method, only the boundary of the computational domain is discretized. This discretization of the boundary, however, can be performed using typical Finite Elements.¹² When dealing with a two-dimensional domain, a one-dimensional boundary is discretized, while the general three-dimensional case requires the discretization of a two-dimensional surface.

Again, the domain depicted in Figure 2.1a is addressed, but now its boundary Γ is discretized using line-elements. As an example, Figure 2.4 shows one possible three-noded (quadratic) element. The adequate one-dimensional shape functions $N(\eta)$, defined in the local coordinate η are given in Table 2.1. In order to describe the full geometry, a crucial step is to perform a special coordinate transformation for each element. As indicated in Figure 2.4, the coordinate η is defined along the boundary and equals -1 and 1 at the extremities of the element, respectively. This coordinate is simply the one-dimensional representation of a local coordinate system as utilized in the traditional FEM. We now define a point at an arbitrary position within the domain. This point will be referred to as *scaling center*. The second coordinate ξ is defined to equal zero at the scaling center and one everywhere on the boundary. We can think of one element of the SBFEM discretization as the area that is defined by the element on the boundary and the lines connecting the scaling center with the extremities of the element.

We can describe an arbitrary point in the interior of the domain by

$$y(\xi, \eta) = \xi \mathbf{N}(\eta) \mathbf{y}_n \quad (2.42a)$$

$$z(\xi, \eta) = \xi \mathbf{N}(\eta) \mathbf{z}_n \quad (2.42b)$$

where \mathbf{y}_n and \mathbf{z}_n are the nodal coordinates. Hence, we obtain a point inside the domain by *scaling* the boundary in the direction of the scaling center by multiplication with the coordinate ξ . The name of the Scaled Boundary Finite Element Method is derived from this geometric interpretation. Equations (2.42) imply that the same shape functions can be applied for every

¹²This is to say, the concept is not similar to well-known Boundary Element Methods, which involve a fundamentally different strategy to describe the interaction of points on the boundary.

value of ξ within the domain. The same shape functions are also used to interpolate the displacements $\mathbf{u}(\xi, \eta) = [u_y(\xi, \eta) \ u_z(\xi, \eta)]^T$ on the boundary. To describe the displacements at an arbitrary position in the domain we write

$$\mathbf{u}(\xi, \eta) = \mathbf{N}(\eta)\mathbf{u}_n(\xi) \quad (2.43)$$

Note the fundamental difference compared to the interpolation in the Finite Element Method (Equation (2.25)). When applying the FEM, the nodal displacements are discrete values and the interpolation is performed using two-dimensional shape functions on each element. Contrary in the SBFEM the nodal displacements are continuous functions of the radial coordinate ξ and consequently the shape functions depend on one spatial coordinate only. Applying this type of interpolation yields a semi-analytical formulation, meaning that only one spatial coordinate is discretized in the Finite Element sense while in the second direction all equations are (at this stage) treated analytically. It is interesting to note that the partial derivatives of the spatial coordinates that are required to construct the Jacobian matrix, are simply given by

$$y_{,\xi} = \mathbf{N}\mathbf{y}_n \quad y_{,\eta} = \xi\mathbf{N}_{,\eta}\mathbf{y}_n \quad (2.44a)$$

$$z_{,\xi} = \mathbf{N}\mathbf{z}_n \quad z_{,\eta} = \xi\mathbf{N}_{,\eta}\mathbf{z}_n \quad (2.44b)$$

where comma-separated indices denote partial derivatives with respect to the given variable. A very detailed and concise description of the coordinate transformation and the resulting formulation in the general three-dimensional case can be found in [77] and will not be repeated here. For the particular case of guided ultrasonic waves, the novel formulations will be presented in detail in the following chapters. For now it suffices to understand that the interpolation (2.43) can be substituted into the virtual work principle, similar to the procedure in the Finite Element Method. Since we are dealing with semi-analytical equations, we have to treat both spatial coordinates differently. For instance, in the stress-displacement relationship we separate the derivatives with respect to both spatial coordinates and write

$$\boldsymbol{\sigma}(\eta, \xi) = \mathbf{D}(\mathbf{B}_1(\eta)\mathbf{u}_n(\xi)_{,\xi} + \frac{1}{\xi}\mathbf{B}_2(\eta)\mathbf{u}_n(\xi)) \quad (2.45)$$

where \mathbf{B}_1 includes the shape functions and \mathbf{B}_2 their spatial derivatives (similar to Equation (2.37)). Explicit expressions for these matrices are given in Appendix A.2 for the sake of completeness. After substituting the semi-analytical stress-displacement relationship into the virtual work principle, we have to compute three matrices that include the combinations of \mathbf{B}_1

and \mathbf{B}_2 :

$$\mathbf{E}_0 = \int_{\Gamma} \mathbf{B}_1^T \mathbf{D} \mathbf{B}_1 |J| \, d\eta \quad (2.46a)$$

$$\mathbf{E}_1 = \int_{\Gamma} \mathbf{B}_2^T \mathbf{D} \mathbf{B}_1 |J| \, d\eta \quad (2.46b)$$

$$\mathbf{E}_2 = \int_{\Gamma} \mathbf{B}_2^T \mathbf{D} \mathbf{B}_2 |J| \, d\eta \quad (2.46c)$$

These Equations should be compared to the definition of the stiffness matrix in the FEM, Equation (2.40). The SBFEM requires the assemblage of three matrices while the integrations have to be performed along the boundary of the domain only. With these definitions, the potential energy principle can be applied similarly to the Finite Element Method. The formulation for the stresses (2.35) is substituted and the definitions of the coefficient matrices (2.46a) are used. The explicit derivation as given in [77] is not repeated here in detail. An equation for a stiffness matrix only including the degrees of freedom on the boundary is obtained:

$$(\mathbf{K} - \mathbf{E}_1) \mathbf{E}_0^{-1} (\mathbf{K} - \mathbf{E}_1^T) - \mathbf{E}_2 = 0 \quad (2.47)$$

Equation (2.47) can be transferred into an algebraic Riccati equation and then solved to obtain the stiffness matrix. For details again refer to [77]. The procedures to solve the Riccati equation have been adopted from [113] and [114]. After the stiffness matrix has been obtained, solution strategies similar to the ones known in traditional Finite Elements can be employed. Since only the degrees of freedom on the boundary are involved in the computation, the dimensions of the resulting matrix equations are generally many times smaller and consequently the computational costs are drastically reduced.

However, there are certain advantages and drawbacks when applying this method. An obvious restriction lies in the fact that the coordinate transformation can only be employed if there exists a point in the interior of the domain from where the whole boundary is 'visible' (i. e. if the geometry is a *star domain* in the mathematical sense). If this is not the case, the domain has to be divided into subdomains, each of them having its own scaling center (Figure 2.5a). The subdomains can be assembled similar to the elements in the FEM.

When choosing the semi-analytical representation of the displacement field, it is implied that the material is homogeneous along the ξ -direction (while arbitrary distributions of material parameters can easily be accounted for along the discretized η -direction). This assumption can be considered to be the underlying reason why the dimension of the discretization can be reduced by one. On the other hand this concept leads to restrictions regarding the applicability of the method. If the domain contains inhomogeneities, we can again divide it into an appropriate number of subdomains with different material parameters assigned to each of them. However, if the distribution of material properties is very complex, so that the size of the subdomains becomes similar to the element size of a FEM discretization, the difference in computational efficiency of both methods will not be significant. For certain cases, approaches exist to include a continuous variation of the elastic parameters in the ξ -direction [115, 116], but the scope is

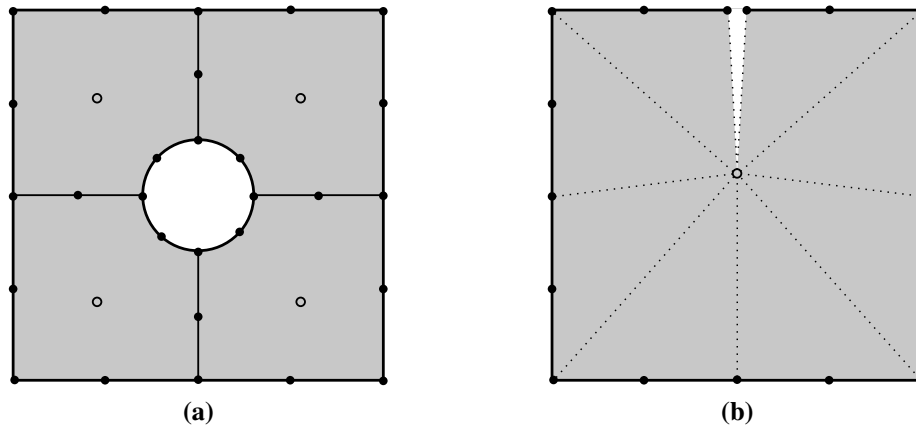


Figure 2.5: (a) Discretization of a plate with a hole, using 4 subdomains; (b) introducing a crack into a subdomain.

fairly limited compared to the possibilities that come with a full discretization in the FEM.

As pointed out in numerous publications on the SBFEM, one particular advantage of this method is that it offers a very elegant way to model cracks in solid structures (see e. g. [87–89, 101, 117]). A simple surface-breaking crack can be introduced into a subdomain by leaving a small gap between two elements on the boundary and placing the scaling center at the crack tip (Figure 2.5b). This way the side faces of the crack do not require discretization as they are defined along the scaling direction. More importantly, since the scaling center is placed at the crack tip, the stress-singularity that can cause severe difficulties in the FEM, is described accurately without the necessity of refinement or other additional treatment. This feature of the method will be used extensively in Chapter 8, where the interaction of guided waves with cracks in plates is modeled.

Finally it should be highlighted that the SBFEM can easily be adopted to model unbounded (infinite) domains¹³ [81, 83]. This is done by scaling the boundary between $\xi = 1$ and $\xi = \infty$. When applied to unbounded media, the SBFEM satisfies the radiation condition exactly [77]. Since the discretization of the boundary is performed using Finite Elements, bounded and unbounded domains can easily be coupled, for example in order to model soil-structure interaction [84, 118, 119]. Similarly, an SBFEM subdomain can easily be coupled to a domain that is fully discretized using a traditional FEM approach [120–123].

¹³In fact the SBFEM originally evolved from concepts to model unbounded domains using Finite Elements (see e. g. [80, 118]).

Chapter 3

Derivation for plate structures

In this chapter, the basic formulation is presented that has been developed in order to compute dispersion curves and mode shapes of guided waves in different structures [91–93]. At first the derivation is limited to the simplest case of guided waves in homogeneous plates (Lamb waves) [20, 91], which are treated using a two-dimensional approach in the plane strain approximation. It is discussed which restrictions are to be imposed on the material's anisotropy in order to apply the two-dimensional formulation. The extension to layered or functionally graded plates as well as general anisotropy is briefly summarized afterwards. The derivations in this chapter are presented in much detail, while in the following chapters the reader will frequently be referred back to the equations and conclusions obtained here. Many aspects of the formulation, for instance the virtual work principle, the discretization by means of higher-order elements or the integration scheme can be applied similarly to the more complex structures discussed in Chapters 4 - 6 and thus will not be repeated in every detail. Moreover, many considerations like the properties of the coefficient matrices, the choice of solution algorithms or the computation of the group velocities are mostly identical for all cases.

Even the simplest cases discussed in this chapter are of high relevance in practical applications. Since many years approaches are being developed to apply guided waves for the non-destructive testing or structural health monitoring of plate structures [23, 24, 26]. For all applications of guided waves, the knowledge of their dispersive behavior is essential. While in many approaches dispersion leads to unwanted effects that are attempted to be minimized, there are other techniques specifically utilizing dispersion effects to obtain information about the specimen. For instance, dispersion curves can be measured and compared with theoretical data to obtain the thickness variation of a plate or its material constants [124–126] as well as anisotropy effects [127, 128]. Concurrently, techniques have been studied to remove the effect of dispersion in structural health monitoring [129, 130] and inspection [131–133] applications. Group velocity dispersion has been assessed using time-frequency analysis [134]. General remarks on the dispersion properties of Lamb waves can be found in [135].

Several different approaches have been presented to obtain the dispersion properties of plate waves. Lamb's solution describes wave propagation in homogeneous isotropic plates of constant thickness analytically [15, 20]. However, since more complex plate structures, such as layered composites [27, 136] and functionally graded materials [137] are becoming more rele-

vant along the trend of lightweight structures, a general approach to obtain dispersion properties is desirable. Early approaches include the calculation of a lumped mass matrix of a layered structure to obtain dispersion relations of Rayleigh waves [138]. The discretization of structures with thin layers has led to eigenvalue problems to compute dispersion relations [139, 140]. This so-called thin-layer method has also been applied to assess the impulse response of layered media in the time domain [141] and for the analysis of piezo-composite layers [142]. Stiffness methods have been used to obtain approximate dispersion equations of layered media [143] and, more recently, for the characterization of multidirectional composites [144].

The well-known matrix methods [43–47], mentioned in the introduction, are often used to compute dispersion curves for simple homogeneous or layered waveguides [145–148]. These methods have been extended to anisotropic cases [149], for instance they have been applied successfully to obtain dispersion curves for orthotropic plates [150]. More recently, a different approach utilizing the Green’s matrix and applying Fourier transformation to derive a boundary problem for ordinary differential equations has been used to describe oscillation in multi-layered anisotropic composites [151]. To compute the dispersion properties of plates with continuously varying material properties in the thickness direction, a power series technique has been employed to derive approximate analytical solutions [137]. Finite Element Method to models for plate structures can be found in e. g. [58, 152]. Also the Boundary Element Method has been applied successfully [153] to obtain dispersion properties. The so-called WFE and SAFE methods can be used to describe waves in complex plate structures by discretizing a short section of the waveguide or only its cross-section, respectively. Particularly, a formulation has been presented for layered plates [154], anisotropic laminated strips [155] or functionally graded piezoelectric plates, assuming the material properties to vary linearly within each element of the discretization [156].

The formulation presented in Section 3.1 can be considered as a special case of the Scaled Boundary Finite Element Method [91, 92]. For simple plate structures the plane strain assumption is valid, so that we can employ the governing equations given in Section 2.1.2. Since the plate is assumed to be of infinite length, it is sufficient to discretize the through-thickness direction and choose the direction of propagation as the scaling direction. In terms of the general Scaled Boundary Finite Element Method this corresponds to placing the scaling center at infinity. Since the through-thickness direction and the scaling direction can be chosen parallel to the axes of a Cartesian coordinate system, the coordinate transformation becomes trivial. After computing the coefficient matrices for this particular geometry and assuming harmonic wave propagation along the structure, a quadratic eigenvalue problem is obtained. The eigenvalues are related to the wavenumbers of modes that can propagate in the plate. The corresponding mode shapes are represented by the eigenvectors. To facilitate the computation, the quadratic eigenvalue problem is transformed into a standard eigenvalue problem. The coefficient matrix of this standard eigenvalue problem is the so called \mathbf{Z} matrix, which is known from other applications of the SBFEM [84, 157].

Since only one eigenvalue problem has to be solved at each frequency, this approach is extremely stable and efficient. To further reduce computational costs, a particular type of higher-order spectral elements is employed for the discretization (Section 3.2). It is demonstrated that

this type of elements drastically reduces the number of nodes that are required to obtain a given accuracy. Some details on the eigenvalue problem, particularly the properties of the involved matrices and available solution algorithms, are discussed in Section 3.3.

By utilizing the Hamiltonian properties of the \mathbf{Z} matrix, it is proven in Section 3.4, that the group velocities of propagating modes can be obtained directly by computing the eigenvalue derivatives [92, 94, 95]. This is highly advantageous, since the computation requires only few vector multiplications and can be performed directly at a given frequency.

In Sections 3.5 and 3.6, the proposed approach is extended to include shear-horizontal modes and arbitrary anisotropic material behavior, respectively. Details on the implementation of the algorithm are described in Section 3.7.

Numerical examples in Section 3.8 demonstrate the applicability of the proposed approach to different plate structures and the extremely fast convergence of the algorithm towards analytical solutions.

3.1 SBFEM formulation for guided waves in plates

The plate of constant thickness h shown in Figure 3.1 is addressed. Without loss of generality the y -coordinate of a Cartesian coordinate system is chosen along the through-thickness direction of the plate while the z -coordinate is parallel to the plate's surfaces. The plate can be assumed to be of infinite dimension in the x -direction, and is thus handled as a two-dimensional problem in the plane strain formulation (Section 2.1.2). It covers a domain Ω of infinite length in positive z -direction with an interface at $z = 0$; the domain's boundary is denoted by Γ .

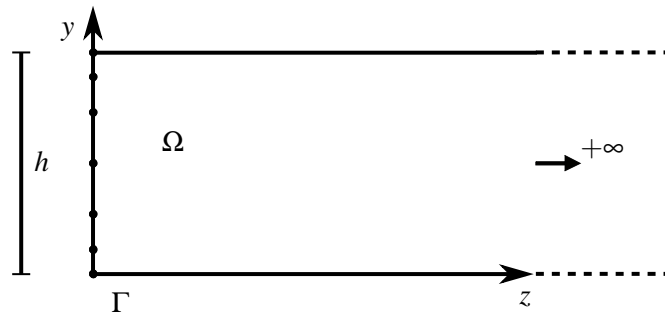


Figure 3.1: Plate geometry for the Scaled Boundary Finite Element formulation with a discretized interface.

The displacement vector $\mathbf{u} = \mathbf{u}(y, z)$ in two dimensions is expressed as $\mathbf{u} = [u_y \ u_z]^T$, where the displacement components in y - and z -direction are denoted as $u_y = u_y(y, z)$ and $u_z = u_z(y, z)$, respectively. As described in Section 2.1, the stress-displacement relationship is given as

$$\boldsymbol{\sigma} = [\sigma_y \ \sigma_z \ \tau_{yz}]^T = \mathbf{D}\boldsymbol{\varepsilon} = \mathbf{D}\mathbf{L}\mathbf{u} \quad (3.1)$$

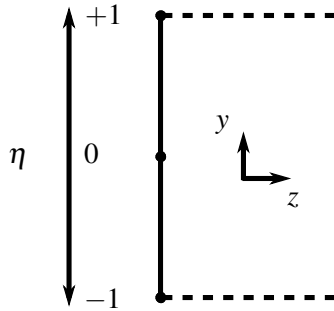


Figure 3.2: One element of the discretization, defined in the local coordinate η .

where the differential operator \mathbf{L} in the two-dimensional case reads [106]

$$\mathbf{L} = \begin{bmatrix} \partial_y & 0 & \partial_z \\ 0 & \partial_z & \partial_y \end{bmatrix}^T \quad (3.2)$$

and \mathbf{D} is the 3×3 elasticity matrix. Using the concept of the Scaled Boundary Finite Element Method, only the through-thickness direction of the plate is discretized in the Finite Element sense. An analytical solution will be employed for the z -direction. Hence, for plate structures we only have to discretize a single straight line, using one-dimensional elements. In this particular case, the coordinate transformation becomes very simple, since the scaling direction is identical with the positive z -axis. Each one-dimensional element is defined in its local coordinate η , which in this case is parallel to the y -axis (Figure 3.2). Hence, the Jacobian determinant can be written as

$$|\mathbf{J}| = \begin{vmatrix} \partial_\eta y & \partial_\eta z \\ \partial_\xi y & \partial_\xi z \end{vmatrix} = \begin{vmatrix} \partial_\eta y & \partial_\eta z \\ \partial_z y & \partial_z z \end{vmatrix} = \begin{vmatrix} y, \eta & 0 \\ 0 & 1 \end{vmatrix} = y, \eta \quad (3.3)$$

For one element, the coordinate transformation reads

$$y = \frac{l}{2}(\eta + 1) \quad (3.4)$$

where the element length (in the global coordinate system) is denoted by l . Consequently, we obtain

$$|\mathbf{J}| = y, \eta = \frac{l}{2} \quad (3.5)$$

For simplicity, the following formulation is derived for one element. If several elements are used for the discretization, they can be assembled following standard Finite Element procedures [107]. In order to separate the derivatives with respect to z and η , the strain-displacement

relationship (Equation (2.8)) is rewritten as

$$\boldsymbol{\varepsilon} = \mathbf{b}_1 \mathbf{u}_{,z} + \frac{1}{y,\eta} \mathbf{b}_2 \mathbf{u}_{,\eta} \quad (3.6)$$

with

$$\mathbf{b}_1 = \begin{bmatrix} 0 & 0 & 1 \\ 0 & 1 & 0 \end{bmatrix}^T \quad (3.7a)$$

$$\mathbf{b}_2 = \begin{bmatrix} 1 & 0 & 0 \\ 0 & 0 & 1 \end{bmatrix}^T \quad (3.7b)$$

The discretization of the element is defined by placing a given number of nodes at the nodal coordinates η_i . The geometry as well as the physical variables are interpolated using the corresponding shape functions $N_i(\eta)$. For a plate of constant thickness, the geometry of the entire plate in two dimensions can be obtained by translating the one-dimensional mesh in z -direction. This implies that the same shape functions apply for all lines with constant z . This procedure is equivalent to scaling the boundary between $z = 0$ and $z = \infty$ with respect to a scaling center placed at $-\infty$ in the general formulation of the SBFEM. Along the horizontal lines passing through the nodes on the vertical boundary and extending to $+\infty$, displacement functions $\mathbf{u}_j(z) = [u_{yj}(z) \ u_{zj}(z)]^T$ are introduced. These nodal displacements are collected in one vector:

$$\mathbf{u}_n = [u_{y1}(z) \ u_{z1}(z) \ u_{y2}(z) \ u_{z2}(z) \ \dots \ u_{yn}(z) \ u_{zn}(z)]^T \quad (3.8)$$

where n is the number of nodes. Consequently, the displacements at a point of the geometry can be expressed as

$$\mathbf{u}(z, \eta) = \mathbf{N}(\eta) \mathbf{u}_n(z) \quad (3.9)$$

Where the matrix of shape functions is assembled as

$$\mathbf{N}(\eta) = \begin{bmatrix} N_1(\eta) & 0 & N_2(\eta) & 0 & \dots & N_n(\eta) & 0 \\ 0 & N_1(\eta) & 0 & N_2(\eta) & \dots & 0 & N_n(\eta) \end{bmatrix} \quad (3.10)$$

Note that, at this stage $\mathbf{u}_n(z)$ can be arbitrary functions of z , while the shape functions depend on η only. For the sake of conciseness, the dependency on η will usually be omitted. Substituting Equation (3.9) into (3.6) leads to

$$\boldsymbol{\varepsilon} = \mathbf{B}_1 \mathbf{u}_{n,z}(z) + \mathbf{B}_2 \mathbf{u}_n(z) \quad (3.11)$$

where the matrices

$$\mathbf{B}_1 = \mathbf{b}_1 \mathbf{N} \quad (3.12a)$$

$$\mathbf{B}_2 = \frac{1}{y,\eta} \mathbf{b}_2 \mathbf{N},\eta \quad (3.12b)$$

are introduced for convenience. Substituting (3.11) into (3.1), the stress field can be written as

$$\boldsymbol{\sigma} = \mathbf{D} (\mathbf{B}_1 \mathbf{u}_{n,z}(z) + \mathbf{B}_2 \mathbf{u}_n(z)) \quad (3.13)$$

With the above definitions, a semi-analytical Scaled Boundary Finite Element equation is derived using the principle of virtual work. The derivation follows the formulation given in [158], while additional terms have to be added for the dynamic problem.

A virtual displacement field $\delta \mathbf{u}(y,z)$ is applied to the structure, leading to corresponding virtual strains

$$\delta \boldsymbol{\varepsilon}(y,z) = \mathbf{L} \delta \mathbf{u}(y,z) \quad (3.14)$$

The virtual work principle for the dynamic case (again in absence of body loads) reads

$$\delta U + \delta K - \delta W = 0 \quad (3.15)$$

where U denotes the internal strain energy, K is the kinetic energy of the structure and W is the external work caused by boundary tractions $\hat{\mathbf{f}}(y,z)$ acting on the interface. The contribution of the three terms to the virtual work will be derived in the following.

Integrating the boundary tractions over the interface of the plate, the virtual external work yields

$$\delta W = \int_{-1}^1 \delta \mathbf{u}^T \hat{\mathbf{f}} |J| d\eta \quad (3.16)$$

Applying the discretization

$$\delta \mathbf{u}(\eta, z) = \mathbf{N} \delta \mathbf{u}_n(z) \quad (3.17)$$

results in

$$\delta W = \delta \mathbf{u}_n^T(0) \int_{-1}^1 \mathbf{N}^T \hat{\mathbf{f}} |J| d\eta \equiv \delta \mathbf{u}_n^T(0) \mathbf{f}_n \quad (3.18)$$

where \mathbf{f}_n are the external nodal forces on the boundary.

The virtual kinetic energy, which requires domain integration, can be written as

$$\delta K = \iint_{\Omega} \delta \mathbf{u}^T(\eta, z) \rho \ddot{\mathbf{u}}(\eta, z) d\Omega = \int_0^\infty \int_{-1}^1 \delta \mathbf{u}_n^T(z) \mathbf{N}^T \rho \mathbf{N} \ddot{\mathbf{u}}_n(z) |J| d\eta dz \quad (3.19)$$

with the mass density ρ . The mass matrix is introduced as

$$\mathbf{M}_0 = \int_{-1}^1 \mathbf{N}^T \rho \mathbf{N} |J| d\eta \quad (3.20)$$

leading to

$$\delta K = \int_0^\infty \delta \mathbf{u}_n^T(z) \mathbf{M}_0 \ddot{\mathbf{u}}_n(z) dz \quad (3.21)$$

The virtual internal strain energy is given as [158]

$$\delta U = \iint_{\Omega} \delta \boldsymbol{\varepsilon}^T \boldsymbol{\sigma} d\Omega \quad (3.22)$$

Substituting Equation (3.11) leads to

$$\delta U = \iint_{\Omega} [\mathbf{B}_1 \delta \mathbf{u}_{n,z}(z)]^T \boldsymbol{\sigma}(\eta, z) |J| d\Omega + \iint_{\Omega} [\mathbf{B}_2 \delta \mathbf{u}_n(z)]^T \boldsymbol{\sigma}(\eta, z) |J| d\Omega \quad (3.23)$$

Applying integration by parts to the first term yields

$$\begin{aligned} \delta U = \int_{\Gamma} \delta \mathbf{u}_n^T(z) \mathbf{B}_1^T \boldsymbol{\sigma}(\eta, z) |J| d\Gamma - \iint_{\Omega} \delta \mathbf{u}_n^T(z) \mathbf{B}_1^T \boldsymbol{\sigma}_{,z}(\eta, z) |J| d\Omega \\ + \iint_{\Omega} \delta \mathbf{u}_n^T(z) \mathbf{B}_2^T \boldsymbol{\sigma}(\eta, z) |J| d\Omega \end{aligned} \quad (3.24)$$

For a free plate (surrounded by vacuum), the stresses at the upper and lower surface vanish.¹⁴ Hence, the first term is reduced to an integration over the interface, leading to

$$\begin{aligned} \delta U = \int_{-1}^1 \delta \mathbf{u}_n^T(0) \mathbf{B}_1^T \boldsymbol{\sigma}(\eta, 0) |J| d\eta - \int_{-1}^1 \int_0^\infty \delta \mathbf{u}_n^T(z) \mathbf{B}_1^T \boldsymbol{\sigma}_{,z}(\eta, z) |J| dz d\eta \\ + \int_{-1}^1 \int_0^\infty \delta \mathbf{u}_n^T(z) \mathbf{B}_2^T \boldsymbol{\sigma}(\eta, z) |J| dz d\eta \end{aligned} \quad (3.25)$$

The first term includes the internal nodal forces on the interface, defined as [78]

$$\mathbf{q}_n(0) = \int_{-1}^1 \mathbf{B}_1^T \boldsymbol{\sigma}(\eta, z) |J| d\eta \quad (3.26)$$

Using Equation (3.26) and substituting Equation (3.13) for the stress field, the strain energy is rewritten as

$$\begin{aligned} \delta U = - \int_{-1}^1 \int_0^\infty \delta \mathbf{u}_n^T(z) \left(\mathbf{B}_1^T \mathbf{D} \mathbf{B}_1 \mathbf{u}_{n,zz}(z) + \mathbf{B}_1^T \mathbf{D} \mathbf{B}_2 \mathbf{u}_{n,z}(z) - \mathbf{B}_2^T \mathbf{D} \mathbf{B}_1 \mathbf{u}_{n,z}(z) \right. \\ \left. - \mathbf{B}_2^T \mathbf{D} \mathbf{B}_2 \mathbf{u}_n(z) \right) |J| dz d\eta + \delta \mathbf{u}_n^T(0) \mathbf{q}_n(0) \end{aligned} \quad (3.27)$$

¹⁴Embedded waveguides, where this assumption is not valid, are discussed in Chapter 6.

Equation (3.27) can be rewritten using the SBFEM coefficient matrices [78]

$$\mathbf{E}_0 = \int_{-1}^1 \mathbf{B}_1^T \mathbf{D} \mathbf{B}_1 |J| d\eta \quad (3.28a)$$

$$\mathbf{E}_1 = \int_{-1}^1 \mathbf{B}_2^T \mathbf{D} \mathbf{B}_1 |J| d\eta \quad (3.28b)$$

$$\mathbf{E}_2 = \int_{-1}^1 \mathbf{B}_2^T \mathbf{D} \mathbf{B}_2 |J| d\eta \quad (3.28c)$$

yielding

$$\delta U = - \int_0^\infty \delta \mathbf{u}_n^T(z) \left(\mathbf{E}_0 \mathbf{u}_{n,zz}(z) + (\mathbf{E}_1^T - \mathbf{E}_1) \mathbf{u}_{n,z}(z) - \mathbf{E}_2 \mathbf{u}_n(z) \right) dz + \delta \mathbf{u}_n^T(0) \mathbf{q}_n(0) \quad (3.29)$$

Note that

$$\mathbf{E}_1^T = \int_{-1}^1 \mathbf{B}_1^T \mathbf{D} \mathbf{B}_2 |J| d\eta \quad (3.30)$$

is valid because \mathbf{D} is always symmetric.

Substituting the derived expressions (3.18), (3.21) and (3.29) into the virtual work statement (Equation (3.15)) leads to

$$\begin{aligned} - \int_0^\infty \delta \mathbf{u}_n^T(z) \left(\mathbf{E}_0 \mathbf{u}_{n,zz}(z) + (\mathbf{E}_1^T - \mathbf{E}_1) \mathbf{u}_{n,z}(z) - \mathbf{E}_2 \mathbf{u}_n(z) - \mathbf{M}_0 \ddot{\mathbf{u}}_n(z) \right) dz \\ + \delta \mathbf{u}_n^T(0) \mathbf{q}_n(0) - \delta \mathbf{u}_n^T(0) \mathbf{f}_n = 0 \end{aligned} \quad (3.31)$$

In order to satisfy (3.31) for arbitrary virtual displacement fields, the following two conditions have to be fulfilled simultaneously

$$\delta \mathbf{u}_n^T(0) \mathbf{q}_n(0) - \delta \mathbf{u}_n^T(0) \mathbf{f}_n = 0 \quad (3.32a)$$

$$\mathbf{E}_0 \mathbf{u}_{n,zz}(z) + (\mathbf{E}_1^T - \mathbf{E}_1) \mathbf{u}_{n,z}(z) - \mathbf{E}_2 \mathbf{u}_n(z) - \mathbf{M}_0 \ddot{\mathbf{u}}_n(z) = 0 \quad (3.32b)$$

Equation (3.32a) implies equilibrium of forces at the interface. This equation will not be used explicitly in absence of external boundary tractions. Equation (3.32b) is the Scaled Boundary Finite Element equation in displacements on the cross-section. Note that (3.32a) and (3.32b) are semi-analytical equations for the displacements, since the y -direction of the plate is discretized in the Finite Element sense, while the nodal displacements $\mathbf{u}_n(z)$ can (until now) be arbitrary analytical functions of z .

Depending on the application, different solution procedures have been proposed to solve for the displacement functions $\mathbf{u}_n(z)$. In the current application, where we aim to describe guided waves propagating along the structure towards infinity, we can postulate the solutions to be of

the form

$$\mathbf{u}_n(z) = e^{\lambda z - i\omega t} \hat{\mathbf{u}}_n \quad (3.33)$$

with the angular frequency ω , time t and imaginary unit i . $\hat{\mathbf{u}}_n$ is the vector of complex displacement amplitudes and λ is defined as

$$\lambda = ik \quad (3.34)$$

where k is the wavenumber in the z -direction of one particular mode. The ansatz (3.33) is valid for structures that are homogeneous in z -direction when assuming linear material behavior. After substituting (3.33) into (3.32b) we obtain

$$\left(\lambda^2 \mathbf{E}_0 + \lambda (\mathbf{E}_1^T - \mathbf{E}_1) - \mathbf{E}_2 + \omega^2 \mathbf{M}_0 \right) \hat{\mathbf{u}}_n = 0 \quad (3.35)$$

For a given frequency ω , Equation (3.35) states a polynomial eigenvalue problem of second order for the eigenvalues λ and eigenvectors $\hat{\mathbf{u}}_n$, which can be solved numerically using standard procedures. If the plate's interface is discretized with n nodes, the number of degrees of freedom is $g = 2n$ and the coefficient matrices have the dimension $2n \times 2n$. For a quadratic eigenvalue problem the number of solutions is $4n$. If λ is an eigenvalue, $-\lambda$ is an eigenvalue as well, representing waves propagating in positive and negative z -direction, respectively. The eigenvalues are either real or pairs of complex conjugates. Eigenvalues with negative and positive real parts correspond to evanescent waves decaying as z tends towards $+\infty$ and $-\infty$, respectively.

For the computation of dispersion curves, only pairs of purely imaginary eigenvalues (real wavenumbers) are of interest as they represent the finite number of propagating wave modes. The number of evanescent modes with complex wavenumber that are obtained depends on the discretization. For increasing number of nodes the number of evanescent modes tends towards infinity. Purely real eigenvalues belong to non-oscillating modes which decay exponentially in positive or negative z -direction, respectively. Generally, the complex spectrum could be used to analyze the dynamic response of the structure in terms of structural dynamics, as in other applications of the SBFEM [90]. The eigenvectors $\hat{\mathbf{u}}_n$ that consist of the displacement amplitudes at all nodes of the discretization can be interpreted as the mode shapes.

The dispersion curves are obtained by solving Equation (3.35) for a given set of frequencies. For each frequency, the wavenumbers of all propagating modes are determined. The phase velocity c_p of a mode with wavenumber k is defined as

$$c_p = \frac{\omega}{k} \quad (3.36)$$

Note that the dispersion relations can also be computed by defining a set of wavenumbers and obtaining the corresponding frequencies from Equation (3.35). This approach reduces Equation (3.35) to a standard eigenvalue problem for ω^2 . However, in practical applications it is usually more feasible to define a set of frequencies as the range of wavenumbers will not be known a priori.

To ease the implementation and improve efficiency, Equation (3.35) is transferred into a stan-

standard eigenvalue problem for the wavenumbers by defining the following vectors

$$\mathbf{q}_n(z) = \mathbf{E}_0 \mathbf{u}_{n,z}(z) + \mathbf{E}_1^T \mathbf{u}_n(z) \quad (3.37a)$$

$$\boldsymbol{\varphi}(z) = \begin{Bmatrix} \mathbf{u}_n(z) \\ \mathbf{q}_n(z) \end{Bmatrix} \quad (3.37b)$$

where $\mathbf{q}_n(z)$ can be identified as the internal nodal forces [82]. Substituting (3.37) into (3.32b) leads to a first order ordinary differential equation for $\boldsymbol{\varphi}(z)$

$$\boldsymbol{\varphi}_{,z}(z) = -\mathbf{Z}\boldsymbol{\varphi}(z) \quad (3.38)$$

with the new coefficient matrix

$$\mathbf{Z} = \begin{bmatrix} \mathbf{E}_0^{-1} \mathbf{E}_1^T & -\mathbf{E}_0^{-1} \\ \omega^2 \mathbf{M}_0 - \mathbf{E}_2 + \mathbf{E}_1 \mathbf{E}_0^{-1} \mathbf{E}_1^T & -\mathbf{E}_1 \mathbf{E}_0^{-1} \end{bmatrix} \quad (3.39)$$

Since the same wavenumbers will apply for the nodal forces and displacements, the solution for $\boldsymbol{\varphi}(z)$ can again be postulated as

$$\boldsymbol{\varphi}(z) = e^{\lambda z} \boldsymbol{\Psi} \quad (3.40)$$

where $\boldsymbol{\Psi}$ contains the amplitudes of both displacements and nodal forces

$$\boldsymbol{\Psi} = \begin{Bmatrix} \hat{\mathbf{u}}_n \\ \hat{\mathbf{q}}_n \end{Bmatrix} \quad (3.41)$$

Hence, the standard eigenvalue problem follows after substitution of (3.40) into (3.38) as

$$-\mathbf{Z}\boldsymbol{\Psi} = \lambda \boldsymbol{\Psi} \quad (3.42)$$

Similar solution techniques are employed in the original formulation of the SBFEM, where the dynamic stiffness matrix is also required [77]. Since then the matrix \mathbf{Z} has often been used in numerous applications of the SBFEM [82, 84, 101, 157, 159].

3.2 Discretization using high-order spectral elements

As mentioned before in Section 2.2, quadratic elements are most commonly utilized in traditional Finite Element approaches. A one-dimensional quadratic element is defined by three nodes and the shape functions are second-order polynomials. More recently, certain classes of higher-order elements have gained more attention, as they can lead to significantly higher accuracy for the same number of nodes. Hence, to obtain a given accuracy, the number of nodes (and thus the computational costs) can be reduced. In this work, one type of higher-order elements [160] has been implemented as they have shown excellent convergence properties in different applications of the SBFEM [82, 84, 87, 101]. The performance of the chosen type of

elements is also influenced by the numerical integration scheme that is employed for the computation of the coefficient matrices (Equations (3.20) and (3.28)). An elegant solution is to choose the shape functions and the integration scheme such that the nodes coincide with the integration points. This concept is generally referred to as spectral elements [161–165].

3.2.1 Shape functions

For plate structures, only one-dimensional elements and shape functions are required. The shape functions can be constructed using the Lagrange interpolation polynomials [166]. An element of order p contains $p + 1$ nodes. The position of node i in the local coordinate system is denoted by η_i and the corresponding shape function is obtained as

$$N_i(\eta) = \prod_{k=1, k \neq i}^{p+1} \frac{\eta - \eta_k}{\eta_i - \eta_k} \quad (3.43)$$

Note that - analogously to Finite Elements - the shape function N_i equals one at node η_i and zero at all other nodes. Using Equation (3.43), the shape functions can generally be defined for arbitrary number and position of nodes. However, the nodal positions have to be chosen carefully in order to obtain stable and converging results, especially if the element order is large. Details can be found in [160]. For instance, equidistant nodes lead to the condition number of the coefficient matrix \mathbf{E}_0 increasing rapidly with the element order. Consequently, large numerical errors are introduced by the inversion of \mathbf{E}_0 in Equation (3.39). This is due to the fact that the shape functions become very large close to the extremities of the element as the element order increases. As an example, the shape function of the central node of an element of order 10 is illustrated in Figure 3.3a.

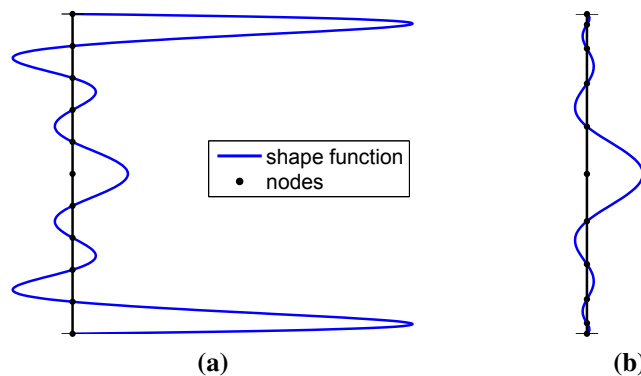


Figure 3.3: Shape function N_6 (—) of the central node of an element of order 10 if the nodes (•) are (a) equidistant and (b) positioned at the Gaussian-Lobatto-Legendre points.

As demonstrated in [160], highly accurate and stable results can be obtained by placing two

nodes at the extremities of the elements

$$\eta_1 = -1 \quad (3.44a)$$

$$\eta_{p+1} = 1 \quad (3.44b)$$

and the inner $p - 1$ nodes at the Gauss-Lobatto-Legendre points (Figure 3.3b). These points satisfy the condition

$$\frac{d}{d\eta} P_p(\eta_i) = 0 \quad \text{for } i = 2 \dots p \quad (3.45)$$

where P_p denotes the Legendre polynomial of order p [167]. Using these nodal coordinates, the maximum of each shape function is one (at the corresponding node). Hence, large values are avoided and the condition numbers of the coefficient matrices are drastically reduced compared to evenly spaced nodes. Additionally, based on these nodal coordinates, the concept of spectral elements can be applied, as there exists a numerical quadrature scheme that utilizes the same positions for the integration.

3.2.2 Numerical integration

The numerical integration scheme that uses the coordinates η_i as defined in (3.44) and (3.45) as integration points, is the Gaussian-Lobatto-Legendre quadrature [168, 169]. Analogously to traditional Gaussian quadrature, the integral is replaced by a sum. The function to be integrated is evaluated at the integration points η_i and multiplied by a corresponding weight w_i . Consequently, the coefficient matrices and the mass matrix are obtained as

$$\mathbf{E}_0 = \sum_{\alpha=1}^{p+1} w_{\alpha} \mathbf{N}^T(\eta_{\alpha}) \mathbf{b}_1^T \mathbf{D} \mathbf{b}_1 \mathbf{N}(\eta_{\alpha}) |J| \quad (3.46a)$$

$$\mathbf{E}_1 = \sum_{\alpha=1}^{p+1} w_{\alpha} \mathbf{N}_{,\eta}^T(\eta_{\alpha}) \mathbf{b}_2^T \mathbf{D} \mathbf{b}_1 \mathbf{N}(\eta_{\alpha}) |J| \quad (3.46b)$$

$$\mathbf{E}_2 = \sum_{\alpha=1}^{p+1} w_{\alpha} \mathbf{N}_{,\eta}^T(\eta_{\alpha}) \mathbf{b}_2^T \mathbf{D} \mathbf{b}_2 \mathbf{N}_{,\eta}(\eta_{\alpha}) |J| \quad (3.46c)$$

$$\mathbf{M}_0 = \sum_{\alpha=1}^{p+1} w_{\alpha} \rho \mathbf{N}^T(\eta_{\alpha}) \mathbf{N}(\eta_{\alpha}) |J| \quad (3.46d)$$

Since the integration points coincide with the element nodes, and each shape function equals zero at all but one nodes, many entries of the coefficient matrices vanish [84]. Note that the derivatives $\mathbf{N}_{,\eta}$ generally have non-zero values at all nodes. More specifically, we obtain the

following expressions for the 2×2 submatrices, relating nodes i and j

$$\mathbf{E}_{0ij} = \delta_{ij} w_i \mathbf{b}_1^T \mathbf{D} \mathbf{b}_1 |J| \quad (3.47a)$$

$$\mathbf{E}_{1ij} = w_j N_{i,\eta}^T(\eta_j) \mathbf{b}_2^T \mathbf{D} \mathbf{b}_1 |J| \quad (3.47b)$$

$$\mathbf{E}_{2ij} = \sum_{\alpha=1}^{p+1} w_\alpha N_{i,\eta}^T(\eta_\alpha) \mathbf{b}_2^T \mathbf{D} \mathbf{b}_2 N_{j,\eta}^T(\eta_\alpha) |J| \quad (3.47c)$$

$$\mathbf{M}_{0ij} = \delta_{ij} w_i \rho \mathbf{I}_2 |J| \quad (3.47d)$$

with the weights w , the Kronecker delta δ_{ij} and the 2×2 identity matrix \mathbf{I}_2 . Hence, when using spectral elements the summation is only required to compute the submatrices of \mathbf{E}_2 . The mass matrix \mathbf{M}_0 is always diagonal. \mathbf{E}_0 is generally block-diagonal if arbitrary anisotropic material behavior is assumed. On the other hand, if the material can be considered as isotropic or orthotropic, i. e. the elasticity matrix is given as

$$\mathbf{D} = \begin{bmatrix} D_{11} & D_{12} & 0 \\ D_{12} & D_{22} & 0 \\ 0 & 0 & D_{33} \end{bmatrix} \quad (3.48)$$

the coefficient matrix \mathbf{E}_0 is diagonal as well. In that case we obtain

$$\mathbf{b}_1^T \mathbf{D} \mathbf{b}_1 = \begin{bmatrix} 0 & 0 & 1 \\ 0 & 1 & 0 \end{bmatrix} \begin{bmatrix} D_{11} & D_{12} & 0 \\ D_{12} & D_{22} & 0 \\ 0 & 0 & D_{33} \end{bmatrix} \begin{bmatrix} 0 & 0 \\ 0 & 1 \\ 1 & 0 \end{bmatrix} = \begin{bmatrix} D_{33} & 0 \\ 0 & D_{22} \end{bmatrix} \quad (3.49)$$

and the blocks on the diagonal can be simplified as

$$\mathbf{E}_{0ij} = \delta_{ij} w_i |J| \begin{bmatrix} D_{33} & 0 \\ 0 & D_{22} \end{bmatrix} \quad (3.50)$$

Consequently, the matrices \mathbf{M}_0 and \mathbf{E}_0 can then be stored as vectors. More importantly, the inversion of \mathbf{E}_0 , which is required for the computation of the \mathbf{Z} -matrix (Equation (3.39)), becomes trivial, increasing numerical stability and efficiency of the computation.

The Gaussian-Lobatto-Legendre quadrature is exact for polynomials up to order $2p - 1$ [170]. The coefficient matrices \mathbf{E}_1 and \mathbf{E}_2 that require integration of polynomials of order $2p - 1$ and $2p - 2$, are fully integrated. \mathbf{E}_0 and \mathbf{M}_0 are of order $2p$ and consequently will be under-integrated by one order [84].

3.2.3 Element order

The through-thickness direction of the plate has to be discretized with a given number of elements. The numerical studies in Section 3.8 show examples of how to choose the number and

order of elements. The discretization that leads to converged results depends on the complexity of the modes which are of interest. The complexity and number of modes tend to increase with frequency, hence, a finer discretization is required for higher frequencies. Furthermore, the number of required nodes depends on the chosen type and order of elements. As shown in the numerical examples, the use of higher-order elements lead to more accurate results for the same number of nodes compared to elements of low order.

3.2.4 Plates with varying material parameters

One advantage of the proposed method lies in the fact that it can easily be applied to structures with varying material parameters in the thickness direction. These can be composites consisting of several layers of different materials as well as functionally graded materials, where the elastic constants vary continuously along the thickness. The material parameters only affect the coefficient matrices, which can easily be modified. For a layered structure, this can be achieved by discretizing each layer with one element as indicated in Figure 3.4.

In the case of functionally graded materials, the elasticity matrix and density become functions of y . Since the integrations in the y -direction are performed numerically, this can be taken into account by simply assigning different values for \mathbf{D} and ρ to each node, according to its y -coordinates. Hence, the material parameters can be arbitrary functions of y , regardless of the chosen discretization. The parameters can vary within one element as long as the number of nodes is high enough to represent the change in material properties sufficiently.

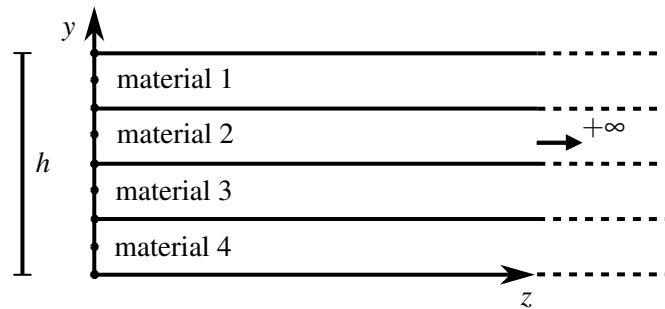


Figure 3.4: Discretization of a layered structure.

Table 3.1: Properties of the coefficient matrices.

	symmetry	diagonal	definiteness
\mathbf{M}_0	symmetric	yes	positive definite
\mathbf{E}_0	symmetric	(block-)diagonal	positive definite
\mathbf{E}_1	non-symmetric	no	indefinite
\mathbf{E}_2	symmetric	no	positive semidefinite
$\mathbf{E}_1^T - \mathbf{E}_1$	skew-symmetric	no	positive semidefinite

3.3 Properties of the eigenvalue problem

3.3.1 Properties of the coefficient matrices

For later reference, some basic properties of the coefficient matrices are briefly summarized in Table 3.1. It has been mentioned before that, when using spectral elements, the matrix \mathbf{M}_0 is always diagonal and \mathbf{E}_0 is diagonal in case of isotropic or orthotropic material behavior and block-diagonal otherwise. Moreover, both matrices are positive definite,¹⁵ i. e. all eigenvalues are positive (when \mathbf{M}_0 and \mathbf{E}_0 are diagonal, this is a trivial property, as all entries on the diagonal are positive, cf. Equations (3.47a) and (3.47d).

The matrix \mathbf{E}_2 is also symmetric, as can be seen directly from Equation (3.47c). It is positive semidefinite since some of the eigenvalues of \mathbf{E}_2 are always zero. Consequently, \mathbf{E}_2 is always singular. Physically, these singularities represent rigid-body motions, corresponding to translations of the complete structure along one of the coordinate axes without deformation [77, 171].

The matrix \mathbf{E}_1 is non-symmetric and indefinite. Typically, it is (close to) singular, depending on the chosen discretization. However, the matrix $\mathbf{E}_1^T - \mathbf{E}_1$ that represents the linear term of the quadratic eigenvalue problem is often non-singular (depending on the application), skew-symmetric and hence positive semidefinite¹⁶.

3.3.2 Hamiltonian structure

The matrix \mathbf{Z} that is assembled in order to derive a standard eigenvalue problem, reveals a Hamiltonian structure [172], i. e.

$$(\mathbf{J}_{2g}\mathbf{Z})^T = \mathbf{J}_{2g}\mathbf{Z} \quad (3.51)$$

¹⁵A real symmetric matrix is positive definite/positive semidefinite if it has only positive/non-negative eigenvalues. More generally, a real quadratic (not necessarily symmetric) matrix \mathbf{A} is positive (semi)definite if its symmetric part $1/2(\mathbf{A}^T + \mathbf{A})$ is positive (semi)definite.

¹⁶For a skew-symmetric matrix, the symmetric part and the corresponding eigenvalues vanish. Hence, a skew-symmetric matrix is always positive semidefinite.

with

$$\mathbf{J}_{2g} = \begin{bmatrix} 0 & \mathbf{I}_g \\ -\mathbf{I}_g & 0 \end{bmatrix} \quad (3.52)$$

where \mathbf{I}_g denotes the $g \times g$ unitary matrix. Note that \mathbf{J}_{2g} is skew-symmetric:

$$\mathbf{J}_{2g}^T = -\mathbf{J}_{2g} \quad (3.53)$$

The validity of Equation (3.51) can be shown by substituting

$$\mathbf{J}_{2g}\mathbf{Z} = \begin{bmatrix} \omega^2\mathbf{M}_0 - \mathbf{E}_2 + \mathbf{E}_1\mathbf{E}_0^{-1}\mathbf{E}_1^T & -\mathbf{E}_1\mathbf{E}_0^{-1} \\ -\mathbf{E}_0^{-1}\mathbf{E}_1^T & \mathbf{E}_0^{-1} \end{bmatrix} \quad (3.54)$$

and

$$(\mathbf{J}_{2g}\mathbf{Z})^T = \begin{bmatrix} \omega^2\mathbf{M}_0^T - \mathbf{E}_2^T + (\mathbf{E}_1\mathbf{E}_0^{-1}\mathbf{E}_1^T)^T & -(\mathbf{E}_0^{-1}\mathbf{E}_1^T)^T \\ -(\mathbf{E}_1\mathbf{E}_0^{-1})^T & (\mathbf{E}_0^{-1})^T \end{bmatrix} \quad (3.55)$$

As the coefficient matrices $\mathbf{M}_0, \mathbf{E}_0, \mathbf{E}_2$ are symmetric, Equation (3.51) follows immediately from (3.54) and (3.55).

3.3.3 Algorithms

The eigenvalue problem (3.42) can be solved using well-established algorithms. When using high-order spectral elements, the number of nodes required to discretize a plate or an axisymmetric structure will be small. Typically, the dimension of the matrix \mathbf{Z} will be of order 100. Standard eigenvalue solvers like the QZ algorithm [173], which is one of the algorithms that are incorporated in the *LAPACK* [174] library (Linear Algebra Package, accessible in *Matlab* through the function `eig`) lead to very accurate and rapidly converging results for this problem. This algorithm will be used for the majority of numerical examples presented in this work. If the dimension of the eigenvalue problem becomes large, e.g. when discretizing a complex three-dimensional waveguide, it can be worthwhile to employ an algorithm that is optimized for solving large eigenvalue problems. The well-known *ARPACK* (ARnoldi PACKage) [175] incorporates an Arnoldi method that makes use of the fact that \mathbf{Z} is a sparse matrix to reduce computational costs (function `eigs` in *Matlab*). It is most efficient, if only a small number of particular eigenvalues of a large sparse matrix have to be computed.

Besides these standard algorithms there exist specific approaches that utilize the Hamiltonian properties of a matrix to improve efficiency [176–179]. *Even-IRA*, an implementation of an implicitly-restarted Krylov subspace method, developed by Mehrmann et al. [180], has been tested in this work for computing the eigenvalues and eigenvectors of the \mathbf{Z} matrix. This implementation, similar to the *Matlab* function `eigs`, is optimized for large sparse matrices. If this is the case, the *Even-IRA* algorithm can significantly reduce computational costs compared to `eigs`. Moreover, this algorithm is structure-preserving, i. e. the real part of the purely imagi-

nary solutions actually vanishes, while a small real part can be obtained when using standard algorithms due to numerical errors.

Independently of these available algorithms, a novel solution procedure for the computation of dispersion curves is presented in Section 7. By tracing the modes and restricting the solutions to eigenvalues that are of interest in the given set-up, computational times can be significantly reduced, if the number of desired solutions is small.

3.4 Group velocity

In many practical applications of guided waves, the group velocities of the propagating wave modes are particularly of interest. For a propagating mode with real wavenumber $\tilde{k}(\omega)$ (imaginary eigenvalue $\tilde{\lambda}$), the group velocity is defined as

$$c_g = \frac{\partial \omega}{\partial \tilde{k}} = i \frac{\partial \omega}{\partial \tilde{\lambda}} \quad (3.56)$$

In different approaches, group velocities are calculated as the gradients from two adjacent points in the dispersion curve $\omega(k)$ [58, 181, 182]. In the proposed method the group velocities of the modes of interest can be obtained directly as the eigenvalue derivatives. Hence, they can be computed accurately at a given frequency and the results do not depend on the chosen frequency increment.

Let λ be an eigenvalue of $-\mathbf{Z}$ with the corresponding eigenvector $\boldsymbol{\Psi}$:

$$\mathbf{Z}\boldsymbol{\Psi} + \lambda\boldsymbol{\Psi} = 0 \quad (3.57)$$

Since \mathbf{Z} is a Hamiltonian matrix, $-\lambda$ is an eigenvalue as well [183]. The corresponding eigenvector is denoted by $\boldsymbol{\Phi}$:

$$\mathbf{Z}\boldsymbol{\Phi} - \lambda\boldsymbol{\Phi} = 0 \quad (3.58)$$

$$\boldsymbol{\Phi} = \begin{Bmatrix} \hat{\mathbf{u}}_n^- \\ \hat{\mathbf{q}}_n^- \end{Bmatrix} \quad (3.59)$$

Pre-multiplying Equation (3.58) with \mathbf{J}_{2g} and taking the transpose results in

$$\boldsymbol{\Phi}^T (\mathbf{J}_{2g} \mathbf{Z})^T - \lambda \boldsymbol{\Phi}^T \mathbf{J}_{2g}^T = 0 \quad (3.60)$$

which is rewritten using Equations (3.51) and (3.53) as

$$\boldsymbol{\Phi}^T \mathbf{J}_{2g} \mathbf{Z} + \lambda \boldsymbol{\Phi}^T \mathbf{J}_{2g} = 0 \quad (3.61)$$

Differentiating Equation (3.57) with respect to ω leads to

$$\frac{\partial}{\partial \omega} (\mathbf{Z}\boldsymbol{\Psi} + \lambda\boldsymbol{\Psi}) = \mathbf{Z}\boldsymbol{\Psi}' + \lambda\boldsymbol{\Psi}' + \mathbf{Z}'\boldsymbol{\Psi} + \lambda'\boldsymbol{\Psi} = 0 \quad (3.62)$$

After pre-multiplying with $\Phi^T \mathbf{J}_{2g}$ we obtain

$$\Phi^T \mathbf{J}_{2g} \mathbf{Z} \psi' + \lambda \Phi^T \mathbf{J}_{2g} \psi' + \Phi^T \mathbf{J}_{2g} \mathbf{Z}' \psi + \lambda' \Phi^T \mathbf{J}_{2g} \psi = 0 \quad (3.63)$$

Using Equation (3.61), the first and second term vanish:

$$\Phi^T \mathbf{J}_{2g} \mathbf{Z}' \psi + \lambda' \Phi^T \mathbf{J}_{2g} \psi = 0 \quad (3.64)$$

The first term of Equation (3.64) can be simplified by using

$$\mathbf{J}_{2g} \mathbf{Z}' = \begin{bmatrix} 2\omega \mathbf{M}_0 & 0 \\ 0 & 0 \end{bmatrix} \quad (3.65)$$

and substituting the displacements and nodal forces

$$\Phi^T \mathbf{J}_{2g} \mathbf{Z}' \psi = 2\omega (\hat{\mathbf{u}}_n^-)^T \mathbf{M}_0 \hat{\mathbf{u}}_n \quad (3.66)$$

The second term in Equation (3.64) can be written

$$\lambda' \Phi^T \mathbf{J}_{2g} \psi = \lambda' \left\{ (\hat{\mathbf{u}}_n^-)^T, (\hat{\mathbf{q}}_n^-)^T \right\} \begin{bmatrix} 0 & \mathbf{I}_g \\ -\mathbf{I}_g & 0 \end{bmatrix} \begin{Bmatrix} \hat{\mathbf{u}}_n \\ \hat{\mathbf{q}}_n \end{Bmatrix} = \lambda' ((\hat{\mathbf{u}}_n^-)^T \hat{\mathbf{q}}_n - (\hat{\mathbf{q}}_n^-)^T \hat{\mathbf{u}}_n) \quad (3.67)$$

Substituting Equations (3.66) and (3.67) into (3.64) results in

$$\frac{1}{\lambda'} = \frac{(\hat{\mathbf{q}}_n^-)^T \hat{\mathbf{u}}_n - (\hat{\mathbf{u}}_n^-)^T \hat{\mathbf{q}}_n}{2\omega (\hat{\mathbf{u}}_n^-)^T \mathbf{M}_0 \hat{\mathbf{u}}_n} \quad (3.68)$$

Equation (3.68) is valid for all eigenvalues of the \mathbf{Z} matrix. The group velocity on the other hand is only well defined for propagating modes with real wavenumber (purely imaginary eigenvalue $\tilde{\lambda}$). For those modes, if ψ is an eigenvector corresponding to $\tilde{\lambda}$, then the eigenvector corresponding to $-\tilde{\lambda}$ is its complex conjugate:

$$\Phi = \bar{\psi} \quad (3.69)$$

and for the group velocity we obtain

$$c_g = \frac{i}{\tilde{\lambda}'} = i \frac{\hat{\mathbf{u}}_n^* \hat{\mathbf{q}}_n - \hat{\mathbf{q}}_n^* \hat{\mathbf{u}}_n}{2\omega \hat{\mathbf{u}}_n^* \mathbf{M}_0 \hat{\mathbf{u}}_n} \quad (3.70)$$

where (*) denotes the conjugate transpose and the same symbols for the eigenvectors as before are used for simplicity. Since the eigenvectors $\hat{\mathbf{u}}_n$ and $\hat{\mathbf{q}}_n$ are known after the solution of the eigenvalue problem and \mathbf{M}_0 is a diagonal matrix, only few vector multiplications are required to obtain the group velocities.

3.5 Shear-horizontal modes

The two-dimensional formulation presented in this chapter allows for the modeling of *Lamb-type* modes.¹⁷ A different type of guided waves in plates - usually referred to as shear-horizontal modes - has been neglected until now. In case of isotropic material behavior, these modes cause displacements in x -direction only (out-of-plane motion). In many practical applications, shear-horizontal modes are not of interest as their excitability is not significant in most experimental set-ups. However, if these modes are relevant, they can be obtained using a three-dimensional formulation. Still, only the through-thickness direction of the plate is discretized, but now three degrees of freedom are assigned to each node (Figure 3.5).

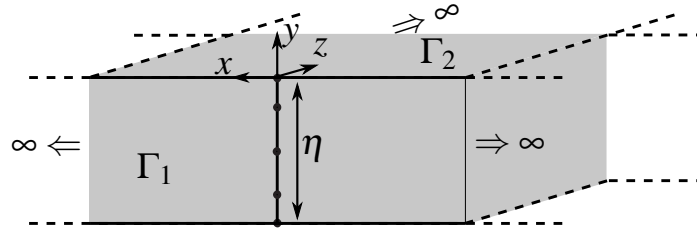


Figure 3.5: Discretization of a plate (a) and cylinder (b) in the SBFEM.

For the sake of conciseness, the same symbols as in the two-dimensional formulation are used when possible. The three-dimensional displacement vector reads $\mathbf{u} = [u_x, u_y, u_z]^T$ and the stress-displacement relationship for the general three-dimensional case reads (see Section 2.1.1)

$$\boldsymbol{\sigma}(x, y, z, \omega) = [\sigma_x \ \sigma_y \ \sigma_z \ \tau_{yz} \ \tau_{xz} \ \tau_{xy}]^T = \mathbf{DLu}(z, x, y, \omega) \quad (3.71)$$

with the three-dimensional differential operator (repeated for easy reference)

$$\mathbf{L} = \begin{bmatrix} \partial_x & 0 & 0 & 0 & \partial_z & \partial_y \\ 0 & \partial_y & 0 & \partial_z & 0 & \partial_x \\ 0 & 0 & \partial_z & \partial_y & \partial_x & 0 \end{bmatrix}^T \quad (3.72)$$

\mathbf{D} is the 6×6 elasticity matrix. As the displacement field is assumed to be constant in x -direction, the partial derivatives ∂_x vanish. Consequently, the discretized stress-displacement

¹⁷Strictly speaking, Lamb's solution refers to guided waves in homogeneous isotropic plates. More generally, the term *Lamb modes* or *Lamb-type modes* is nowadays frequently used to describe guided waves in arbitrary plate structures, as long as the two-dimensional formulation is valid (cf. Section 3.6).

relationship (3.13) is still valid if we substitute the matrices

$$\mathbf{b}_1 = \begin{bmatrix} 0 & 0 & 0 & 0 & 1 & 0 \\ 0 & 0 & 0 & 1 & 0 & 0 \\ 0 & 0 & 1 & 0 & 0 & 0 \end{bmatrix}^T \quad (3.73)$$

$$\mathbf{b}_2 = \begin{bmatrix} 0 & 0 & 0 & 0 & 0 & 1 \\ 0 & 1 & 0 & 0 & 0 & 0 \\ 0 & 0 & 0 & 1 & 0 & 0 \end{bmatrix}^T \quad (3.74)$$

as well as the three-dimensional shape functions

$$\mathbf{N}(\boldsymbol{\eta}) = \begin{bmatrix} N_1(\boldsymbol{\eta}) & 0 & 0 & N_2(\boldsymbol{\eta}) & 0 & 0 & \dots & N_n(\boldsymbol{\eta}) & 0 & 0 \\ 0 & N_1(\boldsymbol{\eta}) & 0 & 0 & N_2(\boldsymbol{\eta}) & 0 & \dots & 0 & N_n(\boldsymbol{\eta}) & 0 \\ 0 & 0 & N_1(\boldsymbol{\eta}) & 0 & 0 & N_2(\boldsymbol{\eta}) & \dots & 0 & 0 & N_n(\boldsymbol{\eta}) \end{bmatrix} \quad (3.75)$$

The virtual work principle can be employed analogously to the two-dimensional case. More precisely, the virtual displacement field can now be a function of x and z :

$$\begin{aligned} \delta U = - \int_0^\infty \int_{-\infty}^\infty \delta \mathbf{u}_n^T(x, z) \left(\mathbf{E}_0 \mathbf{u}_{n,zz}(x, z) + (\mathbf{E}_1^T - \mathbf{E}_1) \mathbf{u}_{n,z}(x, z) - \mathbf{E}_2 \mathbf{u}_n(x, z) \right) dx dz \\ + \int_{-\infty}^\infty \delta \mathbf{u}_n^T(x, 0) \mathbf{q}_n(x, 0) dx \end{aligned} \quad (3.76)$$

$$\delta K = \int_0^\infty \int_{-\infty}^\infty \delta \mathbf{u}_n^T(x, z) \mathbf{M}_0 \ddot{\mathbf{u}}_n(x, z) dx dz \quad (3.77)$$

$$\delta W = \int_{-\infty}^\infty \delta \mathbf{u}_n^T(x, 0) \mathbf{f}_n(x, 0) dx \quad (3.78)$$

However, substituting these equations into the virtual work principle (3.15) leads to the eigenvalue problem to be of the same form as for the two-dimensional case.

3.6 Anisotropy

The current approach is not restricted to isotropic materials. Generally, anisotropic material behavior of a homogeneous layer can be modeled simply by modifying the elasticity matrix \mathbf{D} . For an isotropic material, the elasticity matrix is defined by two independent constants for instance the Poisson's ratio ν and shear modulus G as given in Equation (2.13). Contrary, in the most general form of anisotropy, the elasticity matrix can be defined by up to 21 independent constants. In that case it is fully populated:

$$\mathbf{D} = \begin{bmatrix} D_{11} & D_{12} & D_{13} & D_{14} & D_{15} & D_{16} \\ & D_{22} & D_{23} & D_{24} & D_{25} & D_{26} \\ & & D_{33} & D_{34} & D_{35} & D_{36} \\ \text{sym.} & & & D_{44} & D_{45} & D_{46} \\ & & & & D_{55} & D_{56} \\ & & & & & D_{66} \end{bmatrix} \quad (3.79)$$

Note that the elasticity matrix is always symmetric. This general elasticity matrix can be employed in the three-dimensional formulation as presented in Section 3.5. On the other hand, care has to be taken when applying the two-dimensional formulation. If the elasticity matrix is fully populated, the displacement components in x -direction are not independent of the other directions, as has been implied by the two-dimensional plane strain assumption. Consequently, one cannot distinguish between Lamb-type and shear-horizontal modes. All propagating modes cause displacement fields in all three directions. Generally speaking, the plane strain assumption is valid, if the three-dimensional elasticity matrix is of the form

$$\mathbf{D} = \begin{bmatrix} D_{11} & D_{12} & D_{13} & D_{14} & 0 & 0 \\ & D_{22} & D_{23} & D_{24} & 0 & 0 \\ & & D_{33} & D_{34} & 0 & 0 \\ \text{sym.} & & & D_{44} & 0 & 0 \\ & & & & D_{55} & D_{56} \\ & & & & & D_{66} \end{bmatrix} \quad (3.80)$$

If this is the case, the Lamb-type modes are decoupled from the shear-horizontal modes and the elasticity matrix corresponding to the two-dimensional formulation is given by

$$\mathbf{D} = \begin{bmatrix} D_{11} & D_{12} & D_{13} & D_{14} \\ & D_{22} & D_{23} & D_{24} \\ \text{sym.} & & D_{33} & D_{34} \\ & & & D_{44} \end{bmatrix} \quad (3.81)$$

3.7 Details on the implementation

3.7.1 Non-dimensionalization

To improve numerical stability and comparability with different approaches, dimensionless quantities (denoted with a bar) are used throughout the calculation:

$$\mathbf{E}_0 = Gh \bar{\mathbf{E}}_0 \quad (3.82a)$$

$$\mathbf{E}_1 = G \bar{\mathbf{E}}_1 \quad (3.82b)$$

$$\mathbf{E}_2 = G/h \bar{\mathbf{E}}_2 \quad (3.82c)$$

$$\mathbf{M}_0 = \rho h \bar{\mathbf{M}}_0 \quad (3.82d)$$

$$z = h \bar{z} \quad (3.82e)$$

Substituting these expressions into the Scaled Boundary Finite Element equation (3.32b) and introducing the dimensionless frequency

$$a = \frac{\omega h}{c_s} \quad (3.83)$$

with the shear wave velocity

$$c_s = \sqrt{\frac{G}{\rho}} \quad (3.84)$$

leads to a dimensionless equation of the same form as the original SBFEM equation

$$\bar{\mathbf{E}}_0 \mathbf{u}_{\mathbf{n}, \bar{z}\bar{z}}(\bar{z}) + (\bar{\mathbf{E}}_1^T - \bar{\mathbf{E}}_1) \mathbf{u}_{\mathbf{n}, \bar{z}}(\bar{z}) + (-\bar{\mathbf{E}}_2 + a^2 \bar{\mathbf{M}}_0) \mathbf{u}_{\mathbf{n}}(\bar{z}) = 0 \quad (3.85)$$

Consequently, the solution of the eigenvalue problem leads to dimensionless wavenumbers

$$\bar{k} = h k \quad (3.86)$$

If only one material is present, its parameters can be chosen to be $G = 1 \text{ GPa}$; $h = 1 \text{ mm}$; $\rho = 1 \text{ mg mm}^{-3}$ in the computation. The dimensioned results for a particular geometry and material can then be retrieved using Equations (3.83) and (3.86). If several materials are considered in the same structure, their parameters can be defined relative to the first.

3.7.2 Parallelization

The wavenumbers are obtained from an eigenvalue problem, which can be solved very accurately and efficiently, even if the solutions are very close to each other. Hence, no mode-tracing is required for the calculation in contrast to analytical approaches, where mode-tracing is employed to improve convergence and stability of the solution [47]. After the solutions for all frequencies have been computed, mode-tracing can still be used to sort the solutions belonging to the same mode. However, as the solutions can be obtained independently from each other, the

computations can be efficiently parallelized by simultaneously solving the eigenvalue problem for different frequencies. In the current implementation, the parallelization is realized using a `parfor` loop in *Matlab*. This has been tested to reduce the computational time by about a factor 2.5 on a quadcore processor for the examples presented in Section 3.8.

3.8 Numerical examples

In this section, several numerical examples are analyzed and compared with various approaches presented in the literature. A homogeneous plate is considered first, as the results can directly be compared with analytical calculations. Thereafter, layered composites and functionally graded materials are analyzed and compared with the results obtained by other authors using different approaches.

3.8.1 Homogeneous plate

For a homogeneous isotropic plate, the wavenumbers of Lamb wave modes can be obtained as roots of analytical equations [15].¹⁸ They are separated into two sets of solutions with the displacement fields being symmetric or antisymmetric with respect to the mid-plane of the plate. These sets of modes are commonly referred to as $[S_0, S_1, \dots]$ and $[A_0, A_1, \dots]$, respectively.

Figure 3.6 compares the analytical solution with the results obtained using the SBFEM for a Poisson's ratio of 0.3. Note that since dimensionless parameters are used, a homogeneous isotropic material is sufficiently characterized by its Poisson's ratio. For the analytical solution, the dimensionless frequency increment is about 0.01, and the group velocities have been obtained as the gradient between two adjacent solutions. Contrary in the SBFEM, the group velocities have been computed at each frequency step using the approach presented in Section 3.4.

The results show excellent agreement. The through-thickness direction of the plate has been discretized by a single 15-noded element. The accuracy of the solution depends on the complexity of the considered mode. If very high frequencies are of interest, a finer discretization should be used. The determination of the number of elements needed for the computation can easily be included in the algorithm by performing a convergence test at the highest frequency of interest.

¹⁸Note that even though these equations can be derived analytically, their solution is non-trivial and requires sophisticated numerical root-finding algorithms. The main difficulty lies in the fact that an (a priori unknown) number of solutions has to be found, while standard root-finding algorithms converge to one solution only. Additionally, for a given frequency two solutions can be arbitrarily close to each other.

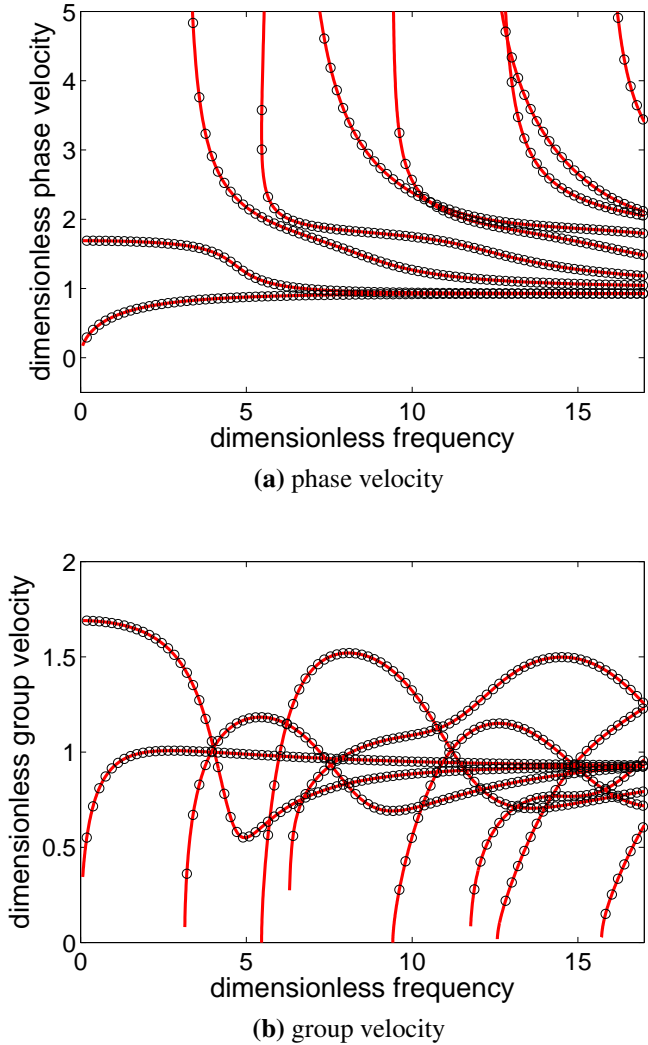


Figure 3.6: Non-dimensional dispersion curves for a homogeneous plate with a Poisson's ratio of 0.3, obtained using the Scaled Boundary Finite Element Method (\circ) and compared to analytical results ($-$).

To compare the accuracy of the proposed method for different discretizations, the computed phase velocities are explicitly given for a dimensionless frequency of $a = 6$ and $a = 16$ in Tables 3.2a and 3.2b, respectively. From the analytical equations, the wavenumbers have been obtained using the function `fminbnd` in *Matlab* with a termination tolerance of 10^{-14} . The error of the analytical solutions can hence be neglected for the comparison with the numerical examples. For the SBFEM discretization, a single element has been used, containing 7, 10 and 15 nodes, respectively. At the lower frequency, a good agreement with the analytical solution can be obtained even for the 7-noded element (Table 3.2a). The maximum error is approximately 0.6 %, while for the 15-noded element the maximum error is about 10^{-8} . For the higher frequency, the 7-noded element is satisfactory only for the lower modes, while the highest mode is not found. However, the use of one 15-noded element still gives very accurate results, with a maximum error of about $2 \cdot 10^{-5}$ occurring for the highest mode.

Table 3.2: Dimensionless phase velocities of all propagating modes for the homogeneous plate at dimensionless frequencies $a = 6$ and $a = 16$ obtained with elements of different order.

(a) $a = 6$				
Mode	7 nodes	10 nodes	15 nodes	analytical
A ₀	0.892377083	0.892368186	0.892368185	0.892368187
S ₀	1.048492444	1.048488054	1.048488054	1.048488043
A ₁	1.905612410	1.905598063	1.905598062	1.905598073
S ₁	2.084448496	2.084397050	2.084397049	2.084397062
(b) $a = 16$				
Mode	7 nodes	10 nodes	15 nodes	analytical
A ₀	0.929820689	0.926634360	0.926592992	0.926592986
S ₀	0.935214851	0.928301089	0.928287063	0.928287069
A ₁	1.053514717	1.053401432	1.053400757	1.053400762
S ₁	1.236567473	1.221083407	1.221086534	1.221086528
A ₂	1.644355175	1.581265790	1.579071811	1.579071814
S ₂	1.882025284	1.835059824	1.834351957	1.834351935
S ₃	2.308292781	2.157421619	2.152748746	2.152748660
A ₃	2.665274120	2.320209648	2.312747860	2.312747619
A ₄		4.979333889	6.230861230	6.230711438

To demonstrate the effect of higher-order elements, the convergence of the results for the highest propagating mode at a dimensionless frequency of 20 is plotted in Figure 3.7. Elements containing 2, 3, 8 and 15 nodes have been used. The computed phase velocity is shown as a function of the total number of nodes, since the computational time is approximately the same for the same number of nodes.¹⁹ It can be seen that the efficiency of the computation can highly be improved by utilizing higher-order elements.

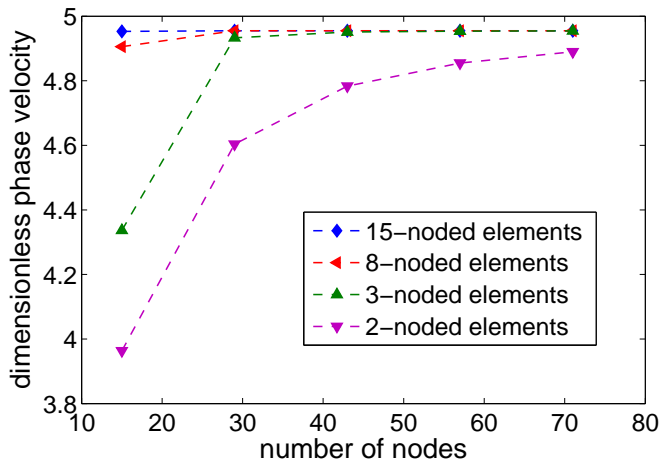


Figure 3.7: Convergence of the results for the highest propagating mode at a dimensionless frequency of 20 in the homogeneous plate.

The mode shapes of the propagating Lamb waves are represented by the eigenvectors (Equation (3.42)). Though the amplitudes $\hat{\mathbf{u}}_{\mathbf{n}}$ are generally complex values, either the real or imaginary part of each component for a particular mode equals zero as the particle movement is elliptical. In a homogeneous plate, each mode is either symmetric or antisymmetric with respect to the midplane of the plate. As an example, the y -components of the displacements of the four modes (two symmetric modes S_0 , S_1 and two antisymmetric modes A_0 , A_1) present at a dimensionless frequency of 6 are shown in Figure 3.8. Again, the results are compared to analytical solutions [15]. Only the values at nodal points are shown for the SBFEM solutions. The displacements at any other position can be obtained by interpolating the nodal values using the applied shape functions (cf. Equation (3.9)). The SBFEM solutions are in excellent agreement with the analytical solution.

¹⁹The dimension of the coefficient matrices increases with the total number of nodes, irrespective of the type of elements. The computational costs for solving the eigenvalue problem is roughly of order n^3 . In comparison, the differences in computational costs spend on the discretization and the computation of the coefficient matrices are negligible.

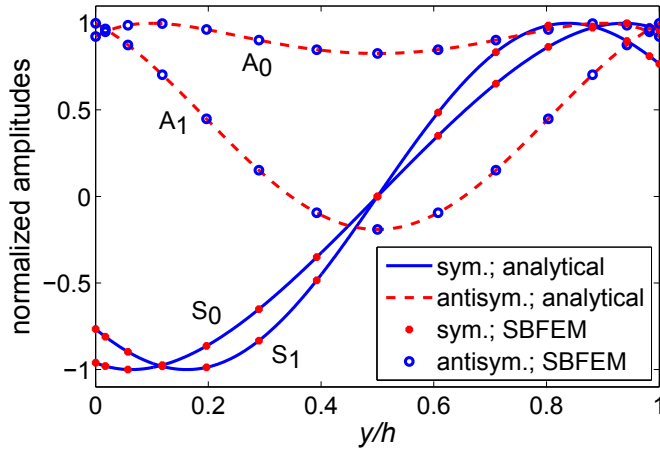
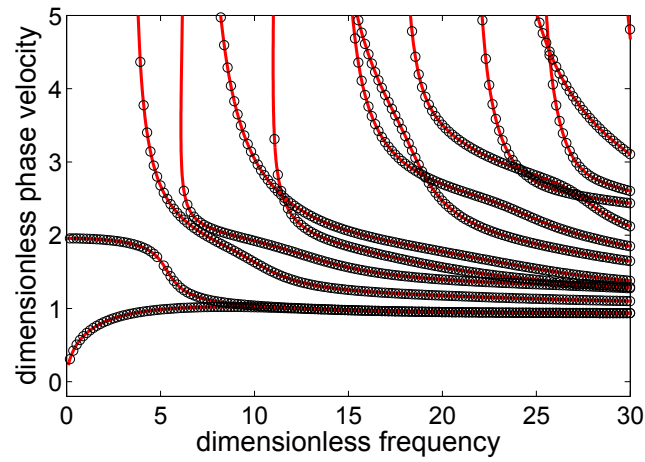


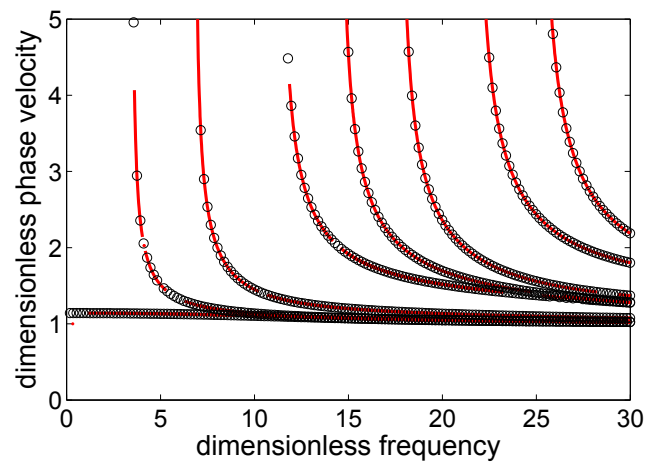
Figure 3.8: Displacement amplitudes in y -direction of the four propagating modes at a dimensionless frequency of 6 in the homogeneous plate.

3.8.2 Layered composite

The extension of the proposed method to plates consisting of multiple layers is straightforward. The easiest way is to discretize every layer of the interface separately, with one or more elements, and assign the material parameters accordingly. If several elements are used for this purpose, the order of each element can be reduced. For instance, in the case of five layers, a discretization with five 6-noded-elements still leads to very accurate results for the first ten modes. If a very high number of layers is considered, even 2 or 3 nodes per element can be sufficient. Complicated structures, with up to 100 layers, have been tested to show good convergence without introducing numerical problems in the solution. To verify the results for multi-layered plates, the commercial software *disperse* [50,51] is used for comparison. This program utilizes the global matrix method [47], where the wavenumbers are obtained as the roots of the characteristic equation of a matrix describing the wave propagation in the given geometry. As an example, a plate consisting of 3 layers of brass and 2 layers of titanium is analyzed. Discretizing the interface with five 6-noded elements has shown to be sufficient, leading to excellent agreement with the solution obtained by *disperse*. Results for Lamb-type modes as well as SH modes are presented in Figure 3.9a and 3.9b, respectively. As only 26 nodes have to be used for the discretization, the computation is very efficient. The total computational time to obtain the dispersion curves using the SBFEM is about 0.3 s (Desktop PC with *Intel i7* CPU and 4 GB RAM). In *disperse* the computational time cannot be obtained exactly, but for this example it is roughly about 30 s on the same computer.



(a) Lamb-type modes



(b) SH modes

Figure 3.9: Dispersion curves for a composite consisting of 3 layers of brass and 2 layers of titanium obtained using the Scaled Boundary Finite Element Method (\circ) and the software *disperse* ($-$) [51].

3.8.3 Functionally graded material

In many applications, it is more realistic to assume the material parameters to vary continuously along the thickness, rather than approximating the distribution by discrete layers. This can be desirable for a more accurate description of complex composites or if the bonding characteristics between two layers become important. Another example is a plate of two components, where the volume fractions of the materials vary continuously from one surface to the other. Such examples have been studied in [137] using a power series technique, and these results are used here for comparison. An example is chosen where the density, as well as the two Lamé parameters λ and G , all follow the same through-thickness distribution of the form

$$\rho(y) = \rho_1 f_1(y/h) + \rho_2 f_2(y/h) \quad (3.87a)$$

$$\lambda(y) = \lambda_1 f_1(y/h) + \lambda_2 f_2(y/h) \quad (3.87b)$$

$$G(y) = G_1 f_1(y/h) + G_2 f_2(y/h) \quad (3.87c)$$

where the volume fractions f_1 and f_2 of the materials are

$$f_1(y/h) = 1 - (y/h)^b \quad (3.88a)$$

$$f_2(y/h) = (y/h)^b \quad (3.88b)$$

with a non-negative integer b . The material parameters are [137]

$$\begin{aligned} \rho_1 &= 7190 \text{ kg m}^{-3}; & \lambda_1 &= 74.2 \text{ GPa}; & G_1 &= 102.5 \text{ GPa} \\ \rho_2 &= 3900 \text{ kg m}^{-3}; & \lambda_2 &= 138 \text{ GPa}; & G_2 &= 118.11 \text{ GPa} \end{aligned}$$

The Poisson's ratio, which is used in the SBFEM formulation instead of the first Lamé parameter, can be calculated using [105]

$$\nu(y) = \frac{\lambda(y)}{2(\lambda(y) + G(y))} \quad (3.89)$$

leading to

$$\nu(y) = \frac{(\lambda_1 - \lambda_2)f_1(y/h) + \lambda_2}{2((\lambda_1 - \lambda_2 + G_1 - G_2)f_1(y/h) + \lambda_2 + G_2)} \quad (3.90)$$

The distribution of the shear modulus and Poisson's ratio is pictured in Figure 3.10 for the case $b = 10$. Dispersion curves for this example are shown in Figure 3.11. The phase velocity is plotted as a function of the dimensionless wave number $\bar{k} = kh$ as in the original work. As in the homogeneous example, only one 15-noded element has been used for the discretization, and again the results obtained by the two different methods are in very good agreement. As the variation of material parameters only affects the coefficient matrices as shown in Section 3.2.4, the increase of computational cost is negligible compared to the homogeneous case. To illustrate the convergence of the present technique, the dimensionless phase velocities of all modes at a dimensionless frequency of 20 are explicitly given in Table 3.3a. The computations

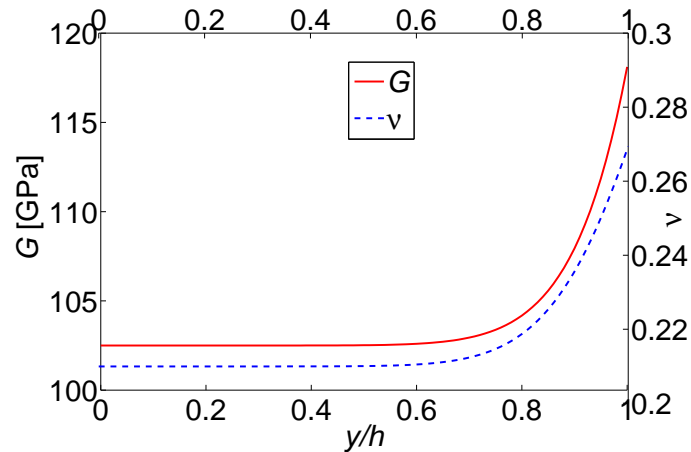


Figure 3.10: Distribution of material parameters in the functionally graded material.

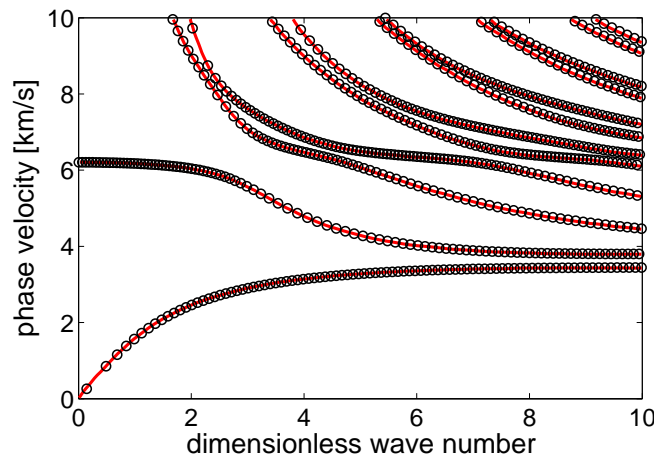


Figure 3.11: Dispersion curves for a functionally graded material obtained using the Scaled Boundary Finite Element Method (\circ) and compared with the results obtained by [137] ($-$).

are performed using one, two and three 15-noded elements, respectively. Again, the algorithm shows very fast convergence. The results for one and two elements differ by about 0.1 % for the highest mode. Adding a third element results in a change in the highest mode's phase velocity of only about 10^{-10} . For comparison, the convergence characteristics have also been assessed using 2-noded elements. In this case the material properties, as well as displacements, vary linearly within each element. This assumption has been made by other authors when investigating functionally graded materials [156, 184, 185]. Results are shown in Table 3.3b, where the number of elements is increased by a factor of four in each step of refinement. It can be seen that the convergence is very poor compared to higher-order elements. For the last step of refinement the change in phase velocity for the highest mode is still about 2.5 %. The values approach the results obtained with the 15-noded elements, but when 320 linear elements are used, the phase velocity of the highest mode still differs by about 0.2 % from the converged

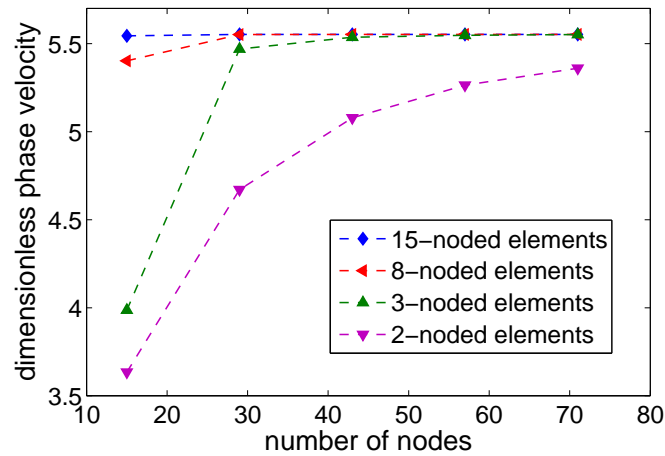


Figure 3.12: Convergence of the results for the highest mode at a dimensionless frequency of 20 in the functionally graded material.

results, while the computational time is increased by approximately a factor 200 in comparison with one 15-noded element. 3-noded (quadratic) elements (Table 3.3c) lead to significantly better convergence than linear elements, but still about 80 elements have to be used to obtain an accuracy comparable with two 15-noded elements.

The convergence is visualized in Figure 3.12 in the same way as for the homogeneous plate (Figure 3.7). All errors are roughly two times larger than compared to the homogeneous case. This is due to the fact that not only the displacements, but also the material parameters are approximated by the shape functions. Since the material parameters are described by a polynomial of order 10, a discretization with linear or quadratic elements yields a poor representation of the physical problem. Consequently, the use of higher-order elements is highly advantageous, especially for the case of functionally graded materials.

This example shows the ability of the proposed method to solve problems with arbitrary through-thickness distributions of material parameters very efficiently, and without any essential modifications of the algorithm.

Table 3.3: Dimensionless phase velocities of all eleven propagating modes at a dimensionless frequency of 20 for the FGM plate - Convergence with (a) 15-noded, (b) linear, (c) quadratic elements.

Mode	(a) 15-noded elements			(b) Linear elements			(c) Quadratic elements		
	1 element	2 elements	3 elements	20 el.	80 el.	320 el.	20 el.	80 el.	320 el.
1	0.912701729635	0.912701725534	0.912701725534	0.9424	0.9157	0.9129	0.913493	0.912705	0.912702
2	1.019802194446	1.019802122176	1.019802122172	1.0235	1.0202	1.0198	1.019935	1.019803	1.019802
3	1.059027416372	1.059027223825	1.059027223816	1.0741	1.0605	1.0591	1.059429	1.059029	1.059027
4	1.143805426793	1.143805354292	1.143805354298	1.1685	1.1456	1.1439	1.144051	1.143807	1.143805
5	1.331808924969	1.331808858898	1.331808858892	1.3760	1.3348	1.3320	1.332122	1.331810	1.331809
6	1.639059636263	1.639058585603	1.639058585589	1.6516	1.6402	1.6391	1.639262	1.639059	1.639059
7	1.724317712691	1.724315457103	1.724315457081	1.7451	1.7257	1.7244	1.724581	1.724317	1.724315
8	1.851554721770	1.851551914066	1.851551914053	1.8638	1.8523	1.8516	1.851775	1.851553	1.851552
9	2.251458355512	2.251445022221	2.251445022197	2.2460	2.2512	2.2514	2.251889	2.251447	2.251445
10	2.434030799982	2.433992420284	2.433992420289	2.4218	2.4334	2.4340	2.434222	2.433993	2.433992
11	5.544707969732	5.552223742323	5.552223741662	4.2062	5.4028	5.5424	5.532855	5.552151	5.552223

Chapter 4

Extension to arbitrary cross-sections

While the formulation presented in the previous chapter is restricted to plate structures, the modeling of waveguides with more complex cross-section becomes relevant in some applications. Examples include waves in bars [186], square pipes [58] or rails [187]. Cylinders will not be focused on in this chapter since they will be covered by the axisymmetric formulation in Chapter 5. For complex cross-sections, the Global Matrix Method cannot be applied. Very few analytical solutions have been presented in the literature e. g. for a triangular bar [41] and anisotropic waveguides with sector-shaped cross-section [42].

On the other hand, the extension of the Finite Element Method to arbitrary cross-sections is straightforward [188, 189]. It has been demonstrated by various authors, how standard Finite Element software can be employed to extract dispersion properties. In order to do that, a representative section of the waveguide is discretized with Finite Elements [56]. Applications include pipes that have a complex cross-section [58] or are filled with a fluid [57]. In a similar way, helical waveguides [190, 191] and waveguides with periodic microstructure [55] have been analyzed. However, these approaches are in general computationally expensive.

Other Finite Element based approaches, like the WFE or SAFE method can be applied to waveguides with complex cross-section in a similar way [59, 62, 192]. Recent applications include the modeling of composite shells [193], wooden bars [186], rods and rails [22, 187] and square rods [194]. More complex geometries are discussed in [195] and modified formulations for pre-stressed materials are presented in [196, 197]. Also fluid filled elastic waveguides have been addressed [181], where the governing equations describing the elastic and acoustic behavior have to be coupled. Numerical issues of the SAFE method are discussed in [198].

In this chapter, the SBFEM formulation is extended to describe waveguides with arbitrary cross-section (see also [94, 95]). The main difficulty lies in the effective discretization of the two-dimensional cross-section and the corresponding coordinate transformations (Section 4.1). However, in many aspects we can refer to well-known Finite Element procedures. Again, higher-order spectral elements are utilized for the discretization, as described in Section 4.2. The two-dimensional analog of the elements used in the previous chapter can be constructed in a straightforward way. Obviously, the computational costs are typically much larger in the

three-dimensional case.²⁰ Some examples are presented on discretizing a complex cross-section in an effective and consistent way. In most practical applications, the cross-section will reveal one or more symmetry axes. It is discussed, how the symmetry can be utilized in order to reduce the mesh. This can be a crucial step in limiting computational costs to an acceptable value.

As in the previous chapter, dispersion curves are computed by solving an eigenvalue problem at each frequency of interest. Hence, the solutions at different frequency steps are obtained independently of each other. This is advantageous in terms of stability and efficiency and allows for parallelization of the algorithm in a trivial way. On the other hand, it can be desired to know which solutions belong to the same mode. This is particularly true in the three-dimensional case, where the mode shapes can become complicated. In Section 4.3, a fast mode-tracing algorithm has been developed to sort the solutions according to the modes they represent [94]. Though the mode-tracing algorithm is presented in the context of general three-dimensional waveguides, it can be applied analogously in the two-dimensional and axisymmetric case.

Numerical examples are presented in Section 4.4 and validated with different approaches.

4.1 SBFEM formulation for guided waves in three-dimensional waveguides

To describe a waveguide with arbitrary cross-section, the three-dimensional governing equations (3.71) and (3.72) still apply. Contrary to the case of shear-horizontal modes in a plate, the derivatives with respect to the Cartesian coordinate x do not vanish. Hence the strain-displacement relationship is written as

$$\boldsymbol{\varepsilon} = \mathbf{b}_1 \mathbf{u}_{,z} + \mathbf{b}_2 \mathbf{u}_{,y} + \mathbf{b}_3 \mathbf{u}_{,x} \quad (4.1)$$

with

$$\mathbf{b}_1 = \begin{bmatrix} 0 & 0 & 0 & 0 & 1 & 0 \\ 0 & 0 & 0 & 0 & 0 & 1 \\ 0 & 0 & 1 & 0 & 0 & 0 \end{bmatrix}^T \quad (4.2a)$$

$$\mathbf{b}_2 = \begin{bmatrix} 0 & 0 & 0 & 1 & 0 & 0 \\ 0 & 1 & 0 & 0 & 0 & 0 \\ 0 & 0 & 0 & 0 & 0 & 1 \end{bmatrix}^T \quad (4.2b)$$

$$\mathbf{b}_3 = \begin{bmatrix} 1 & 0 & 0 & 0 & 0 & 0 \\ 0 & 0 & 0 & 0 & 0 & 1 \\ 0 & 0 & 0 & 0 & 1 & 0 \end{bmatrix}^T \quad (4.2c)$$

²⁰Assume we required n nodes to discretize a plate in the plane strain assumption, leading to computational costs of order $(2n)^3 = 8n^3$. A corresponding square rod (same thickness, material and frequency) would have to be discretized using n^2 nodes, leading to computational costs of order $(3n^2)^3 = 27n^6$.

Note that \mathbf{b}_1 and \mathbf{b}_2 are the same as before (Section 3.5), they are repeated here for clarity. The matrix \mathbf{b}_3 is introduced at this point to account for the derivatives in the x -direction.

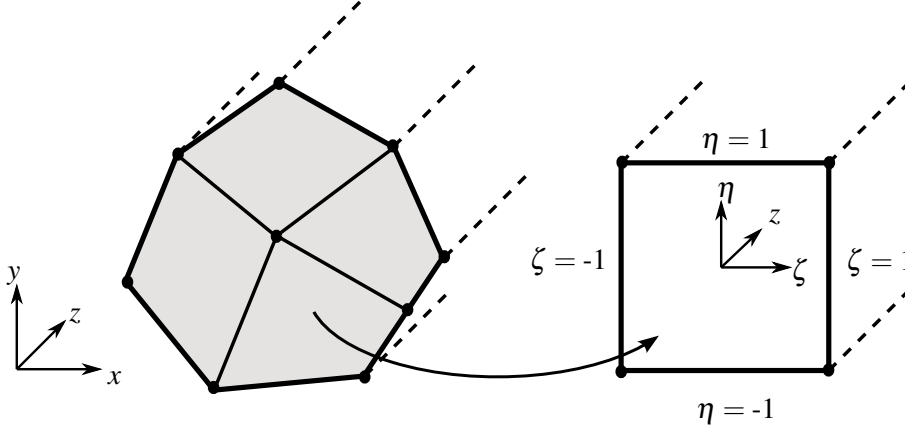


Figure 4.1: Discretization of an arbitrary 3d waveguide with four-sided elements.

A three-dimensional waveguide with arbitrary cross-section is addressed (Figure 4.1). The cross-section is discretized using two-dimensional Finite Elements. Again, the following steps are derived for one element of the Finite Element discretization. Now, each element is defined in a two-dimensional local coordinate system η , ζ . This procedure is analogous to the discretization of a two-dimensional problem in the traditional Finite Element Method (cf. Section 2.2). To rewrite Equation (4.1) in the local coordinate system, the coordinate transformation [81, 82]

$$\begin{Bmatrix} \partial_\eta \\ \partial_\zeta \end{Bmatrix} = \mathbf{J} \begin{Bmatrix} \partial_x \\ \partial_y \end{Bmatrix} \quad (4.3)$$

is required, with the Jacobian matrix

$$\mathbf{J} = \begin{bmatrix} x,\eta & y,\eta \\ x,\zeta & y,\zeta \end{bmatrix} \quad (4.4)$$

Inverting Equation (4.3) leads to

$$\begin{Bmatrix} \partial_x \\ \partial_y \end{Bmatrix} = \frac{1}{|\mathbf{J}|} \begin{bmatrix} y,\zeta & -y,\eta \\ -x,\zeta & x,\eta \end{bmatrix} \begin{Bmatrix} \partial_\eta \\ \partial_\zeta \end{Bmatrix} \quad (4.5)$$

where $|\mathbf{J}|$ is the absolute value of the Jacobian determinant. Substituting the above expressions for the partial derivatives into the strain-displacement relationship yields

$$\boldsymbol{\varepsilon} = \mathbf{b}_1 \mathbf{u}_{,z} + \frac{1}{|\mathbf{J}|} (y,\zeta \mathbf{b}_3 - x,\zeta \mathbf{b}_2) \mathbf{u}_{,\eta} + \frac{1}{|\mathbf{J}|} (-y,\eta \mathbf{b}_3 + x,\eta \mathbf{b}_2) \mathbf{u}_{,\zeta} \quad (4.6)$$

The displacements are interpolated using two-dimensional shape functions

$$\mathbf{u}(z, \eta, \zeta) = \mathbf{N}(\eta, \zeta) \mathbf{u}_n(z) \quad (4.7)$$

Equation (4.7) is formally similar to the interpolation in the general two-dimensional FEM (Equation (2.25)), but now, the nodal displacements are functions of z . The discretized strain-displacement relationship is formulated similar to the case of plate structures

$$\boldsymbol{\varepsilon}(z, \eta, \zeta) = \mathbf{B}_1 \mathbf{u}_{n,z}(z) + \mathbf{B}_2 \mathbf{u}_n(z) \quad (4.8)$$

by defining

$$\mathbf{B}_1 = \mathbf{b}_1 \mathbf{N} \quad (4.9a)$$

$$\mathbf{B}_2 = \frac{1}{|\mathbf{J}|} (y_{,\zeta} \mathbf{b}_3 - x_{,\zeta} \mathbf{b}_2) \mathbf{N}_{,\eta} + \frac{1}{|\mathbf{J}|} (-y_{,\eta} \mathbf{b}_3 + x_{,\eta} \mathbf{b}_2) \mathbf{N}_{,\zeta} \quad (4.9b)$$

It should be noted that the definition of \mathbf{B}_1 is identical to the cases described in the previous chapter (despite the fact that the shape functions are now two-dimensional polynomials). With these definitions, the application of the virtual work principle is analogous to the two-dimensional case and will not be repeated in detail. The resulting SBFEM equation (3.32b) as well as the eigenvalue problem (3.42) are formally identical to the two-dimensional case. In three dimensions, numerical integration over a two-dimensional element has to be performed to obtain the mass matrix \mathbf{M}_0 as well as the SBFEM coefficient matrices \mathbf{E}_0 , \mathbf{E}_1 , \mathbf{E}_2 :

$$\mathbf{M}_0 = \int_{-1}^1 \int_{-1}^1 \mathbf{N}^T \rho \mathbf{N} |\mathbf{J}| d\eta d\zeta \quad (4.10a)$$

$$\mathbf{E}_0 = \int_{-1}^1 \int_{-1}^1 \mathbf{B}_1^T \mathbf{D} \mathbf{B}_1 |\mathbf{J}| d\eta d\zeta \quad (4.10b)$$

$$\mathbf{E}_1 = \int_{-1}^1 \int_{-1}^1 \mathbf{B}_2^T \mathbf{D} \mathbf{B}_1 |\mathbf{J}| d\eta d\zeta \quad (4.10c)$$

$$\mathbf{E}_2 = \int_{-1}^1 \int_{-1}^1 \mathbf{B}_2^T \mathbf{D} \mathbf{B}_2 |\mathbf{J}| d\eta d\zeta \quad (4.10d)$$

In summary, the difference between the formulations for plates and waveguides with arbitrary cross-section become apparent only in the construction of the coefficient matrices. The discretization and the according coordinate transformations become more cumbersome in the general case. However, the techniques to discretize two-dimensional domains can be adopted from well-known Finite Element concepts.

4.2 Discretization of three-dimensional waveguides

4.2.1 Two-dimensional higher-order elements

For the discretization of the cross-section, the two-dimensional counterpart of the one-dimensional higher-order elements as described in Section 3.2 are utilized. Along each of the local coordinates (η, ζ) , the nodal positions are defined analogously to a one-dimensional element [82] (cf. Equation (3.45)):

$$\frac{d}{d\eta}P_p(\eta_i) = 0 \quad i = 2 \dots p \quad (4.11)$$

$$\frac{d}{d\zeta}P_p(\zeta_i) = 0 \quad i = 2 \dots p \quad (4.12)$$

The corresponding one-dimensional shape functions are obtained as

$$N_i(\eta) = \prod_{j=1, j \neq i}^{p+1} \frac{\eta - \eta_j}{\eta_i - \eta_j} \quad i = 1 \dots p+1 \quad (4.13)$$

$$N_i(\zeta) = \prod_{j=1, j \neq i}^{p+1} \frac{\zeta - \zeta_j}{\zeta_i - \zeta_j} \quad i = 1 \dots p+1 \quad (4.14)$$

The shape function corresponding to the q th node of a two-dimensional element can be written as a product of two one-dimensional shape functions

$$N_q(\eta, \zeta) = N_r(\eta)N_s(\zeta) \quad q = 1 \dots (p+1)^2 \quad (4.15)$$

where r and s denote the local number of the node in the η and ζ -direction, respectively, and q is defined as

$$q = (s-1)(p+1) + r \quad (4.16)$$

An example of a two-dimensional shape function of order 6 is depicted in Figure 4.2. Note that, as in the one-dimensional case, each shape function equals one at one node and zero at all other nodes. Again, the Gaussian-Lobatto-Legendre quadrature is employed to perform the numerical integration. The properties of the resulting coefficient matrices as described in Section 3.3 are still valid. The elements do not have to be defined by straight edges. Curved elements can be described in arbitrary coordinate systems. In many cases, curved elements can best be represented by a small number of higher-order elements. Examples for different discretizations are presented in Section 4.4.

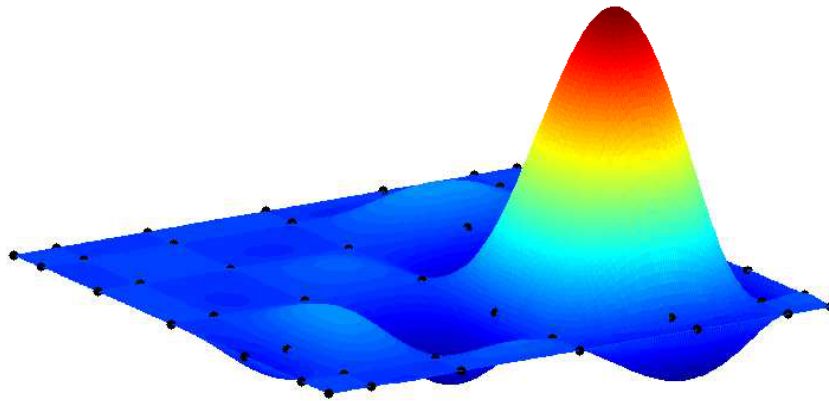


Figure 4.2: Two-dimensional shape function of order 6.

4.2.2 Symmetry

In many practical applications, the geometry of the considered waveguide is symmetric with respect to one or more symmetry axes. Additionally, the material is often either isotropic or the axes of anisotropy coincide with the geometrically symmetrical axes. In those cases the mesh can be reduced to decrease computational costs. Figure 4.3a shows an example for the discretization of the cross-section of a waveguide. The cross-section reveals four symmetry axes, labeled with L_0 , L_{45} , L_{90} and L_{135} . Higher-order spectral elements of order five have been used (36 nodes per element). In this example, 8 elements are required to discretize the whole cross-section. A finer discretization can then be achieved by increasing the element order. However, due to the symmetry axes, it is sufficient to model a quarter of the geometry as depicted in Figure 4.3b. The displacement field of the modes can only be symmetric or antisymmetric with respect to the symmetry axes L_0 and L_{90} . Hence, the complete set of solutions can be obtained by applying all four combinations of symmetric and antisymmetric boundary conditions [107] along the symmetry axes in turn and solving the eigenvalue problem for each type of boundary conditions separately. To apply a symmetric/antisymmetric boundary condition, the displacement components normal to/within the plane of symmetry are set to zero. The boundary conditions can be enforced by eliminating the corresponding degrees of freedom from the coefficient matrices.

Following the suggestion in [58], the modes are denoted as 'SS', 'AA', 'SA' and 'AS', respectively, according to the combination of symmetric and antisymmetric boundary condition applied along L_0 and L_{90} . In the present example, the additional symmetry axis L_{45} leads to the set of modes 'SA' and 'AS' being identical. Consequently, the eigenvalue problem only has to be solved three times with different boundary conditions. The computational costs for the solution of an eigenvalue problem are roughly of order n^3 . Computing the solution for a quarter of the mesh thrice with different boundary conditions thus reduces the costs approximately by a factor $4^3/3 \approx 21$.

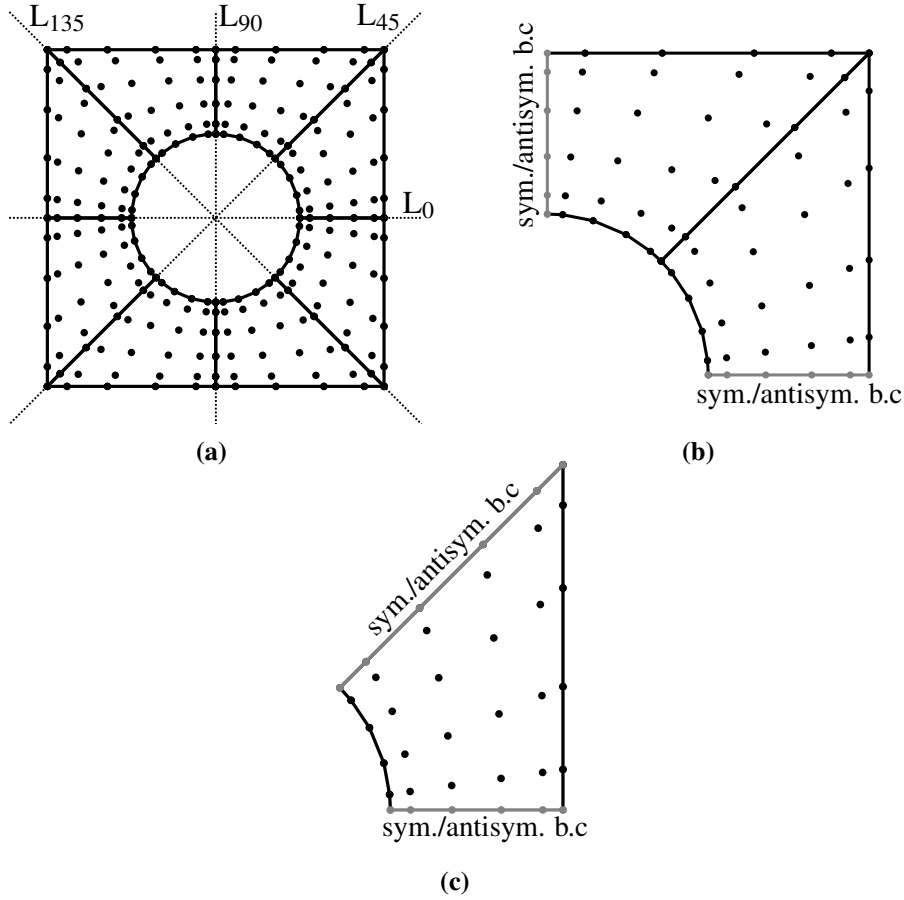


Figure 4.3: The discretization of a two-dimensional cross-section (a) can be reduced by applying boundary conditions along the symmetry axes L_0 and L_{90} (b). For the SS and AA modes, the mesh can be further reduced by utilizing the symmetry axis L_{45} (c).

For computing the 'SS' and 'AA' modes, where the same boundary conditions are applied on both axes, the mesh can be further reduced to only one element as shown in Figure 4.3c. For each of the two cases, the problem has to be solved with both symmetric and antisymmetric boundary conditions along the L_{45} axis to obtain all modes.²¹ This further reduction can be desired, if a high number of modes have to be computed or the calculations have to be performed many times with different material parameters or frequencies. For many applications, the reduction of the mesh to a quarter of the cross-section will result in reasonably short computational times.

To apply the boundary conditions along the L_{45} axis, the according degrees of freedom have to be rotated. This can be done by introducing a rotation matrix \mathbf{R}

$$\hat{\mathbf{u}}_{\mathbf{n}} = \mathbf{R}\hat{\mathbf{u}}_{\mathbf{r}} \quad (4.17)$$

²¹In summary, to compute all modes in this example, we have to solve the eigenvalue problem once for 1/4 of the mesh (SA modes) and 4 times for 1/8 of the mesh (SS and AA modes).

The transformation defined by \mathbf{R} only affects the degrees of freedom along the L_{45} axis. In the modified displacement vector $\hat{\mathbf{u}}_{\mathbf{r}}$ these degrees of freedom are rotated to be parallel and perpendicular to the L_{45} direction, respectively. Specifically, if $[u_{jx}, u_{jy}, u_{jz}]$ are the displacement components of one node on the symmetry axis, the transformation reads

$$\begin{pmatrix} u_{1x} \\ u_{1y} \\ u_{1z} \\ \vdots \\ u_{jx} \\ u_{jy} \\ u_{jz} \\ \vdots \end{pmatrix} = \begin{bmatrix} 1 & & & & & & & & \\ & 1 & & & & & & & \\ & & 1 & & & & & & \\ & & & \ddots & & & & & \\ & & & & 1 & & & & \\ & & & & & \cos(-\frac{\pi}{4}) & -\sin(-\frac{\pi}{4}) & & \\ & & & & & \sin(-\frac{\pi}{4}) & \cos(-\frac{\pi}{4}) & & \\ & & & & & & & \ddots & \end{bmatrix} \begin{pmatrix} u_{1x} \\ u_{1y} \\ u_{1z} \\ \vdots \\ u_{jx} \\ u_{jyr} \\ u_{jzr} \\ \vdots \end{pmatrix} \quad (4.18)$$

with u_{jyr} and u_{jzr} being the displacement components parallel and perpendicular to the symmetry axis, respectively. The quadratic eigenvalue problem (Equation (3.35)) can then be written as

$$\left(\lambda^2 \mathbf{E}_0 + \lambda (\mathbf{E}_1^T - \mathbf{E}_1) - \mathbf{E}_2 + \omega^2 \mathbf{M}_0 \right) \mathbf{R} \hat{\mathbf{u}}_{\mathbf{r}} = 0 \quad (4.19)$$

In order to maintain the symmetry properties of the coefficient matrices, we multiply Equation (4.19) by \mathbf{R}^T to assemble the matrix \mathbf{Z} in the same form as before:

$$\left(\lambda^2 \mathbf{R}^T \mathbf{E}_0 \mathbf{R} + \lambda \mathbf{R}^T (\mathbf{E}_1^T - \mathbf{E}_1) \mathbf{R} - \mathbf{R}^T \mathbf{E}_2 \mathbf{R} + \omega^2 \mathbf{R}^T \mathbf{M}_0 \mathbf{R} \right) \hat{\mathbf{u}}_{\mathbf{r}} = 0 \quad (4.20)$$

The matrix $\mathbf{Z}_{\mathbf{r}}$ can then be defined similarly to Equation (3.39):

$$\mathbf{Z}_{\mathbf{r}} = \begin{bmatrix} \mathbf{E}_{0\mathbf{r}}^{-1} \mathbf{E}_{1\mathbf{r}}^T & -\mathbf{E}_{0\mathbf{r}}^{-1} \\ \omega^2 \mathbf{M}_{0\mathbf{r}} - \mathbf{E}_{2\mathbf{r}} + \mathbf{E}_{1\mathbf{r}} \mathbf{E}_{0\mathbf{r}}^{-1} \mathbf{E}_{1\mathbf{r}}^T & -\mathbf{E}_{1\mathbf{r}} \mathbf{E}_{0\mathbf{r}}^{-1} \end{bmatrix} \quad (4.21)$$

with

$$\mathbf{M}_{0\mathbf{r}} = \mathbf{R}^T \mathbf{M}_0 \mathbf{R}, \quad \mathbf{E}_{0\mathbf{r}} = \mathbf{R}^T \mathbf{E}_0 \mathbf{R}, \quad \mathbf{E}_{1\mathbf{r}} = \mathbf{R}^T \mathbf{E}_1 \mathbf{R}, \quad \mathbf{E}_{2\mathbf{r}} = \mathbf{R}^T \mathbf{E}_2 \mathbf{R} \quad (4.22)$$

4.3 Mode-tracing

In the proposed approach, the dispersion curves for a given geometry are obtained by solving the eigenvalue problem (3.42) multiple times for a given set of frequencies. As a result, the wavenumbers of all modes are obtained as the eigenvalues, and the phase velocities c_p of the

propagating modes can be computed by applying

$$c_p = \frac{\omega}{k} \quad (4.23)$$

At every frequency step, the group velocities of the propagating modes can be obtained using the eigenvectors (Equation (3.70)). The resulting wavenumbers at each frequency are usually simply sorted by their magnitudes. It is generally desirable to group the results that represent the same mode. It has been shown by other authors using the SAFE method that this can be achieved by comparing the eigenvectors obtained at different frequencies [195]. The most common technique is to use the angle θ_{ij} between two normalized eigenvectors Ψ_i and Ψ_j to determine whether they represent the same mode. One particular function of the angle is often referred to as *modal assurance criterion* (MAC) in the literature [199–201]:

$$\text{MAC} = \cos^2 \varphi_{ij} = (\Psi_i^T \Psi_j)^2 \quad (4.24)$$

The use of the angle φ_{ij} offers a simple and often reliable way to sort the modes obtained from the solution of the eigenvalue problem. However, this approach can fail if a high number of modes is considered or the mode shape of a mode changes rapidly within one frequency increment. In those cases a small angle φ_{ij} does not guarantee the eigenvectors i and j belonging to the same mode. Moreover, for this approach to be utilized, all eigenvectors have to be stored until the modes are sorted, which is not always desirable. Furthermore, due to the high number of dot products to be computed, this approach is computationally relatively expensive.

In this work a different approach is developed, which is generally very fast and does not require to store the eigenvectors. It is based on tracing the wavenumbers as well as the group velocities using a Taylor series or Padé expansion. The procedure is somewhat similar to the mode-tracing in the Global Matrix Method, where linear or quadratic extrapolation is used to facilitate the computation of roots [47, 202]. Contrary, in the approach presented here, mode-tracing is employed to sort the modes after the computation of the full set of solutions is completed. The value of each wavenumber at a given frequency is approximated based on the wavenumbers at previous frequency steps. The resulting guess is compared with the wavenumbers that have been obtained from the solution of the eigenvalue problem. The wavenumber being closest to the approximated guess is assumed to represent the same mode. To avoid errors in regions where wavenumbers of two modes are very close, the group velocities are traced as well. The approximations can be calculated with high accuracy since the group velocities are computed as eigenvalue derivatives as described in Section 3.4.

The dispersion curve of one mode in the k - ω -plane is addressed (Figure 4.4). Assuming the wavenumbers $k(\omega)$ have been computed at the frequencies $\omega_0 \dots \omega_3$ and the wavenumbers k_0, k_1, k_2 have already been sorted. An approximate value k_T for the wavenumber k_3 can then be obtained using a Taylor series. The general form of a third-order Taylor approximation reads

$$k_T(\omega_3) = \gamma_0 + \gamma_1 \Delta\omega + \gamma_2 \Delta\omega^2 + \gamma_3 \Delta\omega^3 \quad (4.25)$$

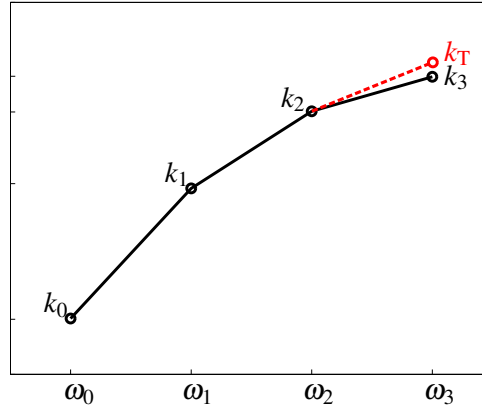


Figure 4.4: To trace a mode, a guess k_T for the wavenumber k_3 is computed, based on the wavenumbers k_0, k_1, k_2 .

with

$$\gamma_0 = k(\omega_2) \quad (4.26a)$$

$$\gamma_1 = k'(\omega_2) \quad (4.26b)$$

$$\gamma_2 = \frac{1}{2}k''(\omega_2) \quad (4.26c)$$

$$\gamma_3 = \frac{1}{6}k'''(\omega_2) \quad (4.26d)$$

For simplicity, the frequency increment $\Delta\omega = \omega_3 - \omega_2$ is assumed to be constant at all frequency steps. If the group velocities $c_{g0} \dots c_{g3}$ have been calculated as eigenvalue derivatives (Equation (3.70)), the first order derivative of the wavenumber can be obtained very accurately:

$$k'(\omega_2) = \frac{1}{c_{g2}} \quad (4.27)$$

The second and third order derivatives are approximated using the previous solutions as

$$k''(\omega_2) \approx \frac{k'(\omega_2) - k'(\omega_1)}{\Delta\omega} = \frac{1}{\Delta\omega} \left(\frac{1}{c_{g2}} - \frac{1}{c_{g1}} \right) \quad (4.28)$$

and

$$k'''(\omega_2) \approx \frac{1}{\Delta\omega^2} \left(\frac{1}{c_{g2}} - \frac{2}{c_{g1}} + \frac{1}{c_{g0}} \right) \quad (4.29)$$

Analogously, higher-order terms can be included in the Taylor approximation. The approximation of the derivatives, however, becomes less accurate with increasing order. Typically the inclusion of the third-order term significantly increases the accuracy of the guessed wavenumber while the term of fourth order does not lead to further improvement. Obviously these results

depend on the chosen frequency increment.

Instead of a Taylor series, the Padé expansion [203,204] can be used. It will be demonstrated in Section 4.4 that this is generally more accurate. The Padé expansion of order [1/2] is of the form

$$k_P = \frac{\alpha_0 + \alpha_1 \Delta\omega}{1 + \beta_1 \Delta\omega + \beta_2 \Delta\omega^2} \quad (4.30)$$

The coefficients $\alpha_0, \alpha_1, \beta_1, \beta_2$ can be obtained from the Taylor coefficients as [204]

$$\beta_2 = \frac{\gamma_2^2 - \gamma_3 \gamma_1}{\gamma_1^2 - \gamma_2 \gamma_0} \quad (4.31a)$$

$$\beta_1 = -\frac{\gamma_2 + \gamma_0 \beta_2}{\gamma_1} \quad (4.31b)$$

$$\alpha_0 = \gamma_0 \quad (4.31c)$$

$$\alpha_1 = \gamma_1 + \gamma_0 \beta_1 \quad (4.31d)$$

Using the Padé expansion, very accurate guesses can be obtained from the previous wavenumbers. The accuracy of the approximation always depends on the chosen frequency increment. For each mode, the guess k_P for the wavenumber is computed and compared with the m solutions k_j ($j = 1 \dots m$) at the subsequent frequency step. The solution that minimizes the deviation

$$\Delta_k = \left| \frac{k_P - k_j}{k_P} \right| \quad (4.32)$$

is assumed to represent the same mode as the previous wavenumbers under consideration. However, as modes can cross, the wavenumbers of two modes at one particular frequency can become arbitrarily close. Hence, it may happen that at some frequencies in the dispersion curves two modes are confused. To avoid this type of error, the group velocities are traced as well, using a linear approximation

$$c_{gT}(\omega_3) = \gamma_{0g} + \gamma_{1g} \Delta\omega = 2c_{g2} - c_{g1} \quad (4.33)$$

with

$$\gamma_{0g} = c_{g2} \quad (4.34a)$$

$$\gamma_{1g} = \frac{c_{g2} - c_{g1}}{\Delta\omega} \quad (4.34b)$$

or a Padé expansion of order [0/1]

$$c_{gP}(\omega_3) = \frac{\alpha_{0g}}{1 + \beta_{1g} \Delta\omega} = \frac{c_{g2}^2}{2c_{g2} - c_{g1}} \quad (4.35)$$

with

$$\alpha_{0g} = \gamma_{0g} \quad (4.36a)$$

$$\beta_{1g} = -\frac{\gamma_{1g}}{\gamma_{0g}} \quad (4.36b)$$

A deviation from the guessed group velocity is defined similarly to Equation (4.32)

$$\Delta_{c_g} = \left| \frac{c_{gP} - c_{gj}}{c_{gP}} \right| \quad (4.37)$$

To identify a mode, the solution is selected which minimizes the total deviation

$$\Delta = \Delta_k^2 + \Delta_{c_g}^2 \quad (4.38)$$

Usually the wavenumbers and group velocities of two modes are not similar simultaneously, so that this procedure gives very reliable results even if a high number of modes has to be traced. If an additional mode appears at its cut-off frequency, the according wavenumbers and group velocities will not be assigned to any of the guessed values, so that the new mode can easily be identified. Obviously, the order of the approximation in Equations (4.30) and (4.35) has to be reduced for that particular mode for the following two frequency steps, as not enough previous data points are available to evaluate a third order approximation. Since usually not more than two new modes will appear within one frequency step and a higher-order approximation can be applied for the other existing modes, this approach is still very robust. In some cases it may also happen that a mode disappears within one frequency step. These branches represent modes having negative group velocity [205–207]. The easiest way to treat those modes is to sort out all solutions with negative group velocity and trace these branches separately. This is another advantage of computing the group velocities directly for each solution.

4.4 Numerical examples

4.4.1 Isotropic circular rod

Dispersion relations are computed for a homogeneous isotropic rod with a radius of 1 mm. This example is chosen to validate the three-dimensional approach. In terms of computational efficiency, it is highly advantageous to utilize the axisymmetric formulation presented in the following chapter.

The material parameters of aluminum are chosen

$$\begin{aligned} \text{shear modulus:} & \quad G = 25 \text{ GPa} \\ \text{density:} & \quad \rho = 2700 \text{ kg m}^{-3} \\ \text{Poisson's ratio:} & \quad \nu = 0.35 \end{aligned}$$

Making use of the waveguide's symmetry, only a quarter of the cross-section has been discretized. Three higher-order elements are required as shown in Figure 4.5. Elements of high order are particularly advantageous to discretize the curvature of the rod, which is not well represented by traditional linear or quadratic elements. To define the mesh, the positions of the nodes A, B and C in Figure 4.5 are chosen at the midpoints of the outer edges of the geometry. The node D is defined such that all adjacent angles are equal to 120° . The order of the elements can be chosen according to the maximum frequency of interest, while the shape of the elements remain constant. Details on the discretization in two dimensions for the SBFEM using higher-order elements can be found in [82].

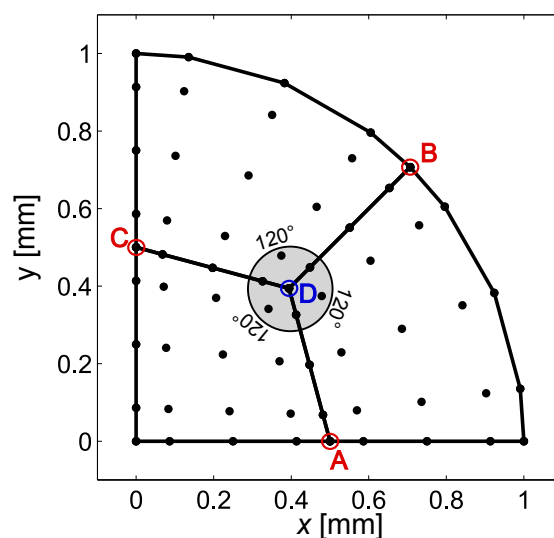


Figure 4.5: Quarter of the cross-section of a circular rod, discretized by three elements of order 4.

Dispersion relations are presented in Figure 4.6. Results have been compared with the software *PCDisp* [52, 53], which is based on the Pochhammer-Chree theory to describe circular waveguides analytically. The propagating modes are then obtained as the roots of the Pochhammer-Chree equation, using the bisection method. The results are in excellent agreement for the given frequency range, if at least an element order of four is used for the SBFEM discretization. The group velocities in Figure 4.6b have been computed as described in Section 3.4. The total CPU time required to obtain the dispersion relations presented here is about 7 s on a desktop PC (Dell Optiplex 780, Intel Core Quad CPU Q8400 @2.66 GHz with 4GB RAM). If the symmetry of the waveguide is ignored and the whole cross-section is discretized instead, it takes about 20 times longer to obtain the same solution. For this comparison, *Matlab*'s function `eig` has been used to solve the eigenvalue problem.

After solving for the wavenumbers and calculating the group velocities at each frequency, the modes have been traced using the approach presented in Section 4.3. Figure 4.7 shows examples for the tracing of some selected modes, using some of the wavenumbers shown in Figure 4.6. For each mode, a Taylor series as well as a Padé expansion have been applied,

based on the solutions obtained at three frequency steps. The resulting approximations can then be compared with the wavenumber solutions at the following frequency steps. As can be seen by comparison in Figure 4.7, the Padé expansion results in a more accurate approximation than the Taylor series. Consequently, the Padé expansion is used to trace the modes.

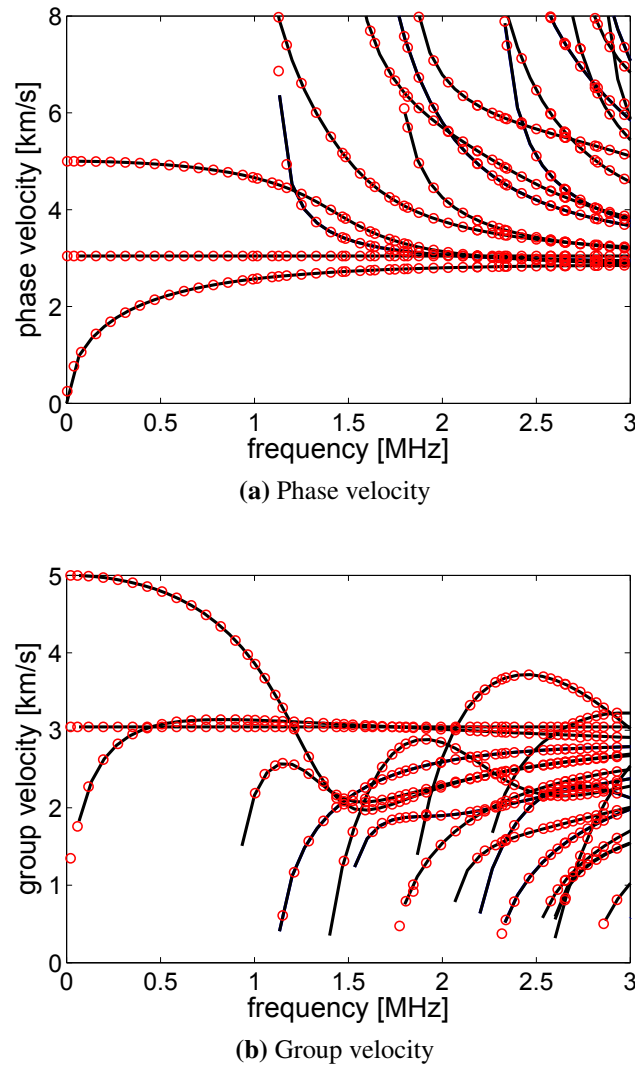


Figure 4.6: Dispersion of the propagating modes in a circular rod, obtained with the SBFEM (–) and compared with *PCDisp* [52, 53] (○).

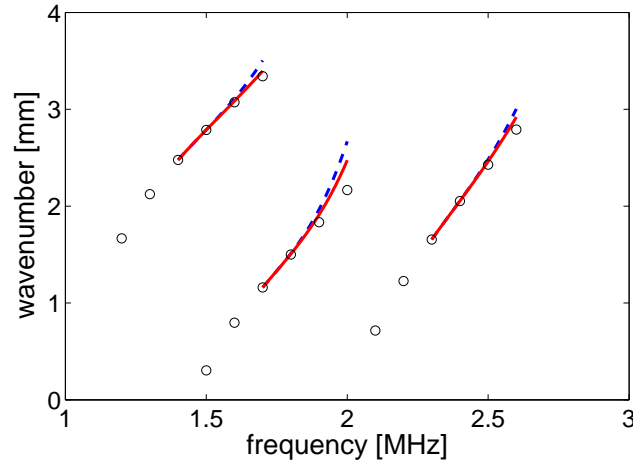


Figure 4.7: Tracing of some selected modes using a Taylor series (---) and the Padé expansion (—). The wavenumbers (○) have been obtained from the solution of the eigenvalue problem.

4.4.2 Square pipe

As a second example, wave propagation in an isotropic square pipe is analyzed. The dispersion relations are compared with results presented in the literature. In the work by Sorohan et al. [58], dispersion relations have been computed using standard Finite Element software, which requires a three-dimensional mesh of a representative part of the waveguide. Using the SBFEM, only a quarter of the cross-section has to be discretized. For this example, it is sufficient to use two elements of order 7, as shown in Figure 4.8. This discretization leads to highly accurate results for the considered frequency range. The total width of the pipe is 100 mm and the wall thickness is 10 mm. The material parameters are

$$\begin{aligned}
 \text{Young's modulus:} & \quad E = 210 \text{ GPa} \\
 \text{density:} & \quad \rho = 7850 \text{ kg m}^{-3} \\
 \text{Poisson's ratio:} & \quad \nu = 0.29
 \end{aligned}$$

The phase velocities of the first propagating modes are presented in Figure 4.9. As in [58], only the SS modes have been computed by applying symmetric boundary conditions on both symmetry axes. Only the first eight modes have been presented in [58], while several additional modes occur in the frequency range under consideration. Again, the results are in good agreement. After the eigenvectors have been computed, the wave propagation can be visualized at arbitrary times by computing the displacements using Equation (3.33). The displacement field is interpolated between the nodes, using the known values of the shape functions at the desired positions. As an example, three modes that can be excited at a frequency of 10 kHz are visualized in Figure 4.10. A snapshot of the deformation is presented for a section of the waveguide. The colors represent normalized absolute displacements. Three solutions have been chosen in order to illustrate the behavior of SS-, AA- and SA-modes, respectively. Particularly,

the top-view clarifies the symmetric and antisymmetric behavior of the displacement field with respect to the geometric symmetry axes. The SS-mode is the first mode (smallest phase velocity) at a frequency of 10 kHz in Figure 4.9, the dispersion curves for AA- and SA-modes are not presented here.

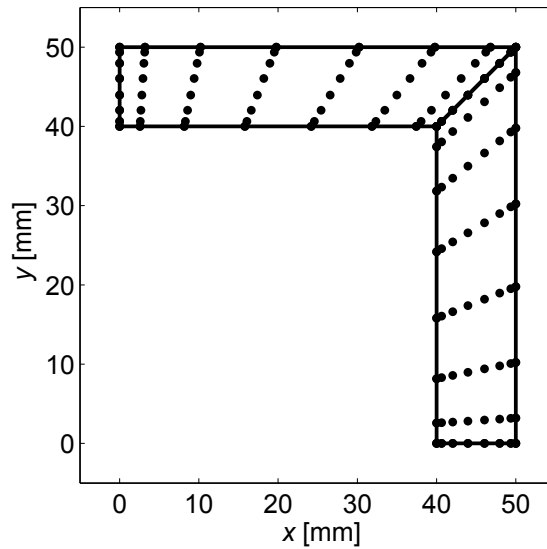


Figure 4.8: Cross-section of a square pipe, discretized with two elements of order 7.

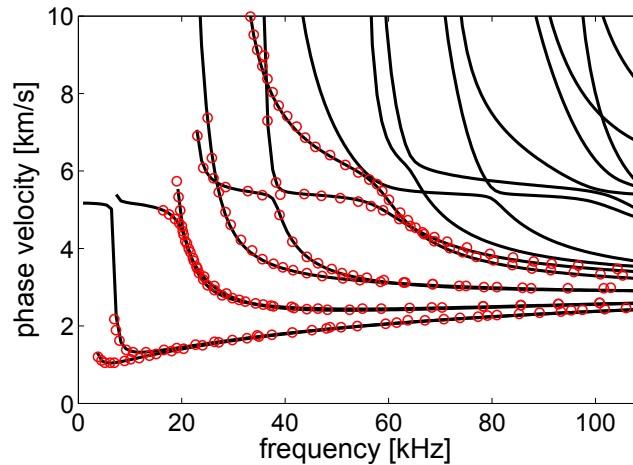


Figure 4.9: Phase velocity dispersion of the SS modes in the square tube, obtained with the SBFEM (—) and compared with [58] (○).

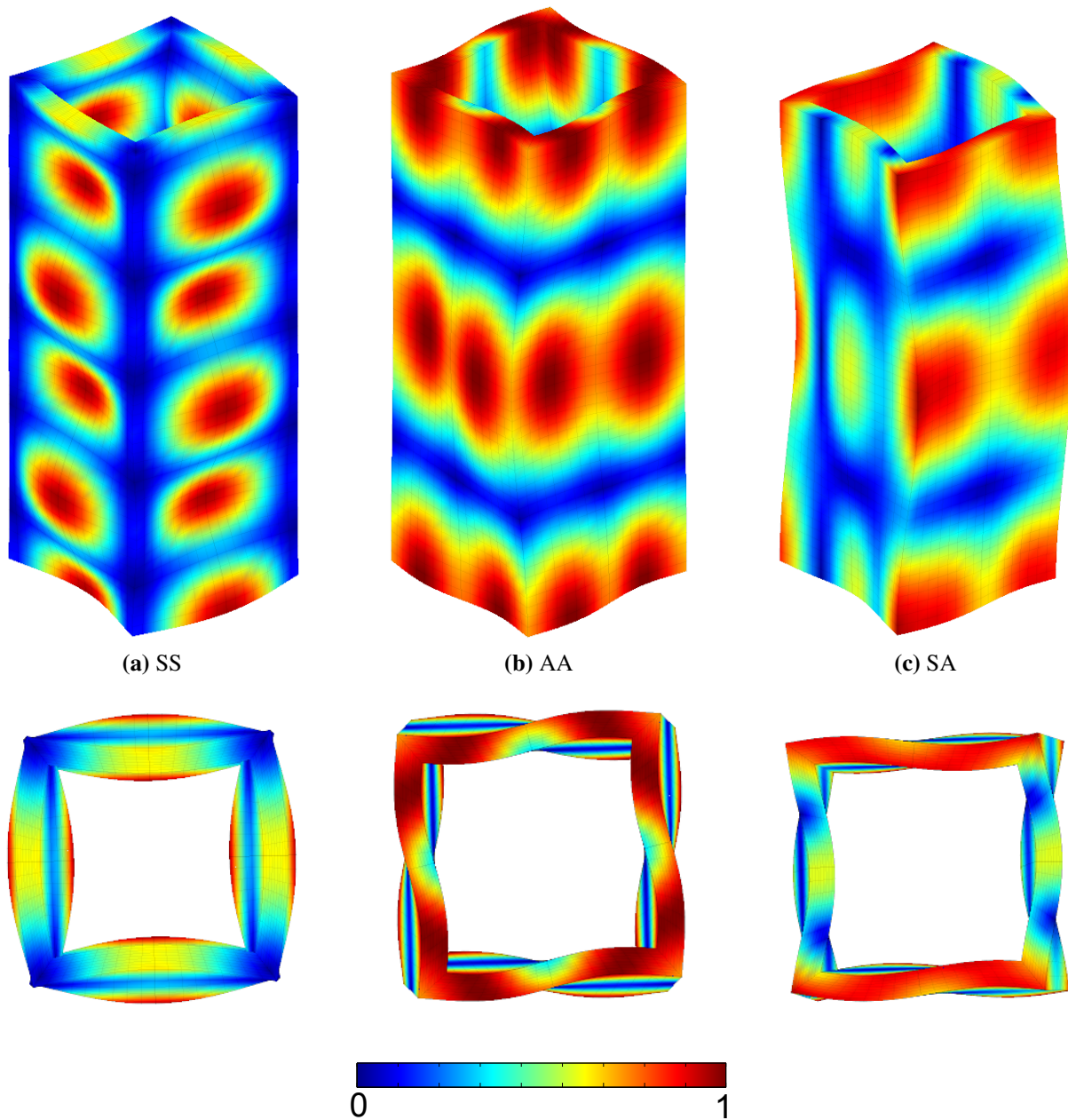


Figure 4.10: Examples of mode shapes in the square pipe at a frequency of 10 kHz. Colours represent the absolute values of the displacements.

Chapter 5

Axisymmetric waveguides

Besides plates, the most common structures that are assessed in guided wave applications are cylindrical pipes and rods. Obviously, these geometries can be treated using the three-dimensional formulation presented in the previous chapter [94]. Even though the proposed solution procedure in conjunction with the discretization by means of higher-order spectral elements allows for a comparably efficient solution, the computational costs can become large, particularly for high frequencies. An example, where very high frequencies are of interest and the computational times become critical, will be described in detail in Chapter 7.

It is a well-known fact that due to the axisymmetry, the mathematical formulation of waves in cylinders can be greatly simplified. After analytical approaches for the calculation of dispersion properties in isotropic homogeneous cylinders have been described by Pochhammer [208] and Chree [40], specific formulations have been derived for isotropic composite cylinders and rods [209, 210] as well as orthotropic cylinders [211] and layered orthotropic composite shells [212, 213]. Many examples for isotropic pipes can be found in [214], while some applications considering different anisotropic material behavior are given in [215]. The orthogonality of modes in circular cylinders is discussed in [216]. More recently, a semi-analytical model that is based on the Pochhammer-Chree theory has been described for axially symmetric modes [217]. Also, an advanced analytical formulation has been presented for pre-stressed and initially twisted bi-material cylinders [196, 218]. The matrix methods [43, 45, 47], previously mentioned in the context of plate structures, can be applied to axisymmetric structures as well, with similar advantages and drawbacks.

An early Finite Element technique for cylinders is described in [54]. Later a different numerical approach that is also based on the weak form of the governing differential equations but uses a power series to approximate the displacement field was introduced [219]. Finite Element models for anisotropic shells and rods [220] as well as pipes exposed to a loading [221, 222] have been presented more recently. Examples using the SAFE method can be found in the literature as well, including for instance damped and undamped cylinders [68, 223], stiffened or pre-stressed pipes [197, 224] or piezoelectric cylinders [225]. Alternatively, for anisotropic cylinders a polynomial approach has been developed [226, 227].

In this chapter, an axisymmetric formulation of the SBFEM approach is derived (Section 5.1, see [96–98]). In order to do that, the governing equations are formulated in a cylindrical

coordinate system. The radial direction is discretized, while a Fourier series is employed in the circumferential direction. Similar to the case of plate structures, only a straight line has to be discretized. Employing the virtual work principle similarly to the cases described in Chapters 3 and 4, leads to an eigenvalue problem for each term of the Fourier expansion. The solutions represent sets of modes with the corresponding circumferential order. If a complex Fourier series is utilized to describe the displacement field in circumferential direction, the resulting eigenvalue problem is generally complex, leading to higher computational costs than for the case of plate structures. Alternatively, a purely real formulation is derived in Section 5.2 by separating the displacement field into its symmetric and antisymmetric parts. While the implementation of the real formulation is more cumbersome, the solution can be computationally more efficient, depending on the material's anisotropy. For simple anisotropic material behavior, longitudinal and torsional modes can be computed separately to further reduce computational costs (Section 5.3).

The case of full cylinders has to be treated more carefully due to the singularity of the governing equations at $r = 0$ in a cylindrical coordinate system. It is discussed in Section 5.4, how the singularity can be avoided by changing the numerical integration scheme for this particular case.

Several numerical examples, including isotropic and anisotropic materials as well as layered pipes and rods are presented in Section 5.5 and compared with results obtained with different software and examples that can be found in the literature.

Since there are applications where very high frequencies are of interest, the discretization is discussed in more detail. Elements of extremely high order (up to 200) have been implemented and tested in the context of axisymmetric waveguides. To the author's knowledge, such high element orders have not been presented in the literature before. It is often assumed that higher-order elements can lead to numerical problems, because the nodes close to the element's extremities become very close to each other. It is demonstrated in Section 5.6 that even for very high order the utilized type of elements reveal excellent convergence properties for this particular application. Guidelines are presented on how to choose the adequate order for the frequency of interest.

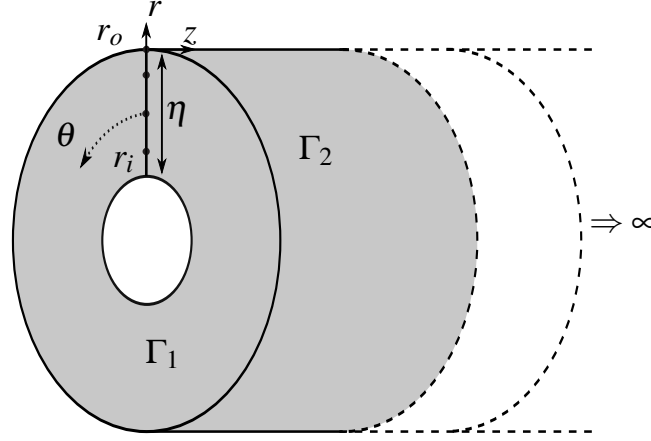


Figure 5.1: Discretization of a cylinder in the SBFEM.

5.1 Axisymmetric formulation of the SBFEM

In order to describe an axisymmetric waveguide, the governing equations are formulated in a cylindrical coordinate system (θ, r, z) . The waveguide depicted in Figure 5.1 is addressed. The three-dimensional volume is denoted by Ω , while Γ_1 and Γ_2 denote the cross-section and the side-faces of the cylinder, respectively. The inner radius r_i can be zero to describe a solid rod. The displacements \mathbf{u} are written as:

$$\mathbf{u} = [u_\theta \ u_r \ u_z]^T \quad (5.1)$$

The strains are obtained as

$$\boldsymbol{\varepsilon} = [\varepsilon_\theta \ \varepsilon_r \ \varepsilon_z \ \gamma_{rz} \ \gamma_{\theta z} \ \gamma_{\theta r}]^T = \mathbf{L} \mathbf{u} \quad (5.2)$$

where the differential operator \mathbf{L} in cylindrical coordinates reads [106]

$$\mathbf{L} = \begin{bmatrix} \frac{1}{r} \partial_\theta & 0 & 0 & 0 & \partial_z & \partial_r - \frac{1}{r} \\ \frac{1}{r} & \partial_r & 0 & \partial_z & 0 & \frac{1}{r} \partial_\theta \\ 0 & 0 & \partial_z & \partial_r & \frac{1}{r} \partial_\theta & 0 \end{bmatrix}^T \quad (5.3)$$

The strain-displacement relationship is decomposed into four terms

$$\boldsymbol{\varepsilon} = \mathbf{b}_1 \mathbf{u}_{,z} + \mathbf{b}_2 \mathbf{u}_{,r} + \mathbf{b}_3 \frac{1}{r} \mathbf{u}_{,\theta} + \mathbf{b}_4 \frac{1}{r} \mathbf{u} \quad (5.4)$$

where the matrix \mathbf{b}_4 is introduced as

$$\mathbf{b}_4 = \begin{bmatrix} 0 & 0 & 0 & 0 & 0 & -1 \\ 1 & 0 & 0 & 0 & 0 & 0 \\ 0 & 0 & 0 & 0 & 0 & 0 \end{bmatrix}^T \quad (5.5)$$

The matrices \mathbf{b}_1 , \mathbf{b}_2 \mathbf{b}_3 are identical to the three-dimensional case (Equation 4.2). Note that only the waveguide's geometry is assumed to be axisymmetric while the displacement field can be arbitrary at this stage. In the circumferential direction, the displacement field is decomposed into a Fourier series [58, 60, 226]

$$\mathbf{u}(\theta, r, z) = \sum_{m=0}^{\infty} \tilde{\mathbf{u}}_m(r, z) e^{im\theta} \quad (5.6)$$

where the integer m denotes the circumferential order. The terms of the Fourier series represent different sets of modes. Solutions will be obtained for each order m separately. The maximum value of m that leads to propagating modes, is frequency-dependent. In the following, only one term of Equation (5.6) is addressed and the subscript m is omitted for conciseness. The derivative with respect to θ is given by

$$\mathbf{u}_{,\theta}(\theta, r, z) = im\mathbf{u}(\theta, r, z) \quad (5.7)$$

Since the θ -dependency of the displacement field is known, it is sufficient to discretize the waveguide in radial direction only (Figure 5.1). As in the formulation for plate structures, only a straight line has to be discretized. Three degrees of freedom are assigned to each node. Again, each element of the discretization is defined in the local coordinate η , which is equal to -1 and 1 at the element's extremities, respectively (cf. Figure 3.2). In the axisymmetric formulation, η is related to the radial coordinate r by

$$r = r_i + \frac{(\eta + 1)l}{2} \quad (5.8)$$

where l denotes the element length. If more than one element is used to discretize the radial direction, then r_i refers to the inner radius of the element under consideration. The thickness h of the cylinder is then given by the sum over the element lengths l_j

$$h = \sum_j l_j \quad (5.9)$$

The derivative of (5.8) with respect to η is given by

$$r_{,\eta} = \frac{l}{2} \quad (5.10)$$

The coordinate transformation from a Cartesian coordinate system is defined as

$$\begin{Bmatrix} \partial_\theta \\ \partial_\eta \\ \partial_z \end{Bmatrix} = \mathbf{J} \begin{Bmatrix} \partial_x \\ \partial_y \\ \partial_z \end{Bmatrix} \quad (5.11)$$

Without loss of generality, the origin of the Cartesian coordinate system is placed at the center of the waveguide's cross-section. Hence, the Jacobian matrix \mathbf{J} is given by

$$\mathbf{J} = \begin{bmatrix} x_{,\theta} & y_{,\theta} & 0 \\ x_{,\eta} & y_{,\eta} & 0 \\ 0 & 0 & 1 \end{bmatrix} = \begin{bmatrix} -(r_i + \frac{(1+\eta)l}{2}) \sin \theta & (r_i + \frac{(1+\eta)l}{2}) \cos \theta & 0 \\ \frac{l}{2} \cos \theta & \frac{l}{2} \sin \theta & 0 \\ 0 & 0 & 1 \end{bmatrix} \quad (5.12)$$

and the absolute value of the Jacobian determinant reads

$$|\mathbf{J}| = \frac{l}{2} r_i + \frac{l^2}{4} (\eta + 1) \quad (5.13)$$

Note that since the Jacobian determinant is a function of η and r_i , it has to be evaluated for each node of the discretization. The same one-dimensional shape functions $\mathbf{N}(\eta)$ as in the case of plate structures are used to interpolate between the nodal values:

$$\mathbf{u}(\theta, \eta, z) = \mathbf{N}(\eta) \mathbf{u}_n(\theta, z) \quad (5.14)$$

Performing the differentiation with respect to θ explicitly (Equation (5.7)) and transforming into the local coordinate η , the discretized strain-displacement relationship reads

$$\begin{aligned} \boldsymbol{\varepsilon} = \mathbf{b}_1 \mathbf{N}(\eta) \partial_z \mathbf{u}_n(\theta, z) + \frac{1}{r_{,\eta}} \mathbf{b}_2 \partial_\eta \mathbf{N}(\eta) \mathbf{u}_n(\theta, z) \\ + \mathbf{b}_3 \frac{1}{r} \mathbf{N}(\eta) \mathbf{u}_n(\theta, z) + \mathbf{b}_4 \frac{im}{r} \mathbf{N}(\eta) \mathbf{u}_n(\theta, z) \end{aligned} \quad (5.15)$$

which is re-written as

$$\boldsymbol{\varepsilon} = \mathbf{B}_1 \mathbf{u}_{n,z} + \mathbf{B}_2 \mathbf{u}_n \quad (5.16)$$

with

$$\mathbf{B}_1 = \mathbf{b}_1 \mathbf{N} \quad (5.17a)$$

$$\mathbf{B}_2 = \frac{1}{r_{,\eta}} \mathbf{b}_2 \mathbf{N}_{,\eta} + \mathbf{b}_3 \frac{im}{r} \mathbf{N} + \mathbf{b}_4 \frac{1}{r} \mathbf{N} \quad (5.17b)$$

The stresses are written as

$$\boldsymbol{\sigma}(\theta, r, z) = [\sigma_\theta \ \sigma_r \ \sigma_z \ \tau_{rz} \ \tau_{\theta z} \ \tau_{\theta r}]^T = \mathbf{D} \boldsymbol{\varepsilon}(\theta, r, z) \quad (5.18)$$

The elasticity matrix \mathbf{D} is of the same form as in a three-dimensional Cartesian coordinate system, because the axes of the cylindrical coordinate system are locally perpendicular to each other for each point of the geometry.

The virtual work principle can be applied analogously to the three-dimensional formulation for plate structures. The derivation will not be repeated in detail. Formally, integrations have to be performed along the circumferential direction (contrary to the infinite plate length in the x -direction in case of plate structures). However, since the θ -dependency is given by Equation (5.6), it is not required to perform the integration explicitly. Equations (3.28) apply for the computation of the coefficient matrices, using the modified expressions for \mathbf{B}_2 (5.17b) and $|\mathbf{J}|$ (5.13). The virtual work statement, after substitution of the coefficient matrices, reads

$$\begin{aligned}
 & - \int_0^{2\pi} \int_0^\infty \delta \mathbf{u}_n^T(\theta, z) \left(\mathbf{E}_0 \mathbf{u}_{n,zz}(\theta, z) + (\mathbf{E}_1^T - \mathbf{E}_1) \mathbf{u}_{n,z}(\theta, z) - \mathbf{E}_2 \mathbf{u}_n(\theta, z) \right. \\
 & \quad \left. - \mathbf{M}_0 \ddot{\mathbf{u}}_n(\theta, z) \right) dz d\theta + \int_0^{2\pi} \delta \mathbf{u}_n^T(\theta, 0) \mathbf{q}_n(\theta, 0) d\theta - \int_0^{2\pi} \delta \mathbf{u}_n^T(\theta, 0) \mathbf{f}_n d\theta = 0 \quad (5.19)
 \end{aligned}$$

The virtual displacements are arbitrary in z - as well as in θ -direction, leading to the SBFEM equation

$$\mathbf{E}_0 \mathbf{u}_{n,zz}(\theta, z) + (\mathbf{E}_1^T - \mathbf{E}_1) \mathbf{u}_{n,z}(\theta, z) - \mathbf{E}_2 \mathbf{u}_n(\theta, z) - \mathbf{M}_0 \ddot{\mathbf{u}}_n(\theta, z) = 0 \quad (5.20)$$

Equation (5.20) is of the same form as for plate structures. In terms of implementation, the difference mainly lies in the computation of \mathbf{B}_2 . Note that the order of the Fourier series is incorporated into the definition of \mathbf{B}_2 . Hence, in the axisymmetric formulation, the Scaled Boundary Finite Element equation has to be solved for each circumferential mode m separately with modified coefficient matrices \mathbf{E}_1 and \mathbf{E}_2 . The nodal displacements of a mode in the circular waveguide can be written as

$$\mathbf{u}_n(\theta, z, t) = \hat{\mathbf{u}}_n e^{\lambda z - i\omega t + im\theta} \quad (5.21)$$

Substituting Equation (5.21) into (5.20) we obtain the formally identical eigenvalue problems (3.35) and (3.42). Note that for $m > 0$, \mathbf{Z} is generally a complex matrix (see Equation (5.17b)). In contrast to that, \mathbf{Z} is a real matrix in case of plate structures, as long as no damping is considered. It is discussed in Section 5.2 how axisymmetric waveguides can be described alternatively using purely real coefficient matrices. \mathbf{Z} is still a Hamiltonian matrix, applying the generalization for complex matrices [172]

$$(\mathbf{J}_{2g} \mathbf{Z})^* = \mathbf{J}_{2g} \mathbf{Z} \quad (5.22)$$

where $(\cdot)^*$ denotes the conjugate transpose.

5.2 Real coefficient matrices

The approach presented in Section 5.1 is easy to implement for very general axisymmetric waveguides. However, it leads to complex coefficient matrices, which can be a disadvantage if a highly efficient algorithm is desired. If e. g. *Matlab*'s function `eig` is used, the computational time required for solving a complex eigenvalue problem is typically 2 to 2.5 times larger than for a real eigenvalue problem of the same dimension (around 100 degrees of freedom). Also as mentioned before, alternative algorithms that are optimized for real Hamiltonian eigenvalue problems can be used. These algorithms are not necessarily implemented for complex matrices. Thus, it is interesting to point out that the same solutions can be obtained using purely real coefficient matrices. The derivation and implementation is somewhat more cumbersome. It will be shown that the use of real matrices is advantageous in terms of computational efficiency, if θ is one of the material's principal directions.

Instead of using a complex Fourier series (Equation (5.6)), we can generally write the displacement components in an axisymmetric solid as [228]:

$$u_\theta(\theta, r, z) = -\tilde{u}_\theta^s \sin m\theta + \tilde{u}_\theta^a \cos m\theta \quad (5.23a)$$

$$u_r(\theta, r, z) = \tilde{u}_r^s \cos m\theta + \tilde{u}_r^a \sin m\theta \quad (5.23b)$$

$$u_z(\theta, r, z) = \tilde{u}_z^s \cos m\theta + \tilde{u}_z^a \sin m\theta \quad (5.23c)$$

where the superscripts s and a denote the symmetric and antisymmetric parts (with respect to $\theta = 0$) of the displacement field, respectively. Using Equations (5.1) and (5.2), the strains are obtained as

$$\begin{aligned} \boldsymbol{\varepsilon} &= \mathbf{L}\mathbf{u} \\ &= \begin{bmatrix} \frac{1}{r}\partial_\theta & 0 & 0 & 0 & \partial_z & \partial_r - \frac{1}{r} \\ \frac{1}{r} & \partial_r & 0 & \partial_z & 0 & \frac{1}{r}\partial_\theta \\ 0 & 0 & \partial_z & \partial_r & \frac{1}{r}\partial_\theta & 0 \end{bmatrix}^T \begin{bmatrix} -\tilde{u}_\theta^s \sin m\theta + \tilde{u}_\theta^a \cos m\theta \\ \tilde{u}_r^s \cos m\theta + \tilde{u}_r^a \sin m\theta \\ \tilde{u}_z^s \cos m\theta + \tilde{u}_z^a \sin m\theta \end{bmatrix} \\ &= \begin{bmatrix} -\frac{m}{r}\tilde{c} & \frac{1}{r}\tilde{c} & 0 \\ 0 & \partial_r\tilde{c} & 0 \\ 0 & 0 & \partial_z\tilde{c} \\ 0 & \partial_z\tilde{c} & \partial_r\tilde{c} \\ -\partial_z\tilde{s} & 0 & -\frac{m}{r}\tilde{s} \\ (-\partial_r + \frac{1}{r})\tilde{s} & -\frac{m}{r}\tilde{s} & 0 \end{bmatrix} \begin{bmatrix} \tilde{u}_\theta^s \\ \tilde{u}_r^s \\ \tilde{u}_z^s \end{bmatrix} + \begin{bmatrix} -\frac{m}{r}\tilde{s} & \frac{1}{r}\tilde{s} & 0 \\ 0 & \partial_r\tilde{s} & 0 \\ 0 & 0 & \partial_z\tilde{s} \\ 0 & \partial_z\tilde{s} & \partial_r\tilde{s} \\ \partial_z\tilde{c} & 0 & \frac{m}{r}\tilde{c} \\ (-\partial_r + \frac{1}{r})\tilde{c} & \frac{m}{r}\tilde{c} & 0 \end{bmatrix} \begin{bmatrix} \tilde{u}_\theta^a \\ \tilde{u}_r^a \\ \tilde{u}_z^a \end{bmatrix} \quad (5.24) \end{aligned}$$

with the abbreviations $\tilde{s} = \sin m\theta$, $\tilde{c} = \cos m\theta$. Defining the vectors $\tilde{\mathbf{u}}^s = [\tilde{u}_\theta^s \ \tilde{u}_r^s \ \tilde{u}_z^s]^T$, $\tilde{\mathbf{u}}^a = [\tilde{u}_\theta^a \ \tilde{u}_r^a \ \tilde{u}_z^a]^T$ and denoting the corresponding matrices in Equation (5.24) by \mathbf{L}^s and \mathbf{L}^a yields

$$\boldsymbol{\varepsilon} = \mathbf{L}^s \tilde{\mathbf{u}}^s + \mathbf{L}^a \tilde{\mathbf{u}}^a \quad (5.25)$$

The differential operators corresponding to symmetric and antisymmetric displacement fields are re-written as

$$\mathbf{L}^s = \mathbf{L}^\alpha \cos m\theta + \mathbf{L}^\beta \sin m\theta \quad (5.26a)$$

$$\mathbf{L}^a = \mathbf{L}^\alpha \sin m\theta - \mathbf{L}^\beta \cos m\theta \quad (5.26b)$$

with

$$\mathbf{L}^\alpha = \begin{bmatrix} -\frac{m}{r} & 0 & 0 & 0 & 0 & 0 \\ \frac{1}{r} & \partial_r & 0 & \partial_z & 0 & 0 \\ 0 & 0 & \partial_z & \partial_r & 0 & 0 \end{bmatrix}^T \quad (5.27a)$$

$$\mathbf{L}^\beta = \begin{bmatrix} 0 & 0 & 0 & 0 & -\partial_z & -\partial_r + \frac{1}{r} \\ 0 & 0 & 0 & 0 & 0 & -\frac{m}{r} \\ 0 & 0 & 0 & 0 & -\frac{m}{r} & 0 \end{bmatrix}^T \quad (5.27b)$$

Applying the discretization, the displacement fields, separated into symmetric and antisymmetric components reads

$$\mathbf{u} = \mathbf{N}^\alpha \cos m\theta \tilde{\mathbf{u}}_n^s - \mathbf{N}^\beta \sin m\theta \tilde{\mathbf{u}}_n^s + \mathbf{N}^\alpha \sin m\theta \tilde{\mathbf{u}}_n^a + \mathbf{N}^\beta \cos m\theta \tilde{\mathbf{u}}_n^a \quad (5.28)$$

and the discretized strain-displacement relationship is obtained as

$$\begin{aligned} \boldsymbol{\varepsilon} = & (\mathbf{B}_1^\alpha \tilde{\mathbf{u}}_{n,z}^s + \mathbf{B}_2^\alpha \tilde{\mathbf{u}}_n^s) \cos m\theta + (\mathbf{B}_1^\beta \tilde{\mathbf{u}}_{n,z}^s + \mathbf{B}_2^\beta \tilde{\mathbf{u}}_n^s) \sin m\theta \\ & + (\mathbf{B}_1^\alpha \tilde{\mathbf{u}}_{n,z}^a + \mathbf{B}_2^\alpha \tilde{\mathbf{u}}_n^a) \sin m\theta - (\mathbf{B}_1^\beta \tilde{\mathbf{u}}_{n,z}^a + \mathbf{B}_2^\beta \tilde{\mathbf{u}}_n^a) \cos m\theta \end{aligned} \quad (5.29)$$

Expressions for $\mathbf{B}_1^\alpha, \mathbf{B}_1^\beta, \mathbf{B}_2^\alpha, \mathbf{B}_2^\beta, \mathbf{N}^\alpha, \mathbf{N}^\beta$ are given in Appendix A.3. We substitute Equations (5.28) and (5.29) into the virtual work principle, analogously to the procedure described in Section 5.1. The virtual displacement field is then separated into its symmetric and antisymmetric components, leading to two displacement equations to be fulfilled simultaneously:

$$\bar{\mathbf{E}}_0 \tilde{\mathbf{u}}_{n,zz}^s + \bar{\bar{\mathbf{E}}}_0 \tilde{\mathbf{u}}_{n,zz}^a + (\bar{\mathbf{E}}_1^T - \bar{\mathbf{E}}_1) \tilde{\mathbf{u}}_{n,z}^s + (\bar{\bar{\mathbf{E}}}_1^T - \bar{\bar{\mathbf{E}}}_1) \tilde{\mathbf{u}}_{n,z}^a - \bar{\mathbf{E}}_2 \tilde{\mathbf{u}}_n^s - \bar{\bar{\mathbf{E}}}_2 \tilde{\mathbf{u}}_n^a - \bar{\mathbf{M}}_0 \ddot{\mathbf{u}}_n^s = 0 \quad (5.30a)$$

$$-\bar{\bar{\mathbf{E}}}_0 \tilde{\mathbf{u}}_{n,zz}^s + \bar{\mathbf{E}}_0 \tilde{\mathbf{u}}_{n,zz}^a - (\bar{\bar{\mathbf{E}}}_1^T - \bar{\bar{\mathbf{E}}}_1) \tilde{\mathbf{u}}_{n,z}^s + (\bar{\mathbf{E}}_1^T - \bar{\mathbf{E}}_1) \tilde{\mathbf{u}}_{n,z}^a + \bar{\bar{\mathbf{E}}}_2 \tilde{\mathbf{u}}_n^s - \bar{\mathbf{E}}_2 \tilde{\mathbf{u}}_n^a - \bar{\mathbf{M}}_0 \ddot{\mathbf{u}}_n^a = 0 \quad (5.30b)$$

The matrices $\bar{\mathbf{E}}_0$ and $\bar{\bar{\mathbf{E}}}_0$ are defined as

$$\bar{\mathbf{E}}_0 = \int_{-1}^1 \mathbf{B}_1^{\alpha T} \mathbf{D} \mathbf{B}_1^\alpha |J| d\eta + \int_{-1}^1 \mathbf{B}_1^{\beta T} \mathbf{D} \mathbf{B}_1^\beta |J| d\eta \quad (5.31a)$$

$$\bar{\bar{\mathbf{E}}}_0 = - \int_{-1}^1 \mathbf{B}_1^{\alpha T} \mathbf{D} \mathbf{B}_1^\beta |J| d\eta + \int_{-1}^1 \mathbf{B}_1^{\beta T} \mathbf{D} \mathbf{B}_1^\alpha |J| d\eta \quad (5.31b)$$

and similar for $\bar{\mathbf{E}}_1, \bar{\bar{\mathbf{E}}}_1, \bar{\mathbf{E}}_2, \bar{\bar{\mathbf{E}}}_2$ (see Appendix A.3). The mass matrix is given as

$$\bar{\mathbf{M}}_0 = \rho \int_{-1}^1 \mathbf{N}^{\alpha T} \mathbf{N}^{\alpha} |J| d\eta + \rho \int_{-1}^1 \mathbf{N}^{\beta T} \mathbf{N}^{\beta} |J| d\eta \quad (5.32)$$

while the terms $\mathbf{N}^{\alpha T} \mathbf{N}^{\beta}$ and $\mathbf{N}^{\beta T} \mathbf{N}^{\alpha}$ vanish. Equations (5.30) can be written in the same form as (3.35) by applying

$$\left(\lambda^2 \tilde{\mathbf{E}}_0 + \lambda (\tilde{\mathbf{E}}_1^T - \tilde{\mathbf{E}}_1) - \tilde{\mathbf{E}}_2 + \omega^2 \tilde{\mathbf{M}}_0 \right) \begin{Bmatrix} \hat{\mathbf{u}}_n^s \\ \hat{\mathbf{u}}_n^a \end{Bmatrix} = 0 \quad (5.33)$$

with

$$\tilde{\mathbf{E}}_0 = \begin{bmatrix} \bar{\mathbf{E}}_0 & \bar{\bar{\mathbf{E}}}_0 \\ -\bar{\mathbf{E}}_0 & \bar{\mathbf{E}}_0 \end{bmatrix}; \quad \tilde{\mathbf{E}}_1 = \begin{bmatrix} \bar{\mathbf{E}}_1 & \bar{\bar{\mathbf{E}}}_1 \\ -\bar{\mathbf{E}}_1 & \bar{\mathbf{E}}_1 \end{bmatrix} \quad (5.34)$$

$$\tilde{\mathbf{E}}_2 = \begin{bmatrix} \bar{\mathbf{E}}_2 & \bar{\bar{\mathbf{E}}}_2 \\ -\bar{\mathbf{E}}_2 & \bar{\mathbf{E}}_2 \end{bmatrix}; \quad \tilde{\mathbf{M}}_0 = \begin{bmatrix} \bar{\mathbf{M}}_0 & 0 \\ 0 & \bar{\mathbf{M}}_0 \end{bmatrix} \quad (5.35)$$

With these definitions, the $12n \times 12n$ matrix $\tilde{\mathbf{Z}}$ can be assembled analogously to Equation (3.39) while the coefficient matrices are now purely real. However, to solve for the symmetric and antisymmetric displacement fields simultaneously, we had to double the dimension of the eigenvalue problem so that this approach seems computationally less efficient in the general case. On the other hand, it can easily be shown by substituting into Equations (5.31) that the matrices $\bar{\mathbf{E}}_0, \bar{\mathbf{E}}_1, \bar{\mathbf{E}}_2$ vanish, if θ is a principal material direction [229], i. e. if the elasticity matrix is given by Equation (3.80). This is the case in the majority of practical applications, where the material is isotropic, cubic, transversely isotropic or orthotropic with the θ -direction being one of the axes of anisotropy. Hence, the symmetric and antisymmetric parts are then decoupled (i. e. we can describe the modes by choosing either the symmetric or antisymmetric components in Equations (5.23)) and we can write

$$\left(\lambda^2 \bar{\mathbf{E}}_0 + \lambda (\bar{\mathbf{E}}_1^T - \bar{\mathbf{E}}_1) - \bar{\mathbf{E}}_2 + \omega^2 \bar{\mathbf{M}}_0 \right) \hat{\mathbf{u}}_n^{s/a} = 0 \quad (5.36)$$

Under these circumstances, it is sufficient to solve a real eigenvalue problem of the same size as the complex one derived earlier. If general anisotropic material behavior has to be considered, the symmetric and antisymmetric parts are coupled and all terms in Equations (5.23) have to be included. It is then more efficient to employ the complex formulation as described in Section 5.1.

5.3 Longitudinal and torsional modes

If the elasticity matrix is given by Equation (3.80), the modes with $m = 0$ are either longitudinal or torsional.²² Both cases can be treated separately to reduce the size of the eigenvalue problem to be solved. This can be desired in the high frequency range, where the number of modes becomes large. It is then significantly more efficient to solve the eigenvalue problem twice with a reduced number of degrees of freedom. Particularly, the excitability of torsional modes is often negligible in practical applications and hence they do not have to be computed. In this section, the governing equations for the modes of circumferential order zero are given explicitly to ease the implementation of the coefficient matrices. Alternatively, the unused degrees of freedom can be eliminated after assembling the coefficient matrices.

5.3.1 Longitudinal modes

For modes with $m = 0$, the displacement field is axisymmetric. Consequently, the derivatives of the displacement components with respect to θ vanish

$$\partial_{\theta}u_z = \partial_{\theta}u_{\theta} = \partial_{\theta}u_r = 0 \quad (5.37)$$

Additionally, in the case of longitudinal modes the displacement components in circumferential direction vanish

$$u_{\theta} = 0 \quad (5.38)$$

Comparing with Equations (5.1)-(5.3), the strains are given as

$$\boldsymbol{\varepsilon} = [\varepsilon_{\theta} \ \varepsilon_r \ \varepsilon_z \ \gamma_{rz}]^T = \mathbf{L}_1 \mathbf{u} \quad (5.39)$$

with the reduced differential operator

$$\mathbf{L}_1 = \begin{bmatrix} \frac{1}{r} & \partial_r & 0 & \partial_z \\ 0 & 0 & \partial_z & \partial_r \end{bmatrix}^T \quad (5.40)$$

Using the same symbols as before for simplicity, the strain-displacement relationship for $m = 0$ reads

$$\boldsymbol{\varepsilon} = \mathbf{b}_1 \mathbf{u}_{,z} + \mathbf{b}_2 \mathbf{u}_{,r} + \mathbf{b}_4 \frac{1}{r} \mathbf{u} \quad (5.41)$$

²²In the rare case that the elasticity matrix is fully populated, the longitudinal and torsional modes are coupled and the following simplifications are not valid. This is equivalent to the SH and Lamb-type modes in plate structures (cf. Section 3.5).

with

$$\mathbf{b}_1 = \begin{bmatrix} 0 & 0 & 0 & 1 \\ 0 & 0 & 1 & 0 \end{bmatrix}^T \quad (5.42a)$$

$$\mathbf{b}_2 = \begin{bmatrix} 0 & 1 & 0 & 0 \\ 0 & 0 & 0 & 1 \end{bmatrix}^T \quad (5.42b)$$

$$\mathbf{b}_4 = \begin{bmatrix} 1 & 0 & 0 & 0 \\ 0 & 0 & 0 & 0 \end{bmatrix}^T \quad (5.42c)$$

In the discretized form, the matrix \mathbf{B}_2 is given by

$$\mathbf{B}_2 = \frac{1}{r,\eta} \mathbf{b}_2 \mathbf{N}_{,\eta} + \mathbf{b}_3 \frac{1}{r} \mathbf{N} \quad (5.43)$$

The elasticity matrix is reduced to

$$\mathbf{D}_1 = \begin{bmatrix} D_{11} & D_{12} & D_{13} & D_{14} \\ & D_{22} & D_{23} & D_{24} \\ \text{sym.} & & D_{33} & D_{34} \\ & & & D_{44} \end{bmatrix} \quad (5.44)$$

The coefficient matrices can then be obtained as in Section 5.1. Obviously, the degrees of freedom corresponding to displacements in circumferential direction have to be removed from the shape function matrix \mathbf{N} .

5.3.2 Torsional modes

For purely torsional modes, Equation (5.37) is valid as well. Additionally, the displacement components in both z - and r -direction vanish

$$u_r = u_z = 0 \quad (5.45)$$

Consequently, the wave motion of these modes is described by a scalar displacement field, similar to a pure out-of-plane motion in a Cartesian coordinate system. Considering Equation (5.37), the strain-displacement relationship reads

$$\boldsymbol{\epsilon} = [\gamma_{\theta z} \ \gamma_{\theta r}]^T = \mathbf{L}_t u_\theta \quad (5.46)$$

with

$$\mathbf{L}_t = \left[\partial_z \quad \partial_r - \frac{1}{r} \right]^T \quad (5.47)$$

Consequently, the strains are written as

$$\boldsymbol{\varepsilon} = \mathbf{b}_1 u_{\theta,z} + \mathbf{b}_2 u_{\theta,r} + \mathbf{b}_3 \frac{1}{r} u_\theta \quad (5.48)$$

with

$$\mathbf{b}_1 = \begin{bmatrix} 1 & 0 \end{bmatrix}^T \quad (5.49)$$

$$\mathbf{b}_2 = \begin{bmatrix} 0 & 1 \end{bmatrix}^T \quad (5.50)$$

$$\mathbf{b}_3 = \begin{bmatrix} 0 & -1 \end{bmatrix}^T \quad (5.51)$$

and the elasticity matrix is simplified to be

$$\mathbf{D}_t = \begin{bmatrix} D_{55} & D_{56} \\ D_{56} & D_{66} \end{bmatrix} \quad (5.52)$$

5.4 Solid cylinders

Care has to be taken when a solid cylinder is modeled using the proposed approach. In that case, the inner radius r_i of the waveguide is set to zero. At $r = 0$, the strain-displacement relationship (5.4) in a cylindrical coordinate system is undefined. Consequently, the matrix \mathbf{B}_2 (5.17b) cannot be evaluated. It should be noted that the shape function corresponding to the node at $r = 0$ is still well-defined (Figure 5.2a). The problem occurs when performing the numerical integration in order to compute \mathbf{E}_1 and \mathbf{E}_2 . When using the Gaussian-Lobatto-Legendre quadrature, one integration point is placed at $r = 0$ and consequently \mathbf{B}_2 has to be evaluated at this point.

An obvious approximation can be obtained by shifting the inner radius to a small non-zero value. This approach seems rather unsatisfactory as the optimal value for r_i and its effect on the accuracy of the solution are not trivial to obtain. Alternatively, we can change the integration scheme to a traditional Gaussian quadrature. The $p + 1$ integration points η_i^g are positioned at the roots of the Legendre polynomial of order $p + 1$ [230, 231]:

$$P_{p+1}(\eta_i^g) = 0 \quad (5.53)$$

No integration points are placed at the element's extremities (Figure 5.2b) so that the singularity is avoided. The Gaussian quadrature with $p + 1$ integration points gives exact results for the integration of polynomials up to order $2p + 1$ [232]. Hence, it fully integrates all coefficient matrices. As the integration points do not coincide with the element nodes, we sacrifice the properties of spectral elements. Particularly, the coefficient matrices \mathbf{E}_0 and \mathbf{M}_0 are now fully populated. However, for axisymmetric waveguides the number of degrees of freedom is typically small. Hence the numerical errors due to the inversion of the fully populated matrix \mathbf{E}_0 are in most cases acceptable and the computational time for computing the matrix \mathbf{Z} is

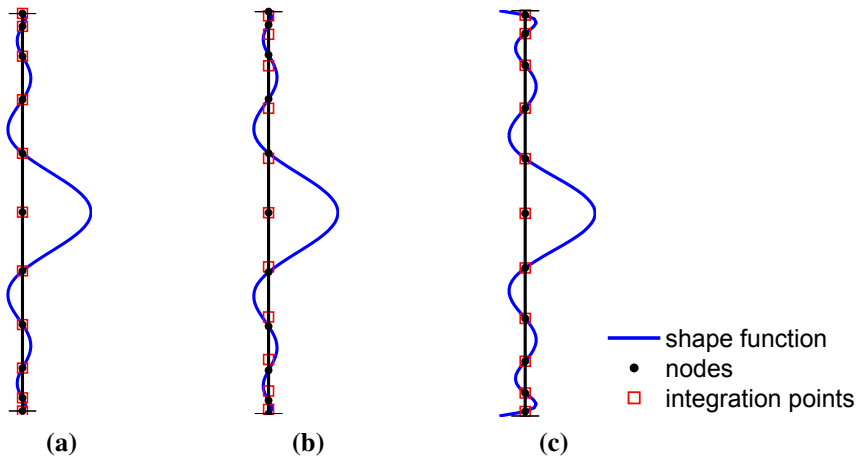


Figure 5.2: Shape functions (—), nodes (●) and integration points (□) for different types of elements: (a) Nodes and integration points at GLL points; (b) nodes at GLL points - integration points at Gauss-points; (c) nodes and integration points at Gauss points.

small in comparison with the solution of the eigenvalue problem. It is then preferred to change the integration scheme rather than shifting the inner radius. If several elements are used for the discretization, it is possible to employ the Gaussian integration for the element containing the singularity and to utilize the Gaussian-Lobatto-Legendre quadrature for the other elements. The higher accuracy of the Gaussian quadrature does not necessarily lead to more accurate results for the wavenumbers, as will be demonstrated in Section 5.5. Generally, both integration schemes result in very similar accuracy for the dispersion curves, if elements of high order are used.

If homogeneous or functionally graded materials are addressed, the discretization can be defined by a single high-order element. In that case, the concept of spectral elements can actually still be applied by positioning the nodes at the Gaussian integration points. The shape functions are only slightly modified as can be seen in Figure 5.2c. Consequently, this leads to similarly small condition numbers for \mathbf{E}_0 and does not effect the accuracy of the integration. On the other hand, this approach cannot be used in a trivial way, if several elements have to be assembled or if boundary conditions are to be applied, as no nodes are positioned at the extremities of the element. For the numerical examples presented in this work, the Gaussian integration is employed for all elements in case of a solid cylinder. For hollow cylinders the Gaussian-Lobatto-Legendre quadrature is used.

5.5 Numerical examples

Several numerical examples are presented in this section to demonstrate the applicability of the proposed approach to isotropic and anisotropic materials as well as layered pipes and rods. These examples have been computed on a current Notebook PC (Intel i7-2637M CPU

@ 1.7 GHz, 8 GB RAM) using the interactive mode of *Matlab*. Using the proposed approach as described in Section 5.1, the computational time to obtain the complete dispersion curves in the frequency range presented here for each example is about 1 s. For modes with $m > 0$, the computational time is reduced by approximately a factor 2, if the real coefficient matrices are used as described in Section 5.2. The aim of this section is to validate the results using rather small test problems. In Chapter 7, examples will be presented, where the computational costs become relevant. All dispersion curves depicted in the Figures are obtained using the complex formulation. However, it has been tested for all examples that no significant differences in the dispersion curves occur if the real coefficient matrices are employed.

5.5.1 Isotropic homogeneous pipe

As a first example, dispersion curves are computed for a simple isotropic homogeneous pipe, as the solutions can easily be verified by different approaches. The material parameters and geometry are chosen to be

Shear modulus:	$G = 1 \text{ GPa}$
Density:	$\rho = 1000 \text{ kg m}^{-3}$
Poisson's ratio:	$\nu = 0.3$
Inner radius:	$r_i = 1 \text{ mm}$
Thickness:	$h = 1 \text{ mm}$

Consequently, the angular frequency ω and dimensionless frequency a are identical (see Equation (3.83), [91]). The phase and group velocities of the propagating modes are presented in Figure 5.3. For the sake of conciseness, only modes with a circumferential order $m \leq 3$ have been depicted. Results have been compared with the software *PCDisp* [52, 53]. For the discretization of the cross-section, one five-noded element is sufficient to obtain very accurate results for the presented frequency range up to $a = 5$. As can be seen in Figure 5.3, the results are in excellent agreement with the analytical solution. More details on the accuracy of the approach will be presented in Section 5.6.

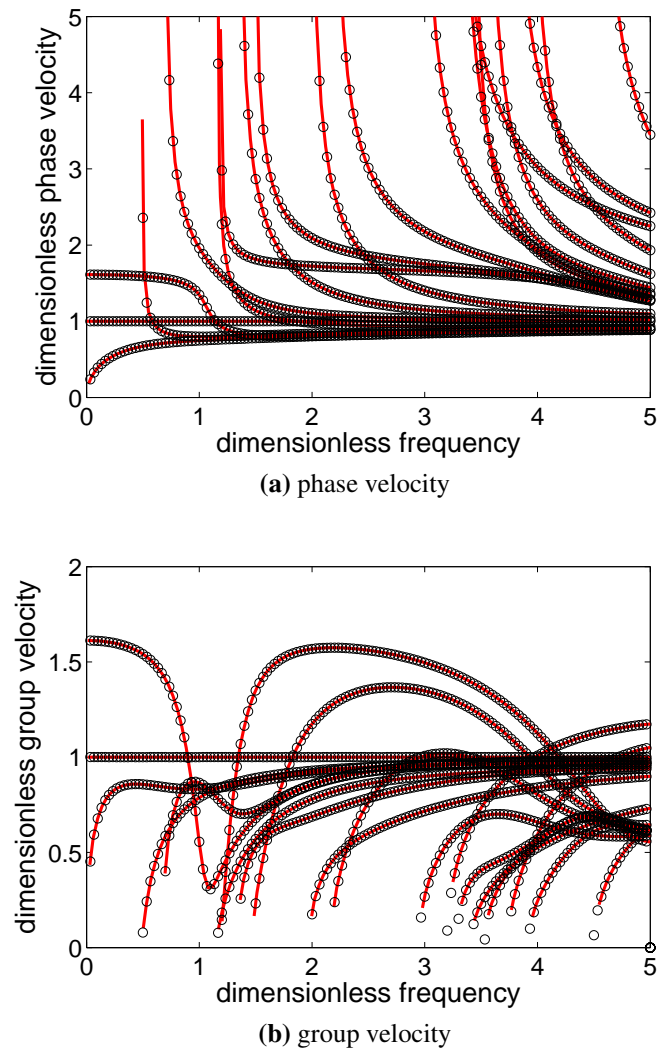


Figure 5.3: Dispersion curves of an isotropic homogeneous pipe with a Poisson's ratio of 0.3, computed using the SBFEM (\circ) and compared with *PCDisp* ($-$).

5.5.2 Layered rod

In a second example, a rod consisting of two layers is analyzed (Figure 5.4). The material properties of brass and titanium are chosen for the inner and outer element, respectively:

	Brass	Titanium
Shear modulus:	$G_1 = 40.65 \text{ GPa}$	$G_2 = 46.5 \text{ GPa}$
Density:	$\rho_1 = 8400 \text{ kg m}^{-3}$	$\rho_2 = 4460 \text{ kg m}^{-3}$
Poisson's ratio:	$\nu_1 = 1/3$	$\nu_2 = 0.3$

The element lengths are $l_1 = l_2 = 0.5 \text{ mm}$. As the inner radius of the inner element equals zero, Gaussian integration is applied as described in Section 5.4. For this example, two four-noded elements have been tested to lead to accurate results up to a frequency of $\omega = 20 \text{ rad/s}$. Again, the phase and group velocities of the modes with circumferential order $m \leq 3$ are computed and compared with results obtained with *PCDisp* (Figure 5.5). The torsional modes could not be obtained using *PCDisp*. All other modes are in excellent agreement. It should be noted that in contrast to homogeneous cylinders, the fundamental torsional mode is dispersive.

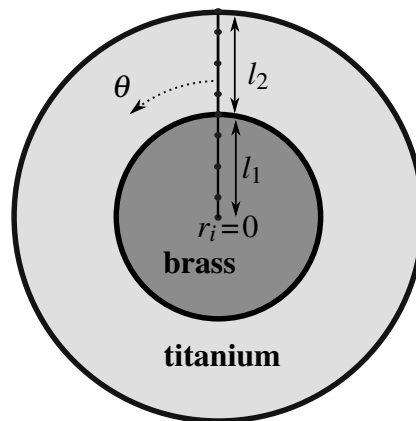


Figure 5.4: Cross-section of a layered cylinder.

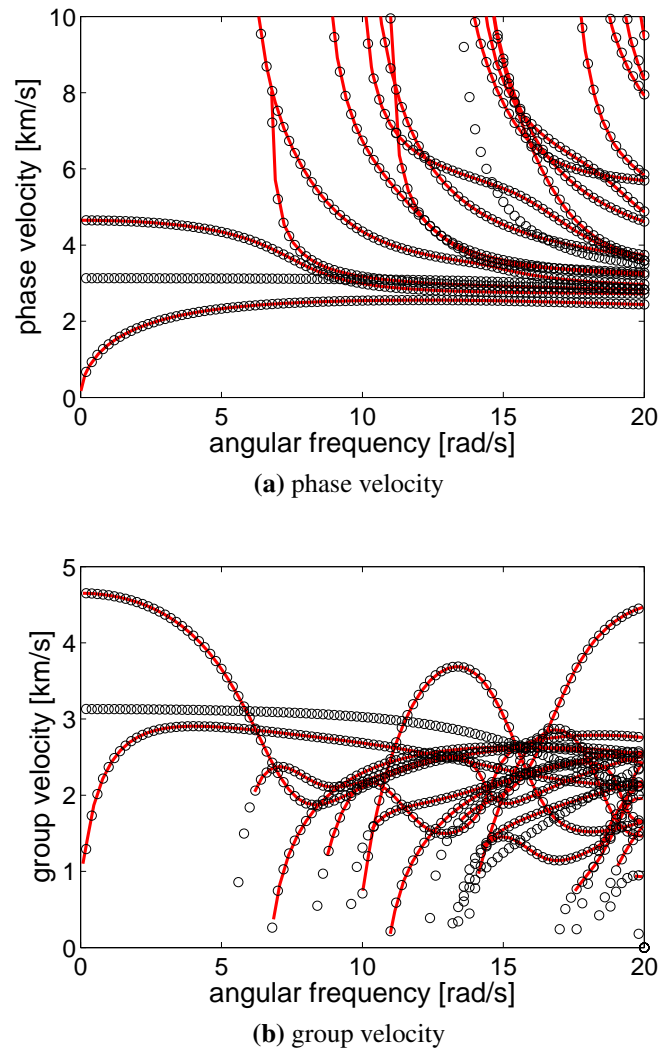


Figure 5.5: Dispersion curves of a layered rod computed using the SBFEM (\circ) and compared with *PCDisp* ($-$).

5.5.3 Anisotropic pipes

As a more advanced example, wave propagation in anisotropic pipes is analyzed and compared with results that are available in the literature. Elmaimouni et al. [226] used a polynomial approach to obtain dispersion curves for pipes with cubic and orthotropic anisotropy. These examples had been presented earlier by Nelson et al. [60] and Armenàkas et al. [215], respectively, using analytical approaches. In the formulation presented in this work, general anisotropic material behavior can be implemented in a trivial way by modifying the elasticity matrix. For the first example in [226], showing cubic anisotropy, the non-zero entries of the elasticity matrix and the geometry parameters are given as

$$\begin{aligned} D_{11} = D_{22} = D_{33} &= 469.6 \text{ GPa} & \rho &= 1000 \text{ kg m}^{-3} \\ D_{12} = D_{13} = D_{23} &= 167.61 \text{ GPa} & r_i &= 0.5 \text{ mm} \\ D_{44} = D_{55} = D_{66} &= 106.8 \text{ GPa} & h &= 1 \text{ mm} \end{aligned}$$

Results are presented in Figure 5.6. Only longitudinal modes are included in this computation. Both the results obtained by Elmaimouni et al. and Nelson et al. are taken from [226]. One seven-noded element is used for the discretization. The results obtained with the SBFEM are generally in good agreement with the results previously published, particularly they agree very well with the polynomial approach presented by Elmaimouni et al.

In Figure 5.7 results are presented for an orthotropic pipe. The nine non-zero entries of the elasticity matrix and the geometry parameters as given in [226] are

$$\begin{aligned} D_{11} = 294 \text{ GPa} & & D_{12} = 88 \text{ GPa} & & D_{44} = 131 \text{ GPa} & & \rho = 1000 \text{ kg m}^{-3} \\ D_{22} = 349 \text{ GPa} & & D_{13} = 84 \text{ GPa} & & D_{55} = 132 \text{ GPa} & & r_i = 4 \text{ mm} \\ D_{33} = 281 \text{ GPa} & & D_{23} = 126 \text{ GPa} & & D_{66} = 108 \text{ GPa} & & h = 1 \text{ mm} \end{aligned}$$

In this example, modes with $m = 1$ have been presented. Again, the results are in good agreement with the polynomial approach by Elmaimouni et al. Two additional modes are found in the presented frequency range that were not included in the earlier work. The solutions at the highest two frequencies are assigned to a different mode than originally suggested in [215].

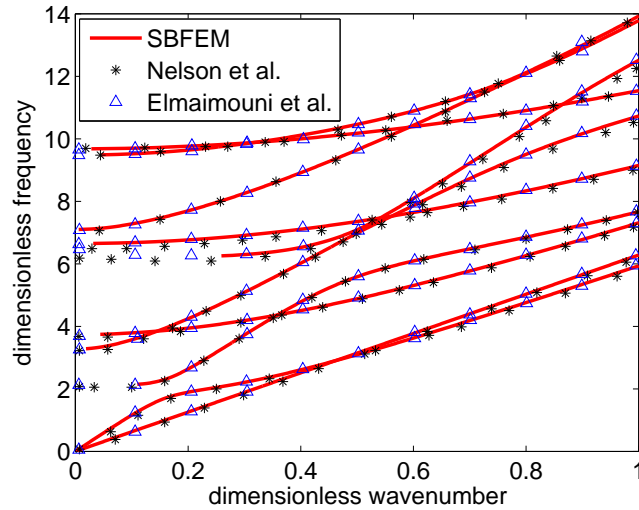


Figure 5.6: Dispersion curves for a pipe with cubic anisotropy, computed using the SBFEM (—) and compared with results obtained by Elmaimouni et al. [226] (\triangle) and Nelson et al. [60] (*).

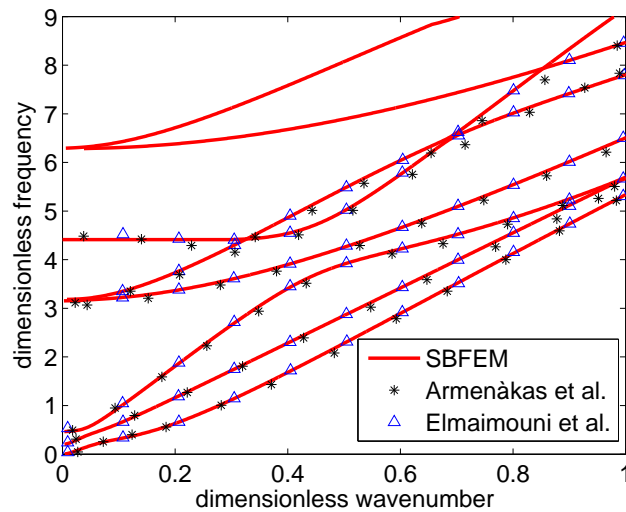


Figure 5.7: Dispersion curves for an orthotropic pipe, computed using the SBFEM (—) and compared with results obtained by Elmaimouni et al. [226] (\triangle) and Armenàkas et al. [215] (*).

5.6 Convergence and adaptive meshing

In this section, guidelines are presented to choose an appropriate number of nodes for the discretization, depending on the frequency range and element order. If the dispersion properties have to be computed over a wide frequency range, it can be desired to modify the mesh according to frequency in order to save computational costs. As higher-order elements are utilized, different options to refine the mesh can be considered. On the one hand, the number of elements can be increased while using a constant element order (*h-refinement*). The meshing procedure becomes very simple and efficient in this case, because the coefficient matrices are identical for each element. Consequently, the numerical integrations have to be performed only once for one element. On the other hand, refinement can be achieved by using only one element (or one element per layer in case of composite materials) for the discretization. The element order is then increased according to frequency (*p-refinement*). It has already been discussed in Chapter 3 that high-order spectral elements generally show excellent convergence rates.

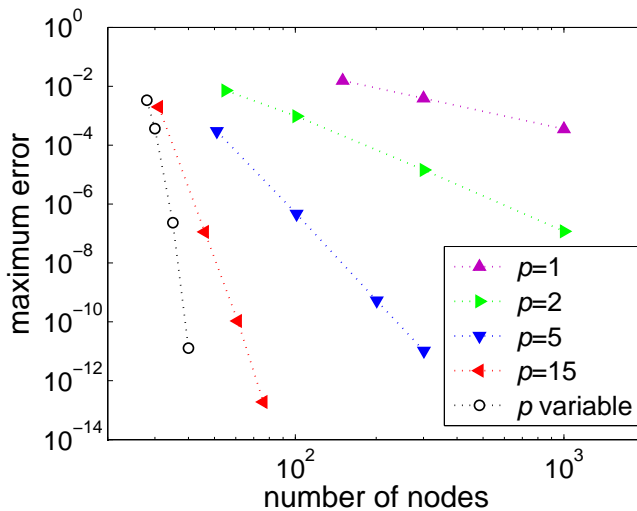


Figure 5.8: Maximum error of the wavenumbers as a function of the number of nodes at a dimensionless frequency of $a = 50$ in an isotropic pipe. Results are presented for fixed element order of 1 (\blacktriangle), 2 (\blacktriangleright), 5 (\blacktriangledown) and 15 (\blacktriangleleft) as well as variable element order (\circ).

The coefficient matrices have to be updated for every refinement step. However, in this application the computational costs for generating the mesh and computing the coefficient matrices are generally negligible in comparison with the solution of the eigenvalue problem. Both *h*- and *p*-refinement have been tested for the case of longitudinal modes in an isotropic pipe. The material and geometry parameters are the same as in Section 5.5.1. As a reference solution, the dispersion curves have been calculated using 12 elements of order $p = 14$. This discretization leads to converged results for all propagating modes within the frequency range discussed in this section. To analyze convergence in detail, the maximum error of all modes has been calculated for increasing number of nodes using *p*-refinement as well as *h*-refinement with different element order. As an example, results for a dimensionless frequency of $a = 50$ are presented in Figure 5.8. At this frequency, 25 propagating modes exist in the waveguide. Gaussian-Lobatto-Legendre quadrature has been used for the numerical integration. Results are presented for traditional linear ($p = 1$) and quadratic ($p = 2$) elements as well as higher-

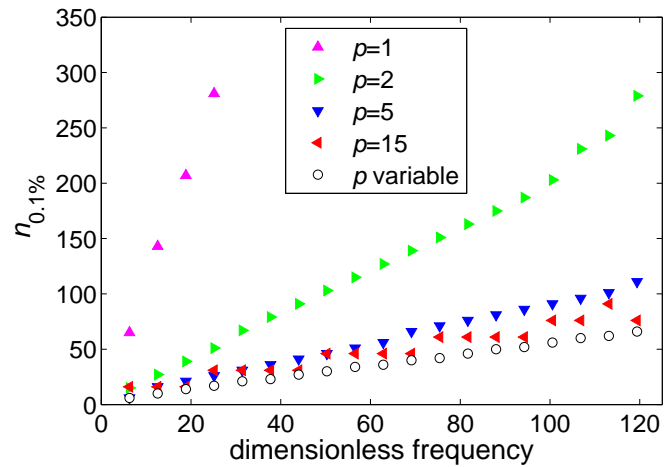
order elements of order $p = 5$ and $p = 15$. In these cases, refinement has been achieved by increasing the number of elements. As can be seen in Figure 5.8, the results converge for each element type, while the convergence rate is drastically improved when increasing the element order. Using p -refinement (' p variable' in Figure 5.8) generally leads to faster convergence than h -refinement.

We are interested in the number of nodes that are required to obtain solutions with sufficient accuracy for practical applications. This number of required nodes is a function of frequency. We discuss the frequency range up to $a = 120$, where 60 propagating longitudinal modes can be excited in the waveguide. The discretization has been refined at each frequency step until the maximum error of all propagating modes is less than 0.1% in comparison with the reference solution.

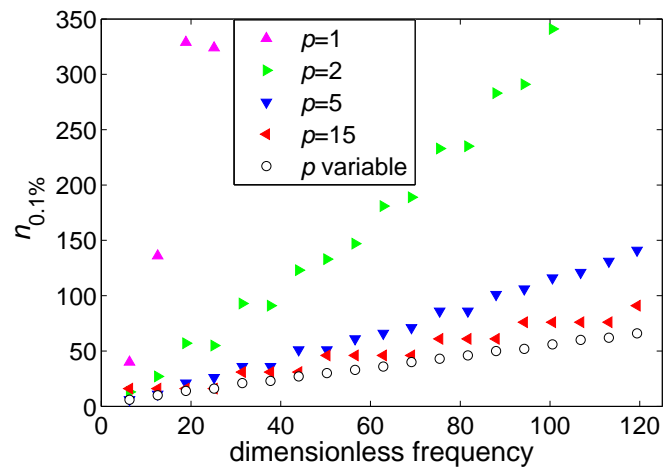
The number of nodes $n_{0.1\%}$ required for the chosen accuracy is plotted as a function of dimensionless frequency a in Figure 5.9a. Gaussian-Lobatto-Legendre quadrature has been utilized for the numerical integrations. For all elements, the number of nodes increases almost linearly with frequency, as long as the frequency is not too large. The non-linear behavior of quadratic elements at very high frequencies can be explained by numerical pollution errors [233, 234]. Obviously, the required number of nodes is much smaller, if higher-order elements are utilized in comparison with linear and quadratic elements. Comparing the results obtained with $p = 5$ and $p = 15$, the benefit from increasing the element order is comparably small. This is because at some frequency steps more nodes have to be used than actually required, due to the high order of each element. Still it should be noted that a rather small change in the number of degrees of freedom can result in a significant increase in computational time.²³

Best results have been obtained using p -refinement. Still the number of required nodes increases linearly with frequency, while it is always smaller or equal to the number of nodes for fixed element order. Figure 5.9b shows the equivalent results, if Gaussian quadrature is used rather than Gaussian-Lobatto-Legendre quadrature. As can be seen from comparison with Figure 5.9a, the required number of nodes is significantly higher, if elements of low order are used. Contrary, for h -refinement with elements of order 15 and for p -refinement the results are almost identical. The effect on the dispersion curves is demonstrated in Figure 5.10. The phase velocities of the longitudinal modes in the same pipe as before are plotted as a function of dimensionless frequency up to $a = 6\pi$. The converged solution is compared to results that are not converged within the whole frequency range. In Figure 5.10a five quadratic elements have been used. If the Gaussian-Lobatto-Legendre quadrature (\circ) is used, the results are slightly more accurate for up to $a \approx 15$ than for the Gaussian integration (\square). On the other hand, if one element of order 7 is used (Figure 5.10b), the accuracy seems very similar.

²³For instance, increasing the number of nodes by 25 % leads to the computational time increasing by a factor $1.25^3 \approx 2$.



(a) GLL quadrature



(b) Gaussian quadrature

Figure 5.9: Number of nodes that are required to obtain a maximum error of 0.1% if the Gaussian-Lobatto-Legendre quadrature (a) or the traditional Gaussian quadrature (b) is employed. Results are presented for fixed element order of 1 (\blacktriangle), 2 (\blacktriangleright), 5 (\blacktriangledown) and 15 (\blacktriangleleft) as well as variable element order (\circ).

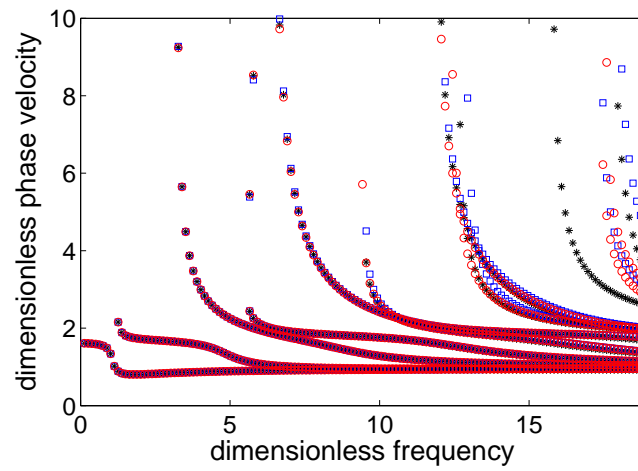
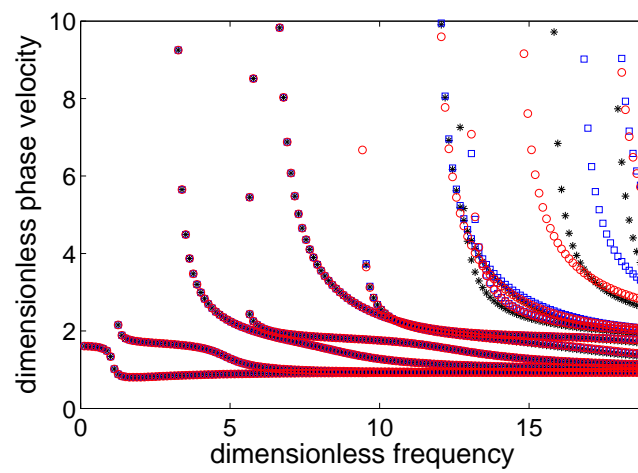
(a) $p = 2$ (b) $p = 7$

Figure 5.10: Converged results for the phase velocities (*) compared with GLL (○) and Gaussian (□) quadrature for the same number of nodes. (a): five elements of order 2; (b): one element of order 7.

The number of required nodes can be compared to the wave length λ_s of shear waves in the considered material at a given frequency. The number of wave lengths n_λ in trough-thickness direction of the pipe is given as

$$n_\lambda = \frac{h}{\lambda_s} = \frac{h\omega}{2\pi c_s} = \frac{a}{2\pi} \quad (5.54)$$

The number of nodes per wavelength that is required, if a variable element order is used, is about 3.5. In contrast to that, using a fixed element order of $p = 5$, about 6 nodes per wavelength should be used. Using quadratic elements, about 13 nodes per wavelength are required. In Table 5.1 the results are summarized for Gaussian and GLL quadrature for a maximum error of 0.1% as well as 1%. It can be seen that the number of nodes required to achieve a maximum error of 0.1% is only slightly larger than to obtain an error of 1% if high-order elements are used. This confirms that the results converge rapidly within the range of accuracy that is relevant for practical applications. Even though the results presented here have been obtained from the computation of longitudinal modes, an analogous procedure for torsional and higher-order modes leads to almost identical results and will not be repeated.

In terms of implementation it can be more feasible to express the required number of nodes as a function of the dimensionless frequency a . Fitting a linear function to the data presented in Figure 5.9, yields a useful approximation for the number of nodes

$$n_{0.1\%} = 4 + 0.5a \quad (5.55)$$

This result will be used to maximize the efficiency of the implementation in Chapter 7.

Table 5.1: Average number of nodes per transversal wavelength in an isotropic material that are required to obtain a maximum error of 0.1% and 1%, respectively.

p	GLL		Gauss	
	$n_{0.1\%}/n_\lambda$	$n_{1\%}/n_\lambda$	$n_{0.1\%}/n_\lambda$	$n_{1\%}/n_\lambda$
1	69.9	22.4	86.5	27.7
2	12.7	6.7	18.1	9.6
5	5.8	4.5	7.1	5.6
15	4.6	4.3	4.7	4.4
variable	3.5	3.3	3.5	3.4

Chapter 6

Embedded waveguides

In some important applications of guided waves (e. g. the non-destructive testing of buried pipes, embedded timber poles or fluid loaded plates), the waveguide is coupled to a quasi-infinite medium, allowing for waves to be transmitted into the surrounding medium. This so-called leakage effect has to be taken into account when modeling the dispersive behavior of guided waves. Not only does it affect the phase velocities, but it causes the wavenumbers of all modes to be complex. The imaginary part of the complex wavenumbers represents the attenuation due to leakage of wave energy into the surrounding medium. As a consequence, the energy velocity is strongly influenced by the material parameters.

Most literature on guided waves addresses waveguides with stress-free surfaces, while the development of adequate techniques to model waveguides embedded in or attached to an infinite medium is still ongoing. Several approaches have been presented in order to account for the influence of a surrounding medium on the propagating modes in a waveguide. The global matrix method and similar models are generally capable of describing the transmission of waves into an infinite medium. However, computing all complex roots of the resulting characteristic equation is not trivial, depending on the combination of material parameters of the waveguide and surrounding medium. Also, the global matrix method can only be applied to simple plates and axisymmetric structures. Most analytical models for embedded waveguides address waveguides in fluids, where the influence of the surrounding medium is comparably small. Examples include rods in fluids [235], leaky Lamb waves in fluid loaded plates [236], plates embedded in fluids [34, 237] and surface waves in embedded cylindrical shells [238]. More recently, an analytical model for cylinders embedded in a solid has been presented [239]. Also interesting discussions on leaky waves [240, 241] and the effect of partial embedment on the scattering of guided waves in cylindrical structures [242] can be found in the literature. More general solutions exist for fluid-loaded anisotropic plates and cylinders [243, 244].

In Finite Element modeling, complex wavenumbers do not introduce severe difficulties, as has been demonstrated for the case of waveguides with material damping [63]. Formulating the effect of a surrounding infinite medium on the other hand is not trivial. Simply discretizing a finite subdomain to represent the infinite medium leads to reflections from the boundary of the discretized region to interfere with the modes in the waveguides. To avoid these reflections, several authors employed the concept of absorbing regions [152, 245–250]. The absorbing re-

gion is assumed to consist of the same material as the surrounding medium while an additional material damping - increasing with the distance to the waveguide's surface - is introduced, causing waves to vanish as they propagate towards the boundary of the discretized domain. It has been demonstrated that absorbing regions can lead to accurate results in transient Finite Element analyses [245–249] as well as the SAFE method [152, 250]. However, particularly for the computation of dispersion relations, the application of absorbing regions can be cumbersome and lead to very high computational costs, as the size of the absorbing region typically has to be many times larger than the waveguide's cross-section. Also it can be difficult to distinguish between modes propagating in the waveguide and unwanted solutions representing waves that are excited in the surrounding medium. As an alternative, perfectly matched layers [251, 252] or infinite elements [253–255] can be implemented to model the infinite medium, leading to similar advantages and drawbacks compared to absorbing regions.

In this chapter the effect of a surrounding medium is modeled by a boundary condition on the waveguide's surface [99]. Numerous approaches have been developed by different authors over the last decades in order to construct a boundary that simulates the effect of an adjacent infinite medium. Depending on the application and the background of the research, these boundaries are referred to as e. g. non-reflecting [256], transmitting [257, 258], radiating [259], open [260] or absorbing [261, 262] boundary conditions. Comprehensive reviews of the different techniques can be found in the literature [263, 264]. It should be noted that the main difficulty addressed in these approaches is to model a truncated part of an infinite homogeneous medium. In that case the boundary condition is required to simulate perfect transmission hence avoiding any reflections at the boundary. In contrast to that, the material parameters of a waveguide and the surrounding medium are typically very different and this difference in acoustic impedances leads to most of the wave energy being reflected inside the waveguide (If this assumption is not valid, the structure cannot be considered as a waveguide).

For this situation a simple dashpot boundary condition is introduced into the existing formulation for guided waves. The idea to replace the infinite medium surrounding the waveguide by a dashpot boundary has been inspired by Hall and Chopra [265], who used a similar concept in the context of dam-reservoir interaction. Hall and Chopra formulated a damping boundary condition applied along the bottom of a semi-infinite reservoir in order to approximately account for the interaction between the fluid and underlying foundation medium. The derivation of the boundary condition is based on the assumption that each component of the displacement vector on the surface obeys the one-dimensional Helmholtz equation. As a result, the surrounding medium acts as a damper with its acoustic impedances being the damping coefficients. This concept of a dashpot boundary has originally been developed to fulfill the Sommerfeld radiation condition and is mentioned in the literature many times in the context of simulating infinite media [264–269]. It is very effective in absorbing waves that propagate perpendicular to the boundary with a known wave velocity, which typically occurs at high wavenumbers. In the majority of other applications, where general infinite media are modeled at low wavenumbers, this type of boundary condition leads to unsatisfactory results due to spurious reflections at the boundary. For the simulation of embedded waveguides, where the wave velocity in the surrounding medium is typically much lower than that of the waveguide, it will be demonstrated

that this approximation leads to very accurate results. The dashpot boundary condition can easily be incorporated into the existing formulation for free waveguides. Since the surrounding medium does not require discretization, the computational effort is drastically reduced in comparison with other Finite Element approaches and the identification of propagating modes in the waveguide is straightforward.

In order to model a waveguide coupled to an infinite medium, first an adequate boundary condition for a one-dimensional system is derived. Similar descriptions can be found in the work presented by Hall and Chopra [265], where the interaction of a solid dam with an infinite fluid medium is modeled. In the following subsections it will be discussed how these considerations can be adapted to model the interaction of a plate or a cylindrical structure with an infinite solid medium.

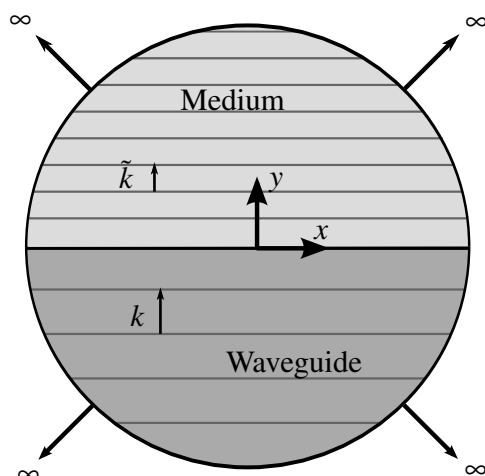


Figure 6.1: One-dimensional wave propagation in two adjoining half spaces.

6.1 SBFEM formulation for embedded waveguides

6.1.1 One-dimensional dashpot boundary condition

The simple wave propagation problem depicted in Figure 6.1 is addressed. It consists of two adjoining half spaces with an interface at $y = 0$. Assume that the lower half space ($y < 0$) represents the waveguide, while the upper half space represents the surrounding medium. In this section, the superscript \sim indicates variables that refer to the surrounding medium. Particularly, the wavenumbers k and \tilde{k} denote the wavenumbers of waves traveling in the waveguide and the surrounding medium, respectively. The structure is of infinite dimension in x - as well as y -direction. For now it is assumed that waves can propagate in the y -direction only and hence can be treated as a one-dimensional problem.

Under this assumption, the displacements u and \tilde{u} in the waveguide and the surrounding medium obey the one-dimensional Helmholtz equation. For instance, for the surrounding medium the Helmholtz equation reads [270]

$$\tilde{u}_{,yy} + \frac{\omega^2}{\tilde{c}^2}\tilde{u} = 0 \quad (6.1)$$

with the wave velocity \tilde{c} . The general solution of Equation (6.1) is given by

$$\tilde{u}(y, \omega) = A(\omega)\exp\left(\frac{i\omega}{\tilde{c}}y\right) + B(\omega)\exp\left(-\frac{i\omega}{\tilde{c}}y\right) \quad (6.2)$$

where the arbitrary frequency-dependent amplitudes $A(\omega)$ and $B(\omega)$ correspond to the amplitudes of waves traveling in negative and positive y -direction, respectively. The stresses σ and $\tilde{\sigma}$ in the waveguide and the surrounding medium must be continuous at the interface, $y = 0$, i. e.

$$\sigma(0, \omega) = \tilde{\sigma}(0, \omega) = \tilde{E}\tilde{u}_{,y}(0, \omega) \quad (6.3)$$

where \tilde{E} denotes the elastic modulus, defined as the ratio of stress $\tilde{\sigma}$ and strain $\tilde{\epsilon} = \tilde{u}_{,y}$

$$\tilde{E} = \frac{\tilde{\sigma}}{\tilde{\epsilon}} \quad (6.4)$$

In case of scalar wave propagation, the elastic modulus can be written as [271]

$$\tilde{E} = \tilde{\rho}\tilde{c}^2 \quad (6.5)$$

with the mass density of the surrounding medium $\tilde{\rho}$. The derivative of the displacement field in the surrounding medium with respect to y is given by

$$\tilde{u}_{,y}(y, \omega) = \frac{i\omega}{\tilde{c}} \left[A(\omega)\exp\left(\frac{i\omega}{\tilde{c}}y\right) - B(\omega)\exp\left(-\frac{i\omega}{\tilde{c}}y\right) \right] \quad (6.6)$$

Substituting Equations (6.5) (6.6) into (6.3) yields

$$\sigma(0, \omega) = i\omega\tilde{\rho}\tilde{c}[A(\omega) - B(\omega)] \quad (6.7)$$

In addition to the stresses, the displacements at the interface $y = 0$ must be continuous, i. e.

$$u(0, \omega) = \tilde{u}(0, \omega) = A(\omega) + B(\omega) \quad (6.8)$$

and consequently

$$B(\omega) = u(0, \omega) - A(\omega) \quad (6.9)$$

Substituting Equation (6.9) into (6.7) leads to

$$\sigma(0, \omega) = 2i\omega\tilde{\rho}\tilde{c}A(\omega) - i\omega\tilde{\rho}\tilde{c}u(0, \omega) \quad (6.10)$$

Equation (6.10) describes the stress at the interface caused by waves that are transmitted from inside the waveguide as well as incident waves from the surrounding medium. In this application the surrounding medium is assumed to be of infinite dimension, hence we can assume the term describing incident waves to vanish (Sommerfeld radiation condition). Consequently we can set

$$A(\omega) = 0 \quad (6.11)$$

and write

$$\sigma(0, \omega) = -i\omega\tilde{\rho}\tilde{c}u(0, \omega) = i\omega qu(0, \omega) \quad (6.12)$$

with

$$q = -\tilde{\rho}\tilde{c} \quad (6.13)$$

The interaction of the waveguide with the surrounding medium has been formulated as a boundary condition for the stresses at the interface. The boundary condition can be interpreted as a dashpot with the damping coefficient q . It should be noted that the coefficient q is given by the (negative) acoustic impedance of the surrounding medium [272].

6.1.2 Application to plate structures

Even though the boundary condition has been derived under drastically simplified prerequisites in the previous subsection, it can similarly be applied to obtain a realistic model for an embedded waveguide. First, the dashpot boundary condition is employed for plate structures. The three-dimensional formulation as described in Section 3.5 is used and the plate may be attached to (different) infinite media at both of its surfaces. For simplicity the plate's upper surface is positioned at $y = 0$. According to Equation (6.12), the effect of the surrounding medium can be represented by imaginary stresses that act on the plate's surface. In the three-dimensional formulation we assign surface tractions to these external stresses, denoted by $\boldsymbol{\tau}(x, y, z, \omega) = [\tau_x \ \tau_y \ \tau_z]^T$. We assume that each component of the surface tractions can be represented by a one-dimensional dashpot (Figure 6.2), i. e.

$$\boldsymbol{\tau}(x, 0, z, \omega) = i\omega\mathbf{Q}u(x, 0, z, \omega) \quad (6.14)$$

where the damping coefficient is replaced by the 3×3 matrix²⁴

$$\mathbf{Q} = -\tilde{\rho} \begin{bmatrix} \tilde{c}_s & 0 & 0 \\ 0 & \tilde{c}_l & 0 \\ 0 & 0 & \tilde{c}_s \end{bmatrix} \quad (6.15)$$

\tilde{c}_l and \tilde{c}_s refer to the shear and longitudinal wave velocities in the surrounding medium, respectively. Since τ_y is directed normal to the plate's surface, it is described by the longitudinal wave velocity, while the in-plane components τ_x and τ_z are associated with the shear wave velocity in

²⁴Note that \mathbf{Q} can have different values at the lower and upper surface. For the sake of conciseness, the η -dependency will be omitted in the equations.

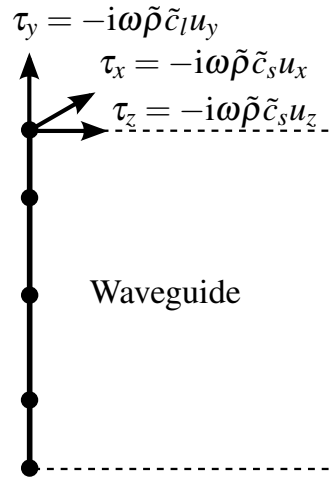


Figure 6.2: Three-dimensional dashpot boundary condition on a plate surface.

the surrounding medium.

Equation (6.14) is an approximation, as it implies that each component of the displacement vector in the surrounding medium obeys the one-dimensional wave equation, while the coupling between the components is neglected. It will be demonstrated by numerical examples that for practical applications this approximation leads to very accurate results, particularly in the high frequency range. Hence, it is generally reliable for the modeling of ultrasonic guided waves.

When introducing the boundary condition in the discretized formulation of the displacement field

$$\mathbf{u} = \mathbf{N}(\boldsymbol{\eta})\mathbf{u}_{\mathbf{n}}(x, z) \quad (6.16)$$

we have to take into account that the shape functions are defined in the local coordinate η . Hence, we have to consider the coordinate transformation when performing the differentiation in Equation (6.6):

$$\tilde{u}_{,y}(\boldsymbol{\eta}) = \frac{1}{y_{,\boldsymbol{\eta}}}\tilde{u}_{,\boldsymbol{\eta}}(\boldsymbol{\eta}) \quad (6.17)$$

For the tractions on the plate's upper surface we obtain

$$\boldsymbol{\tau}(x, 0, z, \boldsymbol{\omega}) = \frac{i\boldsymbol{\omega}}{y_{,\boldsymbol{\eta}}}\mathbf{QN}(\boldsymbol{\eta}=1)\mathbf{u}_{\mathbf{n}}(x, z) \quad (6.18)$$

To include the boundary conditions into the SBFEM formulation, we derive the virtual external work δW_d corresponding to these boundary tractions. Integration is performed over the plate's upper and lower surface, denoted by Γ_2 (in contrast to the integration over the cross-section that

is required to compute the coefficient matrices)

$$\begin{aligned}\delta W_d &= \iint_{\Gamma_2} \delta \mathbf{u}^T \boldsymbol{\tau} d\Gamma = \frac{i\omega}{y,\eta} \iint_{\Gamma_2} \delta \mathbf{u}_n^T(x,z) \mathbf{N}^T \mathbf{Q} \mathbf{N} \mathbf{u}_n(x,z) |J| d\Gamma \\ &= i\omega \int_0^\infty \int_{-\infty}^\infty \delta \mathbf{u}_n^T(x,z) \mathbf{C}_0 \mathbf{u}_n(x,z) dx dz\end{aligned}\quad (6.19)$$

where the matrix \mathbf{C}_0 is introduced as

$$\mathbf{C}_0 = \frac{1}{y,\eta} \mathbf{N}^T \mathbf{Q}_1 \mathbf{N} |J| \Big|_{\eta=-1} + \frac{1}{y,\eta} \mathbf{N}^T \mathbf{Q}_2 \mathbf{N} |J| \Big|_{\eta=+1}\quad (6.20)$$

As a generalization, \mathbf{Q}_1 and \mathbf{Q}_2 denote the damping coefficients at the lower and upper plate surface, respectively. Note that for a plate structure the simple coordinate transformation yields the Jacobian determinant (see Equation (3.5))

$$|J| = y,\eta = \frac{l}{2}\quad (6.21)$$

Consequently, \mathbf{C}_0 is obtained as a simple diagonal matrix with a maximum of 6 non-zero entries:

$$\mathbf{C}_0 = -\text{diag}(\tilde{c}_s^{(1)}, \tilde{c}_s^{(1)}, \tilde{c}_l^{(1)}, 0, \dots, 0, \tilde{c}_s^{(2)}, \tilde{c}_s^{(2)}, \tilde{c}_l^{(2)}) \tilde{\rho}\quad (6.22)$$

Including Equation (6.19) into the virtual work principle (3.15) leads to an additional damping term in the partial differential equation for the nodal displacements:

$$\mathbf{E}_0 \mathbf{u}_{n,zz}(z) + (\mathbf{E}_1^T - \mathbf{E}_1) \mathbf{u}_{n,z}(z) + (-\mathbf{E}_2 + \omega^2 \mathbf{M}_0 - i\omega \mathbf{C}_0) \mathbf{u}_n(z) = 0\quad (6.23)$$

The same term has to be included in the polynomial eigenvalue problem

$$\left(\lambda^2 \mathbf{E}_0 + \lambda (\mathbf{E}_1^T - \mathbf{E}_1) - \mathbf{E}_2 + \omega^2 \mathbf{M}_0 - i\omega \mathbf{C}_0 \right) \hat{\mathbf{u}}_n = 0\quad (6.24)$$

(c. f. Equation (3.35)) as well as the standard eigenvalue problem

$$-\mathbf{Z}_e \boldsymbol{\Psi} = \lambda \boldsymbol{\Psi}\quad (6.25)$$

where the modified coefficient matrix is assembled as

$$\mathbf{Z}_e = \begin{bmatrix} \mathbf{E}_0^{-1} \mathbf{E}_1^T & -\mathbf{E}_0^{-1} \\ -i\omega \mathbf{C}_0 + \omega^2 \mathbf{M}_0 - \mathbf{E}_2 + \mathbf{E}_1 \mathbf{E}_0^{-1} \mathbf{E}_1^T & -\mathbf{E}_1 \mathbf{E}_0^{-1} \end{bmatrix}\quad (6.26)$$

Since in comparison to stress-free surfaces, the \mathbf{Z}_e matrix for embedded structures differs only

by the damping term, it can easily be incorporated into the existing implementation. This term inevitably causes the \mathbf{Z}_e matrix to be complex, leading to higher computational costs. More importantly, all wavenumbers obtained from the solution of the eigenvalue problem are generally complex. While the real part k_r of a wavenumber k is related to the phase velocity c_p of the mode by

$$c_p = \frac{\omega}{k_r} \quad (6.27)$$

the imaginary part k_i represents the attenuation of the mode, caused by radiation of sound energy in the surrounding medium. Solutions with both positive and negative imaginary part exist. Considering wave propagation in positive z -direction, wavenumbers with positive imaginary part represent unphysical solutions, as the amplitude of the corresponding mode increases as the wave propagates. These unphysical solutions can easily be eliminated. On the other hand, there is no trivial distinction between propagating and evanescent modes, since all modes are obtained with complex wavenumber. The only possibility to choose the relevant modes is to consider only wavenumbers with an imaginary part smaller than a predefined value. The optimal choice of this value is problem-dependent.

6.1.3 Application to axisymmetric waveguides

Only minor modifications have to be made when dealing with embedded axisymmetric waveguides, compared to plate structures. Obviously, only the outer radius of the cylindrical structure can be in contact with the infinite medium. Hence, to obtain the virtual work corresponding to the boundary condition, the integration has to be performed over the side faces of the cylinder ($r = r_o$, cf. Figure 5.1)

$$\begin{aligned} \delta W_d &= i\omega \iint_{\Gamma_2} \frac{1}{r,\eta} \delta \mathbf{u}_n^T(z, \theta) \mathbf{N}^T \mathbf{Q} \mathbf{N} \mathbf{u}_n(z, \theta) |\mathbf{J}| d\Gamma \\ &= i\omega \int_0^\infty \int_0^{2\pi} \delta \mathbf{u}_n^T(z, \theta) \mathbf{C}_0 \mathbf{u}_n(z, \theta) d\theta dz \end{aligned} \quad (6.28)$$

and the damping matrix reads

$$\mathbf{C}_0 = \frac{1}{r,\eta} \mathbf{N}^T \mathbf{Q} \mathbf{N} |\mathbf{J}| \Big|_{\eta=+1} \quad (6.29)$$

The Jacobian determinant differs from the case of plate structures:

$$|\mathbf{J}| = \frac{l}{2} r \quad (6.30)$$

$$r,\eta = \frac{l}{2} \quad (6.31)$$

Consequently, the damping matrix can be written as

$$\mathbf{C}_0 = -\text{diag}(0, \dots, 0, \tilde{c}_s, \tilde{c}_s, \tilde{c}_l) \cdot \tilde{\rho} r_o \quad (6.32)$$

With these modifications, Equations (6.23)-(6.26) are still valid for axisymmetric structures.

6.1.4 Absorbing region

To validate the results obtained with the proposed dashpot approach, an alternative technique has been implemented. As described in detail by other authors [152, 250] the influence of a surrounding medium on a waveguide can be incorporated by modeling a representative part of the surrounding medium and adding an absorbing region in order to avoid reflections at the boundary of the discretization to interfere with the modes in the waveguide. The absorbing region is assumed to consist of the same material as the surrounding medium, while an artificial material damping is added, increasing with the distance to the waveguide's surface. The material damping is represented by an additional imaginary part of the shear modulus G_a in the absorbing region [152]

$$G_a = G_r \left[1 + i\alpha \left(\frac{r_a}{d_a} \right)^3 \right] + iG_i \quad (6.33)$$

where G_r and G_i denote the real and imaginary parts of the shear modulus in the surrounding medium, r_a is the position within the absorbing region and d_a its thickness. To determine the required thickness of the absorbing region, the estimation suggested by Castaings and Lowe [152] is followed. First, the minimum angle β of waves radiated into the surrounding medium is obtained from Snell-Descartes' law as

$$\beta = \sin^{-1} \left(\frac{\tilde{c}_l}{\min(c_p)} \right) \quad (6.34)$$

where $\min(c_p)$ is the smallest phase velocity of a propagating mode in the waveguide and \tilde{c}_l denotes the longitudinal wave velocity in the surrounding medium. For a wave propagating at this angle with frequency f , the projection of its wavelength on the y -axis is given by

$$\lambda_y = \frac{\tilde{c}_l/f}{\cos \beta} \quad (6.35)$$

Empirically, the required thickness d_a of the absorbing region is set to twice this value. Substituting Equation (6.34) into (6.35) we obtain

$$d_a = 2\lambda_y = \frac{2\tilde{c}_l}{f} \left[1 - \left(\frac{\tilde{c}_l}{\min(c_p)} \right)^2 \right]^{-\frac{1}{2}} \quad (6.36)$$

In traditional Finite Element approaches, absorbing regions are realized by discretizing the surrounding medium with a high number of quadratic elements and assigning different damping

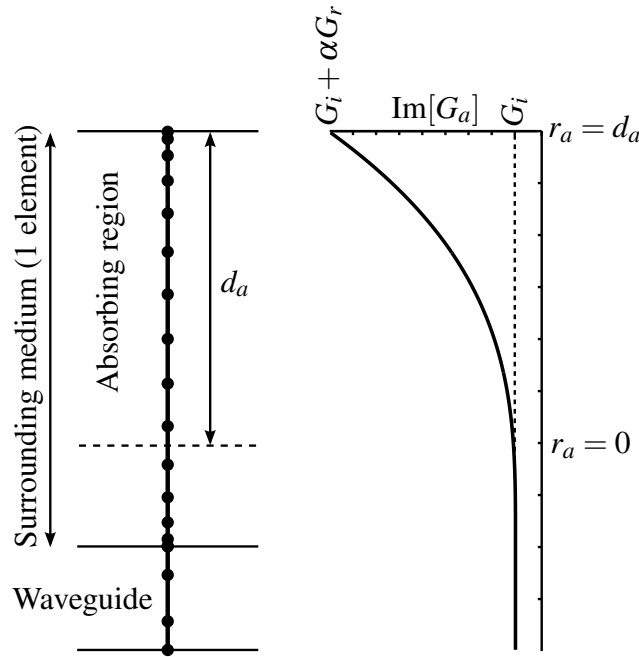


Figure 6.3: Discretization of the waveguide and surrounding medium using two elements of high order. In the absorbing region, an imaginary part of the shear modulus is assigned to each node according to Equation (6.33).

coefficients to each element. Using the proposed SBFEM approach, the surrounding medium (including the absorbing region) can be described using only one element of very high order (Figure 6.3). The procedure is similar to the modeling of functionally graded materials as described in Section 3.2.4. According to Equation (6.33), varying values for the imaginary part of the complex shear modulus are assigned to each node within the element.

One of the problems emerging when using absorbing regions is that modes propagating in the discretized domain of the surrounding medium form additional solutions to the eigensystem. It can be challenging to distinguish modes mainly propagating within the waveguide from unwanted solutions in the surrounding medium. One possible approach to overcome this difficulty is to evaluate the Poynting vector to determine the energy flux density perpendicular to the cross-section of the discretized structure [152]. The desired solutions are expected to reveal the highest energy flux within the waveguide. This technique can easily be implemented in the proposed approach. The z -component of the Poynting vector in a Cartesian coordinate system is given by [273]

$$p_z(y) = \operatorname{Re} \left[\frac{i\omega}{2} (u_z^* \sigma_z + u_x^* \tau_{xz} + u_y^* \tau_{yz}) \right] = \operatorname{Re} \left[\frac{i\omega}{2} \mathbf{u}^* \mathbf{b}_1^T \boldsymbol{\sigma} \right] \quad (6.37)$$

Integrating over one element yields

$$\begin{aligned}
P_z &= \operatorname{Re} \left[\frac{i\omega}{2} \int_{-1}^{+1} \mathbf{u}^* \mathbf{b}_1^T \boldsymbol{\sigma} |J| d\eta \right] \\
&= \operatorname{Re} \left[\frac{i\omega}{2} \int_{-1}^{+1} \hat{\mathbf{u}}_n^* \mathbf{B}_1^T \mathbf{D} (\lambda \mathbf{B}_1 \hat{\mathbf{u}}_n + \mathbf{B}_2 \hat{\mathbf{u}}_n) |J| d\eta \right] \\
&= \operatorname{Re} \left[\frac{i\omega}{2} \int_{-1}^{+1} \hat{\mathbf{u}}_n^* (\lambda \mathbf{B}_1^T \mathbf{D} \mathbf{B}_1 + \mathbf{B}_1^T \mathbf{D} \mathbf{B}_2) \hat{\mathbf{u}}_n |J| d\eta \right] \\
&= \operatorname{Re} \left[\frac{i\omega}{2} \hat{\mathbf{u}}_n^* (\lambda \mathbf{E}_0 + \mathbf{E}_1^T) \hat{\mathbf{u}}_n \right]
\end{aligned} \tag{6.38}$$

Hence, the Poynting vector can easily be obtained after the coefficient matrices, eigenvalues and eigenvectors have been computed. Evaluating the Poynting vector for the element describing the waveguide P_z^w and the total discretized cross-section P_z^t for a given mode, we can define the ratio

$$R_p = \frac{P_z^w}{P_z^t} \tag{6.39}$$

This value should be significantly higher for solutions representing propagating modes in the waveguide compared to modes that are excited in the surrounding medium. However, choosing an appropriate limit for R_p is problem-dependent and not trivial. It can be worthwhile to first eliminate modes with very high attenuation. Particularly, if the wave velocities in the surrounding medium are much smaller than in the waveguide, it can be helpful to eliminate all modes with a phase velocity smaller than the pre-set value for $\min(c_p)$.

6.2 Numerical examples

6.2.1 Plate attached to infinite medium

As a first rather simple example an aluminum plate in contact with an infinite elastomer is analyzed (Figure 6.4). This example has been presented earlier by Castaings and Lowe [152] who employed a Finite Element formulation to compute the phase velocities and attenuations of the first three modes in the low frequency range. The plate thickness is 4 mm. The shear moduli G , densities ρ and Poisson's ratios ν are given as

	G [GPa]	ρ [g/cm ³]	ν
Aluminum	27	2.78	0.3412
Elastomer	0.3(1 + 0.1i)	1	0.2858

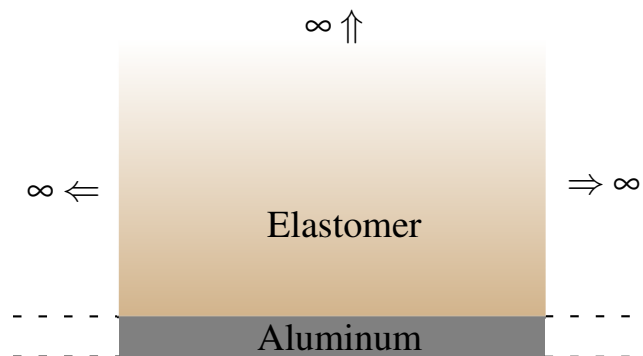


Figure 6.4: Aluminum plate attached to an elastomer of infinite dimensions.

In the approach presented by Castaings and Lowe, a representative part of the two-dimensional cross-section of the plate and the elastomer is discretized using rectangular elements with quadratic shape functions. An absorbing region is employed to avoid reflections from the boundary of the discretized domain to interfere with the guided wave modes in the plate. This example is comparably simple, as the elastic parameters of the considered materials are very different, causing a weak interaction. Moreover, a high (physical²⁵) material damping is assumed for the elastomer. This facilitates the application of an absorbing region. Also, the modes that primarily propagate in the aluminum can easily be identified, as they reveal significantly smaller attenuation than the modes that can propagate in the elastomer. Still a total number of 23 382 degrees of freedom had to be used by Castaings and Lowe, leading to very high computational costs. Using the dashpot approximation in the SBFEM formulation, only the plate has to be discretized with one line element. For the frequency range presented by Castaings and Lowe (0...0.4 MHz), a one-dimensional element of order 4 (5 nodes, cf. Figure 6.2) is sufficient to obtain converged results. Hence, the total number of degrees of freedom required to compute the Lamb-type modes as well as the shear-horizontal modes is 15.

Results are presented in Figure 6.5 and compared with the results by Castaings and Lowe. Both approaches are in very good agreement. For the attenuations, small deviations of about 1%...2% can be observed, which are caused by the one-dimensional approximation of the dashpot boundary condition. However, for practical applications these deviations of the attenuations are negligible. The phase velocities are obtained very accurately. For very low frequencies, no results are presented in [152]. Generally, when using an absorbing region, computations in the low frequency range become cumbersome, since the size of the absorbing region tends towards infinity. In the proposed SBFEM approach, the computation for arbitrary frequencies is straightforward. A more detailed discussion will be presented in the following subsection.

It should be noted that the immense reduction of degrees of freedom compared to the approach presented in the literature is due to several reasons:

²⁵I. e. a constant imaginary part of the shear modulus that represents the physical property of material damping - in contrast to the space-dependent damping that is introduced to simulate the behavior of an infinite domain.

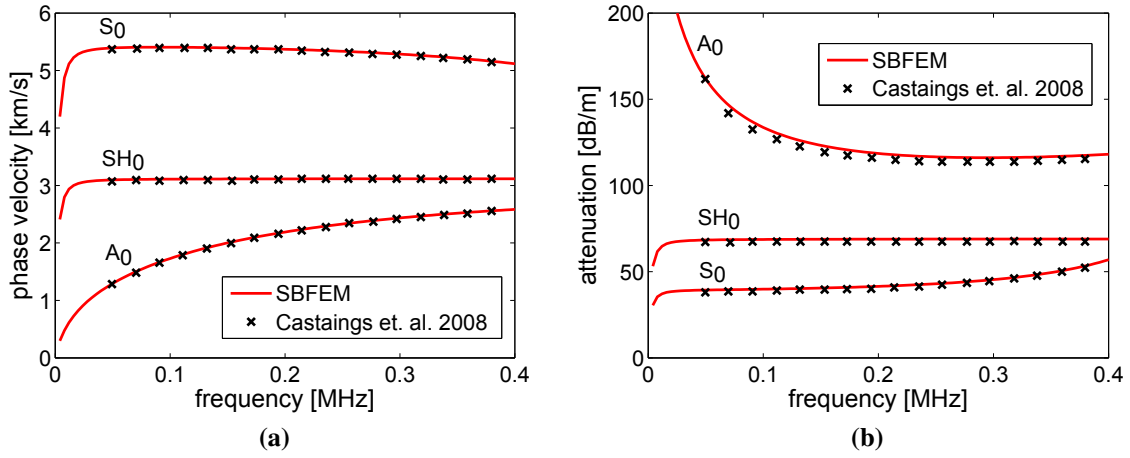


Figure 6.5: (a) Phase velocities and (b) attenuations of the fundamental symmetric (S_0), anti-symmetric (A_0) and shear-horizontal (SH_0) modes in an aluminum plate attached to an infinite elastomer. Dispersion curves are obtained with the proposed SBFEM approach (—) and compared with results presented by Castaings and Lowe [152] (\times).

- First of all, in the current work only the through-thickness direction of the plate is discretized rather than a two-dimensional section.
- Second, only the waveguide has to be discretized, while the surrounding medium is replaced by a boundary condition.
- Third, a uniform mesh was used by Castaings and Lowe for the whole structure, though the size of the elements representing the aluminum plate can be increased by approximately a factor 6 compared to the elastomer, according to the higher wave velocity.
- Finally, in the current work one higher-order element has been employed to discretize the plate rather than using several quadratic elements. As has been demonstrated by previous examples this leads to a significant reduction of the number of degrees of freedom.

6.2.2 Varying acoustic impedances

The influence of a surrounding medium on the propagating modes strongly depends on the material properties of this medium relative to the waveguide's material. If the materials are very different, most of the acoustic wave energy inherent in the guided waves will be reflected from the waveguide's surface. Hence, the damping effect of the surrounding medium will be small. On the other hand, if the material parameters become very similar, the reflection coefficient at the waveguide's surface tends towards zero and the structure cannot be assumed to represent a waveguide anymore. It is important to analyze the reliability of the different approaches for varying materials. To estimate the effect of the surrounding medium, the ratio R_c of the acoustic

impedances

$$R_c = \frac{c_s \rho}{\tilde{c}_s \tilde{\rho}} = \sqrt{\frac{G \rho}{\tilde{G} \tilde{\rho}}} \quad (6.40)$$

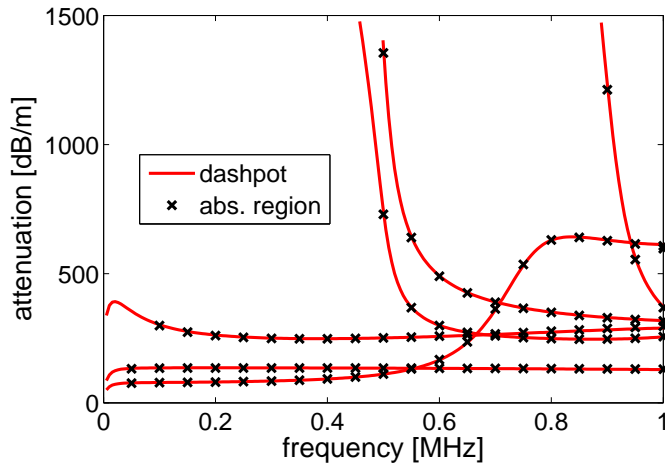
can be used as a helpful parameter. The shear wave velocities of the materials have been used here. The ratio of longitudinal wave velocities will be different, if the Poisson's ratio is different for the two materials. It is expected that the influence of the surrounding medium becomes smaller as R_c increases. To demonstrate this, a simple embedded waveguide has been modeled several times with varying material parameters of the surrounding medium. Again, the example consists of a homogeneous plate with one surface being attached to an infinite medium. Results for axisymmetric structures are very similar and will be omitted. For simplicity, the parameters of the waveguide's material are chosen to be $G = 1 \text{ GPa}$, $\rho = 1000 \text{ kg/m}^3$, $\nu = 1/3$. The plate thickness is 1 mm and frequencies up to 1 MHz have been considered. The surrounding medium is assumed to have the same density and Poisson's ratio as the waveguide. Its acoustic impedance is modified by varying the shear modulus. A constant imaginary part $G_i = 0.1 G_r$ has been incorporated in the shear modulus as in the previous subsection. This additional material damping facilitates the application of the absorbing region while the results are not affected significantly. For the given frequency range, one element of order 7 (8 nodes) is sufficient to discretize the plate's cross-section. Consequently, using the SBFEM approach an eigenvalue problem of the dimension 48×48 is solved at each frequency. The solutions have been obtained using the function `eig` in *Matlab*. The computational time to evaluate the set of solutions at 20 frequencies is only about 0.1 s on a desktop PC (Intel Quad CPU Q8400 @2.66 GHz, 4GB RAM).

For comparison, the same structures have been modeled using an absorbing region. All parameters can be found in Table 6.1. The size of the absorbing region has been estimated as summarized in Section 6.1.4. In order to do so, the minimal phase velocity $\min(c_p)$ of a mode in the waveguide has been estimated from the solution of the waveguide with free surfaces. However, the phase velocity of the A_0 mode tends to zero for $\omega \rightarrow 0$. Considering Equation (6.36), the required size of the absorbing region tends to infinity for $\min(c_p) \rightarrow \tilde{c}_l$. To obtain realistic results, the minimal phase velocity of interest has been set to $\min(c_p) = 1.2 \tilde{c}_l$. The size of the absorbing region has been evaluated at the frequency f_{\min} , where the phase velocity of the A_0 mode reaches this value. Consequently, for frequencies below f_{\min} this approach is not reliable. In Table 6.1, 'DOF' denotes the total number of degrees of freedom that are required. The number of nodes increases with the size of the discretized domain and decreases with the wave velocities. Consequently, the computational times become larger for increasing values of R_c . When using the absorbing region, the computational times are at least several hundred times larger compared to the dashpot approach.

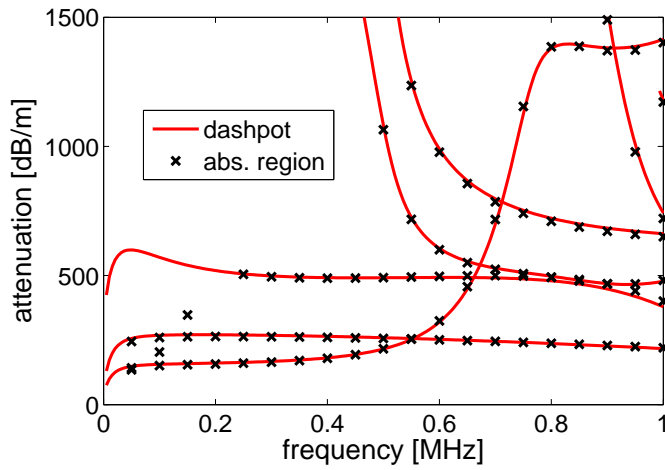
Table 6.1: Numerical study to analyze the effect of varying acoustic impedances of the surrounding medium on a waveguide. Results have been obtained with the dashpot boundary and compared with an alternative approach utilizing an absorbing region.

R_c	\tilde{c}_s [km/s]	\tilde{c}_l [km/s]	$\min(c_p)$ [km/s]	Absorbing region				Dashpot			
				f_{\min} [MHz]	d_a [mm]	DOF	t_c [s]	DOF	t_c [s]	Δ_c [%]	Δ_a [%]
8	0.125	0.250	0.3	0.040	23	1161	1645			0.2	2.1
6	1.667	0.333	0.4	0.065	19	741	484			0.3	2.8
4	0.250	0.500	0.6	0.160	11	519	188	24	0.1	0.4	5.3
3	0.333	0.667	0.8	0.400	6	237	27			1.2	7.6
2	0.500	1.000	1.2	∞	143	1521	4001			8.0	≈ 50

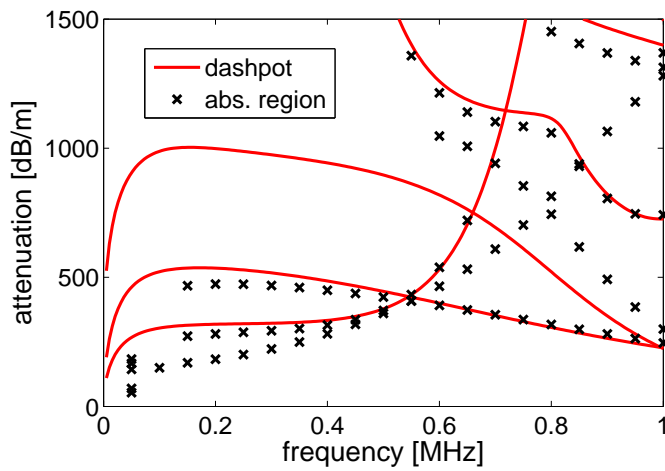
The results have been compared with the proposed approach utilizing the dashpot boundary condition. The maximum relative deviations of the phase velocities and attenuations between both approaches are denoted by Δ_c and Δ_a , respectively. Examples are presented in Figure 6.6. Only the attenuations are plotted as the phase velocities are always obtained with higher accuracy. For large values of R_c , both approaches are in very good agreement. It should be noted that for most practical applications (e. g. steel in water, timber in soil) R_c is still much larger than the values considered here. For smaller values of R_c the deviations between both approaches become larger. Also the minimum frequency, where the absorbing region leads to reliable results increases. Still, even for $R_c = 3$ the maximum deviation in phase velocities is 1.2% and the attenuations differ by no more than 7.6%. For $R_c = 2$ the phase velocity of the A_0 mode is always smaller than the longitudinal wave velocity in the surrounding medium. Consequently, the minimum frequency cannot be reached. Arbitrarily a discretization using 500 nodes for the surrounding medium has been chosen, leading to an absorbing region with a thickness of 143 mm. It has been tested that this discretization leads to converged results. For this extreme case, the deviations between both approaches become significant (Figure 6.6c). However, if the materials are that similar, it is usually not appropriate to model the structure as an embedded waveguide.



(a) $R_c = 8$



(b) $R_c = 4$



(c) $R_c = 2$

Figure 6.6: Attenuation of the propagating modes in a plate attached to an infinite medium, computed using a dashpot boundary condition (—) and an absorbing region (×). Results are presented for different ratios R_c of acoustic impedances: (a) $R_c = 8$; (b) $R_c = 4$; (c) $R_c = 2$.

soil can be assumed to be isotropic with the material parameters

$$\tilde{G} = 0.04 \text{ GPa} \quad \tilde{\rho} = 1500 \text{ kg m}^{-3} \quad \tilde{\nu} = 0.3$$

Again, dispersion curves have been computed using the proposed dashpot boundary and compared with results obtained by utilizing an absorbing region. For both approaches, one element of order 7 has been used to discretize the pole. Using the absorbing region, a total thickness of the surrounding medium of 850 mm leads to converged results for frequencies above 2 kHz. For frequencies up to 10 kHz one element of order 250 has been used to obtain accurate results. The phase velocities and attenuations of the longitudinal and first order flexural modes are presented in Figure 6.8. The results obtained with both approaches are in very good agreement, showing that the dashpot boundary condition leads to a very good approximation for this practical application.

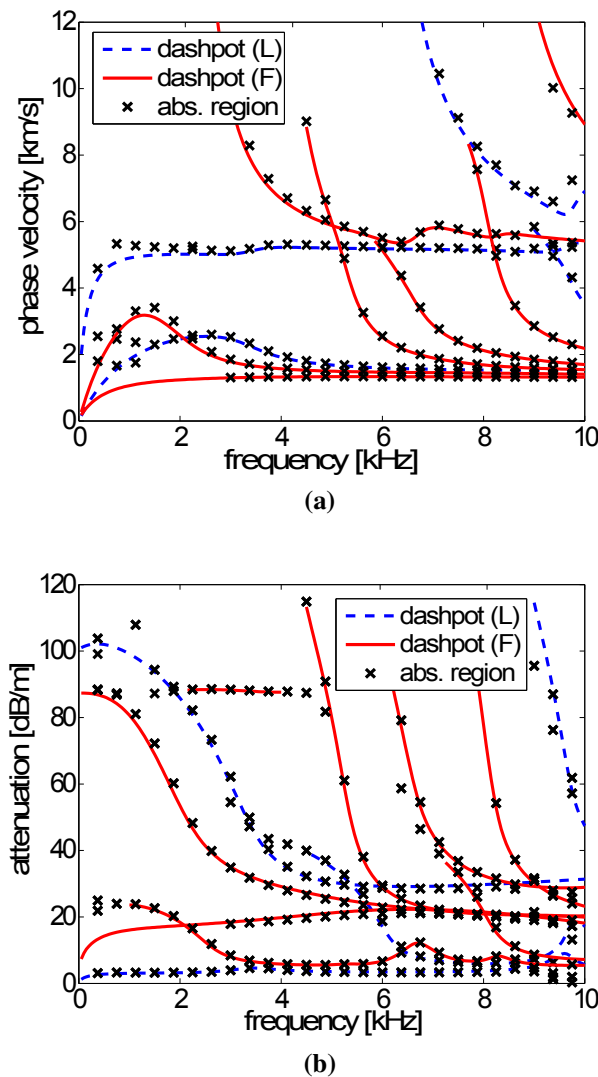


Figure 6.8: (a) Phase velocities and (b) attenuations of longitudinal (---) and flexural (—) modes in an embedded timber pole, obtained using the proposed dashpot boundary condition. Results have been verified using the authors' implementation of an absorbing region (×).

Chapter 7

Novel solution procedure

While the algorithms presented in the previous chapters offer generally highly efficient and reliable ways to compute dispersion curves for many different applications, it can sometimes be worthwhile to further improve efficiency by considering the specific requirements of the set-up.

This chapter focuses on an algorithm developed for a measurement system that utilizes guided waves for material characterization [36, 274–276]. In this particular application, dispersion curves have to be computed for a large frequency range. As the computation has to be performed many times with varying material parameters, the efficiency of the algorithm is crucial. The current measurement set-up utilizes guided waves in hollow cylinders, so that the axisymmetric formulation as described in Chapter 5 applies. A novel solution procedure is proposed in order to significantly increase its computational efficiency. Details have also been published in [100]. Similar to many other applications of guided waves, only few modes can actually be excited at each frequency, due to the geometrical characteristics of the excitation. In the proposed approach, only the modes of interest are computed, rather than solving for the complete set of solutions at each frequency. This is done by tracing the selected modes and computing the required solutions using the concept of inverse iteration [277, 278]. The current formulation focuses on homogeneous axisymmetric waveguides with isotropic or orthotropic material behavior. However, the proposed algorithm can easily be adopted to include more general waveguides.

7.1 Background

7.1.1 Motivation

The proposed algorithm is utilized in the context of ultrasonic material characterization of cylindrical waveguides as presented in [36, 276, 279]. The experimental set-up (Figure 7.1a) consists of an ultrasonic transmitter, a hollow cylindrical waveguide and an ultrasonic receiver. Measurements are performed in transmission between the parallel faces. Figure 7.1b shows an example for the pulse excited by the transmitter and the resulting signal at the receiver. A plane-wave approximation yields a first estimation of the material parameters. The estimated values are

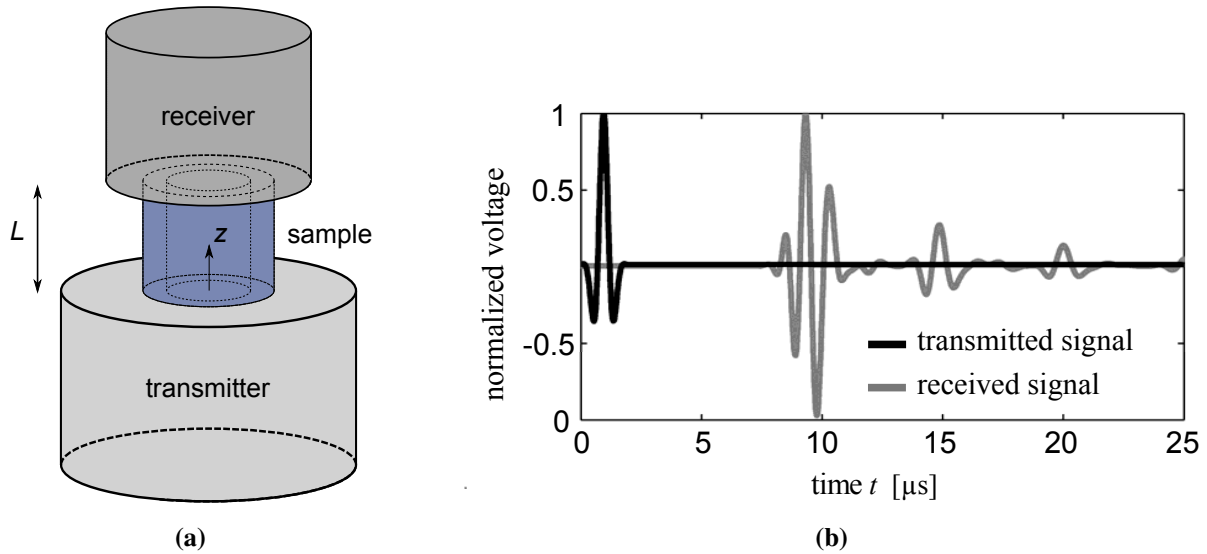


Figure 7.1: (a) Experimental set-up for the material characterization of cylindrical waveguides and (b) example of a measured signal.

used to initialize an inverse approach. Using an optimization algorithm, the material parameters of the waveguide are modified until the simulated and measured signals are consistent. As the simulation of the waveguide's dispersive behavior has to be performed in every iteration of the optimization process, an efficient and numerically stable waveguide model is desired.

To increase efficiency, we first have a closer look at the required waveguide modes to be computed. Due to the spatially homogeneous excitation on the cylinder's cross-section, only longitudinal modes are propagating through the sample. If we model a plane excitation of normal tractions on the cylinder's cross-section using a least-squares approach [36, 276] and considering the reciprocity theorem [53, 280], we obtain the modal amplitude of each mode at a given frequency. Figure 7.2 shows typical results that have been computed at the University of Paderborn [36, 276]. A polymeric waveguide consisting of natural polypropylene (PPN) with a longitudinal wave velocity of $c_l = 2.7$ km/s and a Poisson's ratio of $\nu = 0.35$ is analyzed. The inner and outer radius in this example is chosen as 3 mm and 9 mm, respectively. Due to the symmetric and normal excitation, only modes with a phase velocity close to c_l propagate in the waveguide. Additionally, the spectral range of the transmitter defines the frequency range of interest. It is interesting to note that only every second mode has a significant amplitude. This is due to the fact that the tractions are constant over the cross-section and hence lead to an excitation of modes with (quasi-)symmetric mode shapes.²⁶ This prior knowledge of the waveguide modes that can be excited using the given experimental set-up, will be utilized to

²⁶This is similar to the symmetric and antisymmetric Lamb wave modes in a plate, which will be discussed in more detail in Chapter 8. Contrary to plate waves, the modes in an axisymmetric waveguide do not show exact symmetric or antisymmetric behavior. In Figure 7.2, the fundamental mode $L(0,0)$, which is quasi-antisymmetric, shows a significant amplitude at low frequencies. This is simply because no other propagating modes exist for very low frequencies and hence the relative excitability for this mode becomes large.

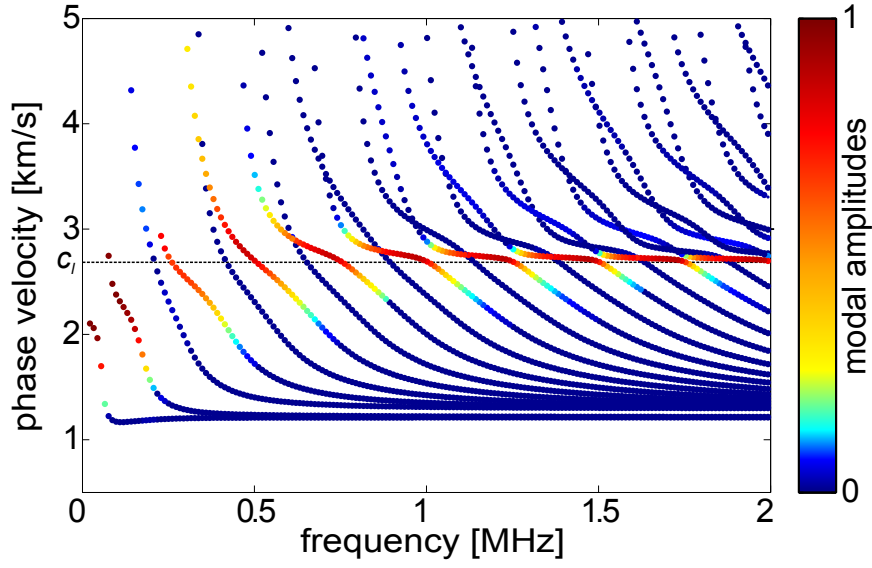


Figure 7.2: Normalized modal amplitudes of the longitudinal modes in a hollow PPN cylinder.

develop an efficient algorithm for computing the dispersive behavior of a cylindrical waveguide.

7.1.2 Fundamental equations

We are focusing on longitudinal modes, so that the displacement field is always considered as axisymmetric. Hence, we can employ the simplified formulation as described in Section 5.3.1, where two degrees of freedom are assigned to each node of the one-dimensional discretization. We allow isotropic as well as transversely isotropic and orthotropic material behavior. Consequently, the elasticity matrix \mathbf{D} for the case of longitudinal modes is of the form

$$\mathbf{D} = \begin{bmatrix} D_{11} & D_{12} & D_{13} & 0 \\ & D_{22} & D_{23} & 0 \\ \text{sym.} & & D_{33} & 0 \\ & & & D_{44} \end{bmatrix} \quad (7.1)$$

Particularly, for an isotropic material the elasticity matrix reads

$$\mathbf{D}_{\text{isotr.}} = \frac{2G}{(1-2\nu)} \begin{bmatrix} 1-\nu & \nu & \nu & 0 \\ & 1-\nu & \nu & 0 \\ \text{sym.} & & 1-\nu & 0 \\ & & & \frac{1-2\nu}{2} \end{bmatrix} \quad (7.2)$$

By substituting the expressions for the shear and longitudinal wave velocities in an infinite isotropic material

$$c_s = \sqrt{\frac{G}{\rho}} \quad (7.3a)$$

$$c_l = \sqrt{\frac{2(1-\nu)G}{(1-2\nu)\rho}} \quad (7.3b)$$

we can write

$$\mathbf{D}_{\text{isotr.}} = \begin{bmatrix} \rho c_l^2 & \frac{2G\nu}{(1-2\nu)} & \frac{2G\nu}{(1-2\nu)} & 0 \\ & \rho c_l^2 & \frac{2G\nu}{(1-2\nu)} & 0 \\ \text{sym.} & & \rho c_l^2 & 0 \\ & & & \rho c_s^2 \end{bmatrix} \quad (7.4)$$

To simplify notations in case of anisotropic material behavior, we define more generally

$$c_l = \sqrt{\frac{D_{33}}{\rho}} \quad (7.5)$$

$$c_s = \sqrt{\frac{D_{44}}{\rho}} \quad (7.6)$$

With these definitions, the relationship

$$\mathbf{b}_1^T \mathbf{D} \mathbf{b}_1 = \begin{bmatrix} 0 & 0 & 0 & 1 \\ 0 & 0 & 1 & 0 \end{bmatrix} \begin{bmatrix} D_{11} & D_{12} & D_{13} & 0 \\ & D_{22} & D_{23} & 0 \\ \text{sym.} & & \rho c_l^2 & 0 \\ & & & \rho c_s^2 \end{bmatrix} \begin{bmatrix} 0 & 0 \\ 0 & 0 \\ 0 & 1 \\ 1 & 0 \end{bmatrix} = \rho \begin{bmatrix} c_s^2 & \\ & c_l^2 \end{bmatrix} \quad (7.7)$$

holds as long as the elasticity matrix is of the form (7.1). Since we apply the concept of spectral elements (Section 3.2), the matrices \mathbf{E}_0 and \mathbf{M}_0 are diagonal, and the non-zero submatrices, relating nodes i and j are given as (cf. Equations (3.47))

$$\mathbf{E}_{0ij} = \delta_{ij} w_i \mathbf{b}_1^T \mathbf{D} \mathbf{b}_1 |J(\eta_i)| = \delta_{ij} w_i |J(\eta_i)| \rho \begin{bmatrix} c_s^2 & \\ & c_l^2 \end{bmatrix} \quad (7.8)$$

$$\mathbf{M}_{0ij} = \delta_{ij} w_i \rho \mathbf{I}_2 |J(\eta_i)| = \delta_{ij} w_i |J(\eta_i)| \rho \begin{bmatrix} 1 & \\ & 1 \end{bmatrix} \quad (7.9)$$

7.2 Solution procedure

The algorithm developed in this chapter involves four major steps, which are described in the following subsections. First, since we will always compute eigenvalues close to a given solution, the polynomial eigenvalue problem (3.35) is approximated using a simple Taylor expansion of first order. Second, we compute the frequencies where the phase velocities of the modes of interest equal the longitudinal wave velocity in the given material. Third, these solutions are used as initial values for a mode-tracing procedure, where the wavenumbers at subsequent frequency steps are estimated from previous solutions using a Padé expansion [94, 203]. Fourth, at each frequency step, the estimated eigenvalues are improved by means of inverse iteration [277].

7.2.1 Linear approximation

In this application we are particularly interested in modes with a phase velocity close to the longitudinal wave velocity. In other words, at each frequency we have to compute eigenvalues in the vicinity of a pre-defined value. For the general case let this eigenvalue be denoted by λ_+ . One obvious approach to simplify the computation of solutions in the vicinity of this value is to approximate the quadratic eigenvalue problem (3.35) by means of a first order Taylor expansion around λ_+ :

$$\begin{aligned} & \lambda^2 \mathbf{E}_0 + \lambda (\mathbf{E}_1^T - \mathbf{E}_1) - \mathbf{E}_2 + \omega^2 \mathbf{M}_0 \\ &= \lambda_+^2 \mathbf{E}_0 + \lambda_+ (\mathbf{E}_1^T - \mathbf{E}_1) - \mathbf{E}_2 + \omega^2 \mathbf{M}_0 + (2\lambda_+ \mathbf{E}_0 + \mathbf{E}_1^T - \mathbf{E}_1)(\lambda - \lambda_+) + \mathcal{O}(\lambda^2) \\ &= \lambda (2\lambda_+ \mathbf{E}_0 + \mathbf{E}_1^T - \mathbf{E}_1) - \lambda_+^2 \mathbf{E}_0 - \mathbf{E}_2 + \omega^2 \mathbf{M}_0 + \mathcal{O}(\lambda^2) \end{aligned} \quad (7.10)$$

Substituting this approximation into Equation (3.35) we obtain

$$(\lambda (2\lambda_+ \mathbf{E}_0 + \mathbf{E}_1^T - \mathbf{E}_1) - \lambda_+^2 \mathbf{E}_0 - \mathbf{E}_2 + \omega^2 \mathbf{M}_0) \hat{\mathbf{u}}_n = 0 \quad (7.11)$$

which can be written as a generalized eigenvalue problem for λ :

$$\mathbf{A}_1 \hat{\mathbf{u}}_n = \lambda \mathbf{A}_2 \hat{\mathbf{u}}_n \quad (7.12)$$

with

$$\mathbf{A}_1 = (\lambda_+^2 \mathbf{E}_0 + \mathbf{E}_2 - \omega^2 \mathbf{M}_0) \quad (7.13)$$

$$\mathbf{A}_2 = (2\lambda_+ \mathbf{E}_0 + \mathbf{E}_1^T - \mathbf{E}_1) \quad (7.14)$$

By inversion of \mathbf{A}_2 , Equation (7.12) can be transformed into a standard eigenvalue problem

$$\mathbf{A}_2^{-1} \mathbf{A}_1 \hat{\mathbf{u}}_n = \lambda \hat{\mathbf{u}}_n \quad (7.15)$$

As the size of the eigenvalue problem has been reduced by a factor of two compared to the \mathbf{Z} -matrix in Equation (3.39), it can be solved several times faster, depending on the employed algorithm. Note that we could also solve the generalized eigenvalue problem (7.12) directly

(for instance, the `eig` function in *Matlab* can handle both standard and generalized eigenvalue problems). Nevertheless, the solution of the standard eigenvalue problem is much faster, even taking into account the computational time for the inversion of \mathbf{A}_2 . As an example, Figure 7.3 shows results that have been computed using this approximation in comparison with solutions obtained from Equation (3.42). The material parameters for PPN are chosen as defined in Section 7.1.1. Phase velocities c_p have been computed in the vicinity of $c_p \approx c_l$ by substituting $\lambda_+(\omega) = i\omega/c_l$. As can be seen from this example, the linear approximation leads to accurate results close to λ_+ . It can be employed in this form if the range of relevant phase velocities is very small. Comparing Figure 7.3 with Figure 7.2 shows that this approximation does not suffice to accurately compute all modes that have a significant modal weight. However, the generalized eigenvalue problem (7.12) that has been derived using this approximation will be an essential step to simplify the inverse iteration.

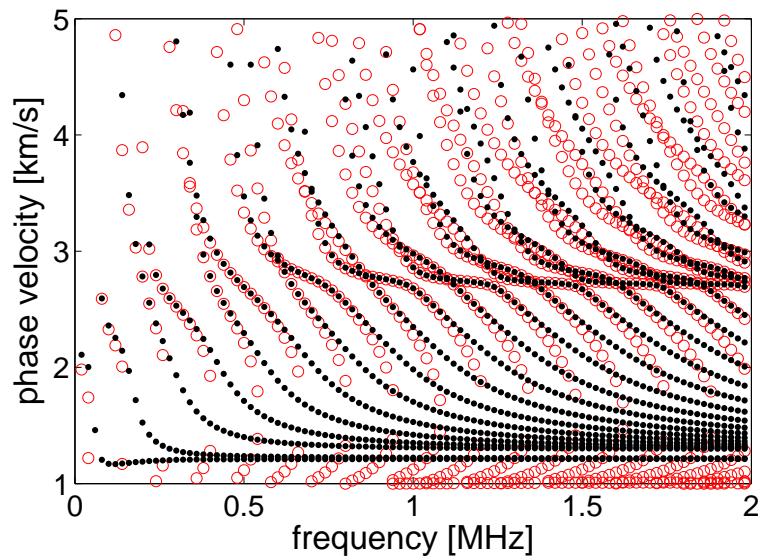


Figure 7.3: Phase velocities of propagating modes in a hollow PPN cylinder, computed using the \mathbf{Z} -matrix (\bullet) and the linear approximation (\circ).

7.2.2 Initial values

The second step of the proposed solution procedure is to compute starting points to initialize the mode-tracing. These initial values are obtained by computing the frequencies of all modes where the phase velocities equal the longitudinal wave velocity c_l . The corresponding eigenvalues and frequencies are denoted by λ_0 and ω_0 , respectively. Starting from these values, the modes can be traced in direction of both increasing and decreasing frequency to obtain all solutions in the frequency range of interest. Choosing these particular starting points is advantageous for two additional reasons: First, the solutions are generally well separated (see Figure

7.2), which facilitates the first steps of the mode-tracing algorithm. Second, for $c_p = c_l$ the eigenvalue problem can be simplified, as will be demonstrated in this subsection.

The computation of the initial values only has to be performed once to obtain the dispersion curves for a given structure. However, it has to be done with the discretization that is required for the highest frequency of interest. For this reason it causes computational costs of the same order as the sum of the other parts of the algorithm. Thus it is worthwhile to have a closer look at this problem. We rewrite the polynomial eigenvalue problem (3.35) in terms of frequencies by applying

$$\lambda_0 = \frac{i\omega_0}{c_l} =: \frac{\tilde{\omega}}{c_l} \quad (7.16)$$

where the imaginary frequencies $\tilde{\omega} = i\omega_0$ have been defined for convenience. The polynomial eigenvalue problem for the frequencies yields

$$\left(\tilde{\omega}^2 \left(\frac{1}{c_l^2} \mathbf{E}_0 - \mathbf{M}_0 \right) + \frac{\tilde{\omega}}{c_l} (\mathbf{E}_1^T - \mathbf{E}_1) - \mathbf{E}_2 \right) \hat{\mathbf{u}}_n = 0 \quad (7.17)$$

After left multiplication with $c_l^2 \mathbf{E}_0^{-1}$ we obtain

$$\left(\tilde{\omega}^2 (\mathbf{I} - c_l^2 \mathbf{E}_0^{-1} \mathbf{M}_0) + \tilde{\omega} c_l \mathbf{E}_0^{-1} (\mathbf{E}_1^T - \mathbf{E}_1) - c_l^2 \mathbf{E}_0^{-1} \mathbf{E}_2 \right) \hat{\mathbf{u}}_n = 0 \quad (7.18)$$

From Equations (7.8) and (7.9) it follows immediately that

$$\mathbf{E}_0^{-1} \mathbf{M}_0 = \begin{bmatrix} 1/c_s^2 & & & & \\ & 1/c_l^2 & & & \\ & & 1/c_s^2 & & \\ & & & 1/c_l^2 & \\ & & & & \ddots \end{bmatrix} \quad (7.19)$$

so that the first term of Equation (7.18) can be simplified as

$$(\mathbf{I} - c_l^2 \mathbf{E}_0^{-1} \mathbf{M}_0) = \left(1 - \frac{c_l^2}{c_s^2} \right) \begin{bmatrix} 1 & & & & \\ & 0 & & & \\ & & 1 & & \\ & & & 0 & \\ & & & & \ddots \end{bmatrix} \quad (7.20)$$

In order to facilitate the following steps, we re-arrange the degrees of freedom by separating the displacement components in r - and z -direction. We define

$$\bar{\mathbf{u}} = [\mathbf{u}_r \ \mathbf{u}_z]^T = [u_{r1} \ u_{r2} \ \dots \ u_{z1} \ u_{z1}]^T \quad (7.21)$$

We re-arrange the rows and columns of the coefficient matrices accordingly and denote the modified matrices by $\bar{\mathbf{M}}_0$, $\bar{\mathbf{E}}_0$, $\bar{\mathbf{E}}_1$ $\bar{\mathbf{E}}_2$. As a consequence, Equation (7.20) is transformed into

$$(\mathbf{I} - c_l^2 \bar{\mathbf{E}}_0^{-1} \bar{\mathbf{M}}_0) = \left(1 - \frac{c_l^2}{c_s^2}\right) \begin{bmatrix} \mathbf{I}_n & \\ & 0 \end{bmatrix} \quad (7.22)$$

where n is the number of nodes and \mathbf{I}_n is the $n \times n$ identity matrix. Considering Equation (7.22), the polynomial eigenvalue problem (7.18) can be written as

$$\left(\tilde{\omega}^2 \mathbf{C} + \tilde{\omega} \mathbf{B} - \mathbf{A}\right) \bar{\mathbf{u}} = 0 \quad (7.23)$$

with

$$\mathbf{C} = \begin{bmatrix} \mathbf{I}_n & \\ & 0 \end{bmatrix} \quad (7.24)$$

$$\mathbf{B} = \frac{c_l}{1 - c_l^2/c_s^2} \bar{\mathbf{E}}_0^{-1} (\bar{\mathbf{E}}_1^T - \bar{\mathbf{E}}_1) \quad (7.25)$$

$$\mathbf{A} = \frac{c_l^2}{1 - c_l^2/c_s^2} \bar{\mathbf{E}}_0^{-1} \bar{\mathbf{E}}_2 \quad (7.26)$$

Using classical linearization [281,282], Equation (7.23) is transformed into a generalized eigenvalue problem, yielding

$$\tilde{\omega} \begin{bmatrix} \mathbf{B} & \mathbf{C} \\ \mathbf{I}_{2n} & 0 \end{bmatrix} \begin{Bmatrix} \bar{\mathbf{u}} \\ \tilde{\omega} \bar{\mathbf{u}} \end{Bmatrix} = \begin{bmatrix} \mathbf{A} & 0 \\ 0 & \mathbf{I}_{2n} \end{bmatrix} \begin{Bmatrix} \bar{\mathbf{u}} \\ \tilde{\omega} \bar{\mathbf{u}} \end{Bmatrix} \quad (7.27)$$

Considering the displacement components

$$\tilde{\omega} \begin{bmatrix} \mathbf{B}_{rr} & \mathbf{B}_{rz} & \mathbf{I}_n & 0 \\ \mathbf{B}_{zr} & \mathbf{B}_{zz} & 0 & 0 \\ \mathbf{I}_n & 0 & 0 & 0 \\ 0 & \mathbf{I}_n & 0 & 0 \end{bmatrix} \begin{Bmatrix} \mathbf{u}_r \\ \mathbf{u}_z \\ \tilde{\omega} \mathbf{u}_r \\ \tilde{\omega} \mathbf{u}_z \end{Bmatrix} = \begin{bmatrix} \mathbf{A}_{rr} & \mathbf{A}_{rz} & 0 & 0 \\ \mathbf{A}_{zr} & \mathbf{A}_{zz} & 0 & 0 \\ 0 & 0 & \mathbf{I}_n & 0 \\ 0 & 0 & 0 & \mathbf{I}_n \end{bmatrix} \begin{Bmatrix} \mathbf{u}_r \\ \mathbf{u}_z \\ \tilde{\omega} \mathbf{u}_r \\ \tilde{\omega} \mathbf{u}_z \end{Bmatrix} \quad (7.28)$$

it is obvious that the last set of equations is decoupled from the others and can be neglected.²⁷ Hence we can write

$$\tilde{\omega} \begin{bmatrix} \mathbf{B} & \mathbf{I}_n \\ \mathbf{I}_n & 0 \end{bmatrix} \begin{Bmatrix} \mathbf{u}_r \\ \mathbf{u}_z \\ \tilde{\omega} \mathbf{u}_r \end{Bmatrix} = \begin{bmatrix} \mathbf{A} & 0 \\ 0 & 0 & \mathbf{I}_n \end{bmatrix} \begin{Bmatrix} \mathbf{u}_r \\ \mathbf{u}_z \\ \tilde{\omega} \mathbf{u}_r \end{Bmatrix} \quad (7.29)$$

²⁷Note that this is a consequence of Equation (7.20) and hence originates in the choice $c_p = c_l$. If any other value for c_p was chosen to compute the initial values, this simplification would not apply.

To improve computational efficiency, it is desirable to transform this generalized eigenvalue problem into a standard eigenvalue problem. Generally, this can be done by inverting either one of the matrices in Equation (7.29). However, both matrices are (close to) singular. The matrix on the right hand side is singular due to the singularities of \mathbf{E}_2 . It is well understood that these singularities are caused by rigid body motions (see Section 3.3.1). Note that due to the structure of this matrix, we only have to compute the inverse of \mathbf{A} . In order to do that, we can transform \mathbf{A} into a non-singular matrix by adding small real numbers to its diagonal. An adequate choice is to add a multiple of the non-singular diagonal matrix \mathbf{E}_0 . This results in an approximation for \mathbf{A} that can be inverted using standard algorithms. We define the inverse of this matrix as

$$\hat{\mathbf{A}} = (\mathbf{A} + \kappa \mathbf{E}_0 \|\mathbf{E}_2\|_{\max})^{-1} \quad (7.30)$$

Multiplication with the max norm $\|\mathbf{E}_2\|_{\max}$ (largest absolute value of \mathbf{E}_2) ensures the condition number of $\hat{\mathbf{A}}$ to be of approximately the same order, irrespective of the number of nodes. κ is a small real number. A value of $\kappa = 10^{-8}$ has been chosen for the current application.²⁸ Note that $\hat{\mathbf{A}}$ is symmetric, because \mathbf{E}_0 and \mathbf{E}_2 are both symmetric:

$$\hat{\mathbf{A}} = \begin{bmatrix} \hat{\mathbf{A}}_{11} & \hat{\mathbf{A}}_{12} \\ \hat{\mathbf{A}}_{12} & \hat{\mathbf{A}}_{22} \end{bmatrix} \quad (7.31)$$

Equation (7.29) can be re-written as

$$\tilde{\omega} \begin{bmatrix} \hat{\mathbf{A}} & 0 \\ 0 & 0 \end{bmatrix} \begin{bmatrix} \mathbf{B} & \mathbf{I}_n \\ \mathbf{I}_n & 0 \end{bmatrix} \begin{Bmatrix} \mathbf{u}_r \\ \mathbf{u}_z \\ \tilde{\omega} \mathbf{u}_r \end{Bmatrix} = \begin{Bmatrix} \mathbf{u}_r \\ \mathbf{u}_z \\ \tilde{\omega} \mathbf{u}_r \end{Bmatrix} \quad (7.32)$$

or

$$\begin{bmatrix} \hat{\mathbf{A}}\mathbf{B} & \hat{\mathbf{A}}_{11} \\ \mathbf{I}_n & 0 \end{bmatrix} \begin{Bmatrix} \mathbf{u}_r \\ \mathbf{u}_z \\ \tilde{\omega} \mathbf{u}_r \end{Bmatrix} = \frac{1}{\tilde{\omega}} \begin{Bmatrix} \mathbf{u}_r \\ \mathbf{u}_z \\ \tilde{\omega} \mathbf{u}_r \end{Bmatrix} \quad (7.33)$$

From (7.33), the eigenvalues $1/\tilde{\omega}$ can be computed using standard solvers. All eigenvalues are purely imaginary (i.e. all frequencies ω_0 are real). As the solutions are obtained from a quadratic eigenvalue problem, the negative of each eigenvalue is an eigenvalue as well. Solutions are selected within the desired frequency range. The discretization of the cross-section has to be chosen fine enough in order to lead to accurate results at the highest frequency of interest (see Section 5.6).

²⁸This leads to the condition number of $\hat{\mathbf{A}}$ being roughly of order 10^9 , which is small enough to avoid significant numerical errors in the inversion. On the other hand, this value for κ ensures that the modification of \mathbf{A} does not lead to a relevant change in the resulting eigenvalues.

7.2.3 Mode-tracing

Starting from the initial values, each mode is traced separately in positive as well as negative direction for the pre-defined frequency range. Let ω_0 and λ_0 be the initial values of one particular mode, and c_{g0} its group velocity, computed using Equation (3.70). We obtain an estimation λ_+ of the eigenvalue at the subsequent frequency step, say ω_1 , using a linear approximation:

$$\lambda_+ = \lambda_0 + \frac{i(\omega_1 - \omega_0)}{c_{g0}} \quad (7.34)$$

Improving the estimated value λ_+ by means of inverse iteration (Section 7.2.4) leads to the subsequent eigenvalue λ_1 . The estimation λ_+ is then updated to obtain an approximation for λ_2 . For the following frequency steps, more accurate estimations can be obtained by utilizing a Padé expansion, similarly to the procedure described in Section 4.3. For instance, the third eigenvalue λ_3 is approximated by

$$\lambda_3 \approx \frac{\alpha_0 + \alpha_1 \Delta\omega}{1 + \beta_1 \Delta\omega + \beta_2 \Delta\omega^2} \quad (7.35)$$

with the frequency increment $\Delta\omega = \omega_3 - \omega_2$ and the Padé coefficients $\alpha_0, \alpha_1, \beta_1, \beta_2$ as defined in Equations (4.31). In contrast to Section 4.3, the frequency increment will typically not be constant. This is because the frequencies of the initial values are obtained from Equation (7.33) (and thus are not known a priori), while the subsequent solutions are typically desired at pre-defined frequency steps. For varying frequency increments, the parameters $\gamma_0, \gamma_1, \gamma_2, \gamma_3$ read

$$\gamma_0 = \lambda_2 \quad (7.36a)$$

$$\gamma_1 = \frac{i}{c_{g2}} \quad (7.36b)$$

$$\gamma_2 = \frac{1}{2} \left(\frac{1}{c_{g2}} - \frac{1}{c_{g1}} \right) \frac{i}{\omega_2 - \omega_1} \quad (7.36c)$$

$$\gamma_3 = \frac{1}{6} \left[\frac{c_{g1} - c_{g2}}{(\omega_2 - \omega_1)c_{g1}c_{g2}} - \frac{c_{g0} - c_{g1}}{(\omega_1 - \omega_0)c_{g0}c_{g1}} \right] \frac{2i}{\omega_2 - \omega_1} \quad (7.36d)$$

7.2.4 Inverse iteration

At each frequency step, an accurate solution for the desired eigenvalue is computed, based on the estimated value λ_+ . In contrast to general eigenvalue solvers, where the main difficulty lies in the computation of the complete set of eigenvalues and eigenvectors, we can use a very simple scheme to obtain only one particular eigenvalue that is close to a given estimation. Assume \mathbf{M} is an arbitrary $n \times n$ matrix and $\mathbf{y}^{(0)}$ is a $n \times 1$ vector with random non-zero entries. The so-called *power iteration* [283]

$$\mathbf{y}^{(j+1)} = \mathbf{M}\mathbf{y}^{(j)} \quad j = 0, 1, 2, \dots \quad (7.37)$$

converges towards the eigenvector corresponding to the largest eigenvalue of \mathbf{M} . Generally very few iteration steps are required to obtain converged results while each step involves only one matrix-vector multiplication. This simple approach forms the basis of a number of modern eigenvalue solvers. For this reason, the largest eigenvalues of a matrix can generally be computed very efficiently. We can modify this algorithm to obtain the *inverse iteration* [284]

$$\mathbf{M}\mathbf{y}^{(j+1)} = \mathbf{y}^{(j)} \quad j = 0, 1, 2, \dots \quad (7.38)$$

which converges towards the smallest eigenvalue of \mathbf{M} . Note the difference in terms of the implementation: While the power iteration (7.37) only requires a matrix multiplication, Equation (7.38) implies the solution of a linear system of equations in each step of the iteration (or alternatively the inversion of \mathbf{M} , if \mathbf{M} is non-singular). We can now apply a shift to the matrix \mathbf{M} :

$$(\mathbf{M} - \tau\mathbf{I})\mathbf{y}^{(j+1)} = \mathbf{y}^{(j)} \quad j = 0, 1, 2, \dots \quad (7.39)$$

where τ is an arbitrary scalar. Compared to the matrix \mathbf{M} , the complete spectrum of the matrix $(\mathbf{M} - \tau\mathbf{I})$ is shifted by τ and the iteration (7.39) converges to the eigenvector with the corresponding eigenvalue closest to τ . Hence, if we have an approximation of one particular eigenvalue and apply this approximation as a shift, the inverse iteration can be utilized to accurately compute the eigenvector corresponding to the desired eigenvalue [277].

Since we want to employ this procedure to compute solutions to Equation (7.12), we extend the inverse iteration to include generalized eigenvalue problems. The proof is along the lines of the formulation for standard eigenvalue problems as described in [277]. Details are presented in Appendix A.4. Let $\lambda_+^{(0)}$ be the approximation of one particular eigenvalue, obtained from previous solutions via mode-tracing, and $\mathbf{x}^{(0)}$ is an arbitrary vector. Similar to the case of standard eigenvalue problems we can compute an approximation of the corresponding eigenvector by solving

$$(\mathbf{A}_1 - \lambda_+^{(0)}\mathbf{A}_2)\mathbf{x}^{(1)} = \mathbf{A}_2\mathbf{x}^{(0)} \quad (7.40)$$

The frequency as well as the current estimation for the eigenvalue have to be substituted into \mathbf{A}_1 and \mathbf{A}_2 as defined in Equations (7.13) and (7.14). If the estimation $\lambda_+^{(0)}$ for the eigenvalue is accurate enough²⁹, the solution $\mathbf{x}^{(1)}$ is close to the corresponding eigenvector. The improved solution for the eigenvalue can then be obtained by substituting the computed vector into the generalized eigenvalue problem and solving for the eigenvalue:

$$\mathbf{A}_1\mathbf{x}^{(1)} = \lambda_+^{(1)}\mathbf{A}_2\mathbf{x}^{(1)} \quad (7.41)$$

For instance, in *Matlab* Equation (7.41) can be solved using the backslash operator, which

²⁹Typically, the accuracy of the estimation is sufficient, if no eigenvalue is closer to $\lambda_+^{(0)}$ than the desired one - unless $\mathbf{x}^{(0)}$ is accidentally very close to a different eigenvector.

computes the optimal value for $\lambda_+^{(1)}$ in the least squares sense.³⁰ This leads to significantly faster convergence than the eigenvalue computation described in [277].

The procedure is iterated by replacing $\mathbf{x}^{(0)}$ with the solution for $\mathbf{x}^{(1)}$ and updating the coefficient matrices. Hence, we have the following iteration:

$$(\mathbf{A}_1(\lambda_+^{(j)}) - \lambda_+^{(j)} \mathbf{A}_2(\lambda_+^{(j)}))\mathbf{x}^{(j+1)} = \mathbf{A}_2(\lambda_+^{(j)})\mathbf{x}^{(j)} \quad j = 0, 1, 2, \dots \quad (7.42)$$

$$\mathbf{A}_1(\lambda_+^{(j)})\mathbf{x}^{(j+1)} = \lambda_+^{(j+1)} \mathbf{A}_2(\lambda_+^{(j)})\mathbf{x}^{(j+1)} \quad j = 0, 1, 2, \dots \quad (7.43)$$

Note that the matrices \mathbf{E}_0 and \mathbf{M}_0 are diagonal and hence can be stored as vectors. At each step of the iteration, only the main diagonal of \mathbf{A}_1 and \mathbf{A}_2 has to be modified. For the starting vector $\mathbf{x}^{(0)}$ of the iteration we can choose the eigenvector corresponding to the same mode at the previous frequency step. As the eigenvectors (mode shapes) at two adjacent frequencies are typically very similar, this leads to slightly faster convergence of the iteration and, more importantly, helps to avoid convergence towards an eigenvalue of a different mode. Obviously, the accuracy and convergence rate of this approach depend on the frequency increment and the quality of the eigenvalue estimation. The frequency increment has to be small enough, to ensure that the inverse iteration converges towards the correct eigenvalue. If this is the case, typically two iterations are sufficient to obtain the eigenvalues with a relative error in the order of $10^{-3} \dots 10^{-5}$.

7.3 Details of the implementation

7.3.1 Dimensionless parameters

Again, it is advantageous to compute the dispersion curves in terms of the dimensionless frequency (cf. Section 3.7.1)

$$a = \frac{\omega l}{c_s} \quad (7.44)$$

This is done by using the dimensionless material parameters

$$\bar{\rho} = 1, \quad \bar{l} = 1, \quad \bar{\mathbf{D}} = \mathbf{D}/D_{44}, \quad \bar{r}_i = r_i/l \quad (7.45)$$

As a result we obtain the dimensionless phase velocities

$$\bar{c}_p = c_p/c_s \quad (7.46)$$

³⁰Note that there is no unique solution for $\lambda_+^{(1)}$ until the iteration has converged. To be precise, Equation (7.41) should be written as a system of equations resulting in a different approximation for the eigenvalue for each component of the estimated vector. The most obvious solution is to use the mean value as the approximation of the eigenvalue. However, optimizing the eigenvalue in the least squares sense as done by *Matlab*'s backslash operator results in more reliable convergence. The computational costs for this operation are negligible compared to the solution of the matrix equation (7.40).

Using dimensionless variables, the entries of the coefficient matrices are always of approximately the same order. Each mode is traced for a given range of dimensionless frequencies $[a_0 - a_-, a_0 + a_+]$, where a_0 denotes the initial value for the mode under consideration. The values a_- and a_+ as well as the dimensionless frequency increment Δa can also be kept approximately constant for all considered material properties in this application.

7.3.2 Adaptive meshing

Since the dispersion curves are computed for a large frequency range, the discretization of the cross-section should be refined according to frequency. As detailed in Section 5.6, it is most efficient to discretize a homogeneous waveguide with only one element and increase the element order with frequency (p -refinement). By doing so, the number of equations that have to be solved at each frequency step is reduced to a minimum. However, the coefficient matrices have to be computed for each discretization. In the current implementation, assembling the coefficient matrices can become computationally more expensive than the computation of the few desired eigenvalues at several frequency steps. Hence, the element order is kept constant for each mode, since each mode is only traced over a comparably small frequency range. This also facilitates the implementation of the mode-tracing, as the eigenvector at a previous frequency step can directly be used as a starting vector at the subsequent step, without having to interpolate the displacement amplitudes to the modified nodal coordinates. Based on the results in Section 5.6, we choose the number of nodes n according to the dimensionless frequency as

$$n \approx 4 + 0.5a \quad (7.47)$$

The shape functions \mathbf{N} and their derivatives $\mathbf{N}_{,\eta}$ are computed once for element orders up to $p = 200$ and stored in a separate file.

7.3.3 Parallelization

After the initial values (Section 7.2.2) have been obtained, the computation of each mode is performed independently of the others. Hence, the main part of the algorithm can easily be parallelized by performing the mode-tracing for several modes simultaneously. In the current *Matlab* implementation this is realized by using a *parfor* loop.

7.3.4 The L(0,0) mode

The phase velocity of the zeroth order longitudinal mode is always smaller than the longitudinal wave velocity c_l . Hence, it will not be obtained as a solution to Equation (7.33). In the current application, the computation of this mode is not required, as it cannot be excited within the frequency range of interest. However, if this mode is of relevance, we can trace it starting from

$\omega = 0$, where its wavenumber equals zero and its phase velocity equals the bar speed c_b

$$c_b = \sqrt{\frac{E}{\rho}} \quad (7.48)$$

with the Young's modulus E . We can choose a random vector to initialize the inverse iteration in the first step of the mode-tracing algorithm. Alternatively, we can solve Equation (3.42) once for a low frequency (i. e. with a very small number of degrees of freedom) to obtain initial values for this mode.

7.4 Numerical examples

7.4.1 Natural polypropylene (PPN)

Dispersion curves Dispersion curves have been computed for PPN with the parameters defined in Section 7.1.1. In Figure 7.4 results are presented for frequencies between 0.2 MHz and 1.8 MHz with a step size of 0.02 MHz. Each mode is traced for dimensionless frequency ranges of $a_- = 14$ and $a_+ = 7$ in negative and positive direction, respectively. This range approximately corresponds to the frequencies where the excitability of each mode is significant (cf. Figure 7.2). The computational time for the proposed approach is about 0.5 s on a current notebook PC (Intel i7-2637M CPU 1.7 GHz, 8GB RAM). For validation, the phase velocities are compared to results obtained using an improved implementation of the Global Matrix Method developed at the University of Paderborn [285–287]. In this implementation of the GMM enhanced reliability is achieved by employing an interval-Newton approach in combination with algorithmic differentiation. It leads to similar reliability and accuracy compared with the SBFEM, but the computational times are about 10 minutes to obtain the dispersion curves presented in this example.

Convergence In the proposed approach, the accuracy of the results is mainly affected by two types of errors. On the one hand, discretization errors arise, depending on the element order p and the complexity of the mode shape. This type of error is discussed in Sections 3.8 and 5.6. It has been demonstrated that the utilization of higher-order spectral elements together with p -refinement leads to excellent convergence rates for the present application.

On the other hand, the accuracy of the eigenvalues depends on the number of iterations used in the inverse iteration. For this type of error, convergence is obviously affected by the quality of the estimation $\lambda_+^{(0)}$ and hence by the frequency increment that is employed in the mode-tracing algorithm. As an example, convergence is demonstrated for one particular eigenvalue (Figure 7.5). At a frequency of 1.06 MHz, the mode with the largest phase velocity is selected. The computation of this value is critical due to the adjacency of a different mode. Figure 7.5a shows the estimated values based on the mode-tracing algorithm, for a dimensionless frequency increment Δa of 0.2, 2 and 4. The latter is an extreme case, where the accuracy of the estimation is very poor.

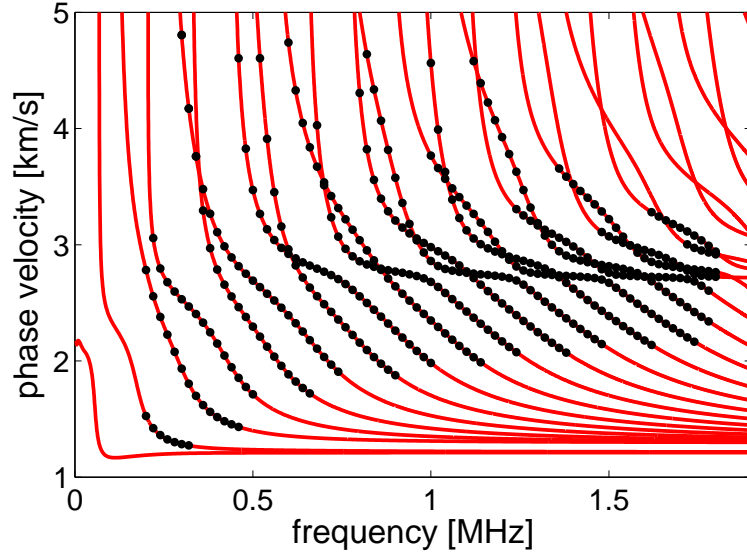


Figure 7.4: Dispersion curves computed with the proposed algorithm (●) and compared to results obtained with the Global Matrix Method (—).

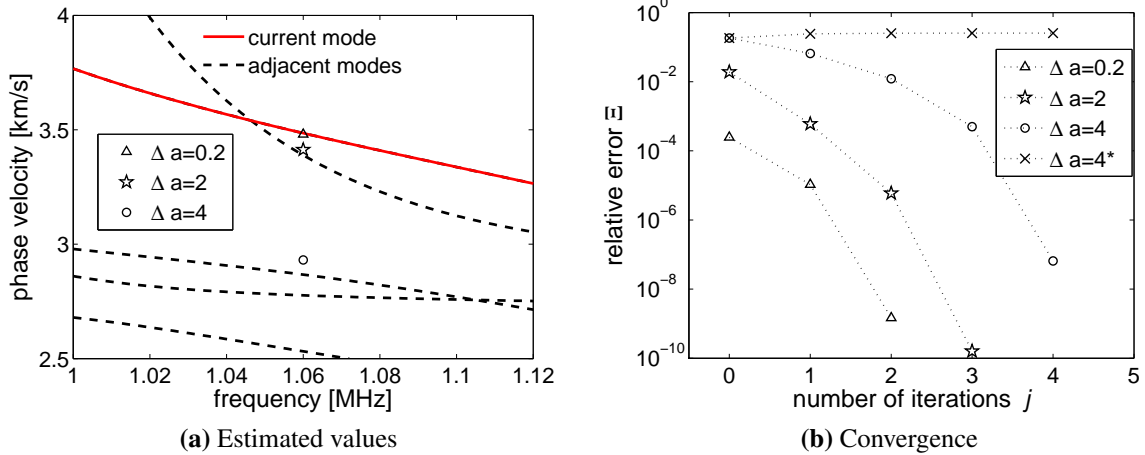


Figure 7.5: (a) Example of estimated phase velocities in the mode-tracing algorithm using different frequency increments: (Δ) 0.2, (\star) 2, (\circ) 4. (b) Convergence of the estimated values towards the desired eigenvalue in the inverse iteration. If the inverse iteration is initialized with a random starting vector (\times), the results tend to converge to a different eigenvalue.

For each of these starting values, the inverse iteration is performed. The relative error $\Xi^{(j)}$ compared to the solutions obtained with an eigenvalue solver is computed for each step of the iteration. Results are presented in Figure 7.5b, showing very fast convergence to the desired eigenvalue. Numerical values are summarized in Table 7.1. We can conclude that for a reasonable dimensionless frequency increment of about 0.1 ... 2.0 (corresponding to dimensioned frequency increments of about 3.5kHz...70kHz in the present example), two iterations are typically sufficient to obtain results with a relative error of order 10^{-3} ... 10^{-5} . It is interesting to note that even for $\Delta a = 4$ results converge to the correct eigenvalue despite the fact that there exist 4 modes with phase velocities closer to the estimated value than the desired mode. This demonstrates the advantage of utilizing the eigenvector of the same mode at a previous frequency step as the starting vector for the iteration. Additional results for $\Delta a = 4$ are plotted in Figure 7.5b using a random vector to initialize the iteration. In that case results usually³¹ converge to one of the two modes that are closest to the initial eigenvalue.

³¹Since the starting vector is random, there is a chance that the iteration still converges towards the desired or any other eigenvalue. Figure 7.5b only shows a typical example.

Table 7.1: Numerical study to test convergence of the inverse iteration for one eigenvalue. The converged value as obtained from an eigenvalue solver is 11.466188389355709i.

iterations		$\Delta a = 0.2$		$\Delta a = 2.0$	
j	$\lambda_+^{(j)}$	$\Xi^{(j)}$	$\lambda_+^{(j)}$	$\Xi^{(j)}$	
0	11.463354550602942i	0.000247147409107	11.684958039461105i	0.019079544367899	
1	11.466309738480760i	0.000010583213961	11.459286380635245i	0.000601944472400	
2	11.466188406145180i	0.00000001464259	11.466256335455268i	0.000005925779104	
3	11.466188389355732i	0.000000000000002	11.466188391186350i	0.00000000159656	
4	11.466188389355747i	0.000000000000003	11.466188389355755i	0.000000000000004	
5	11.466188389355748i	0.000000000000003	11.466188389355739i	0.000000000000003	

iterations		$\Delta a = 4.0$		$\Delta a = 4.0^*$	
j	$\lambda_+^{(j)}$	$\Xi^{(j)}$	$\lambda_+^{(j)}$	$\Xi^{(j)}$	
0	13.576547638310428i	0.184050634552089	13.576547638310428i	0.184050634552089	
1	12.218290644873470i	0.065593048882395	14.248599693107099i	0.242662270082215	
2	11.605610708329149i	0.012159430338932	14.355176932856883i	0.251957184497603	
3	11.460461351093260i	0.000499471844346	14.393490265468426i	0.255298602875755	
4	11.466187639108806i	0.000000065431238	14.393174002843981i	0.255271020682466	
5	11.466188389358267i	0.0000000000000223	14.393175401138297i	0.255271142631824	

** random starting vector*

Efficiency As demonstrated by this example, the proposed approach allows for a highly efficient computation of parts of the dispersion curves. Currently, the proposed algorithms are implemented in *Matlab*. The computational times might vary significantly, if different solvers are utilized. Nevertheless it is worthwhile to compare the computational efficiency of the current implementation to the basic approach presented in the previous chapters, where the complete set of solutions is obtained from the standard eigenvalue problem (3.42) at each frequency. In the current implementation, about 80 % of the computational time is required for solving Equations (7.42) and (7.43). In Figure 7.6 computational times T_{it} are presented to obtain solutions for one mode at a given frequency step, using two iterations. Computations are performed for a varying number of degrees of freedom. For comparison, computational times T_{eig} are presented to solve the eigenvalue problem (3.42) using the *Matlab* function `eig`. Note that T_{eig} is the time to obtain the complete set of solutions while T_{it} is the time required to solve for one mode only.

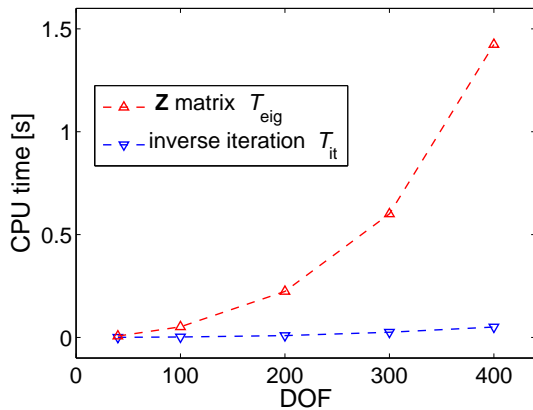


Figure 7.6: Computational time to obtain one eigenvalue using the inverse iteration (∇) compared to solving the full eigenvalue problem (Δ).

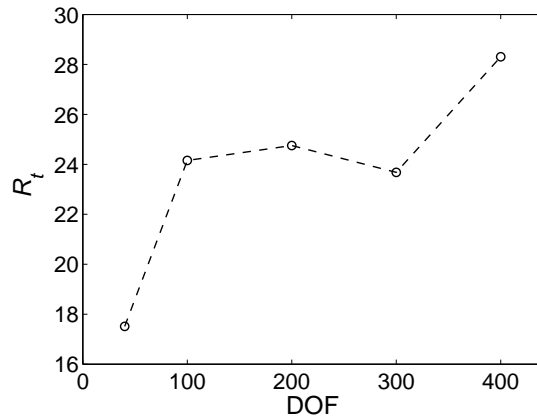


Figure 7.7: Ratio of computational times required for the eigenvalue solver and inverse iteration.

Figure 7.7 shows the ratio $R_t = T_{eig}/T_{it}$ of computational times. This ratio is approximately of the same order irrespective of the number of degrees of freedom. This is expected, since the costs for solving the eigenvalue problem (3.42) and the linear system of equations (7.43) are both roughly of order $\mathcal{O}(n^3)$. As a rule of thumb, the proposed approach is superior, if no more than 20...25 modes have to be computed at each frequency step. For the example presented here, the proposed approach would still be faster if we computed the complete dispersion curves, as the maximum number of propagating modes at the highest frequency of interest is 24. Depending on the application, an additional advantage of the proposed algorithm can lie in the fact that the modes are traced within the computation. Contrary, when using Equation (3.42), the modes have to be traced and sorted separately when required (Section 4.3), increasing computational costs.

7.4.2 Polyphenylene oxide (PPO-GF30)

As a second example dispersion curves for Polyphenylene oxide with 30% glass fiber content (PPO-GF30 [36]) are presented. This composite material shows transversely isotropic behavior. Hence, its elasticity matrix can be defined by five independent parameters:

$$\mathbf{D}_{\text{ti}} = \begin{bmatrix} \frac{1}{E_L} & \frac{\nu_L}{E_L} & \frac{\nu_L}{E_L} & 0 \\ \text{sym.} & \frac{1}{E_T} & \frac{\nu_T}{E_T} & 0 \\ & & \frac{1}{E_T} & 0 \\ & & & \frac{1}{G_L} \end{bmatrix}^{-1} \quad (7.49)$$

The material parameters are given as [36]

$$E_L = 5.606 \text{ GPa}, \quad \nu_L = 0.303, \quad G_L = 1.978 \text{ GPa} \quad (7.50)$$

$$E_T = 0.857 \text{ GPa}, \quad \nu_T = 0.909, \quad \rho = 1.319 \text{ g/cm}^3 \quad (7.51)$$

As in the previous example, the inner radius is $r_i = 3$ mm and the element length is $l = 6$ mm. Results are presented in Figure 7.8. For this anisotropic case, no reliable implementation of the Global Matrix Method was available to the author. Hence the results have been validated using the alternative approach based on Equation (3.42). The results obtained by the two different solution techniques are in excellent agreement, showing the applicability of the proposed approach to anisotropic materials. Again the computational time is about 0.5 s.

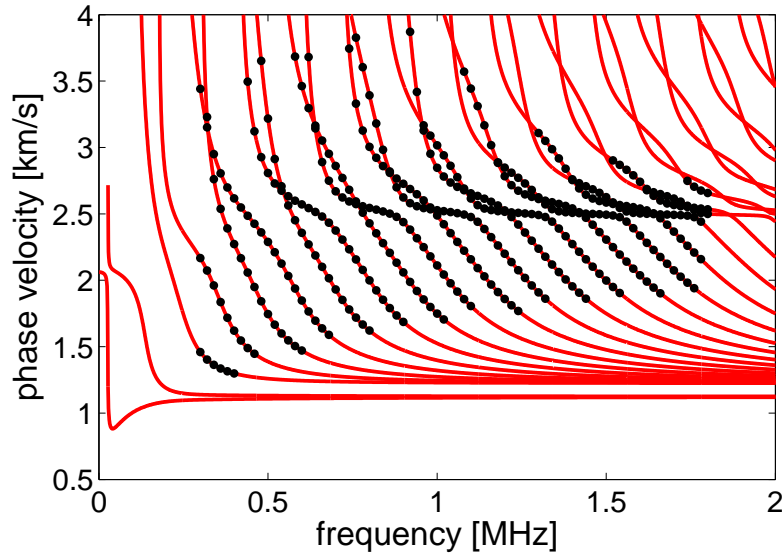


Figure 7.8: Dispersion curves for a PPO-GF30 cylinder, computed using the proposed approach (●) and compared to solutions obtained by solving the full eigenvalue problem (—).

Chapter 8

Simulations in the time domain

This chapter is fundamentally different to the other parts of the thesis. While the Chapters 3-7 almost exclusively address the computation of dispersion relations and mode shapes for different waveguides, this chapter deals with the simulation of guided wave propagation in actual (bounded) structures in the time domain (see also [101–104]). Particularly, attention is drawn to the interaction of guided waves with cracks. A very general transient elastodynamic formulation of the SBFEM is utilized for this purpose. The underlying algorithms have been developed by Song et al. and evolved over years. The main solver has not been modified within the current work. The aim of this chapter is to demonstrate, how the SBFEM can be employed for the simulation of guided waves. The discretization of the structure is a crucial step and will be discussed in detail. For now, the discussion is limited to simple homogeneous plate structures with straight cracks in a two-dimensional formulation. These examples suffice to show the applicability of this method in the context of non-destructive testing. The extension to more complex two-dimensional structures is generally straightforward. The SBFEM has also been derived for the three-dimensional case. It will be a future task to effectively discretize a complex three-dimensional (cracked) waveguide in order to apply the SBFEM. The present work is, to the author's knowledge, the first example for the modeling of ultrasonic waves by means of the Scaled Boundary Finite Element Method. Hence, it introduces a promising simulation technique to the broad subject of ultrasonic testing and structural health monitoring.

Different numerical methods have been employed by other authors to model the complex propagation behavior of guided waves and their interaction with defects or other irregularities in the structure. In most cases, the Finite Element Method (FEM) is employed, as it is a very general and flexible tool for the simulation of arbitrary geometries and materials [23, 70, 145, 288]. Many different concepts of Finite Element modeling have been applied, some of them also describing the excitation process [289]. Nevertheless, the modeling of the complete structure with standard FEM software is computationally expensive. In addition, the computational costs are highly increased, if defects of small dimension, compared with the area of the whole structure, have to be modeled. The size of the modeled domain is often reduced by combining the FEM with advanced signal processing [290], wave function expansion [291] or, most commonly, different modal decomposition techniques [292–296]. A different approach combines the Finite Element Method with the Boundary Element Method (BEM) [297, 298] or a Green's function

representation [299] for a more efficient modeling of the flawless regions of the plate. Also, pure Boundary Element modeling has been conducted to assess the reflection properties of Lamb wave modes [71, 300].

Other established numerical methods have also been employed for the simulation of Lamb waves, such as the Finite Difference Method [74], the Elastodynamic Finite Integration Technique (EFIT) [76] or, more recently, the Local Interaction Simulation Approach (LISA) [301, 302]. The Wiener-Hopf technique [303] and other analytical solutions have been considered for some specific scattering problems [304–306].

To apply a transient formulation of the SBFEM, a representation of the fundamental equations in the time domain is required. Since different solution procedures have been proposed in the literature, a very brief summary of the employed algorithm is presented in the following section. The formulation is based on a continued fraction approximation [307] of the dynamic stiffness matrix as described in [90]. It has to be discussed, how the order of the continued fraction approximation affects the solution, depending on the discretization of the boundary [101, 104]. To validate the results and demonstrate the efficiency of the SBFEM for the current application, traditional Finite Element analyses are performed.

As mentioned in the introduction, the SBFEM is particularly advantageous if cracks have to be modeled, since the crack can be extremely small without causing numerical problems and the stress singularity at the crack tip does not require special techniques or refinement. Furthermore, cracks at various possible locations and depths can be modeled with no or minimum re-meshing. The SBFEM can also be used to analyze crack propagation [89, 120, 159] which can be an interesting extension for non-destructive testing applications.

8.1 SBFEM formulation in the time domain

Similarly to the procedure as summarized in Section 2.3, an equation for the dynamic stiffness matrix $\mathbf{S}(\omega)$ of a bounded domain can be derived in the frequency domain [77, 78]

$$(\mathbf{S}(\omega) - \mathbf{E}_1)\mathbf{E}_0^{-1}(\mathbf{S}(\omega) - \mathbf{E}_1^T) - \mathbf{E}_2 + \omega\mathbf{S}_{,\omega}(\omega) + \omega^2\mathbf{M}_0 = 0 \quad (8.1)$$

Note that, for the static case ($\omega = 0$) we obtain the static stiffness matrix (Equation (2.47)). The dynamic stiffness matrix is defined analogously to Equation (2.41) as

$$\mathbf{S}(\omega)\mathbf{u}_n = \mathbf{f}_n \quad (8.2)$$

where \mathbf{f}_n denote the nodal forces on the boundary. As mentioned in Section 2.3, for $\omega = 0$ Equation (8.1) states an algebraic Riccati equation, which can be solved in order to compute the static stiffness matrix. Furthermore, when addressing problems in structural dynamics by means of traditional Finite Element analyses, a mass matrix \mathbf{M} for a bounded domain is often defined by [308]

$$\mathbf{S}(\omega) = \mathbf{K} - \omega^2\mathbf{M} \quad (8.3)$$

Equation (8.3) can be considered as a low-frequency expansion of the dynamic stiffness matrix, where terms of order in ω higher than two are neglected. Substituting (8.3) into (8.1) and neglecting the higher-order terms in ω we obtain

$$\mathbf{K}\mathbf{E}_0^{-1}(\mathbf{K} - \mathbf{E}_1^T) + \mathbf{E}_1\mathbf{E}_0^{-1}(-\mathbf{K} + \mathbf{E}_1^T) - \mathbf{E}_2 + \omega^2 [(-\mathbf{K} + \mathbf{E}_1)\mathbf{E}_0^{-1}\mathbf{M} + \mathbf{M}\mathbf{E}_0^{-1}(-\mathbf{K} + \mathbf{E}_1^T) + \mathbf{M}_0] = 0 \quad (8.4)$$

The constant term is independent of \mathbf{M} . The coefficient matrix corresponding to the quadratic term can be interpreted as a real continuous Lyapunov equation [309, 310]

$$\tilde{\mathbf{A}}\mathbf{M} + \mathbf{M}\tilde{\mathbf{A}}^T + \mathbf{M}_0 = 0 \quad (8.5)$$

with

$$\tilde{\mathbf{A}} = (-\mathbf{K} + \mathbf{E}_1)\mathbf{E}_0^{-1} \quad (8.6)$$

Note that both \mathbf{K} and \mathbf{E}_0 are symmetric. Equation (8.5) can be solved using standard techniques [311–313]. An alternative solution procedure is presented in [77]. After solving Equations (2.47) and (8.5) for \mathbf{K} and \mathbf{M} , respectively, the dynamic stiffness matrix can be approximated by Equation (8.3). This procedure has been applied successfully to solve dynamic problems in the low-frequency range [77, 79, 80].

More recently, an improved solution procedure that includes the higher-order terms in ω and hence can be applied for a large frequency range, has been developed [86, 87, 90]. The idea is to expand the dynamic stiffness matrix as a continued fraction solution

$$\mathbf{S}(\hat{\omega}) = \mathbf{K} + \hat{\omega}\mathbf{M} - \hat{\omega}^2[\mathbf{S}_0^{(1)} + \hat{\omega}\mathbf{S}_1^{(1)} - \hat{\omega}^2[\mathbf{S}_0^{(2)} + \hat{\omega}\mathbf{S}_1^{(2)} - \dots - \hat{\omega}^2[\mathbf{S}_0^{(M_{cf})} + \hat{\omega}\mathbf{S}_1^{(M_{cf})}]^{-1}]^{-1}]^{-1} \quad (8.7)$$

where M_{cf} denotes the order of continued fraction and

$$\hat{\omega} = -\omega^2 \quad (8.8)$$

is introduced for convenience. The first step in computing the coefficient matrices in Equation (8.7) is to substitute the ansatz

$$\mathbf{S}(\omega) = \mathbf{K} + \hat{\omega}\mathbf{M} - \hat{\omega}^2(\mathbf{S}^{(1)})^{-1} \quad (8.9)$$

into Equation (8.1). Since \mathbf{K} and \mathbf{M} are already known, this leads to an Equation for $\mathbf{S}^{(1)}$. A recursive procedure is then established to obtain the higher-order terms as

$$\mathbf{S}^{(i)(\hat{\omega})} = \mathbf{S}_0^{(i)} + \hat{\omega}\mathbf{S}_1^{(i)} - \hat{\omega}^2(\mathbf{S}^{(i+1)})^{-1} \quad (8.10)$$

The explicit derivation of the procedure is lengthy and is formulated comprehensively in [90]. Only the results are presented here. After the coefficient matrices have been computed up to a

given order of continued fraction M_{cf} , an equation of motion can be stated

$$\mathbf{K}_h \mathbf{v} + \omega^2 \mathbf{M}_h \mathbf{v} = \mathbf{r} \quad (8.11)$$

using the following definitions

$$\mathbf{K}_h = \text{diag}(\mathbf{K}, \mathbf{S}_0^{(1)}, \mathbf{S}_0^{(2)}, \dots, \mathbf{S}_0^{(M_{cf})}) \quad (8.12a)$$

$$\mathbf{M}_h = \begin{bmatrix} \mathbf{M} & -\mathbf{I} & 0 & \dots & 0 \\ -\mathbf{I} & \mathbf{S}_1^{(1)} & -\mathbf{I} & \dots & 0 \\ 0 & -\mathbf{I} & \mathbf{S}_1^{(2)} & \dots & 0 \\ \vdots & \vdots & \vdots & \ddots & \vdots \\ 0 & 0 & 0 & \dots & \mathbf{S}_1^{(M_{cf})} \end{bmatrix} \quad (8.12b)$$

$$\mathbf{v} = \begin{Bmatrix} \mathbf{u} \\ \mathbf{u}^{(1)} \\ \mathbf{u}^{(2)} \\ \vdots \\ \mathbf{u}^{(M_{cf})} \end{Bmatrix}, \quad \mathbf{r} = \begin{Bmatrix} \mathbf{f}_n \\ 0 \\ 0 \\ \vdots \\ 0 \end{Bmatrix} \quad (8.12c)$$

where \mathbf{r} denote the external tractions on the boundary and \mathbf{I} is the identity matrix. \mathbf{K}_h and \mathbf{M}_h can be interpreted as higher-order stiffness and mass matrices. Equation (8.11) can as well be written in the time domain as

$$\mathbf{K}_h \mathbf{v} + \mathbf{M}_h \ddot{\mathbf{v}} = \mathbf{r} \quad (8.13)$$

The equation of motion (8.13) can be solved by applying a numerical time integration procedure. In this work a simple Newmark scheme [90, 314, 315] is employed.

It should be noted that the size of the system of equations (8.11) increases with the order of continued fraction, which on the other hand has to be chosen according to frequency. The higher the frequency, the more terms of the continued fraction approximation have to be included. In other words, a certain number of terms have to be considered per wavelength in radial direction. Thus, similar considerations have to be applied compared with a Finite Element discretization, where a certain number of nodes per wavelength have to be employed. The displacements $\mathbf{u}^{(i)}$ corresponding to the higher-order terms can be considered as additional degrees of freedom. Hence, the continued fraction expansion can be interpreted as a novel strategy to 'discretize' the interior of the domain (This is in contrast to the static and low-frequency formulations where solely the degrees of freedom on the boundary have to be considered).

However, it will be demonstrated by the numerical examples in this chapter that the total number of degrees of freedom required for the continued fraction approximation is significantly smaller than the number of degrees of freedom in a Finite Element analysis leading to comparable accuracy. This is particularly valid for the simulation of cracked structures, where a very fine discretization is required in the vicinity of the crack tip in the FEM.

8.2 Problem definition

In this chapter, Lamb wave propagation in a steel plate of 2 mm thickness is analyzed as an example to demonstrate the applicability of the SBFEM. The material parameters are chosen to be

$$\begin{aligned} \text{Young's modulus:} & \quad E = 200 \text{ GPa} \\ \text{density:} & \quad \rho = 7850 \text{ kg/m}^3 \\ \text{Poisson's ratio:} & \quad \nu = 0.3 \end{aligned}$$

The same parameters are used throughout the numerical studies in this chapter. Figure 8.1 shows the dispersion curves in terms of group velocity for the given example. The current analysis will be restricted to the frequency range around 600 kHz, where only the fundamental symmetric and antisymmetric Lamb wave modes (S_0 and A_0) can be excited. To generate Lamb wave modes, a typical ultrasonic pulse is applied to one side of the structure, while everywhere else stress-free boundary conditions are used. The pulse is a uniformly distributed load with a time-dependent pressure distribution $P(t)$ described as

$$P(t) = \sin(2\pi ft) \cdot e^{-\frac{1}{2}\left(\frac{t-\mu}{\sigma}\right)^2} [\text{GPa}] \quad (8.14)$$

with $\mu = 6\mu\text{s}$, $\sigma = 2\mu\text{s}$ and a frequency of $f = 600 \text{ kHz}$ (Figure 8.2). Depending on the orientation of the applied pressure distribution, either symmetric or antisymmetric modes (or a superposition of both) can be excited. Cracks of different depth and opening angle will be introduced in the plate to model the interaction of the different Lamb wave modes with defects in the material.

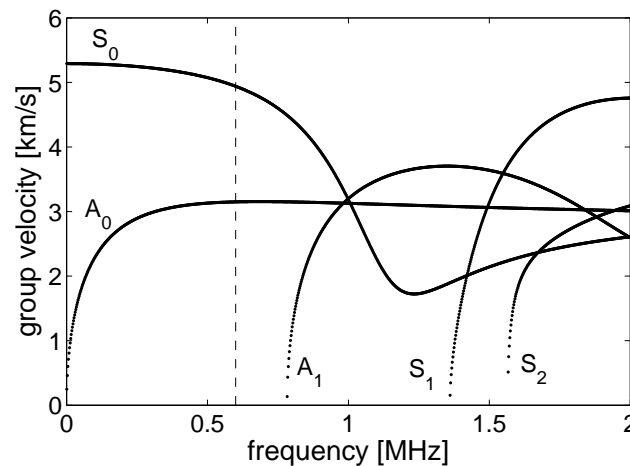


Figure 8.1: Group velocity dispersion for the first Lamb wave modes in a 2 mm thick steel plate.

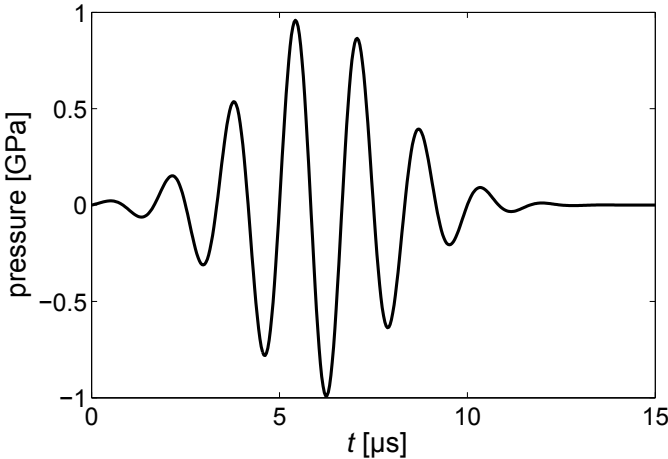


Figure 8.2: Pulse applied to the structure for the excitation of Lamb waves.

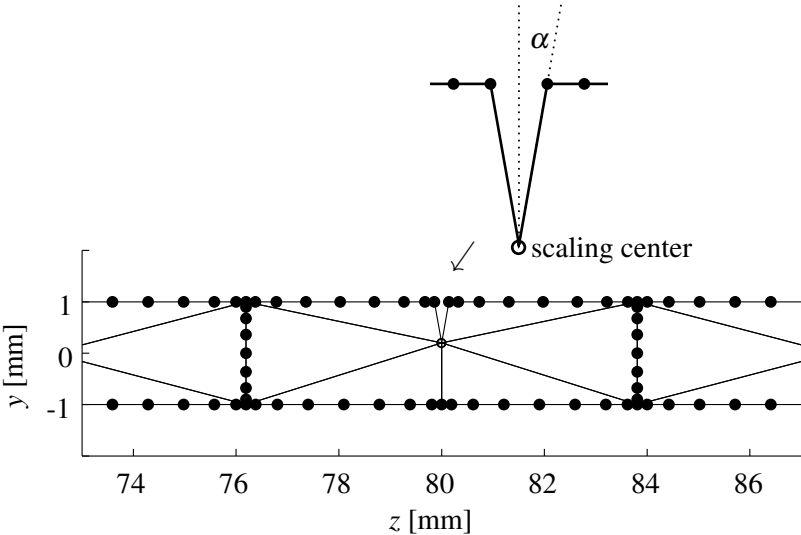


Figure 8.3: Representative part of the discretization of a cracked plate using the SBFEM.

8.3 Discretization

To model the propagation of guided waves, typically a large structure with a small aspect ratio has to be discretized. Hence, it is essential to optimize the discretization in order to reduce computational cost. As only the boundary of a domain has to be meshed in the SBFEM, the discretization process is very simple and straightforward compared to the FEM. However, if a long plate has to be modeled with the SBFEM, it should be divided into subdomains rather than describing the whole structure as a simply connected boundary. This is due to the fact that the order of continued fraction M_{cf} needed to approximate the solution in the interior of the domain, depends on the distance between the boundary and the scaling center. For a structure with a small aspect ratio, this distance would differ strongly for different sections of the boundary. In that case, a rather high continued fraction order, related to the longest distance to the boundary has to be used. The dimension of the equation of motion increases with the continued fraction order (cf. Equation (8.12)). This results in a rather inefficient computation for domains with a small aspect ratio.

Consequently, the plate is divided into subdomains with a maximum aspect ratio of 4, which has been tested to give excellent results. An example for the discretization is presented in Figure 8.3. Only a representative part of the mesh is depicted, including a subdomain containing a crack with opening angle α . The crack is introduced simply by leaving a small gap between two elements and positioning the scaling center at the crack tip. In contrast to the Finite Element Method, the crack is not discretized and the stress singularity at the crack tip does not require special treatment. Furthermore, the depth and the opening angle of the crack can easily be modified by changing the position of the scaling center.

As can be seen in Figure 8.3, only six higher-order elements are used for the discretization of one subdomain. Hence, the mesh generation and integration over the boundary can be done with very high efficiency. The subdomains are assembled similar to the elements in the standard Finite Element Method.

8.4 Results

8.4.1 Comparison with Finite Element Analysis

To assess the accuracy and efficiency of the Scaled Boundary Finite Element Method for this specific application, a test problem is chosen to compare with a standard Finite Element Analysis. A representative section of the steel plate with a length of 4 mm is modeled. The plate contains a 1 mm deep crack with a width of $2 \cdot 10^{-9}$ mm at the surface³². For the Finite Element Analysis, the commercial software ANSYS [316] is used. Examples for the discretization are shown in Figure 8.4. Creating the optimal mesh for the Finite Element Method is not trivial and can become very time consuming if both a high accuracy and a low computational time are

³²The extremely small value has been chosen here to demonstrate that there are no limitations on the crack width in the SBFEM in terms of numerical stability. The results, however, are almost identical for a crack width of $2 \cdot 10^{-2}$ mm.

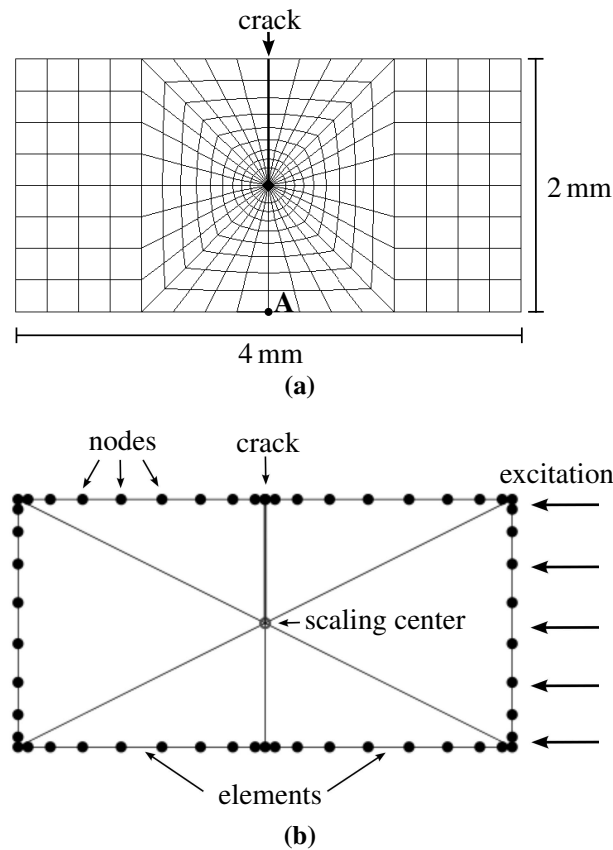


Figure 8.4: Discretization of a test problem in the (a) Finite Element Method and (b) Scaled Boundary Finite Element Method.

desired. Several aspects have to be considered in the meshing: Due to the stress singularity, a very fine discretization is required for the FEM in the vicinity of the crack tip, while a rather coarse mesh is sufficient in the regular areas of the structure. Consequently, the optimal growth rate has to be found, taking into account that the difference in size of two adjacent elements cannot be arbitrarily big. Furthermore, elements with very small angles in one corner as well as elements with a high aspect ratio can lead to numerical problems and should be avoided. To prove convergence of the results, a consistent way of refinement is desired, offering for instance the possibility to divide every element into four in every step of refinement.

Because of these requirements, there is no general way to create an optimal mesh for complex geometries. However, the best results have been obtained with the type of discretization shown in Figure 8.4a. The structure is divided into a square containing the continuously growing elements close to the crack tip and two rectangles with highly regular rectangular elements.

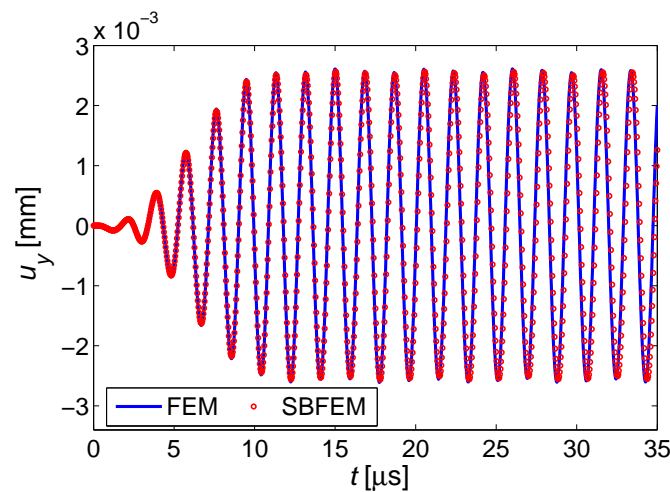


Figure 8.5: Vertical displacement at point A computed with the FEM and the SBFEM.

Hence, the plate can always be extended by increasing the area of the regular mesh without changing the discretization of the crack. Within a circle around the crack tip, quarter-point elements are used to better describe the stress singularity (KSCON-command in ANSYS), leading to more accurate results for the same number of nodes than conventional elements. Everywhere else four-sided elements with quadratic shape functions are applied. Obviously, the mesh generation is very cumbersome in the FEM and the whole mesh has to be modified, when the crack depth or opening angle is varied. When comparing the efficiency of both approaches it should be kept in mind that the meshes used for the FEM have been highly optimized through a time-consuming process. Using a simple automatic meshing algorithm results in much higher computational costs for the same order of accuracy.

In contrast to that, the meshing is straightforward when applying the SBFEM, as only the boundary has to be discretized (Figure 8.4b). If higher-order elements are utilized, a minimum of six elements has to be used for this application. Figure 8.4b shows the discretization with six 10-noded elements. A finer discretization can be achieved by either increasing the number of elements on the boundary or the element order. The crack is described by leaving a gap of given size between two elements and placing the scaling center at the crack tip. Note that the crack's surfaces do not need to be discretized and the crack depth can be varied by changing the position of the scaling center without modifying the discretization.

A uniformly distributed pressure with a time-dependency given by Equation (8.14) is applied to one side of the structure as indicated in Figure 8.4. The response of the structure is computed in the time domain using a Newmark time integration procedure with the Newmark parameters [107] $\delta = 0.5$ and $\alpha = 0.25$. 1000 time steps are computed with a time increment of 35 ns. The analysis is performed with numerous discretizations using the FEM as well as the SBFEM. As an example, Figure 8.5 shows vertical displacements u_y for the discretizations presented in Figure 8.4, computed at the position A (as indicated in Figure 8.4a). The methods are generally in good agreement. However, in this example the difference between the results of both methods increases slightly with the number of time steps. To compare the methods in

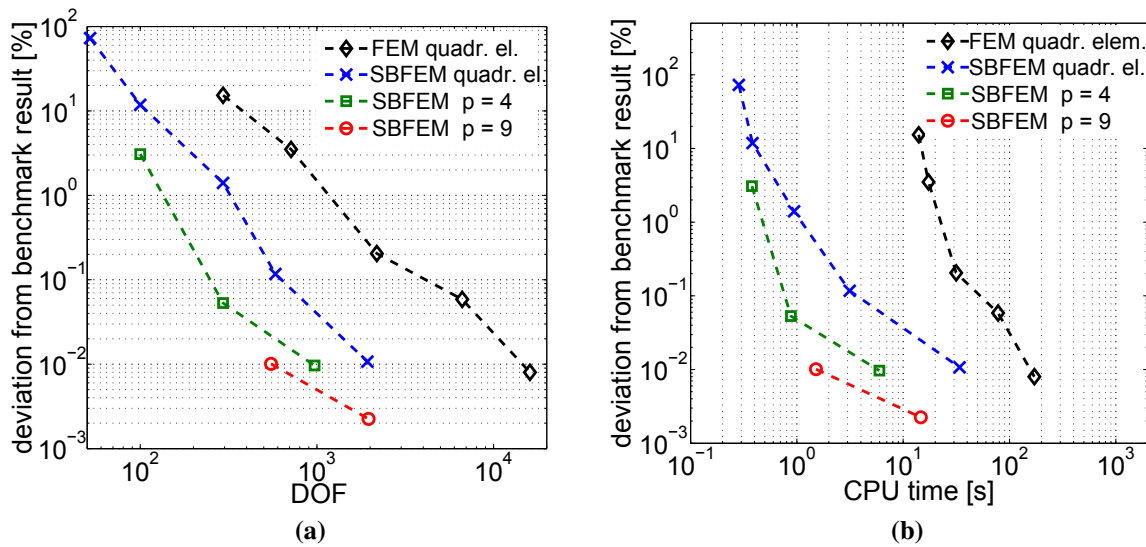


Figure 8.6: Average deviation from the FE result with the finest discretization as a function of (a) the number of degrees of freedom (DOF) and (b) the computational time.

terms of accuracy and efficiency, a Finite Element result with a very fine discretization (131 648 quadratic elements) is chosen as a benchmark result. The accuracy of the computations with different discretizations is calculated as the relative deviation from the benchmark result, averaged over the time steps. Time steps with a displacement close to zero are neglected, as they can lead to large deviations in terms of percentage without having a relevant absolute value.

This average deviation is plotted in Figure 8.6a as a function of the total number of degrees of freedom (DOF). Results are shown for the Finite Element Method using quadratic elements and for the Scaled Boundary Finite Element Method using quadratic as well as higher-order elements of order 4 and 9. When quadratic elements are utilized, the nodes on the boundary are in exactly the same positions for both methods. In the SBFEM, the number of degrees of freedom depends on the number of nodes on the boundary as well as the order of continued fraction. The required order of continued fraction is related to the smallest wave length that can be represented by the mesh on the boundary [90]. Typically, 3-4 terms of continued fraction are sufficient to represent one wavelength, which is significantly smaller than the number of nodes required by Finite Elements. For the finest discretizations, an order of continued fraction of 10 has shown to result in converged solutions while for the coarsest discretizations an order of 1 was used.

As can be seen in Figure 8.6a, the methods are in excellent agreement for a sufficient number of DOF. It cannot be proven which method gives more accurate results when the deviation is very small (say, smaller than 0.01 %) as there is obviously no analytical solution available for complex geometries. However, for practical applications such a high accuracy is usually not required. If we are looking at a reasonably good accuracy of about 0.1 % ... 1 %, the SBFEM is always about ten times more accurate for the same number of DOF, if quadratic elements are

used. On the other hand, if higher-order elements are applied, Figure 8.6a shows the extremely fast convergence of the results. Even if only six elements of order 9 are used, the SBFEM result has nearly converged, while the FEM with quadratic elements produces an average error of about 5 % for the same number of DOF.

If the same values of the deviation are plotted as a function of the computational time required for the solution (not including the mesh generation), the large difference in efficiency of the two methods is revealed (Figure 8.6b). If quadratic elements are used, the CPU time for the SBFEM is roughly about 10 to 20 times less than for the FEM.³³ If higher-order elements are applied, the SBFEM is about 100 times faster than the FEM with quadratic elements for comparable accuracy. All computations have been performed on a HP EliteBook 8560w (Intel core i7-2820QM CPU @2.30 GHz with 8GB RAM). Only one core of the processor has been enabled to obtain comparable results because the SBFEM code has not been parallelized yet.

It should be noted that the difference in efficiency of different numerical methods is always problem-dependent. The SBFEM is particularly advantageous for the modeling of cracked structures. Also the meshing is generally much easier, which can be of high advantage, especially when the analysis has to be performed multiple times with slightly modified geometry. It should also be highlighted that the Finite Element Analysis is conducted using a commercial software while the SBFEM code runs in the interactive mode of *Matlab* and has not been optimized for computational efficiency.

Also, at the current stage the SBFEM is especially highly effective for simple geometries with no or simple inhomogeneities. While different material properties can be assigned to every node on the boundary, the treatment of inhomogeneities in the scaling direction is not straightforward. Still it is always possible to divide the structure into subdomains with different material parameters. For highly inhomogeneous materials the difference in efficiency compared to the FEM will be significantly smaller than for the examples presented in this work. The boundary of every subdomain of the SBFEM has to be 'visible' from the scaling center (i. e. the domain has to be a star domain in the mathematical sense), which imposes limitations on the application to complex geometries. Obviously, these drawbacks are similar to the ones of the Boundary Element Method (BEM), which also requires discretization of the boundary only. However, the SBFEM offers several advantages in comparison with the BEM. General anisotropy, for instance can be included in the SBFEM in a trivial way by simply modifying the elasticity matrix. No fundamental solution is required. Because the integration over the elements is performed independently of each other in the SBFEM, different material parameters can simply be assigned to each node of the discretization. Also this fact makes the SBFEM very efficient, if one problem has to be solved several times with only slightly different geometry, because only the integration over the modified parts of the structure has to be repeated.

The boundary of the structure can generally be of arbitrary shape. Hence, other types of defects, such as corrosion, notches or delaminations in composite materials will be analyzed in future work. If cracks of arbitrary shape have to be modeled, they cannot generally be defined

³³Only the computational times required for the solution process are compared. In *ANSYS* the 'Elapsed time spent computing solution' from the *ANSYS statistics* is used. This time does not include any pre- or post-processing.

along the scaling direction as was done in the current work. Alternatively, parts of the crack can be introduced as a gap between two subdomains which can be of arbitrary shape [89, 121]. It should be discussed in future work how this affects the results and the efficiency of the solution.

8.4.2 Reflection of the fundamental Lamb wave modes from a crack

Incident S_0 mode As an example for the interaction of Lamb waves with cracks, a steel plate with a length of 160 mm and a thickness of 2 mm is modeled. The plate is divided into 21 subdomains (Figure 8.3) and in the 11th subdomain a crack is introduced (at $z = 80$ mm). The same pulse as in the previous example (Figure 8.2) is applied to one side of the plate (at $z = 0$ mm). The excitation frequency of 600 kHz is below the cut-off frequency of the first order modes (cf. Figure 8.1). Results are presented for a crack depth of 1 mm and opening angle of 5° .

Figure 8.7 shows the computed vertical displacements at three different time steps. The displacements on both upper and lower surface are plotted to visualize the symmetric and anti-symmetric behavior of the Lamb modes, respectively. Since the pulse is purely symmetric with respect to the z -axis, only the S_0 mode is excited (Figure 8.7a). As the S_0 mode interacts with the crack (Figure 8.7b), it is partly converted into the A_0 mode. Consequently, the reflected and transmitted signals consist of both modes (Figure 8.7c).

To obtain the amplitudes of the different modes in the reflected signal, the displacements on the plate's lower surface are analyzed at one time step. For this analysis, the time $t = 31.5 \mu\text{s}$ is chosen, where the reflection at the crack is completed and the reflected S_0 mode has not reached the edge of the plate yet. Hence, the complete reflected signal is captured at this time step. Only the displacements on one half of the plate ($z \leq 80$ mm) is required to analyze the reflected signal. A spatial Fourier transformation [290, 317] is performed to obtain the displacement amplitudes as a function of the wavenumbers contained in the signal (Figure 8.8). In this depiction the two modes can be clearly identified. The maximum amplitudes occur at $k = 0.741 \text{ mm}^{-1}$ and $k = 1.544 \text{ mm}^{-1}$. These values agree well with the theoretical wavenumbers of the S_0 and A_0 mode at the center frequency of 600 kHz, which are obtained as $k_{S_0} = 0.727 \text{ mm}^{-1}$ and $k_{A_0} = 1.559 \text{ mm}^{-1}$. Denoting with $A_{S_0,r}$ and $A_{A_0,r}$ the maximum amplitudes of the two modes in the reflected signal, the following reflection parameters are defined

$$R_{S_0} = \frac{A_{S_0,r}}{A_i} \quad (8.15a)$$

$$R_{A_0} = \frac{A_{A_0,r}}{A_i} \quad (8.15b)$$

with the amplitude of the incident mode A_i . Note that only the amplitudes of the displacements in y -direction are taken into consideration, which are not proportional to the energy transported by the mode.

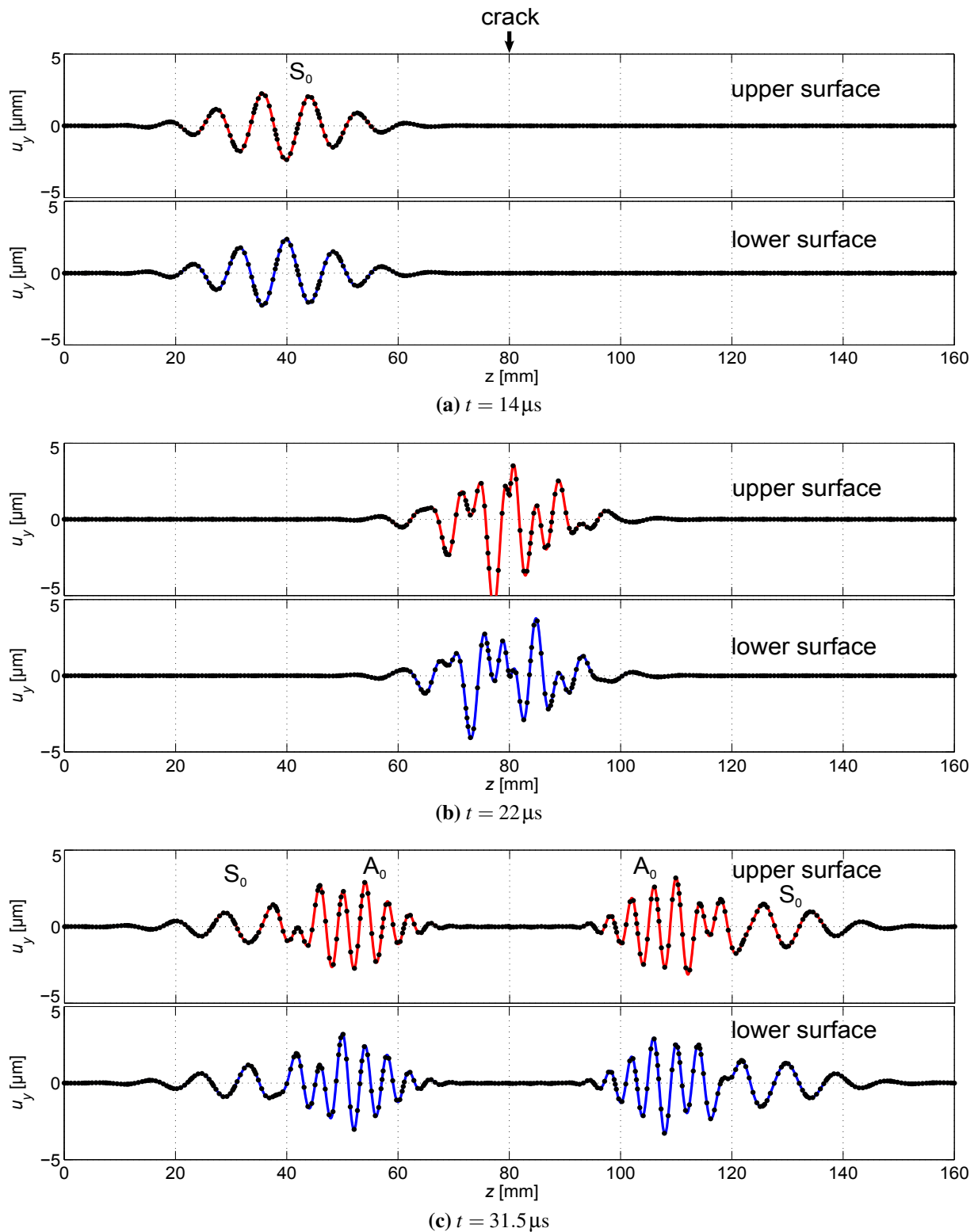


Figure 8.7: Displacements at the upper and lower surface of the plate to visualize (a) the incoming pulse, (b) the interaction with the crack, (c) the reflected and transmitted signals

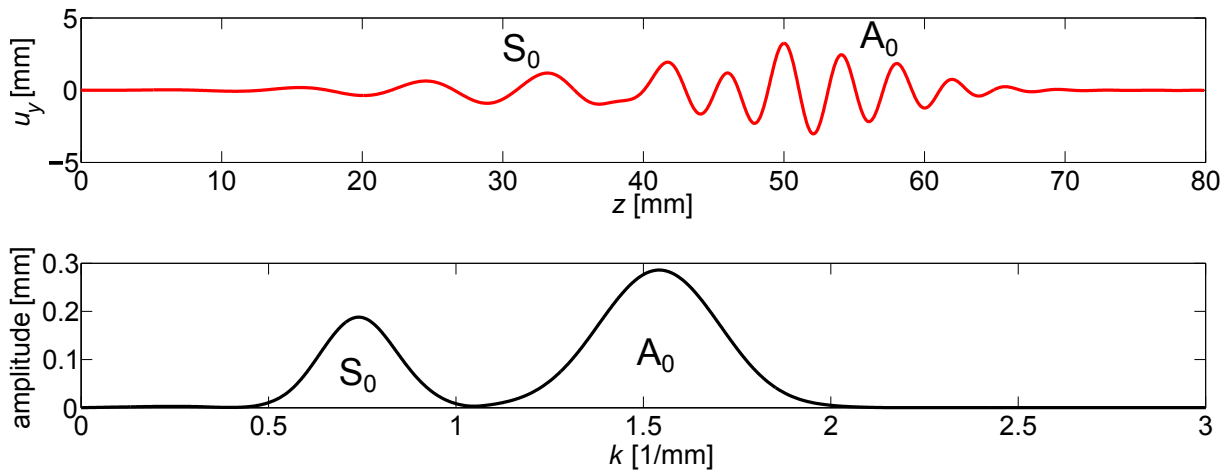
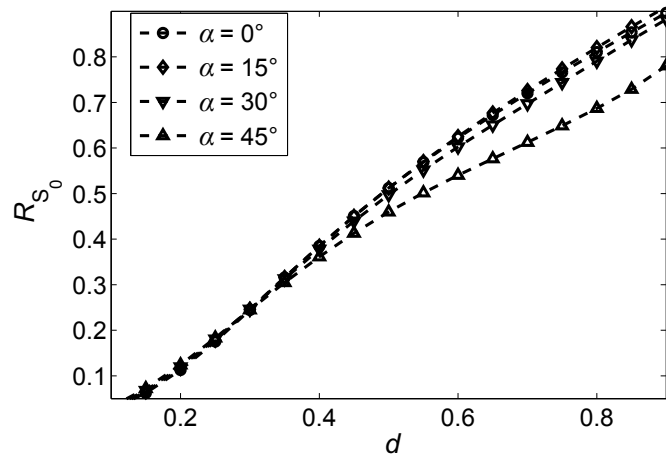


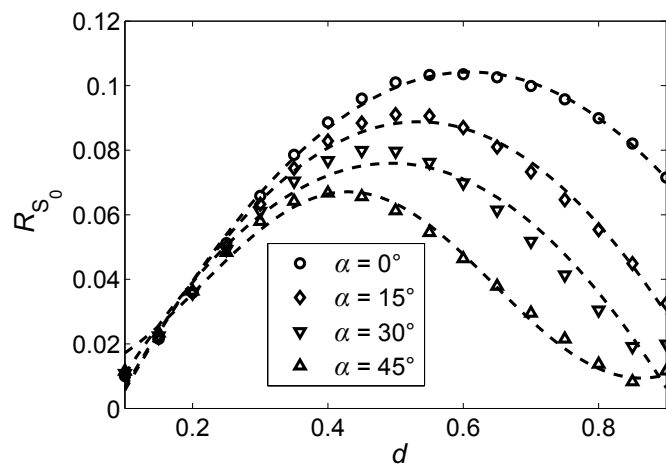
Figure 8.8: Displacement on plate surface at $t = 31.5\mu\text{s}$ and the results of a spatial Fourier transformation.

The reflection parameters are calculated for different crack geometries to demonstrate the applicability of the proposed method. However, it should be noted that the exact results are valid for this example only and that the reflection parameters are generally frequency-dependent. Figure 8.9 shows the reflected amplitudes as a function of the relative crack depth d , which is the ratio of crack depth and plate thickness. The computations are performed for different crack opening angles. An opening angle of 0 refers to the smallest crack with a width of 1 nm. As can be seen in Figure 8.9a, the amplitude of the reflected S_0 mode is monotonically increasing as a function of the crack depth while it is only slightly influenced by the opening angle. On the other hand, the amplitude of the A_0 mode significantly decreases with the opening angle (Figure 8.9b). Thus, the total reflected energy also decreases with increasing crack opening angle. R_{A_0} follows approximately a sinusoidal function of the crack depth. The dotted lines in Figure 8.9b represent sinusoidal fits to the data points.

The computational costs for this example are also compared with the FEM based on the results obtained in Section 8.4.1. As in the previous example, the discretization for the FEM is refined consistently. Except for the small area in the vicinity of the crack the plate is discretized with a highly regular mesh. For the SBFEM, only the element order is increased, while always six elements per subdomain are used. As a benchmark result, an SBFEM analysis with an element order of 14 and a continued fraction order of 15 is used. Some results are summarized in Table (8.1). Note that the SBFEM requires a significantly smaller number of DOFs than the FEM to obtain the same accuracy. Again, the SBFEM is much faster than the FEM, although the difference in efficiency is smaller than in the example in Section 8.4.1. This is due to the fact that the area around the crack tip, where a very fine discretization is required in the FEM, is relatively smaller. However, as highlighted in Table (8.1), the SBFEM is still about 70 times faster for a similar accuracy of about 0.02 %.



(a)



(b)

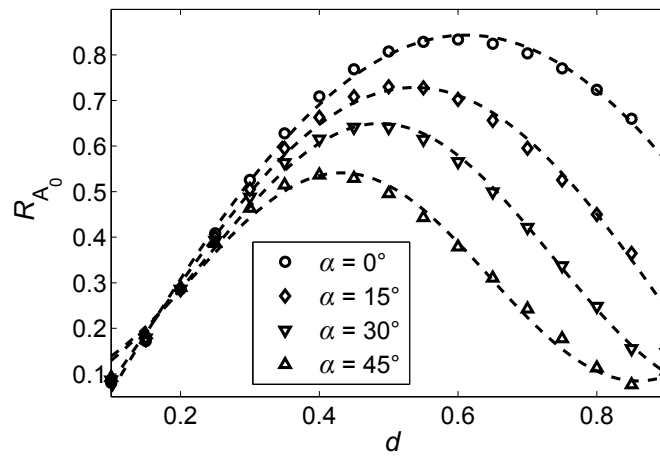
Figure 8.9: Vertical displacement amplitudes of the (a) S_0 and (b) A_0 mode in the reflected signal as a function of the relative crack depth, divided by the amplitude of the incident S_0 mode. In (b), the dashed line corresponds to sinusoidal fits to the data.

Table 8.1: Comparison of different FEM and SBFEM discretizations for the case of an incident S_0 mode.

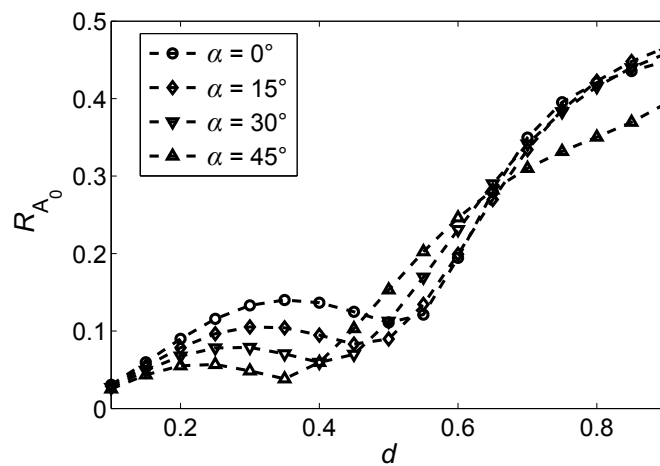
	el. order	# DOF	deviation [%]	CPU [s]
FEM	2	9450	3.727	146
	2	34630	0.240	515
	2	131446	0.018	2006
SBFEM	6	4262	0.463	12
	8	7712	0.017	30
	10	9648	0.008	46

Incident A_0 mode To excite an antisymmetric mode, the same geometry is used as in the previous example. Only the direction of the excitation pulse is changed to have a y -component only. Consequently, the excitation is antisymmetric with respect to the z -axis and a pure A_0 mode is excited. The reflected amplitudes are calculated in the same way as before. But as the group velocity of the incident mode is smaller, more time steps have to be computed and a later time step has to be chosen for the Fourier transformation of the surface displacements. Results are presented in Figure 8.10. The amplitude of the S_0 mode is a sinusoidal function of the crack depth, similar to the A_0 mode in the previous example. The amplitudes of the reflected S_0 mode are very low with a maximum of about 10% of the incident amplitude. The maximum occurs at an opening angle of 0 and a relative crack depth of about 0.6. The amplitude of the reflected A_0 can become as large as nearly half of the incoming amplitude for large crack depths. However, as long as the plate is not fully cracked, a significant fraction of the incoming A_0 mode will always be transmitted.

In practical applications, the amplitude of the incident wave is usually not measured. Furthermore, the damping properties of the specimen are generally difficult to model. Hence, the determination of R_{S_0} and R_{A_0} is not straightforward. On the other hand, the ratio of the amplitudes of both modes in the reflected signal can always be obtained. This amplitude ratio is plotted in Figure 8.11 for the given frequency. If S_0 is the incident mode, the amplitude ratio is monotonically increasing with the crack depth, except for the case where both opening angle and crack depth are large. In most applications, cracks with a small opening angle have to be found and hence this correlation can theoretically be used to obtain an estimation for the crack depth. To obtain more information about the crack geometry, the A_0 or higher-order modes could be used as the incident modes.



(a)



(b)

Figure 8.10: Vertical displacement amplitudes of the (a) S_0 and (b) A_0 mode in the reflected signal as a function of the relative crack depth, divided by the amplitude of the incident A_0 mode.

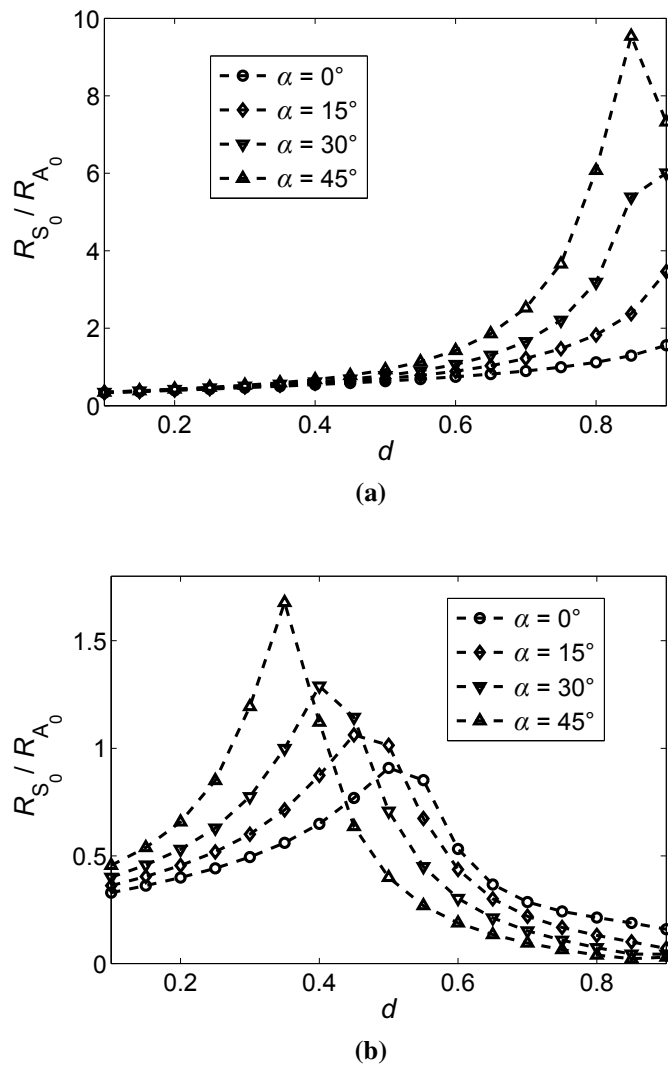


Figure 8.11: Ratio of the amplitudes of the two fundamental modes in the reflected signal in case of an incident (a) S_0 mode and (b) A_0 mode.

Chapter 9

Concluding remarks

In this work, numerical methods have been developed and applied in order to model the propagation of elastic guided waves and their interaction with defects. These simulations are of high relevance in non-destructive testing and structural health monitoring applications as well as material characterization. The presented approaches are based on the Scaled Boundary Finite Element Method, which has, to the author's knowledge, never been applied to model ultrasonic wave propagation phenomena prior to this work. In the predominant part of this thesis, waveguides of infinite length and constant thickness are addressed. Describing these structures with the Scaled Boundary Finite Element Method quite naturally yields an elegant formulation to compute dispersion curves and mode shapes. It has been demonstrated that this concept can be applied to waveguides of any cross-section and arbitrary distribution of material parameters. Particularly for plates and axisymmetric structures, extremely efficient formulations have been presented requiring the discretization of a single straight line only. Many details on the discretization process and the solution of the resulting eigenproblems are presented that are of particular interest if a highly efficient algorithm is required. The novel solution procedure offers an innovative and extremely efficient technique to solve for the dispersion curves and can be employed for many practical applications.

An additional very important development in this work is a novel approach to model embedded waveguides. This has previously been considered a very difficult and computationally expensive task that has been addressed by numerous researchers. The approach presented here is not only surprisingly easy to implement but it also requires only minimal additional computations compared to the formulation for free waveguides.

As a conclusion, a very comprehensive approach to analyze dispersion properties of guided waves has been presented can be used for a large range of applications.

For the transient analysis of bounded domains, as presented in the previous chapter, the situation is very different. The aim of this work is to test the applicability of the SBFEM to the modeling of ultrasonic wave propagation. An already existing general elastodynamic formulation has been utilized. Consequently this part of the current work mainly focuses on discretization issues rather than the development of new formulations. A basic procedure is presented to extract information on the crack geometry from measured data. The comparison with traditional Finite Elements reveals the highly superior efficiency of the SBFEM. How-

ever, comparably simple two-dimensional geometries have been studied until now. A general three-dimensional formulation of the SBFEM exists, but the discretization is obviously more cumbersome. A novel approach to introduce cracks in three-dimensional subdomains is currently under development. The SBFEM will be subsequently used to simulate more complex structures and study multi-mode wave propagation at higher frequencies. An interesting future task will be the inclusion of this method in approaches for defect detection and characterization by means of inverse analysis or artificial neural networks.

Even though this work focuses on ultrasonic guided waves in solids, the formulations can be adapted to model waves in very different applications. For instance, similar wave propagation phenomena can be observed in soil layers and are considered in geophysics and earthquake engineering. Moreover, water reservoirs in contact with a dam can be modeled as waveguides. Guided waves in air are of interest in acoustics, e. g. to model active noise reduction. Finally, similar concepts can be used to model electrodynamic waveguides.

Appendix A

A.1 Parameters used for the simulation in Section 1

The commercial software *Comsol* [318] has been used for the simulations. For convenience, the material parameters are chosen as

$$\begin{aligned}\text{shear modulus:} & \quad G = 1 \text{ Pa} \\ \text{density:} & \quad \rho = 1 \text{ kg/m}^3 \\ \text{Poisson's ratio:} & \quad \nu = 1/3\end{aligned}$$

Consequently, the shear and longitudinal wave velocities yield

$$\begin{aligned}\text{shear wave velocity:} & \quad c_s = \sqrt{\frac{G}{\rho}} = 1 \text{ m/s} \\ \text{longitudinal wave velocity:} & \quad c_l = c_s \sqrt{\frac{2(1-\nu)}{1-2\nu}} = 2 \text{ m/s}\end{aligned}$$

In the first example (large solid) the size of the computational domain is chosen as $32 \text{ m} \times 20 \text{ m}$. The plate in the second example is 32 m long and 0.5 m thick.

The pulse is excited by prescribing the vertical displacements $u_y(t)$ on a 1 m section on the boundary. Its time-dependency is given by

$$u_y(t) = \sin(2\pi ft) \cdot \exp\left(-\frac{(t-\mu)^2}{2}\right) [\text{Pa}] \quad (\text{A.1})$$

with $f = 1 \text{ Hz}$ and $\mu = 3 \text{ s}$. Simulations have been performed in time domain with a time increment of 0.1 s .³⁴

³⁴Obviously, this is not an ultrasonic frequency. Nevertheless, the complete set-up can be scaled to model realistic materials and frequencies (see Section 3.7.1).

A.2 Equations related to Section 2.3

For a two-dimensional problem, defined in the Scaled Boundary coordinates (η, ξ) , the following matrices are defined [81]:

$$\mathbf{b}_1(\eta) = \frac{1}{|J|} \begin{bmatrix} z(\eta)_{,\eta} & 0 \\ 0 & -y(\eta)_{,\eta} \\ -y(\eta)_{,\eta} & z(\eta)_{,\eta} \end{bmatrix} \quad (\text{A.2a})$$

$$\mathbf{b}_2(\eta) = \frac{1}{|J|} \begin{bmatrix} -z(\eta) & 0 \\ 0 & y(\eta) \\ y(\eta) & -z(\eta) \end{bmatrix} \quad (\text{A.2b})$$

where $|J|$ is the Jacobian determinant on the boundary ($\xi = 1$):

$$|J| = \begin{vmatrix} y(\eta) & z(\eta) \\ y(\eta)_{,\eta} & z(\eta)_{,\eta} \end{vmatrix} = y(\eta)z(\eta)_{,\eta} - z(\eta)y(\eta)_{,\eta} \quad (\text{A.3})$$

\mathbf{b}_1 and \mathbf{b}_2 depend on the geometry of the boundary only. With these definitions, the differential operator \mathbf{L} can be written as

$$\mathbf{L} = \mathbf{b}_1 \partial_\xi + \frac{1}{\xi} \mathbf{b}_2 \partial_\eta \quad (\text{A.4})$$

and the matrices \mathbf{B}_1 and \mathbf{B}_2 as introduced in Equation (2.45) are then obtained as

$$\mathbf{B}_1 = \mathbf{b}_1 \mathbf{N} \quad (\text{A.5a})$$

$$\mathbf{B}_2 = \mathbf{b}_2 \mathbf{N}_{,\eta} \quad (\text{A.5b})$$

The coordinate transformation used in Chapter 3 is a simplification of this general formulation, since the Scaled Boundary coordinates can be chosen parallel to the axes of a Cartesian coordinate system.

A.3 Equations related to Section 5.2

The strain components of one mode with circumferential order m follow from Equation (5.23) as [319]

$$\varepsilon_z = \partial_z u_z = u_{z,z}^s \cos m\theta + u_{z,z}^a \sin m\theta \quad (\text{A.6a})$$

$$\varepsilon_\theta = \frac{1}{r} \partial_\theta u_\theta + \frac{1}{r} u_r = \frac{1}{r} (u_r^s - m u_\theta^s) \cos m\theta + \frac{1}{r} (u_r^a - m u_\theta^a) \sin m\theta \quad (\text{A.6b})$$

$$\varepsilon_r = \partial_r u_r = u_{r,r}^s \cos m\theta + u_{r,r}^a \sin m\theta \quad (\text{A.6c})$$

$$\gamma_{r\theta} = \left(\partial_r - \frac{1}{r}\right) u_\theta + \frac{1}{r} \partial_\theta u_r = \left(-u_{\theta,r}^s + \frac{1}{r} u_\theta^s - \frac{m}{r} u_r^s\right) \sin m\theta + \left(u_{\theta,r}^a - \frac{1}{r} u_\theta^a + \frac{m}{r} u_r^a\right) \cos m\theta \quad (\text{A.6d})$$

$$\gamma_{rz} = \partial_r u_z + \partial_z u_r = (u_{z,r}^s + u_{r,z}^s) \cos m\theta + (u_{z,r}^a + u_{r,z}^a) \sin m\theta \quad (\text{A.6e})$$

$$\gamma_{z\theta} = \frac{1}{r} \partial_\theta u_z + \partial_z u_\theta = \left(-\frac{m}{r} u_z^s - u_{\theta,z}^s\right) \sin m\theta + \left(\frac{m}{r} u_z^a + u_{\theta,z}^a\right) \cos m\theta \quad (\text{A.6f})$$

In Section 5.2, the strain-displacement relationship is presented as

$$\begin{aligned} \boldsymbol{\varepsilon} = & (\mathbf{B}_1^\alpha \tilde{\mathbf{u}}_{n,z}^s + \mathbf{B}_2^\alpha \tilde{\mathbf{u}}_n^s) \cos m\theta + (\mathbf{B}_1^\beta \tilde{\mathbf{u}}_{n,z}^s + \mathbf{B}_2^\beta \tilde{\mathbf{u}}_n^s) \sin m\theta \\ & + (\mathbf{B}_1^\alpha \tilde{\mathbf{u}}_{n,z}^a + \mathbf{B}_2^\alpha \tilde{\mathbf{u}}_n^a) \sin m\theta - (\mathbf{B}_1^\beta \tilde{\mathbf{u}}_{n,z}^a + \mathbf{B}_2^\beta \tilde{\mathbf{u}}_n^a) \cos m\theta \end{aligned} \quad (\text{A.7})$$

We define

$$\mathbf{B}_1^\alpha = \mathbf{b}_1^\alpha \mathbf{N} \quad (\text{A.8a})$$

$$\mathbf{B}_2^\alpha = \frac{1}{r,\eta} \mathbf{b}_2^\alpha \mathbf{N},\eta + \mathbf{b}_3^\alpha \frac{m}{r} \mathbf{N} + \mathbf{b}_4^\alpha \frac{1}{r} \mathbf{N} \quad (\text{A.8b})$$

$$\mathbf{B}_1^\beta = \mathbf{b}_1^\beta \mathbf{N} \quad (\text{A.8c})$$

$$\mathbf{B}_2^\beta = \frac{1}{r,\eta} \mathbf{b}_2^\beta \mathbf{N},\eta + \mathbf{b}_3^\beta \frac{m}{r} \mathbf{N} + \mathbf{b}_4^\beta \frac{1}{r} \mathbf{N} \quad (\text{A.8d})$$

It follows that

$$\mathbf{b}_1^\alpha = \begin{bmatrix} 0 & 0 & 0 & 0 & 0 & 0 \\ 0 & 0 & 0 & 1 & 0 & 0 \\ 0 & 0 & 1 & 0 & 0 & 0 \end{bmatrix}^T \quad (\text{A.9a})$$

$$\mathbf{b}_1^\beta = \begin{bmatrix} 0 & 0 & 0 & -1 & 0 & 0 \\ 0 & 0 & 0 & 0 & 0 & 0 \\ 0 & 0 & 0 & 0 & 0 & 0 \end{bmatrix}^T \quad (\text{A.9b})$$

$$\mathbf{b}_2^\alpha = \begin{bmatrix} 0 & 0 & 0 & 0 & 0 & 0 \\ 0 & 1 & 0 & 0 & 0 & 0 \\ 0 & 0 & 0 & 1 & 0 & 0 \end{bmatrix}^T \quad (\text{A.9c})$$

$$\mathbf{b}_2^\beta = \begin{bmatrix} 0 & 0 & 0 & 0 & 0 & -1 \\ 0 & 0 & 0 & 0 & 0 & 0 \\ 0 & 0 & 0 & 0 & 0 & 0 \end{bmatrix}^T \quad (\text{A.9d})$$

$$\mathbf{b}_3^\alpha = \begin{bmatrix} -1 & 0 & 0 & 0 & 0 & 0 \\ 0 & 0 & 0 & 0 & 0 & 0 \\ 0 & 0 & 0 & 0 & 0 & 0 \end{bmatrix}^T \quad (\text{A.9e})$$

$$\mathbf{b}_3^\beta = \begin{bmatrix} 0 & 0 & 0 & 0 & 0 & 0 \\ 0 & 0 & 0 & 0 & 0 & -1 \\ 0 & 0 & 0 & -1 & 0 & 0 \end{bmatrix}^T \quad (\text{A.9f})$$

$$\mathbf{b}_4^\alpha = \begin{bmatrix} 0 & 0 & 0 & 0 & 0 & 0 \\ 1 & 0 & 0 & 0 & 0 & 0 \\ 0 & 0 & 0 & 0 & 0 & 0 \end{bmatrix}^T \quad (\text{A.9g})$$

$$\mathbf{b}_4^\beta = \begin{bmatrix} 0 & 0 & 0 & 0 & 0 & 1 \\ 0 & 0 & 0 & 0 & 0 & 0 \\ 0 & 0 & 0 & 0 & 0 & 0 \end{bmatrix}^T \quad (\text{A.9h})$$

The shape functions in Equation (5.28) are given as [319]

$$\mathbf{N}^\alpha = \begin{bmatrix} 0 & & 0 & & \dots \\ & N_1 & & N_2 & \dots \\ & & N_1 & & N_2 & \dots \end{bmatrix} \quad (\text{A.10a})$$

$$\mathbf{N}^\beta = \begin{bmatrix} N_1 & & N_2 & & \dots \\ & 0 & & 0 & \dots \\ & & 0 & & 0 & \dots \end{bmatrix} \quad (\text{A.10b})$$

Obviously, the products $\mathbf{N}^{\alpha\text{T}}\mathbf{N}^{\beta}$ and $\mathbf{N}^{\beta\text{T}}\mathbf{N}^{\alpha}$ vanish and consequently there is only one mass matrix, contrary to the other coefficient matrices. The real coefficient matrices are obtained as

$$\bar{\mathbf{E}}_0 = \int_{-1}^1 \mathbf{B}_1^{\alpha\text{T}} \mathbf{D} \mathbf{B}_1^{\alpha} |J| d\eta + \int_{-1}^1 \mathbf{B}_1^{\beta\text{T}} \mathbf{D} \mathbf{B}_1^{\beta} |J| d\eta \quad (\text{A.11a})$$

$$\bar{\bar{\mathbf{E}}}_0 = - \int_{-1}^1 \mathbf{B}_1^{\alpha\text{T}} \mathbf{D} \mathbf{B}_1^{\beta} |J| d\eta + \int_{-1}^1 \mathbf{B}_1^{\beta\text{T}} \mathbf{D} \mathbf{B}_1^{\alpha} |J| d\eta \quad (\text{A.11b})$$

$$\bar{\mathbf{E}}_1 = \int_{-1}^1 \mathbf{B}_2^{\alpha\text{T}} \mathbf{D} \mathbf{B}_1^{\alpha} |J| d\eta + \int_{-1}^1 \mathbf{B}_2^{\beta\text{T}} \mathbf{D} \mathbf{B}_1^{\beta} |J| d\eta \quad (\text{A.11c})$$

$$\bar{\bar{\mathbf{E}}}_1 = - \int_{-1}^1 \mathbf{B}_2^{\alpha\text{T}} \mathbf{D} \mathbf{B}_1^{\beta} |J| d\eta + \int_{-1}^1 \mathbf{B}_2^{\beta\text{T}} \mathbf{D} \mathbf{B}_1^{\alpha} |J| d\eta \quad (\text{A.11d})$$

$$\bar{\mathbf{E}}_2 = \int_{-1}^1 \mathbf{B}_2^{\alpha\text{T}} \mathbf{D} \mathbf{B}_2^{\alpha} |J| d\eta + \int_{-1}^1 \mathbf{B}_2^{\beta\text{T}} \mathbf{D} \mathbf{B}_2^{\beta} |J| d\eta \quad (\text{A.11e})$$

$$\bar{\bar{\mathbf{E}}}_2 = - \int_{-1}^1 \mathbf{B}_2^{\alpha\text{T}} \mathbf{D} \mathbf{B}_2^{\beta} |J| d\eta + \int_{-1}^1 \mathbf{B}_2^{\beta\text{T}} \mathbf{D} \mathbf{B}_2^{\alpha} |J| d\eta \quad (\text{A.11f})$$

A.4 Inverse iteration for a generalized eigenvalue problem

The case of a generalized eigenvalue problem can be treated very similarly to the standard eigenvalue problem as described in [277]. Let λ_j, \mathbf{u}_j denote the solutions of the generalized eigenvalue problem

$$\mathbf{A}_1 \mathbf{u}_j = \lambda_j \mathbf{A}_2 \mathbf{u}_j \quad (\text{A.12})$$

We define the vector \mathbf{y} as the solution of the following system of equations

$$[\mathbf{A}_1 - \tau \mathbf{A}_2] \mathbf{y} = \mathbf{A}_2 \mathbf{b} \quad (\text{A.13})$$

where \mathbf{b} is a random nonzero complex vector and τ is a scalar. We expand the vectors \mathbf{y} and \mathbf{b} as linear combinations of the eigenvectors

$$\mathbf{y} = \sum_j \alpha_j \mathbf{u}_j \quad (\text{A.14})$$

$$\mathbf{b} = \sum_j \beta_j \mathbf{u}_j \quad (\text{A.15})$$

Substituting Equations (A.14) and (A.15) into (A.13) yields

$$\sum_j [\mathbf{A}_1 - \tau \mathbf{A}_2] \alpha_j \mathbf{u}_j = \sum_j \beta_j \mathbf{A}_2 \mathbf{u}_j \quad (\text{A.16})$$

or

$$\sum_j \alpha_j (\lambda_j - \tau) \mathbf{A}_2 \mathbf{u}_j = \sum_j \beta_j \mathbf{A}_2 \mathbf{u}_j \quad (\text{A.17})$$

We obtain the same relationship between the coefficients α_j and β_j as for standard eigenvalue problems:

$$\alpha_j = \frac{\beta_j}{\lambda_j - \tau} \quad (\text{A.18})$$

If τ is close to one eigenvalue λ_k , the corresponding coefficient α_k becomes large and the solution \mathbf{y} is close to the eigenvector \mathbf{u}_k , up to a normalization. The vector \mathbf{b} has to be chosen in a way that the coefficient β_k is not accidentally very small compared to the other coefficients. In the current application this is guaranteed by using an eigenvector corresponding to the same mode at a previous frequency step.

Bibliography

- [1] B. Hull, V. John, Non-destructive testing, 1st Edition, Springer-Verlag, 1988.
- [2] J. Krautkrämer, H. Krautkrämer, Ultrasonic testing of materials, 4th Edition, Springer Verlag, 1990.
- [3] O. Büyüköztürk, Imaging of concrete structures, NDT&E International 31 (4) (1998) 233–243.
- [4] B. Helifa, A. Oulhadj, A. Benbelghit, I. Lefkaier, F. Boubenider, D. Boutassouna, Detection and measurement of surface cracks in ferromagnetic materials using eddy current testing, NDT&E International 39 (5) (2006) 384–390.
- [5] D. C. Jiles, Review of magnetic methods for nondestructive evaluation, NDT International 21 (5) (1988) 311–319.
- [6] D. Titman, Applications of thermography in non-destructive testing of structures, NDT&E International 34 (2) (2001) 149–154.
- [7] D. Bates, G. Smith, D. Lu, J. Hewitt, Rapid thermal non-destructive testing of aircraft components, Composites Part B: Engineering 31 (3) (2000) 175–185.
- [8] A. A. Shah, Y. Ribakov, Non-destructive measurements of crack assessment and defect detection in concrete structures, Materials & Design 29 (1) (2008) 61–69.
- [9] J. Schors, K. Harbich, M. P. Hentschel, A. Lange, Non-destructive micro crack detection in modern materials, in: ECNDT, 2006, pp. 1–5.
- [10] X. Chen, J.-Y. Kim, K. Kurtis, J. Qu, C. Shen, L. Jacobs, Characterization of progressive microcracking in Portland cement mortar using nonlinear ultrasonics, NDT&E International 41 (2) (2008) 112–118.
- [11] S. I. Sokolov, Zur Frage der Fortpflanzung ultraakustischer Schwingungen in verschiedenen Körpern, Elektrische Nachrichten-Technik 6 (11) (1929) 454–461.
- [12] E. Meyer, E. Bock, Hörschall-und Ultraschalluntersuchungen von Betonbalken mit Rissen, Akustische Zeitschrift 4 (1939) 231–237.

BIBLIOGRAPHY

- [13] B. A. Auld, *Acoustic fields and waves in solids Volume I*, 2nd Edition, Krieger Publishing Company, 1990.
- [14] J. L. Rose, *Ultrasonic waves in solid media*, 1st Edition, Cambridge University Press, 1999.
- [15] I. A. Viktorov, *Rayleigh and Lamb waves*, Plenum Press, 1967.
- [16] R. Ávila Carrera, A. Rodríguez-Castellanos, F. J. Sánchez-Sesma, C. Ortiz-Alemán, Rayleigh-wave scattering by shallow cracks using the indirect boundary element method, *Journal of Geophysics and Engineering* 6 (2009) 221–230.
- [17] B. Masserey, P. Fromme, Surface defect detection in stiffened plate structures using Rayleigh-like waves, *NDT&E International* 42 (2009) 564–572.
- [18] D. Royer, E. Dieulesaint, *Elastic waves in solids I: Free and guided propagation*, 1st Edition, Springer, 2000.
- [19] R. E. Collin, *Field theory of guided waves*, 2nd Edition, IEEE Press, 1991.
- [20] H. Lamb, On waves in an elastic plate, *Proceedings of the Royal Society of London* 93 (648) (1917) 114–128.
- [21] J. Li, J. L. Rose, Excitation and propagation of non-axisymmetric guided waves in a hollow cylinder, *Journal of the Acoustical Society of America* 109 (2) (2001) 457–464.
- [22] T. Hayashi, W.-J. Song, J. L. Rose, Guided wave dispersion curves for a bar with an arbitrary cross-section, a rod and rail example, *Ultrasonics* 41 (3) (2003) 175–183.
- [23] D. N. Alleyne, P. Cawley, The interaction of Lamb waves with defects, *IEEE Transactions on Ultrasonics, Ferroelectrics and Frequency Control* 39 (3) (1992) 381–97.
- [24] P. D. Wilcox, Lamb wave inspection of large structures using permanently attached transducers, Ph.D. thesis, Imperial College of Science, Technology and Medicine (1998).
- [25] L. Yam, Z. Wei, L. Cheng, W. Wong, Numerical analysis of multi-layer composite plates with internal delamination, *Computers & Structures* 82 (2004) 627–637.
- [26] K. Diamanti, C. Soutis, J. Hodgkinson, Lamb waves for the non-destructive inspection of monolithic and sandwich composite beams, *Composites Part A: Applied Science and Manufacturing* 36 (2) (2005) 189–195.
- [27] Z. Su, L. Ye, Y. Lu, Guided Lamb waves for identification of damage in composite structures: A review, *Journal of Sound and Vibration* 295 (2006) 753–780.
- [28] J. Li, J. L. Rose, Natural beam focusing of non-axisymmetric guided waves in large-diameter pipes., *Ultrasonics* 44 (1) (2006) 35–45.

- [29] A. Baltazar, C. D. Hernandez-Salazar, B. Manzanares-Martinez, Study of wave propagation in a multiwire cable to determine structural damage, *NDT&E International* 43 (2010) 726–732.
- [30] S. Banerjee, F. Ricci, E. Monaco, A. Mal, A wave propagation and vibration-based approach for damage identification in structural components, *Journal of Sound and Vibration* 322 (2009) 167–183.
- [31] R. Gangadharan, D. R. Mahapatra, S. Gopalakrishnan, C. R. L. Murthy, M. R. Bhat, On the sensitivity of elastic waves due to structural damages: Time-frequency based indexing method, *Journal of Sound and Vibration* 320 (2009) 915–941.
- [32] D. Aggelis, T. Matikas, Effect of plate wave dispersion on the acoustic emission parameters in metals, *Computers & Structures* 98-99 (2012) 17–22.
- [33] P. B. Nagy, R. M. Kent, Ultrasonic assessment of Poisson's ratio in thin rods, *Journal of the Acoustical Society of America* 98 (5) (1995) 2694–2701.
- [34] F. B. Cegla, P. Cawley, M. J. S. Lowe, Material property measurement using the quasi-Scholte mode - A waveguide sensor, *Journal of the Acoustical Society of America* 117 (3) (2005) 1098–1107.
- [35] M. Sale, P. Rizzo, A. Marzani, Semi-analytical formulation for the guided waves-based reconstruction of elastic moduli, *Mechanical Systems and Signal Processing* 25 (2011) 2241–2256.
- [36] J. Rautenberg, Ein wellenleiterbasiertes Verfahren zur Bestimmung von Materialdaten für die realitätsnahe Simulation von Schallausbreitungsphänomenen am Beispiel stark absorbierender Kunststoffe, Ph.D. thesis, Universität Paderborn (2012).
- [37] T. K. Vogt, M. J. S. Lowe, P. Cawley, Measurement of the material properties of viscous liquids using ultrasonic guided waves, *IEEE Transactions on Ultrasonics, Ferroelectrics and Frequency Control* 51 (6) (2004) 737–747.
- [38] H. Faustmann, M. Münch, G. Lindner, M. Schmitt, M. Springer, Measurement of the properties of liquids based on the dispersion of Lamb waves in an acoustic waveguide, *Physics Procedia* 3 (1) (2010) 959–964.
- [39] J. Rautenberg, F. Bause, B. Henning, Geführte akustische Wellen zur Flüssigkeitscharakterisierung, *Technisches Messen* 79 (3) (2012) 135–142.
- [40] C. Chree, On the longitudinal vibrations of aeolotropic bars with one axis of material symmetry, *The Quarterly Journal of Pure and Applied Mathematics* 96 (1890) 340–358.
- [41] R. E. Booker, W. B. Fraser, Dispersion of elastic waves in a triangular bar, *Journal of Sound and Vibration* 18 (2) (1971) 261–269.

- [42] A. S. Kosmodamianskii, I. A. Moiseenko, R. R. Troyan, Dispersion spectrum of an anisotropic waveguide with sector-shaped cross section and fixed boundary, *International Applied Mechanics* 41 (9) (2005) 995–999.
- [43] W. T. Thomson, Transmission of elastic waves through a stratified solid medium, *Journal of Applied Physics* 21 (89) (1950) 89–93.
- [44] N. A. Haskell, The dispersion of surface waves on multilayered media, *Bulletin of the Seismological Society of America* 43 (1) (1953) 17–34.
- [45] L. Knopoff, A matrix method for elastic wave problems, *Bulletin of the Seismological Society of America* 54 (1) (1964) 431–438.
- [46] A. H. Nayfeh, The general problem of elastic wave propagation in multilayered anisotropic media, *Journal of the Acoustical Society of America* 89 (1991) 1521–1531.
- [47] M. J. S. Lowe, Matrix techniques for modeling ultrasonic waves in multilayered media, *IEEE Transactions on Ultrasonics, Ferroelectrics and Frequency Control* 42 (4) (1995) 525–542.
- [48] S. Crampin, D. B. Taylor, The propagation of surface waves in anisotropic media, *Geophysical Journal of the Royal Astronomical Society* 25 (1971) 71–87.
- [49] M. Lou, S. Crampin, Dispersion of guided waves in thin anisotropic waveguides, *Geophysical Journal International* 107 (1991) 545–555.
- [50] B. Pavlakovic, M. J. S. Lowe, D. N. Alleyne, Disperse: A general purpose program for creating dispersion curves, in: D. Thompson, D. Chimenti (Eds.), *Review of Progress in Quantitative NDE*, Plenum Press, 1997, pp. 185–192.
- [51] B. Pavlakovic, M. J. S. Lowe, disperse [computer program], version 2.0.16i (2011).
- [52] F. Seco, J. M. Martín, A. Jiménez, J. L. Pons, L. Calderón, R. Ceres, PCDISP: A tool for the simulation of wave propagation in cylindrical waveguides, in: *9th International Congress on Sound and Vibration*, Orlando, Florida, 2002, pp. 1–7.
- [53] F. Seco, A. R. Jiménez, Modelling the generation and propagation of ultrasonic signals in cylindrical waveguides, in: *Ultrasonic waves*, Intech Open Access Publisher, 2012, Ch. 1, pp. 1–28.
- [54] G. M. L. Gladwell, U. C. Tahbildar, Finite element analysis of the axisymmetric vibrations of cylinders, *Journal of Sound and Vibration* 22 (2) (1972) 143–157.
- [55] M. Åberg, P. Gudmundson, The usage of standard finite element codes for computation of dispersion relations in materials with periodic microstructure, *Journal of the Acoustical Society of America* 102 (1997) 2007–2013.

- [56] B. R. Mace, D. Duhamel, M. J. Brennan, L. Hinke, Finite element prediction of wave motion in structural waveguides, *Journal of the Acoustical Society of America* 117 (5) (2005) 2835–2843.
- [57] M. Maess, N. Wagner, L. Gaul, Dispersion curves of fluid filled elastic pipes by standard FE models and eigenpath analysis, *Journal of Sound and Vibration* 296 (2006) 264–276.
- [58] Ş. Sorohan, N. Constantin, M. Găvan, V. Anghel, Extraction of dispersion curves for waves propagating in free complex waveguides by standard finite element codes, *Ultrasonics* 51 (2011) 503–515.
- [59] A.-C. Hladky-Hennion, Finite element analysis of the propagation of acoustic waves in waveguides, *Journal of Sound and Vibration* 194 (2) (1996) 119–136.
- [60] R. B. Nelson, S. B. Dong, R. D. Kalra, Vibration and waves in laminated orthotropic circular cylinders, *Journal of Sound and Vibration* 18 (3) (1971) 429–444.
- [61] B. Aalami, Waves in prismatic guides of arbitrary cross section, *Journal of Applied Mechanics* 40 (4) (1973) 1067–1072.
- [62] L. Gavrić, Finite element computation of dispersion properties of thin-walled waveguides, *Journal of Sound and Vibration* 173 (1) (1994) 113–124.
- [63] I. Bartoli, A. Marzani, F. Lanza di Scalea, E. Viola, Modeling wave propagation in damped waveguides of arbitrary cross-section, *Journal of Sound and Vibration* 295 (2006) 685–707.
- [64] S. K. Datta, A. H. Shah, R. L. Bratton, T. Chakraborty, Wave propagation in laminated composite plates, *Journal of the Acoustical Society of America* 83 (6) (1988) 2020–2026.
- [65] J. M. Galán, R. Abascal, Elastodynamic guided wave scattering in infinite plates, *International Journal for Numerical Methods in Engineering* 58 (7) (2003) 1091–1118.
- [66] K. H. Huang, S. B. Dong, Propagating waves and edge vibrations in anisotropic composite cylinders, *Journal of Sound and Vibration* 96 (1984) 363–379.
- [67] N. Rattanawangcharoen, A. H. Shah, S. K. Datta, Wave propagation in laminated composite circular cylinders, *International Journal of Solids and Structures* 29 (6) (1992) 767–781.
- [68] A. Marzani, E. Viola, I. Bartoli, F. Lanza di Scalea, P. Rizzo, A semi-analytical finite element formulation for modeling stress wave propagation in axisymmetric damped waveguides, *Journal of Sound and Vibration* 318 (2008) 488–505.
- [69] P. Bocchini, A. Marzani, E. Viola, Graphical user interface for guided acoustic waves, *Journal of Computing in Civil Engineering* 25 (2011) 202–211.

- [70] M. J. S. Lowe, O. Diligent, Low-frequency reflection characteristics of the s Lamb wave from a rectangular notch in a plate, *Journal of the Acoustical Society of America* 111 (2002) 64.
- [71] Y. Cho, J. L. Rose, A boundary element solution for a mode conversion study on the edge reflection of Lamb waves, *Journal of the Acoustical Society of America* 99 (4) (1996) 2097–2109.
- [72] J. J. Pérez-Gavilán, M. H. Aliabadi, A Galerkin boundary element formulation with dual reciprocity for elastodynamics, *International Journal for Numerical Methods in Engineering* 48 (9) (2000) 1331–1344.
- [73] P. Fedelinski, Boundary element method in dynamic analysis of structures with cracks, *Engineering Analysis with Boundary Elements* 28 (9) (2004) 1135–1147.
- [74] R. Balasubramanyam, D. Quinney, R. E. Challis, C. P. D. Todd, A finite-difference simulation of ultrasonic Lamb waves in metal sheets with experimental verification, *Journal of Physics D: Applied Physics* 29 (1) (1996) 147–155.
- [75] F. Schubert, A. Peiffer, B. Köhler, T. Sanderson, The elastodynamic finite integration technique for waves in cylindrical geometries, *Journal of the Acoustical Society of America* 104 (November 1998) (1998) 2604–2614.
- [76] F. Schubert, Numerical time-domain modeling of linear and nonlinear ultrasonic wave propagation using finite integration techniques-theory and applications, *Ultrasonics* 42 (2004) 221–229.
- [77] C. Song, J. P. Wolf, The scaled boundary finite-element method - alias consistent infinitesimal finite-element cell method - for elastodynamics, *Computer Methods in Applied Mechanics and Engineering* 147 (1997) 329–355.
- [78] J. P. Wolf, C. Song, The scaled boundary finite-element method - a primer: derivations, *Computers & Structures* 78 (2000) 191–210.
- [79] J. P. Wolf, The scaled boundary finite element method, 1st Edition, John Wiley & Sons Ltd., 2003.
- [80] J. P. Wolf, C. Song, Finite-element modelling of unbounded media, 1st Edition, John Wiley & Sons, 1999.
- [81] C. Song, A matrix function solution for the scaled boundary finite-element equation in statics, *Computer Methods in Applied Mechanics and Engineering* 193 (2004) 2325–2356.
- [82] H. Man, C. Song, W. Gao, F. Tin-Loi, A unified 3D-based technique for plate bending analysis using scaled boundary finite element method, *International Journal for Numerical Methods in Engineering* 91 (2012) 491–515.

-
- [83] C. Song, Dynamic analysis of unbounded domains by a reduced set of base functions, *Computer Methods in Applied Mechanics and Engineering* 195 (33-36) (2006) 4075–4094.
- [84] C. Song, M. H. Bazyar, Development of a fundamental-solution-less boundary element method for exterior wave problems, *Communications in Numerical Methods in Engineering* 24 (2008) 257–279.
- [85] X. Wang, F. Jin, S. Prempramote, C. Song, Time-domain analysis of gravity dam-reservoir interaction using high-order doubly asymptotic open boundary, *Computers & Structures* 89 (7-8) (2011) 668–680.
- [86] C. Birk, C. Song, A continued-fraction approach for transient diffusion in unbounded medium, *Computer Methods in Applied Mechanics and Engineering* 198 (2009) 2576–2590.
- [87] C. Song, Z. Vrcelj, Evaluation of dynamic stress intensity factors and T-stress using the scaled boundary finite-element method, *Engineering Fracture Mechanics* 75 (8) (2008) 1960–1980.
- [88] C. Song, F. Tin-Loi, W. Gao, A definition and evaluation procedure of generalized stress intensity factors at cracks and multi-material wedges, *Engineering Fracture Mechanics* 77 (12) (2010) 2316–2336.
- [89] E. T. Ooi, C. Song, F. Tin-loi, Z. Yang, Polygon scaled boundary finite elements for crack propagation modelling, *International Journal for Numerical Methods in Engineering* 91 (2012) 319–342.
- [90] C. Song, The scaled boundary finite element method in structural dynamics, *International Journal for Numerical Methods in Engineering* 77 (2009) 1139–1171.
- [91] H. Gravenkamp, C. Song, J. Prager, A numerical approach for the computation of dispersion relations for plate structures using the scaled boundary finite element method, *Journal of Sound and Vibration* 331 (2012) 2543–2557.
- [92] H. Gravenkamp, C. Song, J. Prager, Numerical computation of dispersion relations in wave guides, *Proceedings in Applied Mathematics and Mechanics* 12 (2012) 535–536.
- [93] H. Gravenkamp, C. Song, J. Prager, Numerische Berechnung der Dispersionseigenschaften von Lambwellen in Platten mit beliebiger Materialzusammensetzung, in: *DAGA 38. Jahrestagung für Akustik*, 2012, pp. 955–956.
- [94] H. Gravenkamp, H. Man, C. Song, J. Prager, The computation of dispersion relations for three-dimensional elastic waveguides using the Scaled Boundary Finite Element Method, *Journal of Sound and Vibration* 332 (2013) 3756–3771.

- [95] H. Gravenkamp, J. Prager, H. Man, C. Birk, C. Song, Numerical computation of dispersion relations in three-dimensional waveguides, in: B. Samali, M. M. Attard, C. Song (Eds.), *From Materials to Structures: Advancement through Innovation*, 1st Edition, Taylor & Francis Group, London, 2013, pp. 897–902.
- [96] H. Gravenkamp, C. Birk, C. Song, The computation of dispersion relations for axisymmetric waveguides using the Scaled Boundary Finite Element Method, *Ultrasonics* 54 (5) (2014) 1373–1385.
- [97] H. Gravenkamp, C. Song, J. Prager, Numerical simulation of ultrasonic guided waves using the Scaled Boundary Finite Element Method, in: *IEEE International Ultrasonics Symposium*, 2012, pp. 2686–2689.
- [98] M. Subhani, J. Li, H. Gravenkamp, B. Samali, Effect of elastic modulus and Poisson's ratio on guided wave dispersion using transversely isotropic material modelling, *Advanced Materials Research* 778 (2013) 303–311.
- [99] H. Gravenkamp, C. Birk, C. Song, Computation of dispersion curves for embedded waveguides using a dashpot boundary condition, *Journal of the Acoustical Society of America* 135 (3) (2014) 1127–1138.
- [100] H. Gravenkamp, F. Bause, C. Song, On the computation of dispersion curves for axisymmetric elastic waveguides using the Scaled Boundary Finite Element Method, *Computers & Structures* 131 (2014) 46–55.
- [101] H. Gravenkamp, J. Prager, A. A. Saputra, C. Song, The simulation of Lamb waves in a cracked plate using the scaled boundary finite element method, *Journal of the Acoustical Society of America* 132 (3) (2012) 1358–1367.
- [102] H. Gravenkamp, A. A. Saputra, C. Song, J. Prager, Detection of defects in thin-walled structures by means of Lamb waves, *AIP Conference Proceedings* 1433 (2012) 443–446.
- [103] J. Prager, H. Gravenkamp, M.-U. Rahman, E. Köppe, Einsatz geführter Wellen für die Ultraschallprüfung, *Technisches Messen* 79 (5) (2012) 251–261.
- [104] A. A. Saputra, C. Birk, C. Song, H. Gravenkamp, Numerical modelling of Lamb waves in cracked plates using the scaled boundary finite element method, in: B. Samali, M. M. Attard, C. Song (Eds.), *From Materials to Structures: Advancement through Innovation*, 1st Edition, Taylor & Francis Group, London, 2013, pp. 927–932.
- [105] J. D. Achenbach, The linearized theory of elasticity, in: H. A. Lauwerier, W. T. Koiter (Eds.), *Wave propagation in elastic solids*, 1st Edition, North-Holland Publishing Company, 1973, pp. 46–78.
- [106] E. Kausel, Strain, stresses, and the elastic wave equation, in: *Fundamental solutions in elastodynamics*, 1st Edition, Cambridge University Press, 2006, Ch. 1.4, pp. 13–26.

-
- [107] K.-J. Bathe, E. L. Wilson, Numerical methods in finite element analysis, 1st Edition, Prentice-Hall, Inc., Englewood Cliffs, New Jersey, 1976.
- [108] C. S. Desai, Elementary finite element method, 1st Edition, Prentice-Hall, Inc., 1979.
- [109] R. D. Cook, D. S. Malkus, M. E. Plesha, R. J. Witt, Concepts and applications of finite element analysis, 4th Edition, John Wiley & Sons, 2002.
- [110] C. Song, J. P. Wolf, The scaled boundary finite-element method - a primer: solution procedures, *Computers & Structures* 78 (2000) 211–225.
- [111] K.-J. Bathe, E. L. Wilson, Formulation and calculation of isoparametric finite element matrices, in: Numerical methods in finite element analysis, Prentice-Hall, Inc., 1976, Ch. 4.3, pp. 124–171.
- [112] O. C. Zienkiewicz, R. I. Taylor, General problems in solid mechanics and non-linearity, in: The finite element method for solid and structural mechanics, 1st Edition, Butterworth-Heinemann, 2005, Ch. 1, pp. 1–16.
- [113] W. Wonham, On a matrix Riccati equation of stochastic control, *SIAM Journal on Control* 6 (4) (1968) 681–697.
- [114] A. J. Laub, A Schur method for solving algebraic Riccati equations, *IEEE Transactions on Automatic Control*, 24 (6) (1979) 913–921.
- [115] J. P. Wolf, Variation of material properties in radial direction, in: The scaled boundary finite element method, 1st Edition, John Wiley & Sons Ltd., 2003, Ch. 21.1, pp. 271–277.
- [116] M. H. Bazyar, C. Song, Time-harmonic response of non-homogeneous elastic unbounded domains using the scaled boundary finite-element method, *Earthquake Engineering & Structural Dynamics* 35 (3) (2006) 357–383.
- [117] C. Song, F. Tin-Loi, W. Gao, Transient dynamic analysis of interface cracks in anisotropic bimetals by the scaled boundary finite-element method, *International Journal of Solids and Structures* 47 (7-8) (2010) 978–989.
- [118] C. Song, J. P. Wolf, Consistent infinitesimal finite-element cell method: three-dimensional vector wave equation, *International Journal for Numerical Methods in Engineering* 39 (1996) 2189–2208.
- [119] M. Schauer, S. Langer, J. E. Roman, E. S. Quintana-Ortí, Large scale simulation of wave propagation in soils interacting with structures using FEM and SBFEM, *Journal of Computational Acoustics* 19 (1) (2011) 75–93.
- [120] Z. J. Yang, A. J. Deeks, Fully-automatic modelling of cohesive crack growth using a finite element-scaled boundary finite element coupled method, *Engineering Fracture Mechanics* 74 (16) (2007) 2547–2573.

- [121] E. T. Ooi, Z. J. Yang, Modelling crack propagation in reinforced concrete using a hybrid finite element-scaled boundary finite element method, *Engineering Fracture Mechanics* 78 (2) (2011) 252–273.
- [122] M. Schauer, S. Langer, Numerical simulations of pile integrity tests using a coupled FEM SBFEM approach, *Proceedings in Applied Mathematics and Mechanics* 12 (2012) 547–548.
- [123] M. Schauer, J. E. Roman, S. Langer, E. S. Quintana-Ortí, Parallel computation of 3-D soil-structure interaction in time domain with a coupled FEM/SBFEM approach, *Journal of Scientific Computing* 52 (2012) 446–467.
- [124] J. L. Deán, C. Trillo, A. F. Doval, J. L. Fernández, Determination of thickness and elastic constants of aluminum plates from full-field wavelength measurements of single-mode narrowband Lamb waves, *Journal of the Acoustical Society of America* 124 (3) (2008) 1477–1489.
- [125] E. Larose, P. Roux, M. Campillo, Reconstruction of Rayleigh-Lamb dispersion spectrum based on noise obtained from an air-jet forcing, *Journal of the Acoustical Society of America* 122 (6) (2007) 3437–3444.
- [126] Y.-C. Lee, S.-W. Cheng, Measuring Lamb wave dispersion curves of a bi-layered plate and its application on material characterization of coating, *IEEE Transactions on Ultrasonics, Ferroelectrics and Frequency Control* 48 (3) (2001) 830–837.
- [127] Y. H. Kim, S.-J. Song, S.-D. Kwon, Y.-M. Cheong, H.-K. Jung, Determination of ultrasonic wave velocities and phase velocity dispersion curves of an Inconel 600 plate using resonant ultrasound spectroscopy and leaky Lamb waves, *Ultrasonics* 42 (2004) 551–555.
- [128] M.-X. Deng, J. Yang, Characterization of elastic anisotropy of a solid plate using nonlinear Lamb wave approach, *Journal of Sound and Vibration* 308 (2007) 201–211.
- [129] L. Liu, F. G. Yuan, A linear mapping technique for dispersion removal of Lamb waves, *Structural Health Monitoring* 9 (2010) 75–86.
- [130] L. De Marchi, A. Marzani, N. Speciale, E. Viola, A passive monitoring technique based on dispersion compensation to locate impacts in plate-like structures, *Smart Materials and Structures* 20 (3) (2011) 1–9.
- [131] R. Sicard, J. Goyette, D. Zellouf, A numerical dispersion compensation technique for time recompression of Lamb wave signals, *Ultrasonics* 40 (2002) 727–732.
- [132] K. Toiyama, T. Hayashi, Pulse compression technique considering velocity dispersion of guided wave, *Review of Quantitative Nondestructive Evaluation* 27 (2008) 587–593.

- [133] P. D. Wilcox, A rapid signal processing technique to remove the effect of dispersion from guided wave signals., *IEEE Transactions on Ultrasonics, Ferroelectrics and Frequency Control* 50 (4) (2003) 419–27.
- [134] W. H. Prosser, M. D. Seale, B. T. Smith, Time-frequency analysis of the dispersion of Lamb modes, *Journal of the Acoustical Society of America* 105 (5) (1999) 2669.
- [135] P. Wilcox, M. J. S. Lowe, P. Cawley, The effect of dispersion on long-range inspection using ultrasonic guided waves, *NDT&E International* 34 (1) (2001) 1–9.
- [136] S. S. Kessler, S. M. Spearing, C. Soutis, Damage detection in composite materials using Lamb wave methods, *Smart Materials and Structures* 11 (2) (2002) 269–278.
- [137] X. Cao, F. Jin, I. Jeon, Calculation of propagation properties of Lamb waves in a functionally graded material (FGM) plate by power series technique, *NDT&E International* 44 (2011) 84–92.
- [138] J. Lysmer, Lumped mass method for Rayleigh waves, *Bulletin of the Seismological Society of America* 60 (1) (1970) 89–104.
- [139] E. Kausel, Forced vibrations of circular foundations on layered media, Ph.D. thesis, Massachusetts Institute of Technology (1974).
- [140] E. Kausel, Wave propagation in anisotropic layered media, *International Journal for Numerical Methods in Engineering* 23 (1986) 1567–1578.
- [141] E. Kausel, Thin-layer method: Formulation in the time domain, *International Journal for Numerical Methods in Engineering* 37 (1994) 927–941.
- [142] A. Chakraborty, S. Gopalakrishnan, E. Kausel, Wave propagation analysis in inhomogeneous piezo-composite layer by the thin-layer method, *International Journal for Numerical Methods in Engineering* 64 (5) (2005) 567–598.
- [143] A. H. Shah, S. K. Datta, Harmonic waves in a periodically laminated medium, *International Journal of Solids and Structures* 18 (5) (1982) 397–410.
- [144] S. I. Rokhlin, Ultrasonic waves in layered anisotropic media: characterization of multidirectional composites, *International Journal of Solids and Structures* 39 (16) (2002) 4133–4149.
- [145] N. Guo, P. Cawley, The interaction of Lamb waves with delaminations in composite laminates, *Journal of the Acoustical Society of America* 94 (4) (1993) 2240–2246.
- [146] A. Demcenko, L. Mazeika, Calculation of Lamb waves dispersion curves in multi-layered planar structures, *Ultragarsas* 44 (3) (2002) 15–17.

- [147] J. Han, C. Kim, J. Kim, The propagation of Lamb waves in a laminated composite plate with a variable stepped thickness, *Composite Structures* 76 (4) (2006) 388–396.
- [148] X. Qi, J. L. Rose, C. Xu, Ultrasonic guided wave nondestructive testing for helicopter rotor blades, in: *17th World Conference on Nondestructive Testing*, Shanghai, China, 2008, 2008, pp. 1–7.
- [149] S. Crampin, The dispersion of surface waves in multilayered anisotropic media, *Geophysical Journal of the Royal Astronomical Society* 21 (3) (1970) 387–402.
- [150] C. C. Habeger, R. W. Mann, G. A. Baum, Ultrasonic plate waves in paper, *Ultrasonics* 3 (1979) 57–62.
- [151] A. Karmazin, E. Kirillova, W. Seemann, P. Syromyatnikov, Investigation of Lamb elastic waves in anisotropic multilayered composites applying the Green's matrix, *Ultrasonics* 51 (1) (2011) 17–28.
- [152] M. Castaings, M. J. S. Lowe, Finite element model for waves guided along solid systems of arbitrary section coupled to infinite solid media, *Journal of the Acoustical Society of America* 123 (2) (2008) 696–708.
- [153] J. M. Galán, R. Abascal, Numerical simulation of Lamb wave scattering in semi-infinite plates, *International Journal for Numerical Methods in Engineering* 1173 (2002) 1145–1173.
- [154] O. M. Mukdadi, Y. M. Desai, S. K. Datta, A. H. Shah, A. J. Niklasson, Elastic guided waves in a layered plate with rectangular cross section, *Journal of the Acoustical Society of America* 112 (5) (2002) 1766–1779.
- [155] G. R. Liu, J. Tani, K. Watanabe, T. Ohyoshi, Harmonic wave propagation in anisotropic laminated strips, *Journal of Sound and Vibration* 139 (2) (1990) 313–324.
- [156] G. R. Liu, K. Y. Dai, X. Han, T. Ohyoshi, Dispersion of waves and characteristic wave surfaces in functionally graded piezoelectric plates, *Journal of Sound and Vibration* 268 (2003) 131–147.
- [157] C. Song, J. P. Wolf, The scaled boundary finite element method - alias consistent infinitesimal finite element cell method - for diffusion, *International Journal for Numerical Methods in Engineering* 45 (1999) 1403–1431.
- [158] A. J. Deeks, J. P. Wolf, A virtual work derivation of the scaled boundary finite-element method for elastostatics, *Computational Mechanics* 28 (2002) 489–504.
- [159] E. T. Ooi, Z. J. Yang, Modelling dynamic crack propagation using the scaled boundary finite element method, *International Journal for Numerical Methods in Engineering* 88 (2011) 329–349.

- [160] T. H. Vu, A. J. Deeks, Use of higher-order shape functions in the scaled boundary finite element method, *International Journal for Numerical Methods in Engineering* 65 (2006) 1714–1733.
- [161] J.-F. Maitre, O. Pourquier, Condition number and diagonal preconditioning: comparison of the p-version, *Numerische Mathematik* 74 (1996) 69–84.
- [162] G. Seriani, 3-D large-scale wave propagation modeling by spectral element method on Cray T3E multiprocessor, *Computer Methods in Applied Mechanics and Engineering* 164 (1998) 235–247.
- [163] D. Komatitsch, J. Tromp, Introduction to the spectral element method for three-dimensional seismic wave propagation, *Geophysical Journal International* 139 (1999) 806–822.
- [164] M. A. Taylor, B. A. Wingate, A generalized diagonal mass matrix spectral element method for non-quadrilateral elements, *Applied Numerical Mathematics* 33 (2000) 259–265.
- [165] W. Heinrichs, B. I. Loch, Spectral schemes on triangular elements, *Journal of Computational Physics* 173 (2001) 279–301.
- [166] W. H. Press, S. A. Teukolsky, W. T. Vetterling, B. P. Flannery, Interpolation and extrapolation, in: *Numerical recipes in C*, 2nd Edition, Cambridge University Press, 1992, Ch. 3, pp. 105–128.
- [167] J. M. Melenk, On condition numbers in hp-FEM with Gauss-Lobatto-based shape functions, *Journal of Computational and Applied Mathematics* 139 (2002) 21–48.
- [168] S. V. Parter, On the Legendre-Gauss-Lobatto points and weights, *Journal of Scientific Computing* 14 (4) (1999) 347–355.
- [169] T. Warburton, An explicit construction of interpolation nodes on the simplex, *Journal of Engineering Mathematics* 56 (2006) 247–262.
- [170] P. J. Davis, I. Polonsky, Numerical interpolation, differentiation, and integration, in: M. Abramowitz, I. A. Stegun (Eds.), *Handbook of mathematical functions*, 10th Edition, National Bureau of Standards, 1972, Ch. 25, pp. 877–925.
- [171] W. Kerner, Large-scale complex eigenvalue problems, *Journal of Computational Physics* 85 (1989) 1–85.
- [172] N. J. Higham, Special classes of matrices, in: *Functions of matrices*, 1st Edition, Siam, 2008, Ch. B.4, pp. 323–324.
- [173] G. H. Golub, C. F. Van Loan, The unsymmetric eigenvalue problem, in: *Matrix Computations*, 3rd Edition, The John Hopkins University Press, 1996, pp. 308–391.

- [174] E. Anderson, Z. Bai, C. Bischof, S. Blackford, J. Demmel, J. Dongarra, J. Du Croz, S. Greenbaum, A. Hammarling, A. McKenney, D. Sorensen, LAPACK users' guide, 3rd Edition, Society for Industrial and Applied Mathematics, 1999.
- [175] R. B. Lehoucq, D. C. Sorensen, C. Yang, ARPACK users' guide, Siam, 1998.
- [176] C. Van Loan, A symplectic method for approximating all the eigenvalues of a Hamiltonian matrix, *Linear Algebra and its Applications* 61 (1984) 233–251.
- [177] P. Benner, R. Byers, E. Barth, Algorithm 800: Fortran 77 subroutines for computing the eigenvalues of Hamiltonian matrices I: The square-reduced method, *ACM Transactions on Mathematical Software* 26 (1) (2000) 49–77.
- [178] V. Mehrmann, D. Watkins, Structure-preserving methods for computing eigenpairs of large sparse skew-Hamiltonian/Hamiltonian pencils, *SIAM Journal on Scientific Computing* 22 (6) (2001) 1905–1925.
- [179] P. Benner, H. Fassbender, M. Stoll, Solving large-scale quadratic eigenvalue problems with Hamiltonian eigenstructure using a structure-preserving Krylov subspace method, *Electronic Transactions on Numerical Analysis* 29 (2008) 212–229.
- [180] V. Mehrmann, C. Schröder, V. Simoncini, An implicitly-restarted Krylov subspace method for real symmetric/skew-symmetric eigenproblems, *Linear Algebra and its Applications* 436 (2012) 4070–4087.
- [181] J.-M. Mencik, M. N. Ichchou, Wave finite elements in guided elastodynamics with internal fluid, *International Journal of Solids and Structures* 44 (2007) 2148–2167.
- [182] B. R. Mace, E. Manconi, Modelling wave propagation in two-dimensional structures using finite element analysis, *Journal of Sound and Vibration* 318 (2008) 884–902.
- [183] F. Tisseur, K. Meerbergen, The quadratic eigenvalue problem, *SIAM Review* 43 (2) (2001) 235–286.
- [184] X. Han, G. R. Liu, Z. C. Xi, K. Y. Lam, Transient waves in a functionally graded cylinder, *International Journal of Solids and Structures* 38 (2001) 3021–3037.
- [185] X. Han, G. R. Liu, Elastic waves in a functionally graded piezoelectric cylinder, *Smart Materials and Structures* 12 (6) (2003) 962–971.
- [186] I. A. Veres, M. B. Sayir, Wave propagation in a wooden bar, *Ultrasonics* 42 (2004) 495–499.
- [187] V. Damljanović, R. L. Weaver, Propagating and evanescent elastic waves in cylindrical waveguides of arbitrary cross section, *Journal of the Acoustical Society of America* 115 (4) (2004) 1572–1581.

-
- [188] R. M. Orris, M. Petyt, A finite element study of harmonic wave propagation in periodic structures, *Journal of Sound and Vibration* 33 (2) (1974) 223–236.
- [189] D. J. Thompson, Wheel-rail noise generation, part III: rail vibration, *Journal of Sound and Vibration* 161 (3) (1993) 421–446.
- [190] F. Treyssède, Numerical investigation of elastic modes of propagation in helical waveguides, *Journal of the Acoustical Society of America* 121 (6) (2007) 3398–3408.
- [191] F. Treyssède, Elastic waves in helical waveguides, *Wave Motion* 45 (2008) 457–470.
- [192] L. Gavrić, Computation of propagative waves in free rail using a finite element technique, *Journal of Sound and Vibration* 185 (3) (1995) 531–543.
- [193] Z. C. Xi, G. R. Liu, K. Y. Lam, H. M. Shang, Dispersion and characteristic surfaces of waves in laminated composite circular cylindrical shells, *Journal of the Acoustical Society of America* 108 (5) (2000) 2179–2186.
- [194] T. Hayashi, C. Tamayama, M. Murase, Wave structure analysis of guided waves in a bar with an arbitrary cross-section, *Ultrasonics* 44 (2006) 17–24.
- [195] L. Houillon, M. N. Ichchou, L. Jezequel, Wave motion in thin-walled structures, *Journal of Sound and Vibration* 281 (2005) 483–507.
- [196] S. D. Akbarov, M. S. Guliev, T. Kepceler, Dispersion relations of axisymmetric wave propagation in initially twisted bi-material compounded cylinders, *Journal of Sound and Vibration* 330 (2011) 1644–1664.
- [197] M. Mazzotti, A. Marzani, I. Bartoli, E. Viola, Guided waves dispersion analysis for prestressed viscoelastic waveguides by means of the SAFE method, *International Journal of Solids and Structures* 49 (2012) 2359–2372.
- [198] Y. Waki, B. R. Mace, M. J. Brennan, Numerical issues concerning the wave and finite element method for free and forced vibrations of waveguides, *Journal of Sound and Vibration* 327 (2009) 92–108.
- [199] J. E. Mottershead, M. I. Friswell, Model updating in structural dynamics: a survey, *Journal of Sound and Vibration* 167 (2) (1993) 347–375.
- [200] R. J. Allemang, The modal assurance criterion - twenty years of use and abuse, *Sound and Vibration* August (2003) 14–21.
- [201] C. A. Morales, Comments on the MAC and the NCO, and a linear modal correlation coefficient, *Journal of Sound and Vibration* 282 (2005) 529–537.
- [202] M. J. S. Lowe, Plate waves for the NDT of diffusion bonded titanium, Ph.D. thesis, University of London (1992).

BIBLIOGRAPHY

- [203] W. H. Press, S. A. Teukolsky, W. T. Vetterling, B. P. Flannery, Padé approximants, in: Numerical recipes in C, 2nd Edition, Cambridge University Press, 1992, Ch. 5.12, pp. 200–203.
- [204] G. A. Baker Jr, P. Graves-Morris, Introduction and definitions, in: Padé approximants, 2nd Edition, Cambridge University Press, 1996, Ch. 1, pp. 1–8.
- [205] J. Wolf, T. D. K. Ngoc, R. Kille, W. G. Mayer, Investigation of Lamb waves having a negative group velocity, *Journal of the Acoustical Society of America* 83 (1) (1988) 122–126.
- [206] M. F. Werby, H. Überall, The analysis and interpretation of some special properties of higher order symmetric Lamb waves: The case for plates, *Journal of the Acoustical Society of America* 111 (6) (2002) 2686–2691.
- [207] F. Simonetti, M. J. S. Lowe, On the meaning of Lamb mode nonpropagating branches, *Journal of the Acoustical Society of America* 118 (1) (2005) 186–192.
- [208] L. Pochhammer, Ueber die Fortpflanzungsgeschwindigkeiten kleiner Schwingungen in einem unbegrenzten isotropen Kreiscylinder, *Journal für die reine und angewandte Mathematik* 81 (1876) 324–336.
- [209] J. H. Baltrukonis, Axial-shear vibrations of an infinitely long composite circular cylinder, *Journal of the Acoustical Society of America* 33 (11) (1961) 1447–1457.
- [210] H. D. McNiven, J. L. Sackman, A. H. Shah, Dispersion of axially symmetric waves in composite, elastic rods, *Journal of the Acoustical Society of America* 35 (10) (1963) 573–578.
- [211] I. Mirsky, Vibrations of orthotropic, thick, cylindrical shells, *Journal of the Acoustical Society of America* 36 (1) (1964) 41.
- [212] S. Markus, D. J. Mead, Wave motion in a three-layered, orthotropic-isotropic-orthotropic composite shell, *Journal of Sound and Vibration* 181 (1) (1995) 127–147.
- [213] F. G. Yuan, C. C. Hsieh, Three-dimensional wave propagation in composite cylindrical shells, *Composite Structures* 42 (1998) 153–167.
- [214] A. E. Armenàkas, D. C. Gazis, G. Herrmann, Tables of frequencies of free vibrations of cylindrical shells, in: Free vibrations of circular cylindrical shells, 1st Edition, Pergamon Press, 1969, Ch. 2, pp. 17–201.
- [215] A. E. Armenàkas, E. S. Reitz, Propagation of harmonic waves in orthotropic circular cylindrical shells, *Journal of Applied Mechanics* 40 (1973) 168–174.
- [216] W. B. Fraser, An orthogonality relation for the modes of wave propagation in an elastic circular cylinder, *Journal of Sound and Vibration* 43 (3) (1975) 568–571.

- [217] A. D. Puckett, M. L. Peterson, A semi-analytical model for predicting multiple propagating axially symmetric modes in cylindrical waveguides, *Ultrasonics* 43 (2005) 197–207.
- [218] S. D. Akbarov, A. N. Guz, Axisymmetric longitudinal wave propagation in pre-stressed compound circular cylinders, *International Journal of Engineering Science* 42 (2004) 769–791.
- [219] P. R. Heyliger, Axisymmetric free vibrations of finite anisotropic cylinders, *Journal of Sound and Vibration* 148 (3) (1991) 507–520.
- [220] T. Mazúch, Wave dispersion modelling in anisotropic shells and rods by the finite element method, *Journal of Sound and Vibration* 198 (4) (1996) 429–438.
- [221] C. H. Huang, S. B. Dong, Analysis of laminated circular cylinders of materials with the most general form of cylindrical anisotropy. I. Axially symmetric deformations, *International Journal of Solids and Structures* 38 (2001) 6163–6182.
- [222] C. H. Huang, S. B. Dong, Analysis of laminated circular cylinders of materials with the most general form of cylindrical anisotropy. II. Flexural deformations, *International Journal of Solids and Structures* 38 (2001) 6183–6205.
- [223] F. Benmeddour, F. Treyssède, L. Laguerre, Numerical modeling of guided wave interaction with non-axisymmetric cracks in elastic cylinders, *International Journal of Solids and Structures* 48 (5) (2011) 764–774.
- [224] M. L. Accorsi, M. S. Bennett, A finite element based method for the analysis of free wave propagation in stiffened cylinders, *Journal of Sound and Vibration* 148 (2) (1991) 279–292.
- [225] E. Taciroglu, C. Liu, S. Dong, C. Chun, Analysis of laminated piezoelectric circular cylinders under axisymmetric mechanical and electrical loads with a semi-analytic finite element method, *International Journal of Solids and Structures* 41 (2004) 5185–5208.
- [226] L. Elmaimouni, J. E. Lefebvre, V. Zhang, T. Gryba, A polynomial approach to the analysis of guided waves in anisotropic cylinders of infinite length, *Wave Motion* 42 (2005) 177–189.
- [227] Y. Jiangong, W. Bin, H. Cunfu, Characteristics of guided waves in graded spherical curved plates, *International Journal of Solids and Structures* 44 (2007) 3627–3637.
- [228] R. D. Cook, D. S. Malkus, M. E. Plesha, R. J. Witt, Solids of revolution, in: *Concepts and applications of finite element analysis*, 4th Edition, John Wiley & Sons, 2002, Ch. 14, pp. 508–524.
- [229] M. H. Sadd, *Principal values and directions for symmetric second-order tensors*, 1st Edition, Academic Press Inc., 2004.

- [230] W. H. Press, S. A. Teukolsky, W. T. Vetterling, B. P. Flannery, Gaussian quadratures and orthogonal polynomials, in: *Numerical recipes in C*, 2nd Edition, Cambridge University Press, 1992, Ch. 4.5, pp. 147–161.
- [231] F. G. Lether, On the construction of Gauss-Legendre quadrature rules, *Journal of Computational and Applied Mathematics* 4 (1) (1978) 47–52.
- [232] R. D. Cook, D. S. Malkus, M. E. Plesha, R. J. Witt, Isoparametric elements, in: *Concepts and applications of finite element analysis*, 4th Edition, John Wiley & Sons, 2002, Ch. 6, pp. 202–258.
- [233] I. Babuška, T. Strouboulis, A. Mathur, C. S. Upadhyay, Pollution-error in the h-version of the finite-element method and the local quality of a-posteriori error estimators, *Finite Elements in Analysis and Design* 17 (1994) 273–321.
- [234] F. Ihlenburg, I. Babuška, S. A. Sauter, Reliability of finite element methods for the numerical computation of waves, *Advances in Engineering Software* 28 (1997) 417–424.
- [235] P. B. Nagy, Longitudinal guided wave propagation in a transversely isotropic rod immersed in fluid, *Journal of the Acoustical Society of America* 98 (1) (1995) 454–457.
- [236] A. H. Nayfeh, P. B. Nagy, Excess attenuation of leaky Lamb waves due to viscous fluid loading, *Journal of the Acoustical Society of America* 101 (5) (1997) 2649–2658.
- [237] A. Bernard, M. J. S. Lowe, M. Deschamps, Guided waves energy velocity in absorbing and non-absorbing plates, *Journal of the Acoustical Society of America* 110 (1) (2001) 186–196.
- [238] G. V. Borgiotti, E. M. Rosen, Power flow analysis of surface waves on a cylindrical elastic shell in an acoustic fluid, *Journal of the Acoustical Society of America* 95 (1) (1994) 244–255.
- [239] L. Laguerre, A. Grimault, M. Deschamps, Ultrasonic transient bounded-beam propagation in a solid cylinder waveguide embedded in a solid medium, *Journal of the Acoustical Society of America* 121 (4) (2007) 1924–1934.
- [240] W. Hassan, P. B. Nagy, Why fluid loading has an opposite effect on the velocity of dilatational waves in thin plates and rods, *Journal of the Acoustical Society of America* 102 (6) (1997) 3478–3483.
- [241] O. Lenoir, J. M. Conoir, J. L. Izbicki, The complex phase gradient method applied to leaky Lamb waves, *Journal of the Acoustical Society of America* 112 (4) (2002) 1335–1345.
- [242] T. Vogt, M. J. S. Lowe, P. Cawley, The scattering of guided waves in partly embedded cylindrical structures, *Journal of the Acoustical Society of America* 113 (3) (2003) 1258–1272.

- [243] F. Ahmad, Guided waves in a transversely isotropic cylinder immersed in a fluid, *Journal of the Acoustical Society of America* 109 (3) (2001) 886–890.
- [244] C. Baron, S. Naili, Propagation of elastic waves in a fluid-loaded anisotropic functionally graded waveguide: application to ultrasound characterization, *Journal of the Acoustical Society of America* 127 (3) (2010) 1307–1317.
- [245] M. Castaings, C. Bacon, B. Hosten, M. V. Predoi, Finite element predictions for the dynamic response of thermo-viscoelastic material structures, *Journal of the Acoustical Society of America* 115 (3) (2004) 1125–1133.
- [246] M. Drozd, E. Skelton, R. V. Craster, M. J. S. Lowe, Modeling bulk and guided waves in unbounded elastic media using absorbing layers in commercial finite element packages, *AIP Conference Proceedings* 894 (2007) 87–94.
- [247] M. Drozd, L. Moreau, M. Castaings, M. J. S. Lowe, P. Cawley, Efficient numerical modelling of absorbing regions for boundaries of guided waves problems, *AIP Conference Proceedings* 820 (2006) 126–133.
- [248] P. Rajagopal, M. Drozd, E. A. Skelton, M. J. S. Lowe, R. V. Craster, On the use of absorbing layers to simulate the propagation of elastic waves in unbounded isotropic media using commercially available finite element packages, *NDT&E International* 51 (2012) 30–40.
- [249] Z. Fan, M. J. S. Lowe, Interaction of weld-guided waves with defects, *NDT&E International* 47 (2012) 124–133.
- [250] Z. Fan, M. J. S. Lowe, M. Castaings, C. Bacon, Prediction of the propagation and leakage of torsional waves in a waveguide of arbitrary cross-section immersed in a fluid, *AIP Conference Proceedings* 975 (2008) 1567–1574.
- [251] F. Treyssede, K.-L. Nguyena, A.-S. Bonnet-Bendhia, C. Hazard, On the use of a SAFE-PML technique for modeling two-dimensional open elastic waveguides, in: *Acoustics*, 2012, pp. 1–6.
- [252] K. L. Williams, S. G. Kargl, E. I. Thorsos, D. S. Burnett, J. L. Lopes, M. Zampolli, P. L. Marston, Acoustic scattering from a solid aluminum cylinder in contact with a sand sediment: measurements, modeling, and interpretation, *Journal of the Acoustical Society of America* 127 (6) (2010) 3356–3371.
- [253] L. G. Olson, K.-J. Bathe, An infinite element for analysis of transient fluid-structure interactions, *Eng. Comput.* 2 (1985) 319–329.
- [254] X. Qi, X. Zhao, Guided wave propagation in solid structures of arbitrary crosssection coupled to infinite media, *AIP Conference Proceedings* 1681 (2010) 1681–1688.

BIBLIOGRAPHY

- [255] H. Jia, M. Jing, L. R. Joseph, Guided wave propagation in single and double layer hollow cylinders embedded in infinite media, *Journal of the Acoustical Society of America* 129 (2) (2011) 691–700.
- [256] D. Givoli, J. B. Keller, Non-reflecting boundary conditions for elastic waves, *Wave Motion* 12 (1990) 261–279.
- [257] A. J. Deeks, M. F. Randolph, Axisymmetric time-domain transmitting boundaries, *Journal of Engineering Mechanics* 120 (1) (1994) 25–42.
- [258] C. Birk, S. Prempramote, C. Song, An improved continued-fraction-based high-order transmitting boundary for time-domain analyses in unbounded domains, *International Journal for Numerical Methods in Engineering* 89 (2012) 269–298.
- [259] R. Huan, L. L. Thompson, Accurate radiation boundary conditions for the time-dependent wave equation on unbounded domains, *International Journal for Numerical Methods in Engineering* 47 (2000) 1569–1603.
- [260] S. Prempramote, Development of high-order doubly asymptotic open boundaries for wave propagation in unbounded domains by extending the Scaled Boundary Finite Element Method, Ph.D. thesis, University of New South Wales (2011).
- [261] R. Clayton, B. Engquist, Absorbing boundary conditions for acoustic and elastic wave equations, *Bulletin of the Seismological Society of America* 67 (6) (1977) 1529–1540.
- [262] A.-C. Hladky-Hennion, R. Bossut, M. de Billy, Time analysis of immersed waveguides using the finite element method, *Journal of the Acoustical Society of America* 104 (1) (1998) 64–71.
- [263] E. Kausel, Local transmitting boundaries, *Journal of engineering mechanics* 114 (6) (1988) 1011–1027.
- [264] D. Givoli, Non-reflecting boundary conditions, *Journal of Computational Physics* 94 (1991) 1–29.
- [265] J. F. Hall, A. K. Chopra, Two-dimensional dynamic analysis of concrete gravity and embankment dams including hydrodynamic effects, *Earthquake Engineering & Structural Dynamics* 10 (1982) 305–332.
- [266] J. Lysmer, R. L. Kuhlemeyer, Finite dynamic model for infinite media, *Journal of Engineering Mechanics, ASCE* 95 (4) (1969) 859–877.
- [267] O. C. Zienkiewicz, D. W. Kelly, P. Bettess, The Sommerfeld (radiation) condition on infinite domains and its modelling in numerical procedures, in: *Lecture Notes in Mathematics*, Vol. 704, Springer Verlag, Heidelberg, 1979, pp. 169–203.

-
- [268] J. P. Wolf, C. Song, Radiation condition, in: *Finite-element modelling of unbounded media*, 1st Edition, John Wiley & Sons, 1999, Ch. 1.2, pp. 2–4.
- [269] L.-Y. Fu, R.-S. Wu, Infinite boundary element absorbing boundary for wave propagation simulations, *Geophysics* 65 (2) (2000) 596–602.
- [270] E. Kausel, Solution to the Helmholtz and wave equations, in: *Fundamental solutions in elastodynamics*, 1st Edition, Cambridge University Press, 2006, Ch. 8, pp. 98–124.
- [271] J. D. Achenbach, One-dimensional motion of an elastic continuum, in: H. A. Lauwrier, W. T. Koiter (Eds.), *Wave propagation in elastic solids*, 1st Edition, North-Holland Publishing Company, 1973, Ch. 1, pp. 10–45.
- [272] J. L. Rose, Reflection and refraction, in: *Ultrasonic waves in solid media*, 1st Edition, Cambridge University Press, 1999, Ch. 4, pp. 40–53.
- [273] V. Laude, A. Reinhardt, A. Khelif, Equality of the energy and group velocities of bulk acoustic waves in piezoelectric media, *IEEE Transactions on Ultrasonics, Ferroelectrics and Frequency Control* 52 (10) (2005) 1869–1871.
- [274] M. B. Reynolds, The determination of the elastic constants of metals by the ultrasonic pulse technique, *Transactions of the American Society of Metals* 45 (1953) 839–861.
- [275] J. Vishnuvardhan, C. V. Krishnamurthy, K. Balasubramaniam, Genetic algorithm based reconstruction of the elastic moduli of orthotropic plates using an ultrasonic guided wave single-transmitter-multiple-receiver SHM array, *Smart Materials and Structures* 16 (5) (2007) 1639–1650.
- [276] J. Rautenberg, F. Bause, B. Henning, Messsystem zur Bestimmung akustischer Kenngrößen stark absorbierender transversal isotroper Kunststoffe/ Measurement system for the determination of highly absorbing, transverse isotropic polymers, *Technisches Messen* 80 (1) (2013) 28–37.
- [277] W. H. Press, S. A. Teukolsky, W. T. Vetterling, B. P. Flannery, Improving eigenvalues and/or finding eigenvectors by inverse iteration, in: *Numerical Recipes in C*, 2nd Edition, Cambridge University Press, 1992, pp. 493–495.
- [278] G. H. Golub, Q. Ye, Inexact inverse iteration for generalized eigenvalue problems, *BIT Numerical Mathematics* 40 (4) (2000) 671–684.
- [279] F. Bause, J. Rautenberg, B. Henning, Sensitivity study of signal characteristics for an inverse waveguide based approach of material characterization, in: *IEEE International Ultrasonics Symposium*, Dresden, 2012, pp. 719–722.
- [280] B. A. Auld, Excitation of waveguide modes, in: *Acoustic fields and waves in solids Volume II*, 2nd Edition, Krieger Publishing Company, 1990, pp. 161–162.

BIBLIOGRAPHY

- [281] D. Afolabi, Linearization of the quadratic eigenvalue problem, *Computers & Structures* 26 (6) (1987) 1039–1040.
- [282] T.-M. Hwang, W.-W. Lin, V. Mehrmann, Numerical solution of quadratic eigenvalue problems with structure-preserving methods, *SIAM Journal on Scientific Computing* 24 (4) (2003) 1283–1302.
- [283] J. H. Wilkinson, Iterative methods, in: *The algebraic eigenvalue problem*, Oxford University Press, 1999, Ch. 9, pp. 570–649.
- [284] K.-J. Bathe, Wilson, E. L. Wilson, Inverse iteration, in: *Numerical methods in finite element analysis*, Prentice-Hall, Inc., 1976, Ch. 11, pp. 420–443.
- [285] F. Bause, J. Rautenberg, B. Henning, An improved mode-tracing algorithm to compute dispersion curves of acoustic waveguides, *2010 IEEE International Ultrasonics Symposium* (2010) 719–722.
- [286] A. Walther, F. Bause, B. Henning, Computing roots for the modelling of waves in acoustic waveguides, *Pamm* 12 (1) (2012) 763–764.
- [287] F. Bause, A. Walther, J. Rautenberg, B. Henning, Reliable computation of roots in analytical waveguide modeling using an interval-newton approach and algorithmic differentiation, *IEEE Transactions on Ultrasonics, Ferroelectrics and Frequency Control* 60 (12) (2013) 2597–2606.
- [288] M. J. S. Lowe, P. Cawley, J.-Y. Kao, O. Diligent, The low frequency reflection characteristics of the fundamental antisymmetric Lamb wave a_0 from a rectangular notch in a plate, *Journal of the Acoustical Society of America* 112 (6) (2002) 2612–2622.
- [289] C. Yang, L. Ye, Z. Su, M. Bannister, Some aspects of numerical simulation for Lamb wave propagation in composite laminates, *Composite Structures* 75 (2006) 267–275.
- [290] D. N. Alleyne, P. Cawley, A two-dimensional Fourier transform method for the measurement of propagating multimode signals, *Journal of the Acoustical Society of America* 89 (March) (1991) 1159–1168.
- [291] J. Tian, U. Gabbert, H. Berger, X. Su, Lamb wave interaction with delaminations in CFRP laminates, *CMC* 1 (4) (2004) 327–336.
- [292] M. Castaings, E. Le Clezio, B. Hosten, Modal decomposition method for modeling the interaction of Lamb waves with cracks, *Journal of the Acoustical Society of America* 112 (6) (2002) 2567–2582.
- [293] Y. N. Al-Nassar, S. K. Datta, A. H. Shah, Scattering of lamb waves by a normal rectangular strip weldment, *Ultrasonics* 29 (3) (1991) 125–132.

-
- [294] F. Benmeddour, S. Grondel, J. Assaad, E. Moulin, Study of the fundamental Lamb modes interaction with asymmetrical discontinuities, *NDT&E International* 41 (1) (2008) 330–340.
- [295] M. V. Predoi, M. Castaings, L. Moreau, Influence of material viscoelasticity on the scattering of guided waves by defects, *Journal of the Acoustical Society of America* 124 (5) (2008) 2883–2894.
- [296] N. Terrien, D. Royer, F. Lepoutre, a. Déom, Numerical predictions and experiments for optimizing hidden corrosion detection in aircraft structures using Lamb modes., *Ultrasonics* 46 (3) (2007) 251–65.
- [297] J. M. Galán, R. Abascal, Lamb mode conversion at edges. A hybrid boundary element-finite-element solution, *Journal of the Acoustical Society of America* 117 (4) (2005) 1777.
- [298] J. M. Galán, R. Abascal, Boundary element solution for the bidimensional scattering of guided waves in laminated plates, *Computers & Structures* 83 (2005) 740–757.
- [299] S. W. Liu, S. K. Datta, T. H. Ju, Transient scattering of Rayleigh-Lamb waves by a surface-breaking crack: Comparison of numerical simulation and experiment, *Journal of Nondestructive Evaluation* 10 (3) (1991) 111–126.
- [300] J. Rose, S. Pelts, Y. Cho, Modeling for flaw sizing potential with guided waves, *Journal of nondestructive evaluation* 19 (2) (2000) 55–66.
- [301] B. C. Lee, W. J. Staszewski, Lamb wave propagation modelling for damage detection: I. Two-dimensional analysis, *Smart Materials and Structures* 16 (2007) 249–259.
- [302] S. Sundararaman, D. Adams, Modeling guided waves for damage identification in isotropic and orthotropic plates using a local interaction simulation approach, *Journal of Vibration and Acoustics* 130 (2008) 1–16.
- [303] S. I. Rokhlin, Analysis of Lamb wave diffraction by a finite crack using the method of generalized scattering matrices, *1980 Ultrasonics Symposium* 67 (4) (1980) 922–926.
- [304] S. I. Rokhlin, Resonance phenomena of Lamb waves scattering by a finite crack in a solid layer, *Journal of the Acoustical Society of America* 69 (4) (1981) 922–928.
- [305] J. C. P. McKeon, M. K. Hinders, Lamb wave scattering from a through hole, *Journal of Sound and Vibration* 224 (5) (1999) 843–862.
- [306] O. Diligent, T. Grahn, A. Boström, P. Cawley, M. J. S. Lowe, The low-frequency reflection and scattering of the S₀ Lamb mode from a circular through-thickness hole in a plate: Finite Element, analytical and experimental studies, *Journal of the Acoustical Society of America* 112 (6) (2002) 2589–2601.

BIBLIOGRAPHY

- [307] D. Wells, *The Penguin book of curious and interesting numbers*, 2nd Edition, Penguin Books, 1998.
- [308] J. P. Wolf, Mass matrix of bounded medium, in: *The scaled boundary finite element method*, 1st Edition, John Wiley & Sons Ltd., 2003, Ch. 17, pp. 235–241.
- [309] Z. Gajic, M. T. J. Qureshi, Continuous algebraic Lyapunov equation, in: *Lyapunov matrix equation in system stability and control*, 1st Edition, Academic Press Inc., 1995, Ch. 2, pp. 21–77.
- [310] C. C. K. Mikkelsen, Numerical methods for large Lyapunov equations, Ph.D. thesis, Purdue University (2009).
- [311] F. T. Man, A high-order method of solution for the Lyapunov matrix equation, *The Computer Journal* 14 (3) (1971) 291–292.
- [312] R. H. Bartels, G. W. Stewart, Solution of the matrix equation $AX + XB = C$, *Communications of the ACM* 15 (9) (1972) 820–826.
- [313] Z. Tian, C. Gu, A numerical algorithm for Lyapunov equations, *Applied Mathematics and Computation* 202 (1) (2008) 44–53.
- [314] N. M. Newmark, A method of computation for structural dynamics, *Proceedings of the American Society of Civil Engineers* 85 (3) (1959) 67–94.
- [315] K.-J. Bathe, E. L. Wilson, The Newmark method, in: *Numerical methods in finite element analysis*, Prentice-Hall, Inc., 1976, Ch. 8.2.4, pp. 322–326.
- [316] Ansys Inc., Ansys, version 13.0 [computer program] (2010).
- [317] J.-C. Hong, K. H. Sun, Y. Y. Kim, Dispersion-based short-time Fourier transform applied to dispersive wave analysis, *Journal of the Acoustical Society of America* 117 (5) (2005) 2949–2960.
- [318] Comsol Ltd., Comsol Multiphysics [computer program], version 4.0a (2010).
- [319] J. P. Wolf, C. Song, Summary of coefficient matrices for axisymmetric vector wave equation, in: *Finite element modelling of unbounded media*, 1st Edition, John Wiley & Sons, 1999, pp. 81–87.

List of Figures

1.1	Detection of a defect by means of traditional ultrasonic material testing.	2
1.2	(a) Excitation of waves in a large homogeneous solid. (b) Propagation of longitudinal, shear and Rayleigh waves.	2
1.3	Cross-sectional view of a homogeneous plate with an ultrasonic transducer coupled to the upper surface.	3
1.4	(a) Horizontal and (b) vertical displacements of the fundamental guided wave modes.	4
1.5	Phase velocities of propagating modes in a homogeneous isotropic plate.	4
2.1	(a) Computational domain Ω with boundary Γ ; (b) schematic discretization using four-sided elements.	15
2.2	Rectangular element and examples for quadratic shape functions corresponding to (a) a corner node and (b) a node on the edge.	16
2.3	(a) Distorted four-sided element and (b) mapped element in local coordinate system.	17
2.4	Discretization using the Scaled Boundary Finite Element Method.	20
2.5	(a) Discretization of a plate with a hole, using 4 subdomains; (b) introducing a crack into a subdomain.	23
3.1	Plate geometry for the Scaled Boundary Finite Element formulation with a discretized interface.	27
3.2	One element of the discretization, defined in the local coordinate η	28
3.3	Shape function N_6 of the central node of an element of order 10.	35
3.4	Discretization of a layered structure.	38
3.5	Discretization of a plate (a) and cylinder (b) in the SBFEM.	43
3.6	Non-dimensional dispersion curves for a homogeneous plate with a Poisson's ratio of 0.3.	48
3.7	Convergence of the results for the highest propagating mode at a dimensionless frequency of 20 in the homogeneous plate.	50
3.8	Displacement amplitudes in y -direction of the four propagating modes at a dimensionless frequency of 6 in the homogeneous plate.	51
3.9	Dispersion curves for a composite consisting of 3 layers of brass and 2 layers of titanium.	52

LIST OF FIGURES

3.10	Distribution of material parameters in the functionally graded material.	54
3.11	Dispersion curves for a functionally graded material.	54
3.12	Convergence of the results for the highest mode at a dimensionless frequency of 20 in the functionally graded material.	55
4.1	Discretization of an arbitrary 3d waveguide with four-sided elements.	59
4.2	Two-dimensional shape function of order 6.	62
4.3	Reducing the discretization of a two-dimensional cross-section by applying boundary conditions.	63
4.4	To trace a mode, a guess k_T for the wavenumber k_3 is computed, based on the wavenumbers k_0, k_1, k_2	66
4.5	Quarter of the cross-section of a circular rod, discretized by three elements of order 4.	69
4.6	Dispersion of the propagating modes in a circular rod.	70
4.7	Tracing of some selected modes using a Taylor series and the Padé expansion.	71
4.8	Cross-section of a square pipe, discretized with two elements of order 7.	72
4.9	Phase velocity dispersion of the SS modes in the square tube.	72
4.10	Examples of mode shapes in the square pipe at a frequency of 10 kHz.	73
5.1	Discretization of a cylinder in the SBFEM.	77
5.2	Shape functions, nodes and integration points for different types of elements.	87
5.3	Dispersion curves of an isotropic homogeneous pipe.	89
5.4	Cross-section of a layered cylinder.	90
5.5	Dispersion curves of a layered rod.	91
5.6	Dispersion curves for a pipe with cubic anisotropy.	93
5.7	Dispersion curves for an orthotropic pipe.	93
5.8	Maximum error of the wavenumbers as a function of the number of nodes at a dimensionless frequency of $a = 50$ in an isotropic pipe.	94
5.9	Number of nodes that are required to obtain a maximum error of 0.1% if the Gaussian-Lobatto-Legendre quadrature (a) or the traditional Gaussian quadrature (b) is employed.	96
5.10	Converged results for the phase velocities compared with GLL and Gaussian quadrature for the same number of nodes.	97
6.1	One-dimensional wave propagation in two adjoining half spaces.	101
6.2	Three-dimensional dashpot boundary condition on a plate surface.	104
6.3	Discretization of the waveguide and surrounding medium using two elements of high order.	108
6.4	Aluminum plate attached to an elastomer of infinite dimensions.	110
6.5	(a) Phase velocities and (b) attenuations of the fundamental symmetric, anti-symmetric and shear-horizontal modes in an aluminum plate attached to an infinite elastomer.	111

6.6	Attenuation of the propagating modes in a plate attached to an infinite medium for different ratios of acoustic impedances.	114
6.7	Cross-section of a timber pole embedded in soil.	115
6.8	(a) Phase velocities and (b) attenuations of longitudinal and flexural modes in an embedded timber pole.	116
7.1	(a) Experimental set-up for the material characterization of cylindrical waveguides and (b) example of a measured signal.	118
7.2	Normalized modal amplitudes of the longitudinal modes in a hollow PPN cylinder.	119
7.3	Phase velocities of propagating modes in a hollow PPN cylinder, computed using the \mathbf{Z} -matrix and the linear approximation.	122
7.4	Dispersion curves computed using the proposed algorithm and compared to results obtained with the Global Matrix Method.	131
7.5	(a) Example of estimated phase velocities in the mode-tracing algorithm using different frequency increments. (b) Convergence of the estimated values towards the desired eigenvalue in the inverse iteration.	131
7.6	Computational time to obtain one eigenvalue using the inverse iteration compared to solving the full eigenvalue problem.	134
7.7	Ratio of computational times required for the eigenvalue solver and inverse iteration.	134
7.8	Dispersion curves for a PPO-GF30 cylinder.	135
8.1	Group velocity dispersion for the first Lamb wave modes in a 2 mm thick steel plate.	141
8.2	Pulse applied to the structure for the excitation of Lamb waves.	142
8.3	Representative part of the discretization of a cracked plate using the SBFEM.	142
8.4	Discretization of a test problem in the (a) Finite Element Method and (b) Scaled Boundary Finite Element Method.	144
8.5	Vertical displacement at point A computed with the FEM and the SBFEM.	145
8.6	Average deviation from the FE result with the finest discretization as a function of (a) the number of degrees of freedom (DOF) and (b) the computational time.	146
8.7	Displacements at the upper and lower surface of the plate to visualize (a) the incoming pulse, (b) the interaction with the crack, (c) the reflected and transmitted signals	149
8.8	Displacement on plate surface at $t = 31.5 \mu\text{s}$ and the results of a spatial Fourier transformation.	150
8.9	Vertical displacement amplitudes of the (a) S_0 and (b) A_0 mode in the reflected signal as a function of the relative crack depth, divided by the amplitude of the incident S_0 mode.	151
8.10	Vertical displacement amplitudes of the (a) S_0 and (b) A_0 mode in the reflected signal as a function of the relative crack depth, divided by the amplitude of the incident A_0 mode.	153

LIST OF FIGURES

8.11 Ratio of the amplitudes of the two fundamental modes in the reflected signal in case of an incident (a) S_0 mode and (b) A_0 mode.	154
---	-----

List of Tables

2.1	Nodal coordinates η_i, ξ_i and corresponding shape functions for a quadratic element in one and two dimensions.	16
3.1	Properties of the coefficient matrices.	39
3.2	Dimensionless phase velocities of all propagating modes for the homogeneous plate at dimensionless frequencies $a = 6$ and $a = 16$ obtained with elements of different order.	49
3.3	Dimensionless phase velocities of all eleven propagating modes at a dimensionless frequency of 20 for the FGM plate.	56
5.1	Average number of nodes per transversal wavelength in an isotropic material that are required to obtain a maximum error of 0.1% and 1%, respectively. . . .	98
6.1	Numerical study to analyze the effect of varying acoustic impedances of the surrounding medium on a waveguide.	113
7.1	Numerical study to test convergence of the inverse iteration for one eigenvalue.	133
8.1	Comparison of different FEM and SBFEM discretizations for the case of an incident S_0 mode.	152

Acknowledgements

The work presented in this thesis was carried out during my employment at the Federal Institute for Materials Research and Testing (BAM) in Berlin in cooperation with the Technische Universität Braunschweig and with support of the University of New South Wales (UNSW) in Sydney, Australia. I would like to take the opportunity to thank the numerous supporters for the great help I received during these years.

- First of all I cannot thank **Prof. Chongmin Song** enough for the guidance and supervision of this project. With his brilliant ideas, hard work and enthusiasm he took the quality of this research to a whole new level.
- I would like to thank **Prof. Marc Kreutzbruck** for his supportive and respectful supervision during the last years.
- Many thanks to my supervisor **Prof. Sabine Langer** for her encouraging support and for reviewing my thesis.
- I would also like to thank **Prof. Laura de Lorenzis** and **Prof. Dieter Dinkler** for the interesting and friendly discussions during the defense.
- Furthermore, I want to thank **Dr. Carolin Birk** for her considerable contributions and financial support of the cooperation.
- Also many thanks to **Dr. Jens Prager** for his organizational and technical support.
- I am very grateful to my friends and colleagues **Dr. Hou Man** and **Irene Chiong** who were always there for me with professional or personal advice and technical support on numerous occasions.
- I would like to thank all my co-workers at BAM and UNSW who contributed to the friendly and fruitful atmosphere and shared their knowledge and expertise.
- Many thanks to the students and interns who contributed to my work, particularly **Albert Artha Saputra**, **Joschua Dilly** and **Jason Van**.
- I wish to thank **Fabian Bause**, **Dr. Jens Rautenberg** and **Prof. Bernd Henning** at the University of Paderborn for the successful cooperation on material characterization applications.
- I would also like to thank **Prof. Volker Mehrmann** and **Dr. Christian Schröder** at the Technische Universität Berlin for sharing their knowledge and algorithms on Hamiltonian eigenvalue problems.

- Thanks to **Mahbube Subhani, Dr. Ulrike Dackermann** and **Prof. Jianchun Li** at the University of Technology Sydney for fruitful discussions on embedded waveguides.
- The subsidy of the **German Academic Exchange Service** (DAAD Doktorandenstipendium) is gratefully acknowledged.
- Many thanks to my colleagues and friends who helped me by proofreading, asking critical questions, adding interesting information or improving figures: **Maxim Daschewski, Christian Hoffmann, Matthias Tuma, Jessica Kitze, Verena Reimund, David Coverly, Regina Richter, Kathrin Stavenhagen, Sascha Hoffmann, Martin Claus, Gregor Fischer.**
- A big thank you to my close friends in Berlin, Hamburg and Sydney for making this PhD project a most enjoyable time and backing me up many times with support and advice.
- Lastly, I want to thank my loving family for their never-ending trust and support.